

VRIJE UNIVERSITEIT

**Gemmology, geology and origin
of the Sandawana emerald deposits,
Zimbabwe**

ACADEMISCH PROEFSCHRIFT

ter verkrijging van de graad Doctor aan
de Vrije Universiteit Amsterdam,
op gezag van de rector magnificus
prof.dr. T. Sminia,
in het openbaar te verdedigen
ten overstaan van de promotiecommissie
van de faculteit der Aard- en Levenswetenschappen
op donderdag 26 januari 2006 om 13.45 uur
in de aula van de universiteit,
De Boelelaan 1105

door

Johannes Cornelis Zwaan

geboren te Leiden

promotor: prof.dr. J.L.R. Touret
copromotor: prof.dr. L.M. Kriegsman

Gemmology, geology and origin of the Sandawana emerald deposits, Zimbabwe

J.C. Zwaan

Zwaan, J.C. Gemmology, geology and origin of the Sandawana emerald deposits, Zimbabwe. *Scripta Geologica*, **131**: 1-211, 82 figs., 25 tables, 3 appendices, January 2006.

J.C. Zwaan, Nationaal Natuurhistorisch Museum Naturalis, P.O. Box 9517, NL-2300 RA Leiden, The Netherlands (zwaan@naturalis.nnm.nl).

Key words – Emerald, Sandawana, Zimbabwe, gemmology, petrology, geothermometry, geochronology.

Abstract

As one of the most valuable gemstones, emeralds are known to occur in several countries of the world, such as Colombia, Zambia, Brazil, Pakistan, Afghanistan, Russia, Madagascar and Zimbabwe. The emerald deposits at Sandawana, Zimbabwe, are described, the emeralds from this deposit characterised and a model of emerald formation presented; this is compared with existing models.

The emeralds from Sandawana, Zimbabwe, show relatively constant physical properties, with high refractive indices and specific gravities. They are characterized by laths and fibres of amphibole, both actinolite and cummingtonite. Other common inclusions are albite and apatite. Rare, opaque and chromium-rich inclusions constitute a new variety of ilmenorutile. Compared to emeralds from most other localities, fluid inclusions are rare and small. Sandawana emeralds have very high contents of chromium, sodium, magnesium, lithium and caesium. They can be readily separated from emeralds from most other localities by using traditional gem testing techniques, on the basis of a combination of physical properties, inclusions and chemistry. In cases of possible doubt, such as in comparison with emeralds from Rajasthan (India), the use of oxygen isotopes is helpful.

Sandawana emeralds occur at the contact between greenstones of the Mweza Greenstone Belt (MGB) and pegmatite intrusions. Rare-element granitic pegmatites intruded the MGB just prior to and/or during a main deformation event at 2.6 Ga, at the southern border of the Zimbabwe craton. Subsequently, a late-stage Na-rich 'solution-melt' containing F, P, Li, Be and Cr was injected along shear zones, causing albitisation of the pegmatite and phlogopitization in the greenstone wall-rock. Coeval ductile deformation is indicated by boudinage, pinch-and-swell and folding of pegmatites, by differentiated layering in associated amphibole-phlogopite schist and by the presence of (micro)shear zones. The synkinematic growth of not only phlogopite, but also emerald, fluorapatite, holmquistite and chromian ilmenorutile, indicates enrichment of Na, K, Li, Be, F, P, Rb, Cs, Ta and Nb in the emerald-bearing shear zone. This suggests that emerald formation is closely related to syntectonic K-Na metasomatism. In this process, microcline, oligoclase, quartz (from the pegmatite) and chlorite (from the greenstones) were consumed, in favour of albite (in the pegmatite), phlogopite, some new actinolite and cummingtonite, holmquistite, fluorapatite and emerald (at the contact and in the greenstone). Mass

balance calculations indicate that a Na- and F-rich hydrous fluid must have been involved in the alterations that ultimately caused emerald formation. The presence of small, isolated, highly saline brine inclusions in emerald supports this result. Formation of gem-quality emerald occurred in relatively low-pressure domains, such as 'traps' under folded pegmatite or pinch areas near pegmatites with pinch-and-swell or boudin structures.

Apatite-phlogopite thermometry gives $T = 560\text{--}650^\circ\text{C}$, interpreted as the temperature range at which emerald was formed. These temperatures imply contact metamorphic rather than regional metamorphic conditions. From the general conditions of primary consolidation of rare element pegmatites, and from the inferred crystallisation path of the similar Bikita pegmatite, a corresponding pressure of around 2.5-3 kbar appears plausible at Sandawana. Because of the intimate spatial and temporal relationship with magmatic activity, the pegmatitic/hydrothermal nature of the involved fluid, and the near magmatic temperatures of phlogopite and apatite formation, a magmatic source for the Na-rich fluids is very likely. It means that intrusion of the pegmatites, and subsequent albitisation and metasomatism during deformation, have been part of a continuous process in a restricted period of time.

The Sandawana data lead to a new model of emerald formation, as a product of contact metasomatism at the border of ultramafic rocks and rare-element pegmatites during a deformation event, involving late stage magmatic/hydrothermal activity channelled by shearing. Hence, Sandawana emeralds were formed in the Late Archaean, around 2.6 Ga, at the border of a major Late Archaean suture zone. As a consequence, they are by far the oldest, compared to other commercially available emeralds. $^{40}\text{Ar}/^{39}\text{Ar}$ dates, varying from 1900 to 2400 Ma, are interpreted as Archaean ages that became partially to completely reset during a Proterozoic thermal overprint.

The Sandawana model for emerald genesis does not fit into any of the genetic classification schemes proposed in the literature, and shows that no single theory can be applied to all schist-type deposits. Emeralds of gem quality can be formed in very different geological settings, as long as basic conditions are fulfilled. In this respect, the following factors are essential: availability of beryllium and chromium (\pm vanadium); means of transport to bring the elements together, that is, fluids of magmatic, hydrothermal, metamorphic or a combined origin; conditions in which emerald may form as a stable mineral, with temperatures generally from 600° down to 300°C ; and sufficient space to grow transparent and well-formed crystals.

Samenvatting – Abstract in Dutch

Smaragd, een van de meest waardevolle edelstenen, wordt gevonden in verschillende landen, zoals Colombia, Zambia, Brazilië, Pakistan, Afghanistan, Rusland, Madagascar en Zimbabwe. In dit proefschrift worden de smaragdvoorkomens van Sandawana, Zimbabwe, beschreven. De smaragden van deze voorkomens worden gekarakteriseerd, en een nieuw model voor de vorming van smaragd wordt gepresenteerd. Dit model wordt vergeleken met bestaande modellen.

De smaragden van Sandawana, Zimbabwe, hebben relatief constante fysische eigenschappen, met hoge brekingsindices en dichtheden. Ze worden gekarakteriseerd door ingesloten latvormige kristallen en vezels van amfibool, zowel actinoliet als cumming-

toniet. Andere insluitsels die gewoonlijk worden aangetroffen zijn albiet en apatiet. Zeldzame, chroomrijke insluitsels vormen een nieuwe variëteit van ilmenorutiel. Vergeleken met smaragden van de meeste andere vindplaatsen zijn vloeistofinsluitsels klein en zeldzaam. Sandawana smaragden bevatten hoge concentraties chroom, natrium, magnesium, lithium en cesium. Met behulp van traditionele edelsteenidentificatie technieken kunnen ze gemakkelijk worden onderscheiden van smaragden afkomstig van andere lokaliteiten, op basis van een combinatie van fysische eigenschappen, insluitsels en chemie. In mogelijke twijfelgevallen, zoals in de vergelijking met smaragd uit Rajasthan (India), is het gebruik van zuurstofisotopen nuttig.

Sandawana smaragden komen dichtbij het contact tussen groenstenen van de Mweza groensteengordel en pegmatietintrusies voor. Voor en/of tijdens de belangrijkste deformatiefase (gedateerd op 2,6 miljard jaar) drongen granitische pegmatieten met zeldzame elementen in de Mweza groensteengordel, aan de zuidelijk grens van het Zimbabwe kraton. Vervolgens drong in een laat stadium van magmatische activiteit een natriumrijke 'oplossing-smelt' met daarin fluor, fosfor, lithium, beryllium en chroom, binnen langs schuifzones. Dit veroorzaakte omzetting van de pegmatiet in albiet en vorming van phlogopiet in de groensteen, direct grenzend aan de pegmatiet. Gelijktijdige buigzame (plastische) vervorming blijkt uit dichtgeknepen en uiteengetrokken ('geboudineerde'), en geploide pegmatieten, uit gedifferentieerde gelaagdheid in geassocieerde amfibool-phlogopiet-schisten en de aanwezigheid van (micro)schuifzones. Het feit dat niet alleen phlogopiet, maar ook smaragd, fluorapatiet, holmquistiet en chroomhoudende ilmenorutiel tijdens de vervorming van de gesteenten zijn gegroeid, wijst op verrijking van natrium, kalium, lithium, beryllium, fluor, fosfor, rubidium, cesium, tantalum en niobium in de smaragdhoudende schuifzones. Dit suggereert dat smaragdvorming sterk is gerelateerd aan syntektonische kalium-natrium metasomatose. In dit proces werden microklien, oligoklaas, kwarts (vanuit de pegmatiet) en chloriet (uit de groensteen) geconsumeerd, ten gunste van de vorming van albiet (in de pegmatiet), phlogopiet, nieuwe actinotiet en cummingtoniet, holmquistiet, fluorapatiet en smaragd (zowel op het contact als in de groensteen naast de pegmatiet). Massabalans berekeningen geven aan dat een Na- en F-rijke vloeistof betrokken moet zijn geweest bij de omzettingen die uiteindelijk de vorming van smaragd hebben veroorzaakt. De aanwezigheid van kleine geïsoleerde vloeistofinsluitsels met een zeer hoog zoutgehalte ondersteunen dit resultaat. De vorming van edelsteenkwaliteit smaragd vond plaats in relatief lage druk domeinen naast vervormde pegmatiet.

Apatiet-phlogopiet thermometrie geeft temperaturen variërend van 560 tot 650°C. Deze hoge temperaturen zijn geïnterpreteerd als indicatief voor het temperatuurbereik waarin smaragd werd gevormd, en wijzen op een samenhang met magmatische activiteit. Op basis van de algemene condities waaronder 'zeldzaam element' pegmatieten consolideren, en het afgeleide kristallisatiepad van de soortgelijke en nabije Bikita pegmatiet, lijkt een druk van 2,5 tot 3 kbar (2500-3000 atm.) aannemelijk tijdens de smaragdvorming in Sandawana. Vanwege de overlap in ruimte en tijd met magmatische activiteit, het pegmatitisch/hydrothermale karakter van de aanwezige vloeistof, en de bijna magmatische temperaturen, is een magmatische oorsprong van de Na-rijke vloeistoffen zeer aannemelijk.

De Sandawana gegevens leiden tot een nieuw model voor smaragdvorming, namelijk smaragdvorming als een product van contact-metasomatose op de grens van

ultramafische gesteenten en 'zeldzaam element' pegmatieten, tijdens een deformatiefase, waarbij laat-magmatische/hydrothermale activiteit, gekanaliseerd door schuifzones, een belangrijke rol heeft gespeeld. Een gevolgtrekking uit dit model is dat Sandawana smaragden gevormd zijn in het late Archeïcum, rond 2,6 miljard jaar, aan de grens van een grote Laat-Archeïsche suturezone. Deze smaragden zijn daarom verreweg de oudste, vergeleken met commercieel beschikbare smaragden uit andere vindplaatsen.

⁴⁰Ar/³⁹Ar dateringen, variërend van 1900 tot 2400 miljoen jaar, zijn geïnterpreteerd als Archeïsche ouderdommen die gedeeltelijk tot geheel werden bijgesteld gedurende opwarming van het gebied tijdens het Proterozoïcum.

Het Sandawana model voor smaragdgenese past in geen van de genetische classificaties in de literatuur, en laat zien dat niet één enkele theorie kan worden toegepast op alle 'schist-type' smaragdvoorkomens. Smaragd van edelsteenkwaliteit kan in heel verschillende geologische omstandigheden worden gevormd, als maar voldaan wordt aan basiscondities. De volgende factoren zijn hierbij essentieel: beschikbaarheid van beryllium en chroom (en/of vanadium); een transportmiddel om deze elementen bij elkaar te brengen, zoals vloeistoffen van magmatische, hydrothermale, metamorfe of een gecombineerde oorsprong; condities waarbij smaragd kan vormen als een stabiel mineraal, met in het algemeen temperaturen van 600° tot aan 300°C, en voldoende ruimte voor de groei van doorzichtige en goed gevormde kristallen.

Contents

1. Introduction and models of emerald formation	7
2. Geology of the Sandawana emerald deposit	26
3. Gemmology of Sandawana emeralds	60
4. Key processes and conditions leading to emerald formation in the Mweza Greenstone Belt	98
5. Oxygen isotopes and Ar-Ar dating: implications for the origin and timing of emerald formation at Sandawana	132
6. Conclusions and model of emerald formation	159
Acknowledgements	164
References	165
Appendix 1. Emerald analyses by EPMA	177
Appendix 2. Emerald analyses by PIXE/PIGE	188
Appendix 3. Representative mineral analyses by EPMA	190

1. Introduction and models of emerald formation

1.1. Scope

Together with diamond, ruby and sapphire, emerald belongs to the group of most valuable gemstones. Emerald, the green variety of the mineral beryl ($\text{Be}_3\text{Al}_2\text{Si}_6\text{O}_{18}$), is not only beautiful, but also very rare. Its rarity can partly be explained by the fact that beryllium is rare in all but a few rocks; for the Earth's crust as a whole Be is the 47th most abundant element (Emsley, 2001). Current estimates are that the upper crust averages 3 ppm Be, which is found to be 50 times more than in primitive mantle (Grew, 2002). The other reason for its rarity is that the colour of emerald is caused by small concentrations of chromium and/or vanadium. In emerald, many trace elements, like lithium, caesium, sodium, magnesium, iron, chromium and vanadium, may be present. Beryllium, lithium, caesium and aluminium are commonly found in pegmatite, a fractionated igneous rock, which especially bears lighter elements. In contrast, chromium, magnesium and iron are common in igneous rocks of an ultrabasic or basaltic nature, which are formed in completely different geological environments. Thus, elements like Be and Li on the one hand, and Cr, Mg and Fe on the other, are geochemically incompatible, which means that apparently very special geological conditions are needed to form emerald.

The 'classical' theory about the genesis of many emerald deposits in the world (e.g., Sinkankas, 1981) considers that emeralds were formed during interaction between invading pegmatitic magma and pre-existing metamorphosed rocks of (ultra)basic composition. In this model, emeralds were formed as a result of a single-stage contact metamorphism at the border zone of intruding pegmatitic bodies. However, in the late 1980s, this contact metamorphism concept was challenged by Grundmann & Morteani (1989). They found that, at Habachtal (Austria) and at Leydsdorp in Transvaal, South Africa, emeralds were formed by reactions that took place during deformation of the rocks and low-grade regional metamorphism. In Habachtal, emeralds were formed in a shear zone and were not found in association with pegmatite (although pegmatites do occur in that region); chromium came from serpentinites, while beryllium came from



Fig. 1. Map of emerald localities in the World; the major commercial mining areas are indicated. (1) Colombia, western emerald zone: Muzo, Coscuez, Yacopi, Peña Blanca; eastern emerald zone: Chivor, Gachalá. (2) Zambia, Kafubu area near Kitwe. (3) Brazil, Minas Gerais: (a) Itabira district (Belmont, Piteiras and Capoeirana mines), (b) Santana dos Ferros; Goiás: (c) Fazenda das Lajes, (d) Santa Terezinha de Goiás, (e) Pirenópolis; Bahia: (f) Fazenda do Pombo, (g) Açude do Sossego, (h) Brumado, (i) Carnaíba, (j) Salinhas, (k) Socotó; Ceará: (l) Tauá. (4) Pakistan: Swat Valley, Malakand and Mohmand region, Bajaur Agency and Khaltaro region. (5) Afghanistan: Panjsher Valley and Badel mine. (6) Russia: (a) Ural Mountains: Malyshewo, Tokowaja (b) Ukraine: Wolodarsk. (7) Madagascar: Mananjary region. (8) Zimbabwe: Sandawana and Filabusi. (9) Australia: (a) Wodgina, (b) Warda Wara, Melville and Poona,



■ minor or former commercial mining

(c) Menzies, (d) Emmaville/Torrington. (10) Austria: Habachtal. (11) Bulgaria: Rhodopa-Rila mountains. (12) Canada, Yukon: Regal Ridge, Finlayson Lake district. (13) China, Yunnan: Malipo county, Ailaoshan region. (14) Egypt, Eastern Desert, Gebel Sikait and Gebel Zabara. (15) India, (a) Rajasthan: Bubani mine, between Ajmer and Udaipur, (b) Tamil Nadu: Sankari Taluka. (16) Mozambique: Morrua district. (17) Namibia: Namaqualand: Neuhof/Hammerstein. (18) Nigeria: Kaduna state, central Nigeria. (19) Norway: Eidsvoll. (20) South Africa, Gravelotte, Leydsdorp district. (21) Somalia: Boorama. (22) Spain, Galicia: Franqueira. (23) Tanzania, Lake Manyara. (24) USA, North Carolina: Hiddenite. Revised and modified from Kazmi & Snee (1989), Giuliani *et al.* (1998) and Grundmann (2001); Brazil after Schwarz *et al.* (1990a, b); Namibia after Schäfer (2002).

mica schists adjacent to the serpentinites. In Leydsdorp, pegmatite was found in relation to emerald, but other evidence indicated that emeralds actually formed during a later deformation event and not when the pegmatite originally intruded. Grundmann & Morteani (1989) also suggested that most if not all of the schist-type emerald deposits in metamorphic rocks may be the product of a deformation event accompanied or followed by regional metamorphism. Taking up the challenge to test this hypothesis in other areas, herein I describe the emerald deposits at Sandawana, Zimbabwe, present a model of emerald formation and show how it relates to existing models.

In gemmology, there is large commercial interest in establishing the geographic origin of cut gemstones, especially of ruby, sapphire and emerald. Once it is established where a cut gem originally came from, it may improve the value considerably. A complicating factor in gathering evidence for a particular locality is that only non-destructive analytical techniques may be used on valuable gemstones. For this reason, the emeralds from Sandawana are thoroughly characterised and compared with emeralds from other localities, using non-destructive identification techniques only.

Unless stated otherwise, number samples form part of the collection of the Nationaal Natuurhistorisch Museum, Leiden (RGM).

1.2. Outline

In Section 1.3, an overview of the most important emerald deposits is given and current models of emerald formation are presented. Subsequently (Chapter 2), the regional setting and geology of the Sandawana emerald deposits are described. Although the Sandawana mines have been exploited since the mid-1950s, only brief articles on the characteristics of Sandawana emeralds had been published until Zwaan *et al.* (1997). There has also been little information about the mining area, and the techniques used for exploration, mining and processing. More and revised information on these topics is given in Chapter 3. Using the information in Chapter 2 and 3, the processes that lead to the formation of emerald at Sandawana are discussed in Chapter 4. Oxygen isotope studies are presented in Chapter 5 and the implications for the characterization of emeralds from different localities are discussed. Subsequently, Ar-Ar dating results and geochronology, including the timing of emerald formation, are discussed. Finally, in the concluding Chapter 6, the results obtained at Sandawana are compared with existing models of emerald formation. Representative mineral analyses (EPMA and PIXE/PIGE) of Sandawana emeralds and associated phases are included in the appendices.

1.3. Current models of emerald formation

Emeralds are known to occur in several countries of the world. Deposits of economical significance occur in Colombia, Zambia, Brazil, Pakistan, Afghanistan, Russia, Madagascar and Zimbabwe (Giuliani *et al.*, 1998). Other countries with emerald occurrences include Australia, Austria, Bulgaria, Canada, China, Egypt, India, Mozambique, Nigeria, Norway, South-Africa, Somalia, Spain, Tanzania and the USA (Fig. 1).

1.3.1. The classic model of emerald formation – Most emeralds are found in ‘schist-type’ deposits, and are attributed to the interaction between invading pegmatitic magmas/

fluids and pre-existing (ultra)mafic rocks (Fig. 2) (e.g., Fersman, 1929; Sinkankas, 1981; Kazmi & Snee, 1989). This interaction was usually envisaged as a single-stage contact metamorphism at the border zone of magmatic intrusive bodies. Components carried by pegmatitic fluids (e.g., Li, Be, Al, Si, K, Na) or leached from the invaded rock (e.g., Si, Mg, Fe, Ca, Cr, V) may combine and form emeralds in the alteration zone at the contact of the intruded rock and host rock. Recent and typical examples of the formation of emerald according to this model are demonstrated by Laurs *et al.* (1996) in the Haramosh Mountains, northern Pakistan, and by Seifert *et al.* (2004) in the Kafubu area, Zambia.

Khaltaro, Haramosh massif, Pakistan – In northern Pakistan, emeralds are found within hydrothermal veins and granitic pegmatites cutting amphibolite, within the Nanga Parbat – Haramosh massif, at Khaltaro. Pegmatites intruded at 9 Ma, after peak Tertiary metamorphism which reached 325-550°C prior to 10 Ma (Laurs *et al.*, 1996). Simply zoned, albite-rich, miarolitic pegmatites and hydrothermal veins, containing various proportions of quartz, albite, tourmaline, muscovite and beryl, are associated with a 1 to 3 m-thick heterogeneous leucogranite sill, that is locally albitized. The pegmatites likely crystallised at 650 to 600°C at pressures of less than 2 kbar. Emerald crystals formed within thin (<30 cm) veins of quartz, tourmaline and albite, and more rarely in

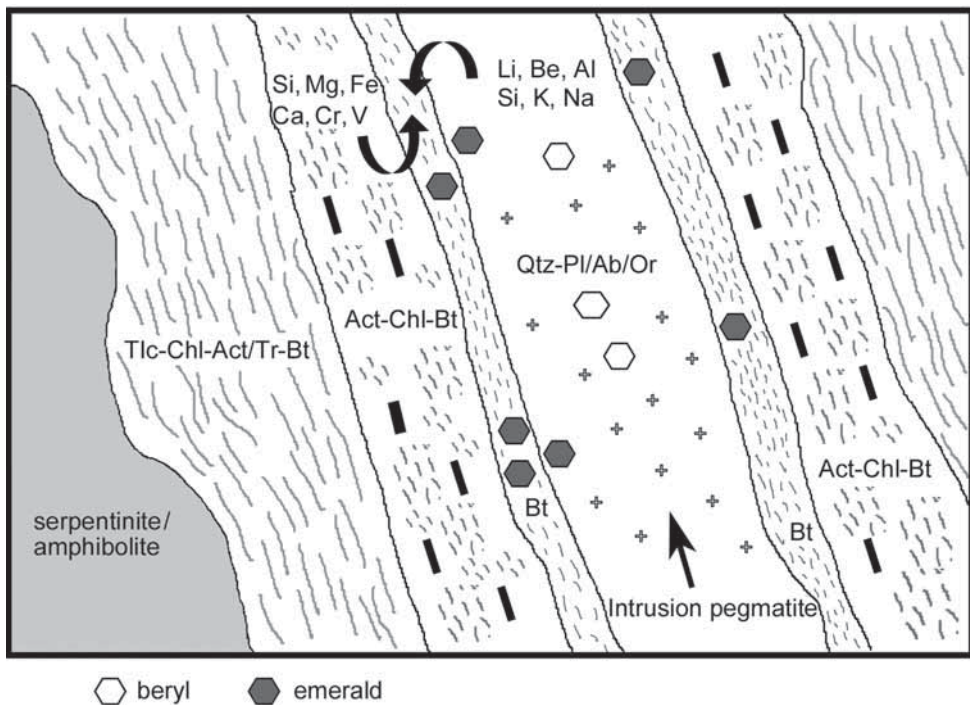


Fig. 2. Traditional model of emerald formation; single stage contact metamorphism at the margin of (ultra)basic rocks and intruding pegmatite (after Fersman, 1929; Beus, 1966; Sinkankas, 1981). Qtz = quartz, Pl = plagioclase, Ab = albite, Or = orthoclase, Act = actinolite, Tr = tremolite, Bt = biotite, Chl = chlorite, Tlc = talc.

pegmatite, near the contacts with altered amphibolite. The amphibolite was metasomatised in less than 20 cm-wide selvages that are symmetrically zoned around veins or pegmatites. A sporadic inner zone (closest to the pegmatite or vein) contains F-rich biotite and tourmaline, with local albite, muscovite, quartz and rare beryl. The intermediate zone contains biotite and fluorite with local plagioclase and quartz, whereas the outer zone consists of amphibolite with sparse biotite and local quartz. The inner and intermediate zones experienced gains of K, H, F, B, Li, Rb, Cs, Be, Ta, Nb, As, Y and Sr, and losses of Si, Mg, Ca, Fe, Cr, V and Sc. The outer alteration zone gained F, Li, Rb, Cs and As. Laurs *et al.* (1996) stated that oxygen isotope analyses of igneous and hydrothermal minerals indicate that a single fluid of magmatic origin (calculated $\delta^{18}\text{O}_{\text{H}_2\text{O}} = 8\text{‰}$) produced the pegmatite-vein system and hydrothermal alteration at temperatures between 550° and 400°C. They concluded that the formation of emerald results from introduction of HF-rich magmatic-hydrothermal fluids into the amphibolite, which caused hydrogen metasomatism and released Cr and Fe into the pegmatite-vein system.

It can be argued, however, whether the temperatures between 550° and 400°C bear any relation with the formation temperature of emerald. The temperatures of isotopic equilibrium are based on coexisting quartz and plagioclase in pegmatite, and a quartz vein, and must be interpreted with extreme caution due to the easy subsolidus re-equilibration of plagioclase. Also, widespread open-system conditions, disequilibrium crystallisation and hydrothermal alteration result in small-scale isotopic heterogeneity (Longstaffe, 1982). The solidus temperature of volatile-rich granitic magma with 1-4 wt.% B and F at 1 to 3 kbar is substantially higher (600-650°C; e.g., Wyllie & Tuttle, 1961; Pichavant, 1987), although London (1990) demonstrated a wider range of consolidation temperatures of rare-element (Li-Be-Ta) pegmatites, between 700° to 450°C at 4 to 2.5 kbar (see Chapter 4).

Kafubu, Zambia – Emerald mines are located in the Kafubu area (also known as the Ndola Rural Restricted area) of central Zambia, about 45 km southwest of the town of Kitwe. The emerald deposits are hosted by metamorphic rocks of the Muva Supergroup (Daly & Unrug, 1983), consisting of quartzites, mica schists and metabasites, that overlay basement granite gneisses along a structural unconformity. Emeralds occur in the metabasites, which consist of talc-chlorite-actinolite \pm magnetite schists (Hickman, 1973; Sliwa & Nguluwe, 1984). These schists are thought to represent metamorphosed volcanic rocks that were dominated by komatiites (i.e., highly magnesian ultramafic rocks, also rich in chromium; Seifert *et al.*, 2004). Deposition of the Muva Supergroup is dated to ~1700 Ma. Subsequent folding and metamorphism, which also involved the basement granite gneisses, took place during the Irumide orogeny (~1010 Ma; De Waele *et al.*, 2003). The basement granite gneisses and the Muva Supergroup were later buried under sediments of the Katanga Supergroup during the Neoproterozoic era (i.e., 900-570 Ma). The entire crustal domain then underwent folding, thrusting and metamorphism during the Pan-African orogeny, culminating at ~530 Ma (John *et al.*, 2004). During late stages of the Pan-African orogeny, rare-element pegmatites and some beryllium-rich granites intruded various crustal units in central, eastern and possibly also northwestern parts of Zambia (see, e.g., Cosi *et al.*, 1992; Parkin, 2000).

In the Kafubu area, field relations at numerous mines and exploration pits indicate the existence of a major field of beryllium-bearing pegmatites and hydrothermal veins

that is some 10 km long. This field overlaps major horizons of metabasites that are enriched in chromium, resulting in emerald mineralisation over a large area. Economic emerald concentrations are almost entirely restricted to phlogopite reaction zones (typically 0.5-3.0 m wide) between quartz-tourmaline veins and the metabasites. The best emerald mineralization is found in phlogopite schist near intersections between the quartz-tourmaline veins and pegmatites, particularly within 'armpits' formed by steeply dipping pegmatites and flat-lying quartz-tourmaline veins (e.g., Seifert *et al.*, 2004; Zwaan *et al.*, 2005). Numerous chemical analyses of the metabasic rocks and the phlogopite reaction zones (Seifert *et al.*, 2004) indicate that the phlogopitisation involved the addition of 8-10 wt.% K₂O, 2.7-4.7 wt.% F, 0.1-0.7 wt.% Li₂O, 1,700-3,000 ppm Rb, 10-56 ppm Nb, up to 1,600 ppm Be and significant amounts of B. Information from a fluid inclusion study (Seifert *et al.*, 2004) indicated that minimum trapping conditions of pseudosecondary fluid inclusions in quartz associated with emerald occurred at temperatures of 360-390°C and pressures between 2 and 4.5 kbar. It is inferred that emerald must have crystallised at similar conditions.

Potassium-argon dating of muscovite from a pegmatite and an associated quartz-tourmaline vein gave cooling ages of 452-447 My (Seifert *et al.*, 2004). This corresponds to the time when the rocks cooled below ~350°C (which is the approximate temperature at which muscovite becomes 'closed' to argon loss; see also Chapter 5). It is considered to approximately date emerald mineralisation, as the emeralds are supposed to have crystallised at only slightly higher temperatures. Thus, like in Pakistan, it appears that emerald mineralisation at Kafubu occurred after regional peak metamorphic conditions, as the direct result of the metasomatic alteration of the Cr-bearing metabasites by Be-bearing fluids derived from intruding pegmatites and hydrothermal veins (see, e.g., Coats *et al.*, 2001; Seifert *et al.*, 2004).

1.3.2. Colombia, an exceptional case – In the early 1990s, Colombian emeralds were presented as an exception to the rule. These relatively young deposits (Eocene), hosted by an Early Cretaceous, black shale-limestone succession, are not related to pegmatites or magmatic fluids. Emeralds formed as a result of hydrothermal growth during tectonic movements in the area (e.g., Ottaway *et al.*, 1994; Giuliani *et al.*, 1995; Cheilletz & Giuliani, 1996; Branquet *et al.*, 1999). This type of emerald mineralization involves generation of brines through dissolution of evaporites by hot basinal waters, leading to Na-Ca metasomatism of black shales, and simultaneous leaching of beryllium, chromium and vanadium. Subsequently, emerald precipitated in extensional carbonate-silicate-pyrite veins, pockets and breccias, present in the black shales (Fig. 3).

The fluids trapped by emerald and pyrite in the Colombian emerald deposits consist predominantly of Na-Ca brines with some KCl. The Na-Ca-K chemistry of the hypersaline brines provides strong evidence for an evaporitic origin of the parent hydrothermal fluids. Sulphur isotope studies on pyrites from six emerald deposits (Giuliani *et al.*, 1995) revealed a narrow range in $\delta^{34}\text{S}$ values between the different deposits, which suggests a uniform and probably unique source for the sulphide-sulphur. The high $\delta^{34}\text{S}$ values suggest the non-participation of magmatic or Early Cretaceous black-shale sulphur sources. Saline diapirs occur in the emeraldiferous areas and, therefore, the most likely explanation for high $\delta^{34}\text{S}$ involves the reduction of sedimentary marine evaporitic sulphates. Hydrothermal brines transported evaporitic sulphate to structurally favour-

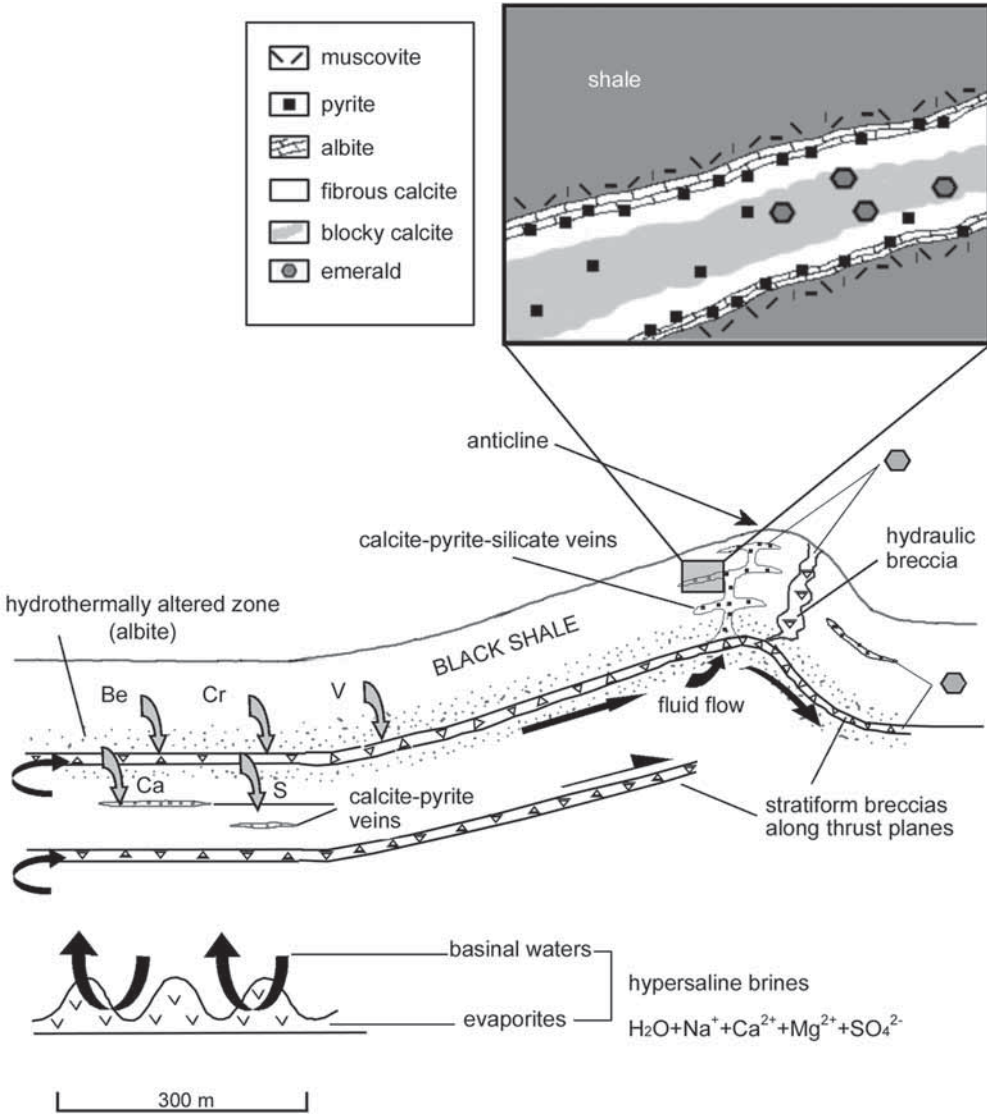


Fig. 3. Model of formation of Colombian emeralds. Emeralds were hydrothermally formed during thrusting and folding of black shales. Highly reactive hypersaline brines, generated by circulation of hot basinal waters through evaporitic beds, infiltrated into thrust planes and caused wall-rock metasomatic alteration. By this process, Be, Cr and V were mobilised, and could precipitate to form emerald in extensional veins and hydraulic breccias, which are also rich in calcite and pyrite. Modified after sketches by Ottoway *et al.* (1994, fig. 1) and Cheillett & Giuliani (1996, fig. 3).

able sites, where it was thermochemically reduced. Ottoway *et al.* (1994) suggested that native sulphur generated by this process reacted with organic matter in the shales to release trapped chromium, vanadium and beryllium, which in turn enabled emerald formation. Cheillett & Giuliani (1996) and Giuliani *et al.* (2000b) emphasised the impor-

tant role of organic matter in the formation of Colombian emerald deposits, but argued against the production of native sulphur by thermochemical sulphate reduction. They proposed a redox reaction, involving large organic molecules, a carbonic hydrate and SO_4^{2-} , that would generate large quantities of HCO_3^- and H_2S , which then reacted with two main cations (Ca^{2+} and Fe^{2+}) extracted from the black shale by the hydrothermal fluid, producing calcite and pyrite, which are closely associated with the occurrence of emerald in the veins and breccias.

The Late Eocene–Early Oligocene age of the Colombian emerald deposits appears to rule out the genetic link of the mineralising fluid with Early Cretaceous basic magmatism. The PTX characteristics of the hydrothermal brine fluids indicate moderate temperatures for emerald mineralization ($320 \pm 40^\circ\text{C}$). Thermal calculations based on the burial history indicate that temperatures of $210\text{--}240^\circ\text{C}$ would have been reached by the end of the Cretaceous through simple subsidence. At the time of emerald formation the hydrothermal fluid ($320^\circ \pm 40^\circ\text{C}$) therefore needed an additional 120 to 150°C thermal input (Cheilletz *et al.*, 1994). Synchronous magmatic intrusions could be heat sources, but are not proved from field evidence. Heat conduction implemented during halokinetic ascent is more probable, as evaporitic plugs are known within Late Cretaceous formations. Oxygen and carbon isotope studies indicate an origin of mineralising fluids in basinal formation waters (Giuliani *et al.*, 1992). Thus, the source of the complex hypersaline brines is likely to be interaction of basinal formation waters with the evaporitic beds.

The origin of beryllium may be local (Kozłowski *et al.*, 1988; Cheilletz *et al.*, 1994). Simple mass balance calculations indicate that beryllium fixed in emeralds is only a small fraction of the average concentration of this metal in the country and wall rocks. The regional black shale, therefore, had a large enough beryllium reservoir to have been a potential source. The distinct stratigraphic control of the emerald-bearing veins supports the idea that the source of beryllium was local.

1.3.3. An alternative model for schist-type emerald deposits – While the Colombian emerald deposits were presented as a unique case, at about the same time the ‘contact metamorphism’ concept for the ‘schist-type’ emerald deposits was also challenged by Grundmann & Morteani (1989), who studied deposits at Habachtal (Austria) and at Leydsdorp in Transvaal, South Africa. They found that emeralds in these deposits were not formed by a single-stage contact metamorphism at the border zone of magmatic intrusives, but formed by syn- to post-tectonic reactions during low-grade regional metamorphism (Fig. 4). Like in Colombia, tectonic deformation played a significant role. Extending their conclusions to most, if not all schist-type deposits, these authors suggested that emerald formation in metamorphic rocks is the product of a deformation event accompanied or followed by regional metamorphism. However, straightforward metasomatism at the contact of amphibolite and a pegmatitic vein system might also occur, as demonstrated by Laurs *et al.* (1996) in the Haramosh Mountains, northern Pakistan, and by Seifert *et al.* (2004) in the Kafubu area, Zambia, as described above. At least, these studies appeared to indicate that the alternative model by Grundmann & Morteani (1989) cannot rigorously be applied to all schist-type deposits. To evaluate the arguments that were used by Grundmann & Morteani (1989), and also by Nwe & Grundmann (1990) and Nwe & Morteani (1993), the Leydsdorp and Habachtal deposits are discussed briefly below.

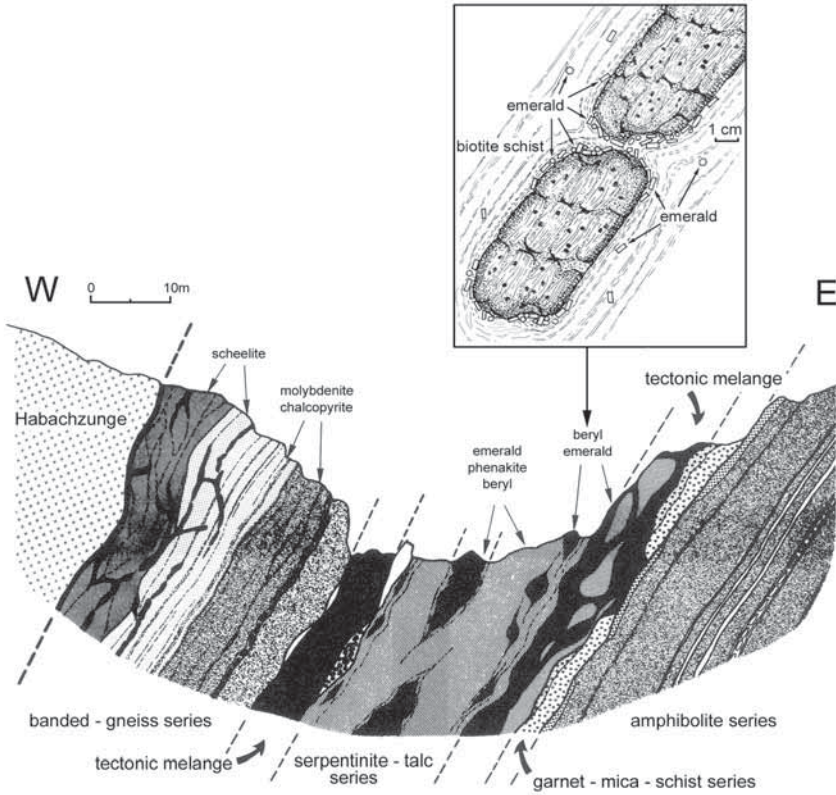
Leydsdorp, South Africa – In South Africa, emerald deposits are located in an area near Leydsdorp and Gravelotte, which lies along the southern margin of the Archaean Murchison Greenstone Belt of the Kaapvaal craton in northeast Transvaal. The Murchison Belt is flanked to the north and south by intrusive Archaean granitoids. The belt itself consists of a number of domains of different and characteristic lithologies, structural and metamorphic histories, with major tectonic breaks occurring between each domain. The emerald deposits occur at the contact between Archaean tonalitic gneisses and a southeasterly trending off-shoot of the Murchison Greenstone Belt. Emeralds and associated phenakites occur on the flanks of a highly metasomatised albitite pegmatoid body, and in the biotite schists at and near its contact. Emeralds occur in the biotite schist as euhedral porphyroblasts or were formed on preexisting phenakite crystals. The biotite schists are 30–40 m wide and, since this zone is spatially restricted to the flanks of a coarse-grained albitite pegmatoid, they are considered to have originated by contact metamorphism and metasomatism of the chlorite- and talc-chlorite schists, which form the dominant lithology in the surrounding rocks. The albitites in the Gravelotte area are considered to have developed from an original granodioritic magma, mainly through a process of alkali metasomatism. These pegmatoids are extremely deformed and show gneissic textures, indicating that the whole series has been affected by deformation and regional (greenschist facies) metamorphism.

The earliest type of fluid inclusions in phenakite consist of aqueous fluid with a bubble, consisting of nearly pure CH_4 supercritical fluid (the inclusions show low salinity; < 6 wt.% NaCl, with up to 18 mol% CH_4). Based on minimum trapping temperatures, upper temperature limits constrained by the absence of high-grade assemblages in the metamorphic rocks hosting the albitites and isochores, P-T conditions defined for these inclusions are around 450–500°C and 4 kb. The low initial f_{O_2} values found in these inclusions are uncharacteristic of granitic pegmatite systems. Further, Nwe & Morteani (1993) argued that the lack of CO_2 -dominated fluids indicates that the phenakites did not form during the magmatic stage. Therefore, they suggested that the phenakites were formed in the post-magmatic stage of alkali metasomatism when the albitisation took place. This is consistent with the work of Barton (1986), who showed that low alumina activities and relatively high alkalinities in the system favour the formation of phenakite. In later stages phenakite was converted to emerald as alumina activities in the system increased. Higher salinity brines were trapped under higher f_{O_2} conditions. Metasomatic exchange with the mafic host rocks also increased, which is evidenced by increasing Cr contents in the later grown emeralds. The emeralds generally show prominent zoning, with colourless inclusion-rich cores and increasingly green-coloured inclusion-poor rims. The fluid evolution appears to have been more or less continuous, from aqueous fluids initially rich in CH_4 , into more and more saline compositions with decreasing CH_4 content. Microthermometric studies of fluid inclusions in emeralds suggest that emerald began to form from an $\text{H}_2\text{O}-\text{CO}_2$ mixed fluid phase, with a salinity of 1 to 7 equiv. wt.% NaCl and homogenisation temperatures around 250°C (Grundmann & Morteani, 1989; Nwe & Morteani, 1993). There is no clear-cut division between the earlier stages of albitisation and metasomatic exchanges with the host rocks, and the slightly later stage of regional deformation. However, some of the higher salinity fluids, such as are present in curved or planar arrays along late fractures traversing emerald crystals, may be connected with the regional deformation. It was

believed by Nwe & Morteani (1993) that the energy necessary for the continued metasomatic exchanges during growth of the later emeralds was probably also supplied by the same regional tectono-metamorphic event. Petrographic observations that indicate a syn- to post-tectonic growth of emerald (Grundmann & Morteani, 1989) appear to support this view. Additionally, fluorite intergrown with emerald shows a rare earth element fractionation pattern and Yb/Ca versus Tb/Ca ratios that indicate the existence of a hydrothermal fluid phase during the formation of emeralds, which is used as another argument emphasizing the non-pegmatitic nature of emerald growth.

In the Leydsdorp case, some of the arguments that are used to disconnect the formation of emerald from magmatic activity raise questions. The absence of CO₂-dominated fluids is seen as an indication that phenakite did not form during the magmatic stage. However, in granitic pegmatite systems the CO₂ content can often be low (e.g., Roedder, 1984; London, 1986), so the composition of the fluids does not have to be in disagreement with a magmatic origin. The low salinity during the formation of phenakite and the initial formation of emerald tends to be related to the later stages of progressive crystallization of granitic magma (see, e.g., Roedder, 1984; Shmonov *et al.*, 1986), and would, therefore, be an argument in favour of a magmatic origin of phenakite and a restriction of early emerald growth to the latest stages of felsic magma crystallization. Also, the REE fractionation patterns in fluorite cannot really be used as an indicator of the non-pegmatitic nature of emerald growth. A hydrothermal fluid may be a pegmatite-derived fluid, which represents the final stage of magmatic activity. These late fluids become increasingly sodium-rich and may be the cause of albitisation of the intruded pegmatites (a process which could be called 'auto-metasomatism' of the pegmatite, see also Chapter 4). For instance, London (1986) indicated the possibility that albitic units of the Tanco rare-element pegmatite were deposited directly from the late pegmatitic fluid and are not the result of subsolidus metasomatism, the mechanism suggested for the albitisation of pegmatites at Leydsdorp. London (1986) also demonstrated that, during the magmatic/hydrothermal transition in the Tanco rare-element pegmatite, a similar fluid evolution took place from a low-density aqueous fluid (approximately 91 mol% H₂O, 5 mol% CO₂, 4 mol% NaCl) at 420°C and 2600 bars, into more saline and CO₂-rich fluids with decreasing P and T, and increasing degree of crystallisation at subsolidus conditions. Thus, although the energy necessary for the continued metasomatic exchanges during the various growth phases of the emeralds at Leydsdorp might have been supplied by the regional tectono-metamorphic event, a link between pegmatitic activity and the growth of phenakite and (at least early) growth of beryl/emerald should not be ruled out.

Habachtal, Austria – The Leckbachscharte in the Habachtal (Hohe Tauern, Salzburg, Austria) is the only place in Western Europe where economically exploitable emeralds are known. The emerald deposit is situated in the Tauern window, near the tectonic contact between ortho-augengneisses of the Zentralgneiss and the Habach Formation, which belong to the lowest tectonic unit of the eastern Alps (Penninicum). The Habach Formation consists of a sequence of metapelites and metavolcanics (amphibolites, mica schists and black phyllites) with interlayered serpentinites (Fig. 4). It is part of the Lower Schist Cover, which is interpreted as an Alpine nappe above the Zentralgneiss. This sequence is known as a metasomatic 'blackwall' zone, developed between metapelites, mafic volcan-



"Habachzunge"

central-gneiss series

 ortho-augengneisses

"Habach Formation"

banded-gneiss series


 amphibole gneisses


 biotite-plagioclase gneisses

 biotite-blast schists


 amphibolites,
amphibole schists

tectonic melange

 mylonites
and cataclasites

 vein-quartz, fissure-quartz

serpentinite-talc series

 talc schists,
talc-actinolite schists,
talc-carbonate schists

 biotite schists,
chlorite schists,
actinolite schists

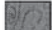
tectonic melange

 white-mica schists
and blackwall rocks

 biotite schist -
vein-quartz breccia

 vein-quartz, fissure-quartz

tectonic melange

 a) emerald-bearing
white-mica schists,
biotite schists,
chlorite schists,
actinolite schists,
talc schists,

b) garnet-mica schists,
white-mica schists,
amphibole gneisses,
amphibolites,
quartz-plagioclase layers,
biotite-plagioclase gneisses

garnet-mica-schist series

 graphite-mica schists,
chlorite-mica schists,
white mica schists

 biotite-plagioclase gneisses

amphibolite series

 biotite-epidote
plagioclase gneisses

 amphibole gneisses

 amphibolites

 finegrained gneissic
quartz-plagioclase layers

ics and ultramafics (Grundmann & Morteani, 1989). Intense schistosity indicates that the blackwall zoning was formed during regional metamorphism involving an intense deformation of the rocks. The entire sequence is interpreted as a tectonic *mélange*, produced mainly by alpine tectonism. Light to dark green emeralds occur in the biotite, chlorite, actinolite and talc-(actinolite)-schists (serpentine-talc series) of the Habach Formation. The most intense emerald mineralisation is associated with muscovite-plagioclase-chlorite boudins surrounded by biotite schists. Emerald porphyroblasts grew syn- to post-tectonically, mainly at the contact of the boudins with the biotite schists (Fig. 4, inset).

The emerald-bearing biotite schist is the result of a metasomatic reaction between the garnet-bearing mica schist protolith and the adjacent ultrabasic protolith (e.g., serpentinite and talc schist). Geochemical analyses show that the entire blackwall zone is enriched in beryllium, and that talc and talc-actinolite schists are rich in chromium. Mass balance analyses suggest that the transformation of the metapelites-metavolcanics and serpentinites replaced Be-rich Al-silicates such as muscovites by biotite and chlorite, which released excess beryllium to form beryl or, in the presence of Cr liberated from the metasomatised ultrabasic rocks, emerald. The original enrichment in Be within the Habach Formation is ascribed to submarine volcanic exhalation. According to Grundmann & Morteani (1989), this is suggested by the presence of rich strata-bound Fe-Cu-Mo sulphide and scheelite mineralisations near the emerald deposit, and the intercalation of metavolcanics and metapelites. Significantly, no pegmatitic rocks of any kind are found as a source of Be in the Habach Formation.

Other critical evidence for the regional metamorphic origin of emeralds includes the polystage growth with simultaneous deformation, which is indicated by sigmoidal inclusion trails in the strongly zoned emeralds. Inclusion trails in garnet and plagioclase porphyroblasts, present in the metapelitic rock type, have orientations similar to those of the emeralds, also indicating multistage syn- to post-tectonic growth, which is characteristic of regional metamorphism (see also Grundmann & Morteani, 1982).

Emeralds from Habachtal commonly contain primary three-phase fluid inclusions (liquid H₂O, liquid CO₂ and vapour) in cavities parallel to the c-axis (Grundmann & Morteani, 1989; Nwe & Grundmann, 1990). Microthermometry gives an average homogenisation temperature of 300°C and salinity of 6 to 9 equiv. wt.% NaCl. The visually estimated CO₂ content is 15 to 20 vol.%. These fluid characteristics match those in syntectonic Alpine fissures in the Habach formation, which was also used as an argument in favour of a regional metamorphic origin of the emeralds. A detailed study of the trapping history of the fluid inclusions present in emerald (Nwe & Grundmann, 1990) indicates at least four phases of deformation and, therefore, emphasizes syntectonic growth of emerald.

..The results indicate that, at the time of maximum crystal growth (i.e., growth of the primary inclusion-filled cores), the fluid pressure was much lower than the maximum pressures indicated later, during a second stage of growth. In order to explain this, Nwe

- ◀ Fig. 4. Alternative to the traditional model of emerald formation. At Habachtal, Austria, it was found that emeralds were formed by syn- to post-tectonic reactions during regional metamorphism, in the absence of pegmatites. The inset shows a schematic section through muscovite-plagioclase-chlorite boudins surrounded by biotite schists. Most intense emerald mineralisation in the area occurs mainly at the contact of the boudins with the biotite schists, where emerald grew post-tectonically. After Grundmann & Morteani (1989, figs. 2, 5).

& Grundmann (1990) proposed that the fluid pressure at the time of entrapment of the inclusions in the first stage of growth was not representative of the regional lithostatic pressures at the time; P_{fluid} was less than P_{total} . This could be highly likely since the emerald-bearing horizon is part of a narrow shear zone within more rigid surrounding rocks. Lower pressure conditions resulting from volume changes due to faulting could have existed for some time in this zone.

The maximum fluid pressure of 7 kbar in the second growth stage compares well with pressure estimates from mineral equilibria. In the cooling period after the second growth stage, fluid pressures were again lower than the lithostatic load. This difference, about 1-2 kbar, was probably also due to (late stage) fracturing.

Emerald deposits in Brazil – The idea that emeralds might be formed in shear-zones, without any connection with pegmatites, or that emeralds might be located near pegmatites at the contact with ultramafics, but were actually not formed as a result of single stage contact-metamorphism, was confirmed by Giuliani *et al.* (1997a, b), who presented data on two types of emerald deposit present in Brazil. Type 1 deposits, such as present in Bahia (Socoto, Carnaiba) and Minas Gerais (Belmont and Capoeirana; Fig. 1), are associated with pegmatites intruding mafic to ultramafic rocks. At these deposits, the formation of emerald resulted from the circulation of hydrothermal fluids that, by infiltration, developed an alkaline (K, Na) metasomatism in the mafic to ultramafic rocks around pegmatite veins that had been desilicified and altered to plagioclase. The fluids were channelled by the pegmatites and the metasomatic substitution of the primary paragenesis of the chromite-bearing mafic to ultramafic rocks caused the formation of phlogopite schists, which host the emerald mineralisation. Type 2 deposits, such as present in Goiás (Santa Terezinha), are linked to ductile shear zones affecting mafic to ultramafic rock formations. Here, emeralds are located in phlogopites and phlogopitised carbonate-talc schists. The talc schists provided sites for thrusting that gave rise to the formation of sheath folds. Emerald-rich zones are commonly found in the cores of the sheath folds and along the foliation. The isotopic data ($\delta^{18}\text{O}$ and δD) of emeralds and coeval phlogopite were consistent with both magmatic (evolved crustal granites) and metamorphic fluids. However, the absence of granites and related pegmatites, and the low Be concentration in the volcano-sedimentary sequence (Be < 2 ppm), appear to exclude a magmatic origin for beryllium; therefore, a metamorphic origin is proposed for the Santa Terezinha parental fluids.

In those cases where pegmatitic sources of beryllium are not immediately obvious, one should be cautious with interpretation. Fluids can travel far from (perhaps hidden) pegmatites, especially along intensely sheared rocks. For instance, in the Zentralgneiss, next to the Habach Formation, pegmatites of pre-Alpine age do occur (e.g., Satir, 1974; Schulz *et al.*, 2001), but Grundmann & Morteani (1989) did not mention their existence and did not give reasons why those pegmatites could not be considered as possible sources of beryllium. Also, the elevated Cs concentrations (up to 760 ppm) in Habachtal emeralds, measured by Calligaro *et al.* (2000), appear to indicate a possible pegmatitic influence (see Chapters 3 and 4). Besides, sulphide deposits related to submarine volcanic exhalation (supposedly the beryllium source for the emerald deposits at Habachtal; Grundmann & Morteani, 1989), generally do not appear to be particularly enriched in beryllium (e.g., Guilbert & Park, 1986; Barton & Young, 2002).

Table 1. Modified genetic classification of emerald deposits after Snee & Kazmi (1989).

	Geological setting	Source of chromium		
		Suture zone	Granite/greenstone terrain Shale/metashale terrain	
Source of beryllium	Pegmatite	India	Western Australia	
		Khaltaro, Pakistan	Bahia, Brazil	
		Egypt	Minas Gerais, Brazil	
		North Carolina, USA	South Africa	
		Ural Mountains, Russia	Zimbabwe	
		Tanzania	Madagascar	
		Bulgaria	Zambia	
		Ukraine	Mozambique	
	Hydrothermal or Connate/ Meteoritic fluids	Afghanistan		Colombia
		Swat Valley, Pakistan		
Metamorphic/ Tectonic	Austria	Goiás (Santa Terezinha), Brazil		

1.3.4. *Genetic classification schemes* – From case studies such as those briefly outlined in the preceding sections, a number of genetic classifications have been proposed for emerald deposits. Most recent classifications were presented by, e.g., Snee & Kazmi (1989), Schwarz & Giuliani (2001), Schwarz *et al.* (2001) and Barton & Young (2002).

1. The classification by Snee & Kazmi (1989) was based on the origin of beryllium and chromium (and vanadium), the source of the parental fluids and the geological setting. They felt this was a preliminary scheme which needed to be tested. Very shortly after their publication, new theories on emerald formation were introduced (Sections 1.3.2 and 1.3.3). Taking this into consideration, a slightly modified classification of the main emerald deposits after Snee & Kazmi (1989) is given in Table 1.

This classification is unclear and, therefore, not very useful, because the variables are caused by a mixture of geological processes. Both geological setting and source of chromium are confused, as well as the source of beryllium and the origin of the parental fluids. For instance, (ultra)mafic rocks are the specific source of chromium, both in suture zones and in granite/greenstone terrains. So, in these cases, the geological setting does not appear to be particularly relevant. Another example is the situation in Colombia, where black shales are considered to be the source of both chromium and beryllium. Both elements were leached out of the shales by hot hypersaline brines.

2. Recognising that the principal mechanism responsible for emerald crystallisation is circulation of fluids and fluid/rock interactions, which allow redistribution of elements normally not related to each other Schwarz & Giuliani (2001) and Schwarz *et al.* (2001) distinguished two main types of emerald deposits, analogue to the types proposed earlier for Brazilian emerald deposits in Giuliani *et al.* (1997a, b; see Section 1.3.3):

Type 1. Emerald mineralisations related to granitic intrusions.

Type 2. Emerald mineralisations, which are mainly controlled by tectonic structures, such as thrust faults and shear-zones.

According to this classification, most emerald deposits fall in the type 1 category (Table 2). These deposits are characterised by mafic, ultramafic or sedimentary rocks, which were intruded by granitic pegmatites or hydrothermal veins. Most deposits of this type occur in Archaean or Precambrian basement, Precambrian or Palaeozoic volcano-sedimentary series and oceanic suture zones. Emeralds are located at the contact zones between the intruded rock and the host rock; they are generally found in phlogopite schists and, uncommonly, within veins with white feldspar and mica. Schwarz & Giuliani (2001) stated that hydrothermal processes, related to granitic-pegmatitic systems, led to the crystallisation of emeralds.

Some deposits are related to pegmatites, but differ from the classic pegmatite/schist occurrences and are therefore put in a subcategory; 'pegmatite without schist at contact zone'. For instance, in Kaduna state, Nigeria, emeralds occur in small pegmatitic pockets in association with aquamarine, quartz, feldspar and topaz (Schwarz *et al.*, 1996). These pockets are found at the contact of Be- and F-rich biotite peralkaline granite with basement rocks, and represent cavities created by gas loss from the cooling magma. Emeralds may also occur in 'soft decomposed' granites. Crystals have grown in small miarolitic cavities formed by gas loss in the roof of the granite. Emeralds grew during a late-magmatic/hydrothermal stage (Schwarz *et al.*, 2001); hydrothermal alteration processes released beryllium from the alkali granite and chromium from basic volcanic rocks, to be incorporated in emerald. In Eidsvoll (Norway), emerald was formed during contact metamorphism (Grundmann, 2001) and occurs at the contact of pegmatite, cutting shales (V, Fe and Cr bearing) and syenite veins (Be bearing). In Emmaville-Torrington (Australia), emeralds are hosted by a Permian metasedimentary sequence of siltstones, slates and quartzites, which were intruded by pegmatites and aplites. Emeralds occur in veins, with quartz, topaz, feldspar and mica (Schwarz, 1991b; Grundmann, 2001).

Groat *et al.* (2002) also classified the new emerald deposit, discovered in Yukon, Canada, as a type I emerald deposit. In the Regal Ridge occurrence, the emerald crystals are contained in tourmaline-scheelite-bearing layers of mica schist at the margins of tourmaline-rich quartz veins, which are related to nearby granite. Therefore, this deposit can be found under the first subcategory type I in Table 2.

According to Schwarz & Giuliani (2001), the second group of emerald deposits (type II deposits) are not related to granitic intrusions, but, instead, tectonic structures (mainly thrust faults and shear zones) are the controlling factors for the formation of emerald. Shear zones allow circulation of fluids that interact with mafic rocks, as at Santa Terezinha and Habachtal, described in Section 1.3.3. In the Swat Valley, Pakistan, emeralds occur as veins with quartz, fracture-fillings and nuggets in talc-magnesite and quartz-magnesite lithologies, within an ophiolitic melange in the Main Mantle Thrust, a major suture zone. The ophiolitic melange mainly consists of altered ultramafic rocks with meta-volcanics and meta-sedimentary rocks. Arif *et al.* (1996) proposed that the magnesites formed due to the carbonation of previously serpentinised ultramafic rocks (which provided chromium for the emerald formation) by a CO₂-bearing fluid of metamorphic origin. This was based on a calculated isotopic composition of the parental fluid for magnesite ($\delta^{13}\text{C} \approx -1.8 \pm 0.7\text{‰}$ PDB; $\delta^{18}\text{O} \approx +13.6 \pm 1.2\text{‰}$ SMOW) in the temperature range of 250-550°C (the presence of quartz and talc in the magnesite-rich assemblages suggests that they might have formed in this temperature range). Arif *et al.* (1996) also stated that emerald formation in this area was probably due to a parental fluid of

Table 2. Genetic classification of emerald deposits, after Schwarz & Giuliani (2001) and Schwarz *et al.* (2001).

Emerald mineralisations			
Type 1: related to granitic intrusions		Type 2: controlled by tectonic structures	
Pegmatite with schist at contact zone	Pegmatite without schist at contact zone	Schists without pegmatites	Black shales with veins and breccias
Kafubu area, Zambia	Kaduna state, Nigeria	Habachtal, Austria	Colombia
Sandawana, Zimbabwe	Eidsvoll, Norway	Goiás (Santa Terezinha), Brazil	
Mananjary, Madagascar	Emmaville-Torrington, Australia	Swat Valley, Pakistan	
Bahia (Socoto, Carnaiba), Brazil		Panjsher Valley, Afghanistan	
Minas Gerais, Brazil		Eastern desert, Egypt	
Tauá, Brazil			
Ural, Mountains, Russia			
Khaltaro, Pakistan			
Poona, Australia			
Hiddenite, North Carolina, USA			
Yukon (Regal Ridge, Finlayson Lake district), Canada			

magmatic origin. This conclusion was based on the mean δD of channel waters measured from emerald ($-42 \pm 6.6\%$ SMOW), which is consistent with both metamorphic and magmatic origin, and on the close similarity between the δD values of the hydroxyl hydrogen in associated fuchsite (-74 to -61%) and tourmaline (-84 and -69%) with pegmatitic muscovite and tourmaline.

In Afghanistan, emerald deposits are located in the Herat-Panjsher suture zone in the Panjsher Valley and occur along Mesozoic shear zones cutting Palaeozoic carbonate rocks, which were intruded by diorite-gabbro and quartz-porphyry dykes and sills (Kazmi & Snee, 1989). Hydrothermal alteration caused phlogopitisation, albitisation, carbonatisation and silicification of the host rocks, and production of a network of quartz-ankerite-pyrite veins, which enclose emerald. Oxygen and hydrogen isotope composition of quartz and emerald are consistent with both a magmatic or metamorphic origin (Giuliani *et al.*, 1997b).

As defined in Section 1.3.2, the Colombian deposits have a unique formation history and are placed in a type II subcategory.

The type II emerald occurrences show that beryllium may not only originate from a magmatic, but also from a metamorphic or even sedimentary environment. However, it is unclear why Schwarz & Giuliani (2001) categorised the Egyptian emerald deposits in a subcategory of type II, without a relation with pegmatite. Abdalla & Mohamed (1999) indicated that, while emerald mineralisation at Um Kabu and Sikait, in southeast Egypt, is indeed confined to the ductile major Nugrus shear zone, it also is closely related to pegmatitic veins, which intruded a sheared schist sequence, including slices of serpentinites. A proximal leucogranite and the associated pegmatites are considered to be

Table 3. Main types of emerald occurrences, after Barton & Young (2002).

Association		Metasomatic		
Type	Variety	Aluminosilicate (greisen, vein)	Carbonate (skarn, replacement)	Mafic/ultramafic (blackwall, vein)
<i>Igneous connection direct</i>				
Granite	Peraluminous			Common; examples: Reft River, Russia; Khaltaro, Pakistan; Carnaiba, Brazil
<i>Igneous connection indirect or absent ('non-magmatic')</i>				
Metamorphic	Shear/vein		Uncommon?; examples: Swat, Pakistan; Brumado, Bahia, Brazil	Uncommon?; example: Habachtal, Austria
Basin	Vein	Uncommon, but premier emerald source: Colombia		

the source rocks for beryllium-bearing fluids. As described above, also in the Swat Valley, Pakistan, there is still a possible link between emerald formation and fluids of pegmatitic origin. From these examples it appears that, although emerald deposits may be located in major suture zones or shear zones, it does not necessarily rule out a relation with granitic intrusions. In addition, deposits categorised under type I may have been influenced severely by tectonic movements in the area (compare, e.g., Carnaiba: Giuliani *et al.*, 1997a; Poona: Grundmann & Morteani, 1998). As discussed above, at Leydsdorp, South Africa, emeralds have grown syntectonically, but are closely related to pegmatites. This deposit has not been classified by Schwarz & Giuliani (2001) and clearly does not fit into their classification. In conclusion, a number of emerald deposits cannot unambiguously be classified as either a type I or type II, and therefore the use of this classification is questioned.

3. In another attempt to classify, Barton & Young (2002) divided beryllium deposits in general, and emerald deposits in particular, into occurrences with a direct igneous connection and occurrences with an indirect or absent igneous connection. They subdivided further by the nature of the associated magma and/or the host rock. Host rock and magma compositions strongly control Be mineralogy as a function of their acidity-basicity and degree of silica saturation. At beryllium occurrences in general, magmatic compositions are uniformly felsic, but may range from strongly peraluminous through metaluminous to peralkaline. Emerald deposits were treated separately from other beryllium deposits and also grouped by origin (Table 3). It was recognised that no single factor controls emerald formation except for the requirement of Cr ($\pm V$) from local host rocks to generate their deep green colour. In general, mafic and ultramafic host rocks are relatively uncommon, but host most emerald deposits, which form where beryl-bearing pegmatites or veins gain Cr and loose silica during original emplacement or subsequent metamorphism. Most of these systems are peraluminous. Biotite-producing metasomatism is ubiquitous. This connection likely reflects the elevated Al_2O_3 activities that are required to make beryl (see also Chapter 4). As in the previous classification, Barton & Young (2002) also considered the Nigerian emerald deposits as a rare

case, but now due to the fact that few emeralds form with metaluminous granitoids. Perhaps the only significant examples are the greisen-affiliated deposits related to the Nigerian Younger Granites (see also Abaa, 1991; Schwarz *et al.*, 1996).

Some arbitrary choices are also made in this classification scheme. For instance, the emeralds at the Swat Valley in Pakistan may occur in magnesite-rich assemblages (as described above), but the geochemistry of the associated ophiolitic melange (the source of chromium) is very similar to that of metasomatised mafic/ultramafic rocks elsewhere, namely FMAS + CO₂/H₂O. So, the Habachtal and Swat Valley emerald deposits could be put into the same mafic/ultramafic category.

1.3.5. Conclusion – The genetic classification schemes, such as presented so far, are ambiguous, and not particularly useful to get an understanding of the mechanisms and conditions that lead to the formation of emerald. Apparently, emeralds of gem quality can be formed in very different geological settings, as long as basic conditions are fulfilled. In general, the basic conditions may be summarised as follows:

Petrological conditions

1. Availability of beryllium and chromium (\pm vanadium).
2. Chemical and physical conditions in which emerald may be formed (conditions corresponding to the stability field of beryl).

Gemmological condition

3. Gem quality emerald (transparent and well-formed crystals) may only form when sufficient free space is available.

The behaviour of beryllium and chromium in fluids (aqueous solutions and silicate melts) is also an important requirement in understanding emerald occurrences. The stability of beryl in terms of pressure-temperature-activity and solubility relationships are discussed in Chapter 4.

Although magmatic-hydrothermal origins appear to be well established in many areas, while presenting their genetic classification, Barton & Young (2002) rightly emphasized that emerald genesis remains controversial in areas that are regionally metamorphosed and where igneous bodies are present. Many emerald occurrences are small bodies that could originate:

1. Through local metasomatic exchange by intergranular diffusion over the relatively long time available during regional metamorphism.
2. By infiltration/diffusion metasomatism generated during shorter lived magmatic/hydrothermal events.

In many cases it is not clear if one mechanism or the other dominates or if both are involved (for instance, in the cases of Leydsdorp/Gravelotte, South Africa; Franqueira, Spain; and Seikeit, Egypt). It clearly merits further investigation for many emerald occurrences that are not yet well documented. With this scope in mind, the case of Sandawana, Zimbabwe, where emerald deposits are closely related to pegmatitic intrusions, will be investigated in the next chapters.

2. Geology of the Sandawana Emerald Deposits

2.1. Location and Access

Zimbabwe is a landlocked country in south-central Africa, covering an area of 390,624 km². It is surrounded by Zambia, Namibia, Botswana, South Africa and Mozambique (Fig. 5). Zimbabwe lies astride the high plateaus between the Zambezi and Limpopo rivers. In the south and southeast of the country are the extensive Limpopo and Save basins, which form part of the Low Veld land below 3,000 feet (915 m).

The Sandawana mines are located in the Low Veld (coordinates roughly 20°55'S and 29°56'E, confirmed by global positioning satellite [GPS] readings), approximately 830 m above sea level. The temperature ranges from a high of 41°C in the summer (November)



Fig. 5. The Sandawana emerald mines are located in southern Zimbabwe, 65 km by gravel road from Mberengwa, the nearest village.

to a low of 6°C in the winter (May). The area has an average summer rainfall of 700 mm, with occasional light drizzle in winter. The natural vegetation is open savanna, characterized by a *Brachystegia* assemblage, including *Brachystegia glaucesceus* (msasa), *Brachystegia speciformis* (mountain acacia), *Themada triandra* (red grass) and *Heterogogon contortus* (spear grass) (Böhmke, 1982).

Zimbabwe has a well-maintained road system. The nearest villages to the Sandawana mines - Mberengwa and West Nicholson - can be reached from Masvingo, Gweru or Bulawayo on good tarred roads (Fig. 5). The exception is the last 65 km traveling via Mberengwa, or 68 km coming via West Nicholson, which are on gravel roads that, during the summer rainy season, are best traversed using a four-wheel-drive vehicle. When the weather conditions are good, however, the easiest way to reach the Sandawana area is by a small plane, as there is a good landing strip near the mines. The mines can be visited by invitation only.

The Sandawana mines have their own medical clinic, which is essential in this remote area, and a primary school. There is also a sports-clubhouse, a soccer club, a community hall and a general store, as well as regular bus service to the capital, Harare.

The mining lease and claim holdings cover a 21 km-long strip along the southern slope of the Mweza hills. They are bordered on the north by the densely populated Communal Lands. On their southern flank, the Sandawana claims share a 16 km-long electrified game fence with 'The Bubiana Conservancy.' This syndicate of seven different ranches, which covers an area of 350,000 acres, represents one of the largest private game reserves in the world and is supported by the World Wildlife Fund.

2.2. Regional geological setting

2.2.1. The Mweza Greenstone Belt – The Sandawana emerald deposits are situated along the southern limb of the Mweza Greenstone Belt (MGB), located at the southern margin of the Archean Zimbabwe Craton (Figs. 6, 7). The northeastern continuation of the MGB is called the Buhwa Greenstone Belt (BGB; Fedo *et al.*, 1995) and corresponds to the same geological domain with comparable evolution.

Greenstone belts are widely distributed across the Archean Zimbabwe craton and formed in three main time periods; ~ 3.5 Ga, ~ 2.9 Ga and 2.7 Ga (Wilson *et al.*, 1978; Wilson, 1990). The oldest and least extensive greenstones are called the 'Sebakwian'; the ~ 2.9 Ga greenstones are commonly referred to as the 'Lower Bulawayan' or 'Lower Greenstones'; and the 2.7 Ga greenstones as the 'Upper Bulawayan' or 'Upper Greenstones'. The predominantly sedimentary Shamvaian Group overlies the Upper Bulawayan and appears to have been deposited in a series of isolated basins. The foundation of this stratigraphy is the Belingwe Greenstone Belt (e.g., Bickle & Nisbet, 1993), but the stratigraphy has been recognised in most of the greenstone belts in Zimbabwe. More recent work in the BGB (Fig. 6) shows that this belt, assumed to belong to the 'Lower Bulawayan' (e.g., Martin *et al.*, 1993), does not entirely conform to the classical stratigraphy (Eriksson & Fedo, 1994; Fedo & Eriksson, 1995, 1996; Fedo *et al.*, 1995).

The BGB consists of a succession of greenschist-facies sedimentary and subordinate volcanic rocks. These rocks are interpreted as a thick, stable shelf succession, either passive margin or cratonic basin, that shows a transition from shallow-marine to deeper water environments (Fedo & Eriksson, 1996). An unconformity with older gneissic

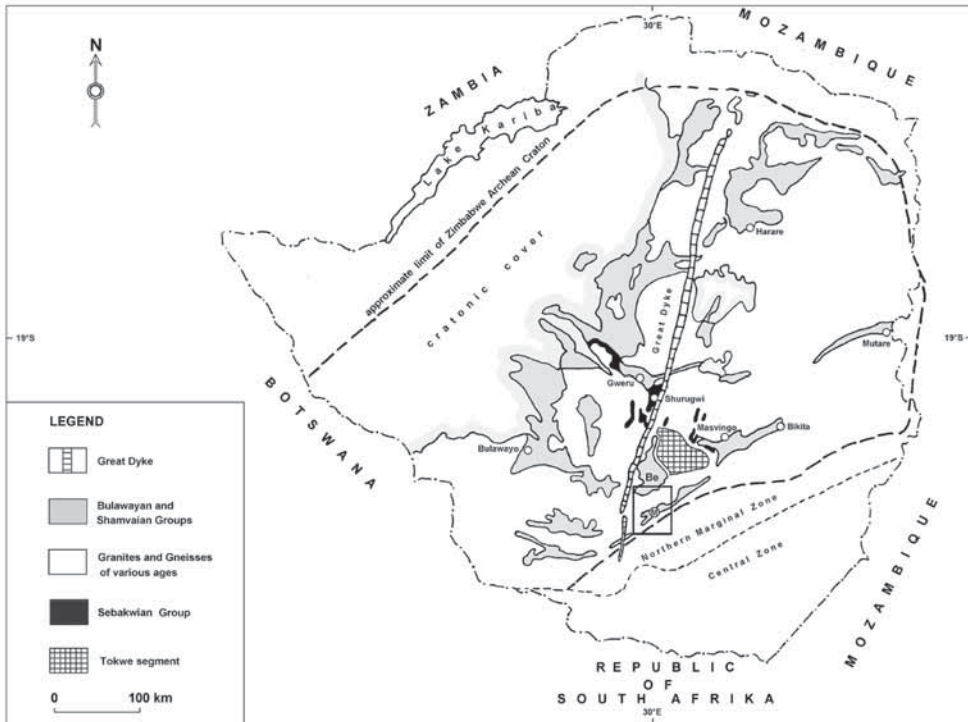


Fig. 6. Simplified geological map of the Zimbabwe craton and Limpopo mobile belt (north marginal and central zones). Be = Belingwe Greenstone Belt, M = Mweza Greenstone Belt. Inset is Fig. 7. Redrawn from Wilson (1990, fig. 1) and Fedo *et al.* (1995, fig. 1).

basement, the ~ 3.5 Ga Tokwe segment (Wilson, 1990, fig. 6) is not exposed in the area, but is inferred from relative age relationships and available absolute dates. Dodson *et al.* (1988) did a reconnaissance study on detrital zircons, extracted from a thick quartzite unit. U-Pb ages ranged from 3.1 to 3.8 Ga and nine of the zircon grains gave ages of 3.75–3.8 Ga, older than any Zimbabwean rocks so far satisfactorily dated; the Tokwe gneisses are a possible source for these old grains. Xenoliths of quartzarenite in plutons adjacent to the greenstone belt indicate that the Tokwe segment and the overlying sedimentary rocks were intruded by a batholith with mainly tonalitic composition. Lithologic similarity with the nearby Mashaba tonalite (e.g., Hawkesworth *et al.*, 1979) and a preliminary single-crystal zircon U-Pb age of ~ 2.9 Ga, which can be interpreted as the crystallisation age (Fedo *et al.*, 1995), suggest that this batholith was emplaced at ~ 2.9 Ga (Fedo & Eriksson, 1996). Thus, field relationships and available dates suggest a depositional age for the Buhwa succession of less than 3.1 Ga, but greater than 2.9 Ga. As the MGB near Sandawana and the BGB form a continuum, the ages should be comparable; therefore, the MGB appears to be younger than the Sebakwian, but slightly older than the 'Lower Bulawayan' greenstones.

Two suites of ~ 2.6 Ga K-feldspar granite, one north of the MGB belt (Chibi Granite) and the other south, comprise the youngest rock types in the Sandawana area (Fig. 7). The Chibi Granite forms an elongate batholith subparallel to orogenic strike of the Lim-

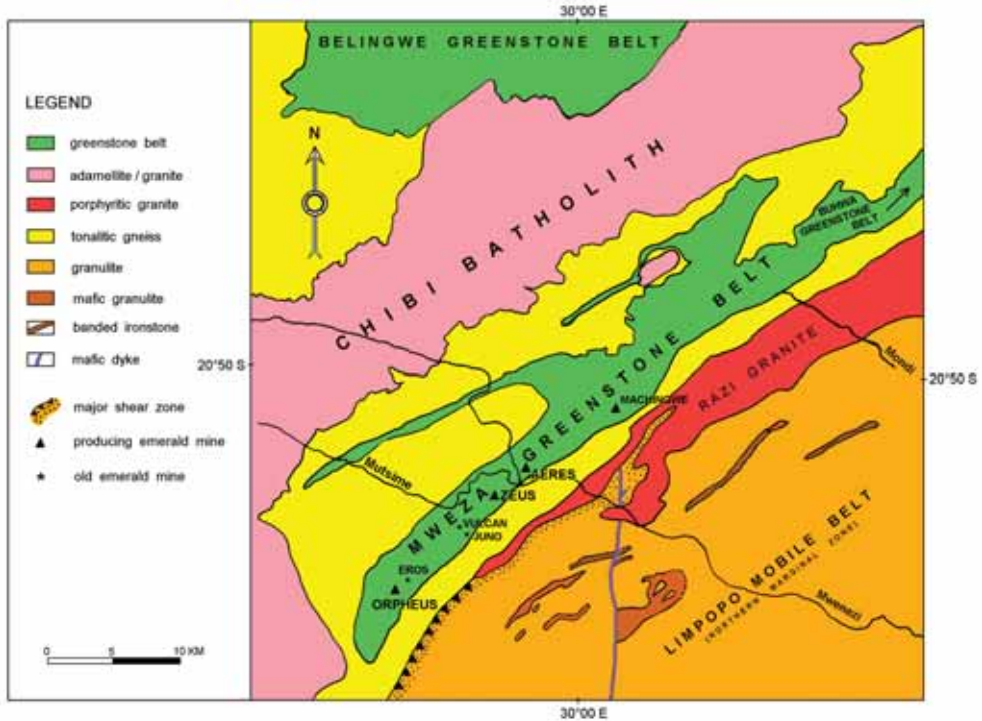


Fig. 7. Simplified geological map showing the location of both the currently producing emerald mines and the old emerald mines in the MGB, near the major shear zone between the Zimbabwe craton and the Limpopo mobile belt. This map is mainly based on data of Robertson (1973), Mkweli *et al.* (1995) and satellite images.

popo Belt and separates the Mweza belt from the Belingwe Greenstone Belt some 25 km to the north. Hawkesworth *et al.* (1979) generated two Rb-Sr whole-rock isochrons for 15 samples of Chibi Granite, one at 2.52 ± 0.04 Ga and the other at 2.62 ± 0.02 Ga, interpreted as emplacement ages.

2.2.2. The Limpopo Mobile Belt – The southern margin of the MGB marks the border between the Zimbabwe Craton and the Limpopo Mobile Belt (Figs. 6, 7). The Limpopo Belt is a major eastnortheast-trending belt, which consists of upper amphibolite- to granulite-facies rocks. The belt is dominated by an eastnortheast-west-southwest structural trend, and consists of the Northern Marginal Zone (NMZ), the Central Zone (CZ) and the Southern Marginal Zone (SMZ). Close to the Sandawana area, recent work has been carried out by Mkweli *et al.* (1995), who showed the unequivocal existence of a tectonic break between the Zimbabwe craton and the NMZ, although this break is obscured by the intrusion of the porphyritic granite bodies (Fig. 7).

The NMZ is a strongly deformed, high-grade terrain consisting of charnockites, en-derbites, narrow dykes of basaltic composition and porphyritic granites. Supracrustal rocks such as mafic granulites, amphibolites and banded iron formations form narrow layers and occupy a minor part of the Zone (Ridley, 1992; Tsunogae *et al.*, 1992; Rollinson & Blenkinsop, 1995). The age of the granulite facies metamorphism is constrained by a

Rb-Sr whole-rock errorchron to 2880 ± 47 Ma (Rollinson & Blenkinsop, 1995). The rocks of the NMZ, which are thought to be of mid- to lower-crustal origin, are now exposed at the surface juxtaposed with supracrustal rocks of the craton. This relationship implies that there has been substantial relative vertical movement between the craton and the NMZ. Mkweli *et al.* (1995) showed that the break is marked by a series of shear zones with a consistent reverse sense of movement, as indicated by, for example, porphyroclast tails, which suggests a northnorthwest thrust transport direction.

As already mentioned, the apparent absence of a shear zone in places is caused by intrusion of porphyritic granites into the shear zone. These potash-rich granites have been described earlier as granites of the Razi sub-province (Robertson, 1973). The porphyritic granite (Fig. 7) is elongate parallel to the regional foliation and the observed foliation trends cannot be distinguished from those in the NMZ. The granite can be found as protomylonite, mylonite and undeformed intrusion (the larger bodies). This implies that the granite intruded the shear zone throughout and even after the main deformation event (Mkweli *et al.*, 1995; Rollinson & Blenkinsop, 1995).

Because the granites were intruded synkinematically into the thrust, zircon dating of the granites should give a minimum date for this event. Mkweli *et al.* (1995) presented a U-Pb zircon age of 2627 ± 7 Ma, obtained from a late-kinematic microgranite cutting a porphyritic granite, as the minimum age of thrusting. This result is within error of an Rb-Sr errorchron of 2583 ± 52 Ma (Hickman, 1984; Mkweli *et al.*, 1995) obtained on the porphyritic granites and retrogressed rocks in the NMZ. The results indicate that the porphyritic granites and the thrusting are of the same age as the (already mentioned and similar) Chibi granite (also a K-feldspar granite) in the Zimbabwe craton (Hawkesworth *et al.*, 1979; Rollinson & Blenkinsop, 1995).

2.2.3. Relation between the Mweza Greenstone Belt and the Northern Marginal Zone – Study of the deformation in the BGB shows that, apart from the shear-zone, three main fold sets can be recognised (Fedó *et al.*, 1995). F1 folds are disharmonic on a centimetre to metre scale within iron-formations. They are typically upright, although variable in orientation. Nearer to the Sandawana region, F2 folds are described as chevron to isoclinal in shape, with axial traces that trend \sim N060E; such trends are very similar to the trend of foliations in the granulites of the NMZ. These structures are in agreement with a bulk strain consisting of northnorthwest-southsoutheast horizontal shortening and vertical extension. The reverse shear zone at the boundary between the NMZ and the craton also indicates a northnorthwest-southsoutheast shortening direction. Therefore, all these structures are interpreted as part of a single progressive deformation (Fedó *et al.*, 1995; Rollinson & Blenkinsop, 1995).

F3 folds are long-wavelength folds (> 40 km) that have axes orientated perpendicular to the orogenic strike of the NMZ. These cross folds were recognised by interpretation of regional-scale map patterns and noticing the apparent polarity reversals in the plunges of F2 folds.

Regional metamorphism and folding are likely to have been synchronous. The chlorite and sericite typical of the low-grade shales in the BGB are axial planar to F2 and, therefore, could have grown during shortening of the cover succession (Fedó *et al.*, 1995). Across strike of the belt, towards the southsoutheast, the metamorphism increases from greenschist to amphibolite facies, which is related to the uplift of the granulite

facies NMZ along the reverse shear zone. In the shear zone, the coexistence of deformed chlorite and epidote with hornblende suggests upper greenschist facies to amphibolite facies metamorphism during shearing (Mkweli *et al.*, 1995). This evidence, together with the earlier mentioned *c.* 2630 Ma age for the reverse shear zone, which lies within error of the Rb-Sr whole rock age of porphyritic granites and retrogressed rocks, suggests that the tectonism and related regional metamorphism, the emplacement of the charnockites and their subsequent retrogression, occurred very close together in time.

Other evidence, presented and discussed in Chapter 5, indicate a low-grade thermal overprint and a possible reactivation of the major shear zone between the Zimbabwe craton and the NMZ around 1.97 Ga. This younger event is not discussed here to avoid duplication.

2.2.4. Summary – Deposition of the volcano-sedimentary series of the Mweza Greenstone Belt began at ~ 3.0 Ga on gneisses of the ~ 3.5 Ga Tokwe segment. At ~ 2.9 Ga the Tokwe segment and the cover succession were intruded by a tonalitic batholith. Most of the events recognised in the region occurred between 2.9 and 2.5 Ga. In the NMZ of the Limpopo Belt, most of the Plutonic Assemblage are intrusive rocks that crystallised from dry melts from 2.8 to 2.6 Ga. They may have been derived from partial melting of a mafic source. Some of the supracrustal rocks have experienced two thermal events at granulite facies conditions (Rollinson & Blenkinsop, 1995).

Northnorthwest-southsoutheast crustal shortening, which caused folding of the greenstone belt and regional greenschist metamorphism, occurred simultaneously with uplift of the NMZ over the Zimbabwe Craton. This uplift took place at *c.* 2.6 Ga, along parallel shear zones which form the tectonic break between the Zimbabwe Craton and the NMZ. Two suites of potassic granites were emplaced north and south of the greenstone belt towards the end of thrusting.

The youngest events (post-2.5 Ga) include the open folding in the greenstone belt as a result of northeast-southwest crustal shortening, which may have occurred in the earliest Proterozoic or at a younger time, and a low grade thermal overprint which occurred around 1.97 Ga.

2.3. Petrography

2.3.1. Introduction – The only published petrographical descriptions of the rocks in the southwestern part of the MGB were by Worst (1956). He described a larger area, which comprised the Belingwe Greenstone Belt, MGB and the granites in between (Fig. 7). Brief descriptions of most rock-types were given and, together with rock-types found in the Belingwe Greenstone Belt, the rocks were successively placed in a stratigraphical framework, which was applied to both greenstone belts. Later, this framework was revised for the Belingwe belt (Bickle & Nisbet, 1993), and for the BGB, the northeastern continuation of the MGB (Fedó & Eriksson, 1996). As explained in Section 2.2, the MGB does not conform to the classical stratigraphy, which is applied to most greenstone belts in Zimbabwe (see also Section 2.4).

The Mweza Greenstone Belt (MGB) consists of a succession of greenschist-facies sedimentary and volcanic rocks. The sedimentary rocks are mainly concentrated in the northern limb and central part of the belt, whereas most of the volcanic rocks are located

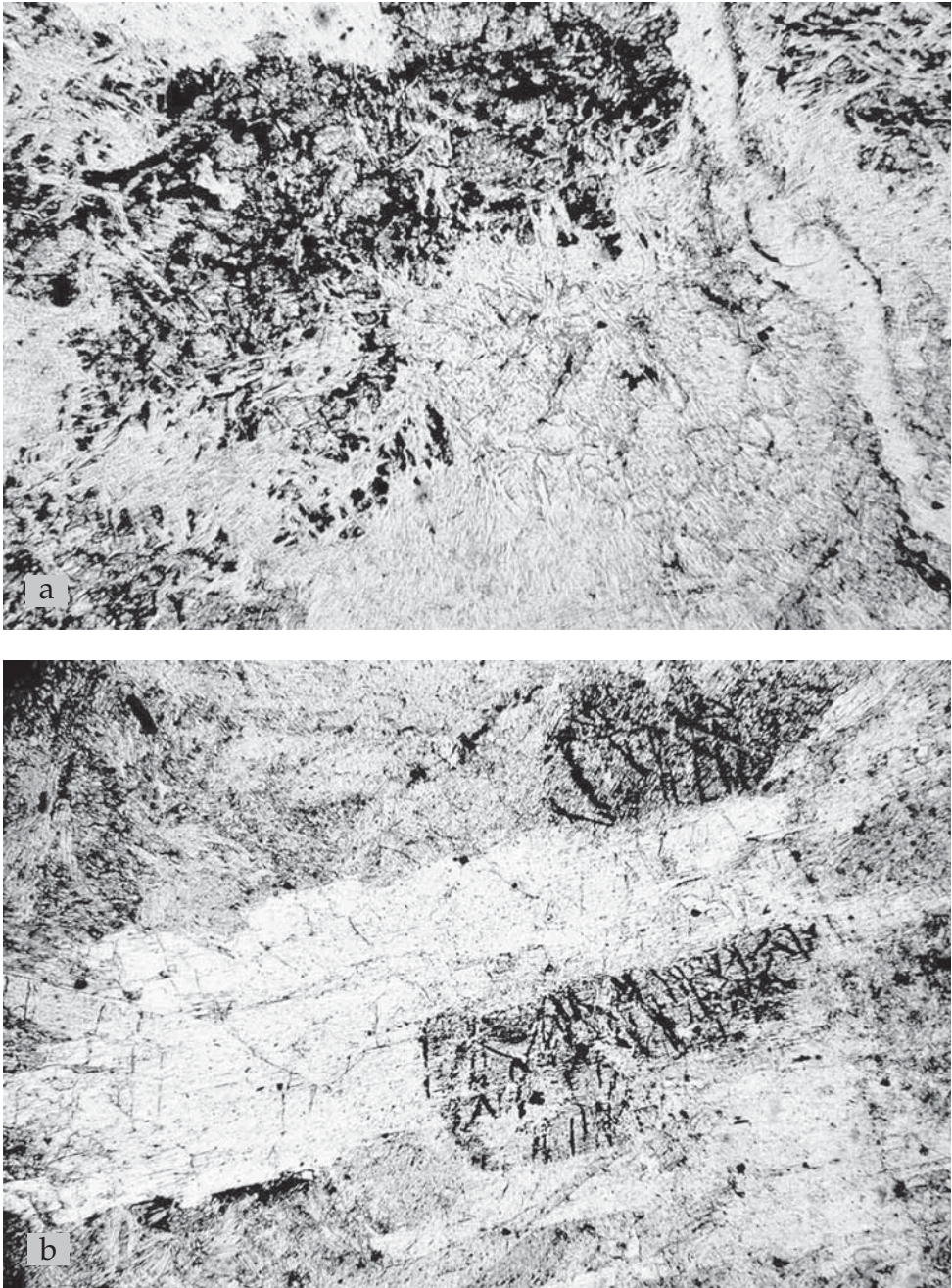


Fig. 8. (a) Olivine and orthopyroxene, partly serpentinized, present in an talc-amphibole schist (width of view: 1.7 mm). Sample 421503. (b) Relic olivine, partly altered to serpentine and magnetite, and overgrown by actinolite (width of view 2.4 mm). Sample 421062.

along the southern limb (Map 1). The sedimentary rocks mainly consist of banded ironstones, quartzites, phyllites, conglomerates and fuchsite schist. The banded ironstones can easily be recognised, forming the high ridges in the landscape. They consist of mm-scale alternations of opaque iron oxides and recrystallised quartz. The additional occurrence of finely grained grunerite in the quartz horizons characterizes the greenschist facies metamorphism (see, e.g., Klein, 1978). Some sedimentary rocks (such as the phyllites) are not exposed in the field, because of the dense vegetation on the MGB. These rocks were formerly recognised by mine geologists, when examining samples from cross-trenches, which were made across the mining claims along the MGB.

Sedimentary and volcanic rocks were intruded by a number of granitic gneisses, pegmatite bodies and metadolerites. The pegmatite bodies mainly occur in the volcanic rocks along the southern flank of the MGB. The emerald occurrences are closely related to the pegmatite bodies. As the focus of this study is on the origin of the emeralds, the related rocks, such as the volcanics, pegmatites and the alterations of the specific ore-zones, were studied in detail and are further described below.

2.3.2. *Volcanics* – At the Sandawana Mines, many rock-types were distinguished in the area, mainly based on what was seen at the underground operations. Field terms such as ‘Serpentinite’, ‘Main Serpentinite’, ‘Silicified Serpentinite’, ‘Footwall Serpentinite’, ‘Hangingwall Serpentinite’ and ‘Metabasalt’ were applied by the mining personnel. Except for Footwall and Hangingwall Serpentinite, which were distinguished purely from their relative position towards the pegmatites, the criteria on which the various terms were based are unclear. Many misunderstandings existed as a result of the use of these terms; for instance, many mine workers thought that ‘Footwall Serpentinite’ had a very different composition compared to ‘Hangingwall Serpentinite’, and during this study ‘metabasalts’ turned out to contain high concentrations of olivine and no feldspar. It became apparent that all these rocks show many similarities in mineral composition, although they cannot be classified as serpentinite. Also, in the field it is hardly possible to make meaningful distinction between the field terms. For this reason, all these rocks are grouped and classified as undifferentiated greenstones.

Undifferentiated greenstones – These greenstones appear as dark green to dark greenish grey, weakly to well-foliated rocks. In places the rocks have a massive character, gradually grading into moderately to well-foliated rocks on a metre scale. Rocks that are weathered are light greyish to brownish green and/or red-brown to orangish brown. They mainly consist of finely to medium-grained actinolite schists, containing various amounts of cummingtonite, talc, chlorite, albite and opaque minerals. Table 4 reports mineral abundance in the rocks that are chlorite-actinolite schists, talc-chlorite-actinolite schists, albite-cummingtonite-actinolite schists, cummingtonite-chlorite-actinolite schists and cummingtonite-talc-actinolite schists, occasionally containing (relic) olivine, (relic) orthopyroxene and serpentine (Fig. 8a). Phlogopite only occurs in the rocks next to intruded pegmatites.

In some cases, the albite-cummingtonite-actinolite schists can be recognised in the field, by parallel, thin and white albite veins of 2 to 7 mm wide. Most albite occurs in either veins, zones or lenses, and shows straight grain boundaries. In no. 421502, zoned plagioclase feldspar could be observed; An% in this rock appears to vary between 10 and 20.

421570	MB	38	10	15	30	5				2	
421860	MB	30	5	20	20	2				3	
421062	MS	50		40			5			3	2
421063	MS	48	30	10			10			1	1
421500	MS	63		15			2			20	x
421002	S	50	5		43					1	1
421003	S	65	5	25	2					3	x
421007	S	85		10						5	
421008	S	80		10	2					8	
421009	S	78		20						2	
421754	S	75	5	5	10					5	x
421755	S	88	5	1	1					5	
421861	S	15				84				1	
421591	SS	5		15	25	5		10	10	5	
421853	U	40 hbl					48	5		7	x
											x

FS = 'Footwall Serpentinite'
 HS = 'Hangingwall Serpentinite'
 MB = 'Metabasalt'
 MS = 'Main Serpentinite'
 S = 'Serpentinite'
 SS = 'Silicified Serpentinite'
 U = 'Ultrabasic rock'

Mineral symbols according to Kretz (1983)
 Carb = carbonate
 Opq = opaque

Some of the olivine-rich rocks can also be recognised in the field. Olivines range in size from about 1 to 5 mm, and weather as reddish brown spheres to ellipsoids that may stand in positive relief.

Amphibole crystals are up to several millimetres in length and have acicular to long prismatic shapes. Typically, they are orientated parallel to foliation planes. Actinolite is faintly pleochroic, which indicates that it is Fe-poor (see Section 3.4.4). The percentage of cummingtonite present in the rocks is difficult to estimate, because complex intergrowths between actinolite and cummingtonite frequently occur. Commonly, these intergrowths only become apparent when a scanning electron microscope is used (see Section 2.3.4).

Among the opaque minerals, magnetite and chromite have been identified. Near the pegmatites, chromian ilmenorutile and minerals of the pyrochlore group have also been encountered (see Sections 2.3.4 and 3.4.4). Magnetite very commonly occurs in octahedral shapes, while chromite grains commonly show frayed edges.

Relic structures mainly show olivine, partly or completely altered into bowlingite, serpentine, talc and magnetite. The presence of olivine, serpentine and magnetite together suggests the reaction: forsterite + H₂O → serpentine + magnetite (Fig. 8b). In a few samples (e.g., nos. 421504 and 421860), relic structures consisting of chlorite could indicate the former presence of clinopyroxene.

A humite-group mineral, which is present in an olivine-rich rock (no. 421591), shows vivid orange and yellow pleochroic colours, and was identified as titanian clinohumite.

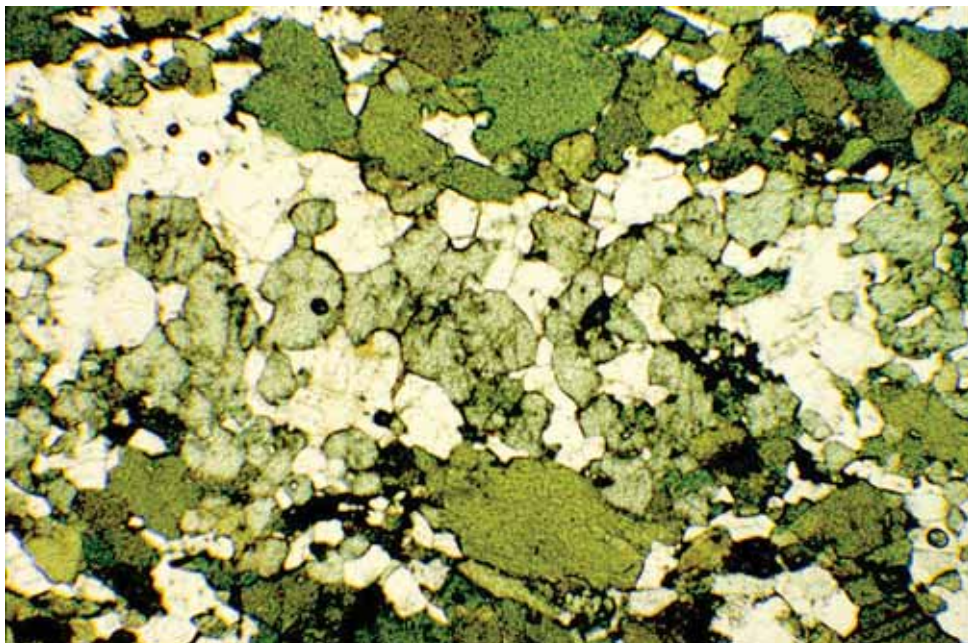


Fig. 9. Amphibolite showing the mineral assemblage diopside-hornblende-titanite-plagioclase (width of view 3.3 mm). Sample 421571.

Amphibolites – Amphibolites appear as very dark greenish grey to black, finely to medium grained, foliated rocks. They may contain narrow whitish layers, usually 1-3 mm thick, parallel to the foliation. The whitish layers are unevenly distributed; alternation of whitish and black layers can occur on a mm scale, but black layers of a cm or more wide are more common. Weathering may change the colour of the rocks into orangish brown to light greenish brown. The amphibolites that are indicated as metadolerites in the field are dark greenish grey to black, finely grained, massive and homogeneous rocks, which weather into reddish and greenish brown.

The amphibolites mainly consist of hornblende and plagioclase, and may contain diopside, titanite and/or quartz (Fig. 9; Table 5). One rock, classified as metadolerite in the field, contains clinozoisite. Plagioclase often shows straight, stable boundaries and occurs in plagioclase-rich zones, but is also evenly distributed interstitially, in between the an- to subhedral hornblende. The estimated anorthite content varies between 10 and 20%. In one of the metadolerites (sample no. 421004), clear ophitic structures are present, which show plagioclase enclosed by hornblende. The plagioclase has an estimated anorthite content of about 50%.

Origin of undifferentiated greenstones and amphibolites – Intense ductile deformation and regional metamorphism have obliterated most primary fabrics. Thus, protolith interpretation is restricted by the degree to which compositional trends and primary fabrics can be recognized.

The greenstones that show relic olivine and pyroxene indicate an ultramafic igneous nature of the initial protolith. This conclusion is supported by the presence of titanian clinohumite, which normally occurs as a rare mineral in serpentinised ultrabasic rocks (e.g., Smith, 1979; Deer *et al.*, 1982; Dymek *et al.*, 1988; Gaspar, 1992). Also, the encountered zoned plagioclase feldspar indicates a magmatic origin. The dominance of Fe-poor actinolite schists (see Section 3.4.4) suggests a Mg-rich/Fe-poor protolith.

Fedo & Eriksson (1996) described a few occurrences of greenstone in the centre of the BGB, which have not had their pre-metamorphic fabrics obliterated. They found a succession with preserved cumulate textures, overlying giant spinifex fans, which are subsequently capped by random pyroxene and olivine spinifex. These subunits are similar to komatiite flows described by Pyke *et al.* (1973) from Munro Township, Ontario, and similar spinifex fans have been recognised from komatiites in the Nondweni greenstone belt, South Africa (Wilson *et al.*, 1989; Wilson & Versfeld, 1994). Jolly (1982)

Table 5. Mineral content of amphibolites in the Mweza Greenstone Belt.

Rock		Mineral content (visual estimation vol. %)							Accessory minerals				
RGM No.	Field-code	Hbl	Ttn	Czo	Di	Pl	Qtz	Opq	Opq	Ap	Rt	Zrn	Chl
421014	A	99						1					
421015	A	93				2	5		x	x			x
421571	A	69	1		5	25			x	x			
421792	A	40				53		7		x	x		
421793	A	50				45		5		x	x		
421004	MD	65	3			25	7		x	x	x	x	
421599	MD	88	2	10		x			x				

A = 'Amphibolite' Mineral symbols according to Kretz (1983)

MD = 'Metadolerite' Opq = opaque

described metamorphosed Archaean mafic and ultramafic rocks from the Abitibi region, Canada, and suggested an olivine-cumulate lava as protolith for an assemblage dominated by tremolite or faintly pleochroic, Fe-poor actinolite at greenschist facies.

Cummingtonite and tremolite occurring together as discrete grains and as lamellar intergrowths were also observed by Gole *et al.* (1987) in Western Australia, together with olivine + chlorite \pm enstatite in metamorphosed komatiite lavas. Hence, it is probable that the olivine-rich rocks and the presence of titanian clinohumite in the MGB indicate an original olivine accumulation in komatiitic lava, rather than a former presence of mantle peridotite. The rocks, richer in albite, could indicate a more basaltic composition at places. Thus, the greenstones of the MGB may be interpreted as being a series of metamorphosed komatiites and possibly, komatiitic basalts.

Metamorphic conditions – The association of actinolite, chlorite and albite indicate greenschist-facies conditions during peak-regional metamorphism. In metamorphosed ultramafic rocks, the mineral assemblages are strongly dependent upon temperature and essentially independent of pressure. The encountered assemblages of olivine, talc and the magnesium-rich actinolite (almost tremolite; see Section 3.4.4), and the absence of serpentine in most rocks, suggests that the metamorphosed ultramafic rocks underwent temperatures that were at least equal or higher than the serpentine-out isograd, which lies around 400-450°C (compare, e.g., Tracy & Frost, 1991). The only rock that rightly could be called a serpentinite (no. 421861) has been collected away from the emerald bearing mines, further north into the MGB (Map 3).

Across strike of the belt towards the southeast, the metamorphism increases from greenschist facies to amphibolite facies in the amphibolites. During amphibolite grade metamorphism, all original features were obliterated and the rocks of the amphibolite facies may therefore be considered as completely recrystallised. The presence of hornblende and plagioclase is typical of amphibolite facies metabasites. In one amphibolite (no. 421571), which is almost at the border between the MGB and the NMZ of the Limpopo belt, clinopyroxene and titanite are present also. This indicates upper amphibolite facies conditions. Spear (1981a) experimentally showed that for fO_2 conditions defined by the quartz-fayalite-magnetite (QFM) buffer, below 775°C the typical assemblage is hornblende + plagioclase + ilmenite \pm titanite. Beginning at approximately 775°C, hornblende begins to break down in a series of continuous reactions first to clinopyroxene + plagioclase (cpx-in), then to clinopyroxene + orthopyroxene + plagioclase (opx-in), and finally to clinopyroxene + orthopyroxene + olivine + plagioclase (ol-in). The cpx-in and opx-in curves are hardly dependent on pressure, which means that the assemblage hornblende + plagioclase + clinopyroxene + titanite and the absence of orthopyroxene in amphibolite no. 421571 suggest temperatures around 775-820°C.

2.3.3. *Pegmatites* – Intrusive pegmatites mainly occur at the southern flank of the MGB. The pegmatites in the greenstones are often strongly folded and sheared (Fig. 10). They also show pinch-and-swell and boudin structures, which indicate that the relatively strong (rigid) pegmatite became stretched and elongated during deformation. The pegmatite bodies vary in thickness, but are often narrow, between 0.4 and 3.0 m thick. They are completely albitised. All feldspars, which at first sight look very different

(larger anhedral crystals with or without unclear or clear polysynthetic albite twinning, in some thin sections showing many subgrains, as well as large 'chessboard' feldspar phenocrysts, small recrystallised grains, with straight, stable boundaries), consist of nearly pure albite. Myrmekites, made of vermicular assemblages of pure albite and quartz (Fig. 11), show that K-feldspar must have originally been present (see Chapter 4). Rarely, feldspar grains have been observed showing brittle deformation. The only quartz that is present occurs as small grains in the myrmekites and in narrow veins, 5 to 100 mm thick, in the middle of the usually thin pegmatites, 1 to 1.5 m away from the contact with the schist.

At Aeres (Fig. 7), in the first underground exploration tunnel that was made in this area, one pegmatite was discovered which contains microcline feldspar that was not completely albitised. The pegmatite is 1.5 m wide and follows the main foliation trend (dip: 340/72). The section that could be studied shows a slightly different picture than the usual one described above. From the footwall to the hanging wall the sequence is:

1. Oligoclase – albite (minor apatite, phlogopite and quartz); oligoclase is medium- to coarse-grained, anhedral, and shows unclear and clear albite twinning. Large chessboard type grains also occur. The estimated anorthite content is 15-20%. Recrystallised albite is fine-grained and shows straight, stable grain boundaries.
2. Oligoclase – quartz – myrmekite – albite (minor beryl, rutile and Li-mica); this zone is quartz-rich. Quartz is anhedral, medium-grained and does not occur in veins, but as single (groups of) grains throughout the pegmatite. Myrmekite consists of albite and small quartz.
3. Oligoclase – 'giant' myrmekite – albite – quartz (minor microcline, beryl, rutile); 'giant' myrmekites are medium-, but more commonly coarse-grained. Quartz is mainly concentrated in patches. Microcline only occurs as very small grains, overgrown by the other feldspars.
4. Oligoclase – microcline – lithian mica (minor myrmekite); microcline is anhedral, medium-grained and occupies an estimated volume of 10%. It is overgrown by large oligoclase and also by developing myrmekites (Fig. 12). Lithium-bearing mica, subhedral and fine-grained, shows a weak pink/lilac and white pleochroism (sometimes with brownish yellow), which is characteristic for lepidolite, although the slight possibility of lithian muscovite cannot be ruled out.
5. 'Giant' myrmekite – albite – (minor quartz and rutile); 'giant' myrmekites and fine-grained, recrystallised albite are dominant.

In another pegmatite body, also at Aeres, located in an open-pit at the southwestern corner (Aeres-1), large, opaque, light green, euhedral beryl crystals were found. The pegmatite is about 2 m thick with a cluster of beryl crystals located slightly off the centre of the body. The largest crystals are up to 150 mm long and 70 to 80 mm wide. Semi-quantitative EDXRF microanalysis of this beryl revealed the presence of sodium and magnesium, and traces of iron, vanadium and rubidium (weight %: Na₂O 2.3, MgO 1.7, FeO 0.95, V₂O₃ 0.04, Rb₂O 0.02). Chromium has not been found.

Locally in the Zeus underground mine, dark violetish-red almandine garnets were found in the pegmatite, in association with black sphalerite. Other minerals that were encountered are manganese oxides, and at the borders emerald, fluorapatite, holmquistite, actinolite, cummingtonite, phlogopite and ilmenorutile (see Section 2.3.4).

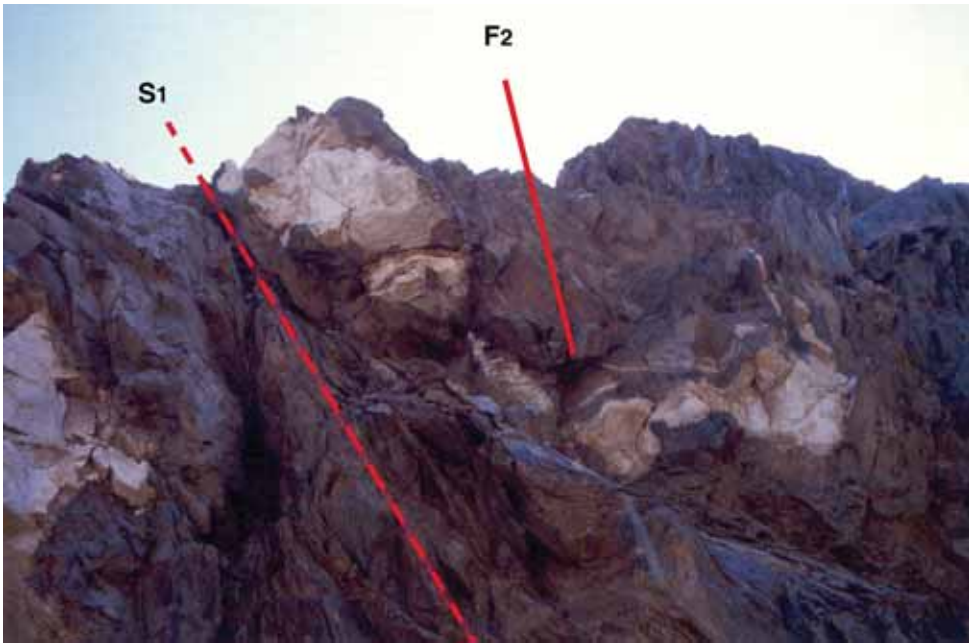


Fig. 10. Boudinaged, sheared and folded pegmatite at the Orpheus Mine. The thickest part of the pegmatite is approximately 1.20 m. At Orpheus Mine the pegmatite shows folding in the direction of shortening and boudin structures in the extensional direction (parallel to the main foliation).

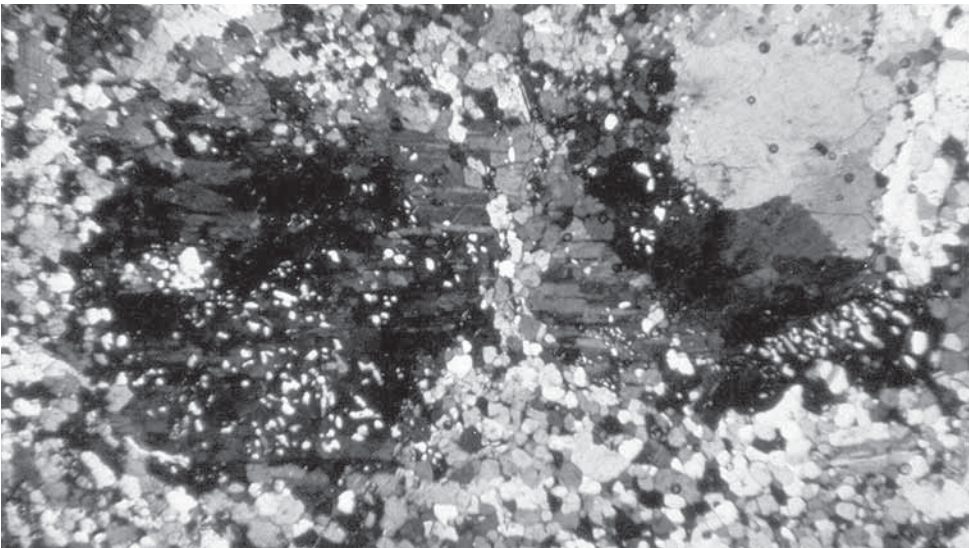


Fig. 11. Myrmekites (300 μm), consisting of albite and quartz, surrounded by recrystallised fine-grained albite. Albite almost at extinction (black, with slight traces of polysynthetic twinning). All quartz vermicules white (maximum illumination, all crystals with the same optical orientation). Crossed nicols, polarized light. Width of view 750 μm . Sample RGM 421369, Zeus underground mine, 300 ft. level, 23/7 stope.

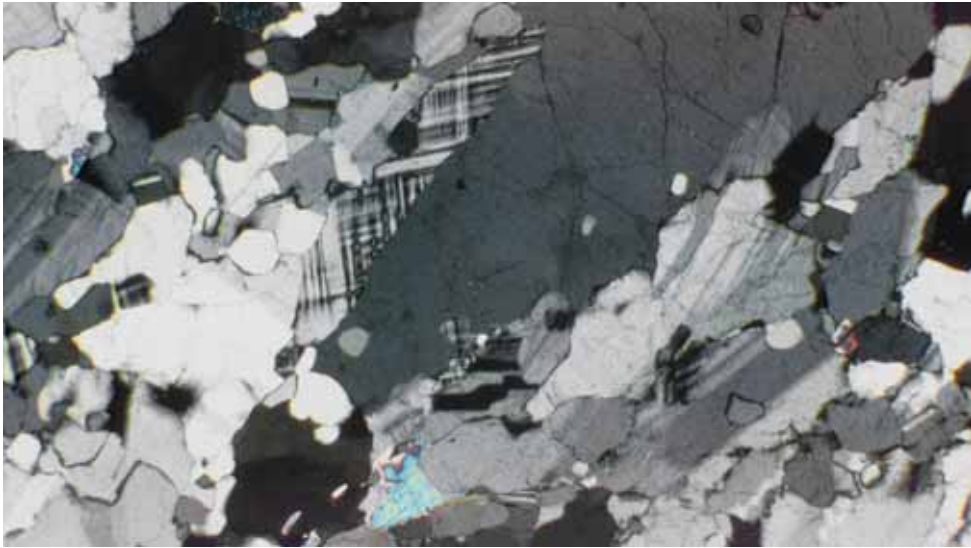


Fig. 12. Microcline feldspar overgrown by albite (dark grey) with a myrmekitic character. Width of view 1.8 mm. Sample RGM 421764, Aeres mine, exploration shaft.

'Bikita-type' pegmatites – The presence of microcline and abundant giant myrmekites indicates that originally a potassium-rich pegmatitic magma intruded into the greenstones (see Chapter 4). This magma contained sufficient Be and Li to form beryl and lithian mica, respectively.

Almost complete albitisation of the pegmatite and phenomena observed in the ore zones, at the contact between pegmatite and greenstone (Section 2.3.4), indicate subsequent pegmatitic/hydrothermal activity (Chapter 4).

Grubb (1973) discussed the stability of lithium-bearing minerals in so-called *'Bikita-type' pegmatites* in Zimbabwe, located in the greenstone belts all along the southern boundary of the Zimbabwe craton (Fig. 6). He described quartz-spodumene ($\text{LiAlSi}_2\text{O}_6$)-petalite ($\text{LiAlSi}_4\text{O}_{10}$) pegmatites at Bikita, which are characterized by petalite and/or fine-grained quartz/spodumene aggregates. Muscovite and microcline crystallised in the wall-zone, whereas coarse-grained microcline-petalite-quartz were formed in the intermediate zone and the core. Based on hydrothermal experiments and study of phase relations, it is concluded that the pegmatites are products of high-temperature crystallization, i.e., probably above 600°C, because petalite is stable above 550-600°C. This is consistent with the data presented by Stewart (1978), who showed that the bulk composition of the petalite-bearing Bikita pegmatites is in the region of minimum melting temperatures on the liquidus (640°C at 2 kb). This correspondence suggests that the lithium pegmatites could have originated out of magmas of similar temperatures and pressures.

In a later stage there was a significant degree of replacement phenomena. Albitisation caused extensive replacement of petalite into albite. According to Grubb (1973), an injection of a late sodic magma during structural movement was responsible for this albitisation. This process released large amounts of K and Li into solution, and an albite-

quartz-lepidolite pegmatite could be formed, provided that the late-stage mineralisation fluids tend to be rather fluorine-rich (Grubb, 1973; Cerny *et al.*, 1985; see discussion in Chapter 4). If the Li-content is high, petalite and spodumene would convert into eucryptite (LiAlSiO_4). This would explain the frequent association of eucryptite with spodumene zones, as at Bikita.

Petalite would convert into 2 quartz + spodumene, when $T > 550^\circ\text{C}$, Na is below a certain level and Li is sufficient. Thus, the replacement of petalite by quartz-spodumene assemblages in highly sodic residual fluids is a rare occurrence.

Non-albitised petalite horizons are only preserved in the Bikita and Portree pegmatites. According to Grubb, derived spodumene is less restricted, lepidolite is abundant throughout the belts, and albitisation increases with distance from the Bikita pegmatites. Emerald-occurrences appear to be largely confined to the more intensely albitised 'extremities', which are located in the MGB.

Grubb claimed that most Zimbabwean pegmatites, but certainly the pegmatites along the southern border of the Zimbabwe craton, are lithium-rich, and that their paragenesis was influenced by three essential factors; time, temperature and extent of late albitisation. However, later work by London (1984) provided a lithium aluminosilicate phase diagram (Fig. 13), which showed that, under quartz-saturated conditions, stability relations between petalite, spodumene and eucryptite are more pressure dependent than originally thought, and are largely independent of the nature and proportions of other phases in the chemically complex pegmatite system. Petalite is stable under much lower T and P than previous experimental work (e.g., Grubb, 1973) would indicate; experiments at 2 kbar indicate a reaction boundary between spodumene and petalite at 380°C . Subsequently, the stability field of eucryptite + quartz is limited to low P and T , below about 320°C and 1.6 kbar. The isochemical breakdown of petalite follows from cooling through the stability field of spodumene or eucryptite or both. Eucryptite + quartz assemblages show that retrograde alteration is operative to low P and T in some lithium pegmatites, such as in Bikita. Figure 13 shows an inferred P - T crystallisation path for the Bikita pegmatites, as indicated by London (1984).

Apart from the fact, that from the observations made by Grubb (1973), one can deduce that there probably is a connection between emerald formation and the intensive albitisation that took place after the pegmatite intrusion, a few remarks can be made on Grubb's statements on the general character of the pegmatites. As described above, in the pegmatites, associated with emerald occurrences in the MGB, lepidolite is not abundant. In the Orpheus and Zeus mines, this mineral was not encountered by the author. Lithian mica was present only at Aeres, in association with microcline and confined to a central zone that largely escaped intense albitisation. This suggests that lithian mica was formed either together with microcline or shortly after, but before albitisation, instead of as a result of albitisation. In the completely albitised pegmatite, not lepidolite, but holmquistite (a lithian amphibole), is commonly present, though only at the contact with the greenstone. Apart from the large quantities of emerald, at or close to the contact of the pegmatites (Section 2.3.4), beryl is commonly found in the pegmatite. This suggests that originally these pegmatites must have had a higher Be/Li ratio than the pegmatite at Bikita, although Russell (1988) reported that, apart from lithium ores, pollucite and beryl are available at Bikita also. Thus, it is likely that the paragenesis of the 'Bikita-type' pegmatites is not only influenced by

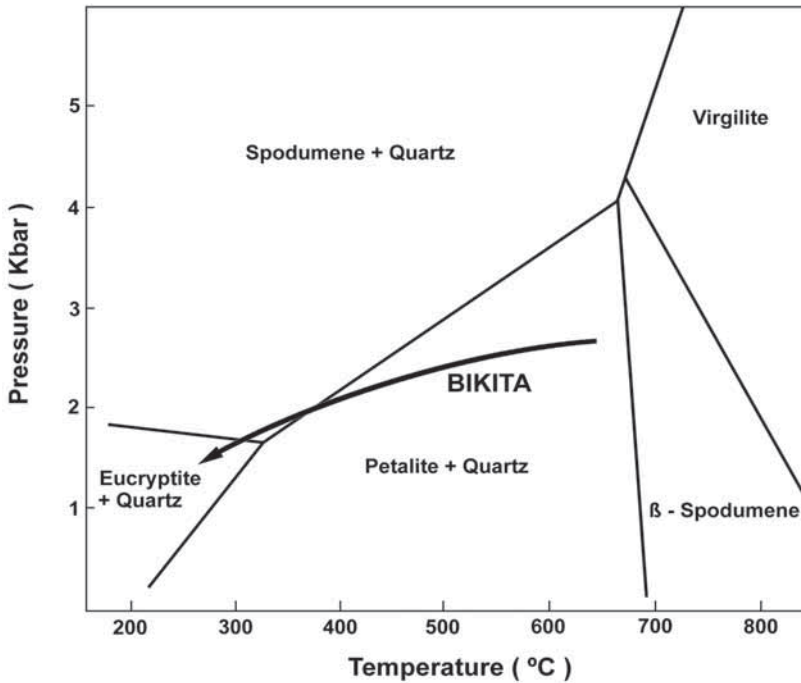


Fig. 13. Inferred P-T crystallisation path for the Bikita pegmatite, as defined by lithium aluminosilicate + quartz assemblages at this deposit. After London (1984, fig. 2).

the cooling path and extent of albitisation, but also by significant compositional differences in the original pegmatitic magmas. This view is supported by the presence of an emerald-barren pegmatite, only 3 km northwest of the Zeus Mine, at the northern side of the MGB, which contains abundant large lepidolite crystals and is locally known as a small lithium mine.

Source of pegmatite magma – It seems logical that the evolved pegmatite is associated with the emplacement of the closest K-feldspar granites (compare, e.g., London, 1996), namely the Razi granite, which intruded in the major shear-zone, just south of the MGB, and the Chibi batholith, respectively (Fig. 7). Both granites intruded at about the same time during the main deformation event (Sections 2.2.1, 2.2.2), corresponding to the synkinematic intrusion of the pegmatites (Section 2.4, also compare Chapter 5). It is unlikely that the pegmatites at Sandawana are associated with the tonalitic batholith, which is present all around the greenstone belt. The tonalite crystallised from a relatively alkali-poor magma, whereas the evolved pegmatite appeared to have been potassium-rich originally.

Baker (1998) calculated the generation of pegmatite dykes during the cooling and crystallization of granitic plutons, using updated models for the prediction of granitic melt viscosities and the propagation of dykes. From these models it was predicted that pegmatites should only rarely be found more than c. 10 km from their host pluton, that more-evolved pegmatites should be found at greater distances from their host pluton

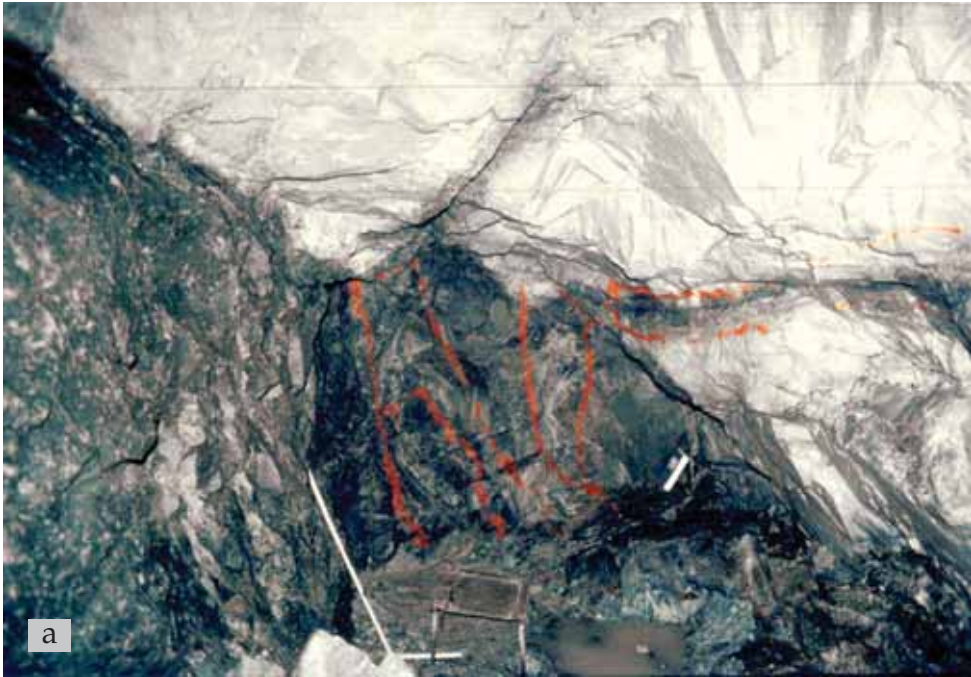


Fig. 14. Folded and sheared pegmatite and strongly foliated schists, with prominent differentiated layering of amphibole-rich and phlogopite-rich layers. (a) In the marked areas (red) many emeralds were found. Zeus underground mine, 200 ft. level, 26/28 stope. (b) Detail of schist at the contact with pegmatite, with amphibole-rich and phlogopite-rich (dark) layers. Zeus underground mine, 200 ft. level, 20/21 drive west.

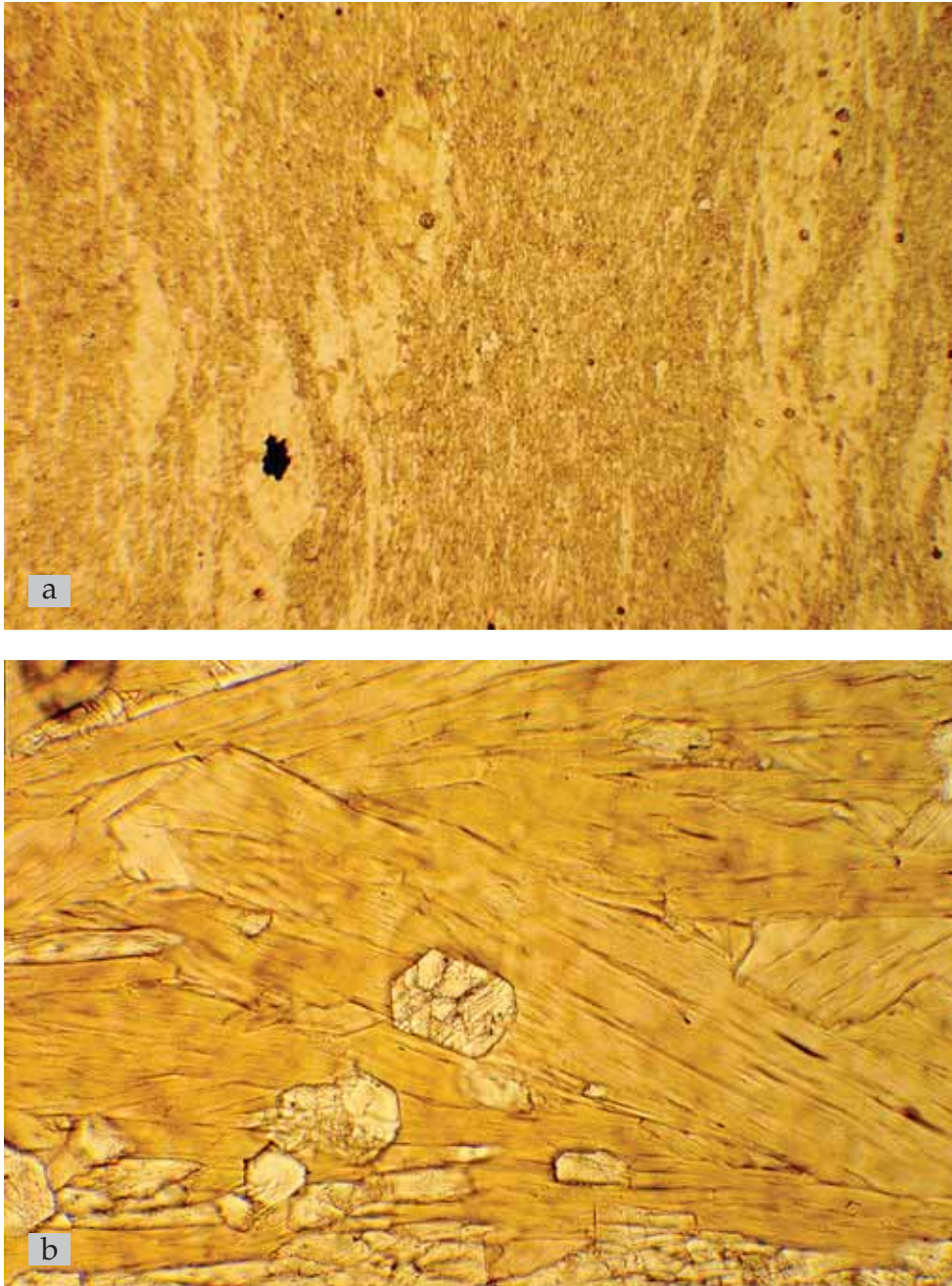


Fig. 15. (a) In microshear zones at the contact between pegmatite and greenschist, nests of phlogopite are present, which look like 'augen' textures. The black inclusion with frayed edges represents a chromian ilmenorutile; length of this crystal is about 300 μm . Width of view 6.34 mm. (b) Idiomorphic amphiboles occur in and around the phlogopite 'augen'; length of this crystal is about 100 μm . Width of view 750 μm . Sample RGM 421354, Zeus underground mine, 250 ft. level, 17/16 stope.

than less-evolved ones and that pegmatites should not be associated with small plutons (less than approximately $5 \times 5 \times 5$ km).

Taking this concept into consideration, at first sight the Chibi batholith seems to be too far away to be the source for most of the intruded pegmatites (Fig. 7, Map 1), whereas the Razi granite seems a pluton of questionable size, especially closer to the Sandawana emerald mines and perhaps also too far away for the pegmatites at the Orpheus mine. However, it can be expected that the Razi granite is considerably larger than it appears on the geological map, as it is present all along the major shear zone. It is also possible that the Chibi batholith is present at depth less than 10 km away.

2.3.4. Emerald bearing zones – Minerals, present in the emerald bearing zones at Sandawana, are listed in Table 6. Emeralds are normally found very near the contact between pegmatite and schist, always in zones near folded and sheared pegmatites, or pinched zones near boudinaged or pinch-and-swell pegmatites, and occur in strongly foliated schists, showing prominent differentiated layering of amphibole-rich and phlogopite-rich layers (Fig. 14). When the differentiated layering is absent at the contact, emeralds do not occur. From thin-section observations it became clear that, at the contacts where emeralds were found, discrete micro shear-zones are present. In the shear-zones, nests of phlogopite occur which look like ‘augen’ textures (Fig. 15a). Straight phlogopite blades as well as folded phlogopite crystals were observed within and out of these ‘augen’. It means that phlogopite has grown synkinematically, i.e., during the shearing event.

Idiomorphic amphiboles are present in and around the phlogopite ‘augen’ (Fig. 15b). This structure suggests growth during peak metamorphism. It also implies that peak metamorphism and shearing took place roughly at the same pressure and temperature conditions.

Chemical analyses indicate actinolite [$\text{Ca}_2(\text{Mg}, \text{Fe}^{2+})_5\text{Si}_8\text{O}_{22}(\text{OH})_2$] compositions, transitional to hornblende, with lower Ca and Si, and higher Al, Na and K. The cores of some larger grains show a clear edenite composition, with even lower Si and more Al (Si: 7.40, Al: 0.88, Na + K: 0.58; compare Leake *et al.*, 1997). These data suggest that peak metamorphism occurred at upper greenschist conditions, near the boundary between greenschist facies and amphibolite facies.

Apart from actinolite, cummingtonite commonly occurs in the ore-zone. At the contact with pegmatite, or within amphibole schlieren in the pegmatite, holmquistite is also found (Table 6). Intergrowths between actinolite and cummingtonite have been com-

Table 6. Essential mineralogy of emerald occurrences at Sandawana, Zimbabwe.

Albite	$\text{NaAlSi}_3\text{O}_8$
Phlogopite	$\text{KMg}_3\text{Si}_3\text{AlO}_{10}(\text{F}, \text{OH})_2$
Cummingtonite	$(\text{Mg}, \text{Fe}^{2+})_7\text{Si}_8\text{O}_{22}(\text{OH})_2$
Actinolite	$\text{Ca}_2(\text{Mg}, \text{Fe}^{2+})_5\text{Si}_8\text{O}_{22}(\text{OH})_2$
Holmquistite	$\text{Li}_2(\text{Mg}, \text{Fe}^{2+})_3\text{Al}_2\text{Si}_8\text{O}_{22}(\text{OH})_2$
Fluorapatite	$\text{Ca}_5(\text{PO}_4)_3\text{F}$
Emerald	$\text{Be}_3\text{Al}_2\text{Si}_6\text{O}_{18}$
Phenakite	Be_2SiO_4
Chromian ilmenorutile	$(\text{Ti}, \text{Nb}, \text{Ta}, \text{Cr}^{3+}, \text{Fe}^{3+})_3\text{O}_6$
Chromite	$\text{Fe}^{2+}\text{Cr}_2\text{O}_4$

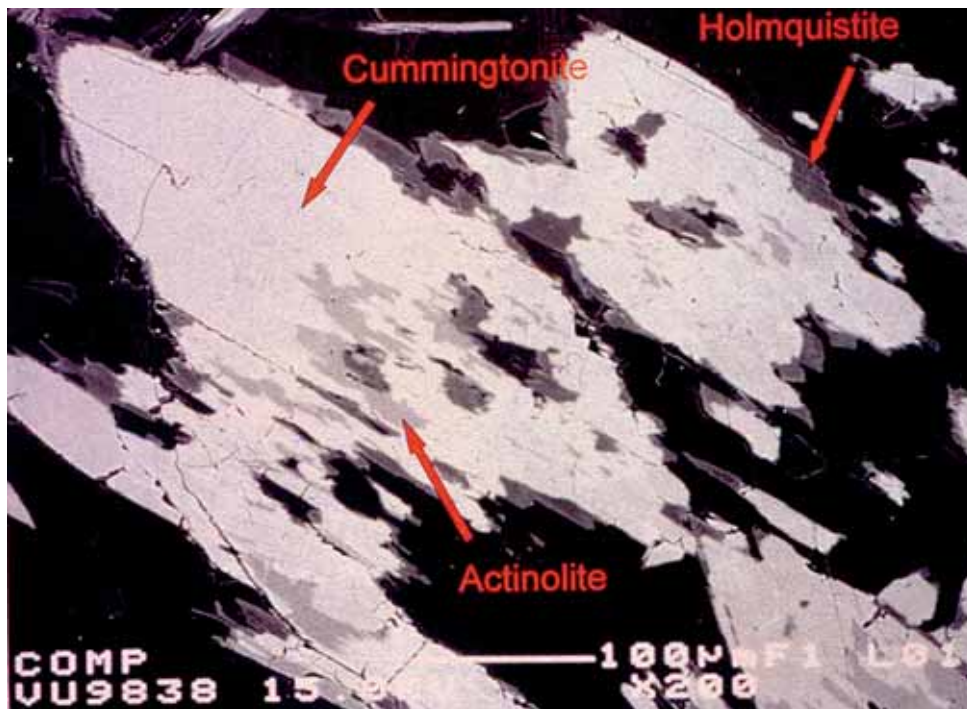


Fig. 16. Electron photomicrograph of amphiboles in albite. Here, the amphibole grains mainly consist of cummingtonite, with, in the centre, small parts of actinolite and holmquistite, and, at the rim, only holmquistite. Sample RGM 421550, at the contact between pegmatite and schist, Zeus underground mine, 200 ft. level, 26/28 stope.

monly observed, but also grains of cummingtonite with actinolite rims, or holmquistite rims close to the pegmatite, and intergrowths between actinolite (or cummingtonite) and holmquistite occur (Fig. 16). Masses of fine-grained asbestiform cummingtonite and actinolite also occur, and both emerald and phlogopite have grown over it.

Emeralds and apatites with similar size usually occur at the contact between pegmatite and schist, often until only 30 cm away from the contact. Emeralds are also present in or near amphibole schlieren running into the pegmatite (Fig. 14a). Usually, the size of both emerald and apatite is small; crystals up to 5 mm are most common, but, as mentioned in Section 3.3.3, larger emerald crystals up to 50 mm in length have been recovered. Also, apatite can grow in large crystals. In 1998 a well formed apatite crystal of 70 × 40 mm was found at the Orpheus Mine, near the surface, right under a folded pegmatite, in the greenschist (Fig. 17). Large emeralds up to 40 mm in length have been recovered near this location, but in schist just near a pinched pegmatite, showing a pinch-and-swell structure.

Emerald porphyroblasts occur, with foliation bent around it, confirming a syntectonic growth of emerald (Fig. 18a); also, both emerald and apatite grew over albite and phlogopite (Fig. 18a-c). As the idiomorphic and larger amphiboles also grew over the phlogopites, they appear to have grown somewhat later than phlogopite, like many emeralds and apatite.

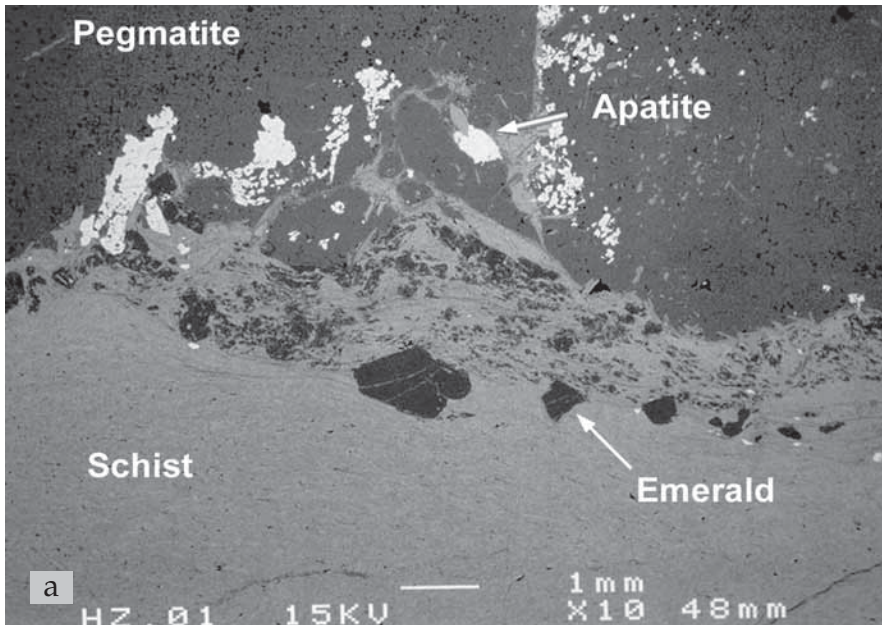
EPMA analysis shows that apatites are fluorapatites and phlogopites consistently contain a fair amount of fluorine (an F varying between 0.27 and 0.45).

Commonly, chromite occurs in the phlogopite; these grains show frayed edges, indicating a partial dissolution of the grain.

Chromian ilmenorutile, although rare as an inclusion in emerald (see Section 3.4.4), is commonly present at the contact. It occurs in association with phlogopite, but grew somewhat later (Fig. 19). Nowhere else in the world are ilmenorutiles found with such high chromium content (Section 3.5.2.; Zwaan & Burke, 1998). Other Nb- and Ta-bearing minerals, members of the pyrochlore-series (e.g., U-bearing microlite), have been found in the pegmatite, but they are extremely small. Phenakite was also observed in the contact-zone, but is rather uncommon; it has only been identified within emeralds. Discussion of metasomatic processes in the ore zones are presented in Chapter 4.



Fig. 17. Apatite and emerald are usually small, but can grow in larger sizes. A well formed apatite crystal with a length of 70 mm was found by the mine geologist at the Orpheus Mine.



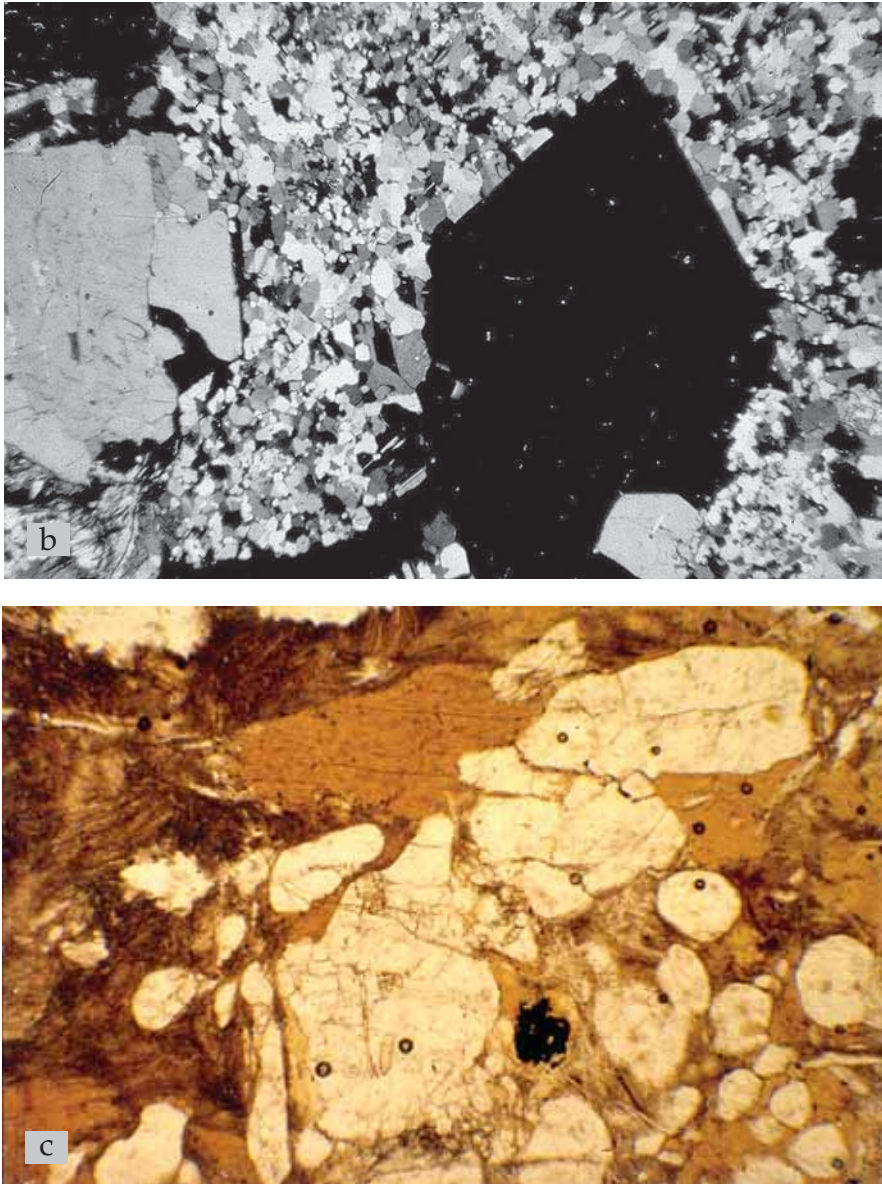


Fig. 18. (a) Electron photomicrograph of the contact-zone between pegmatite and greenschist, showing the distribution of emerald and apatite; here, the foliation bends around the small emerald porphyroblasts, confirming the syntectonic growth of emerald; apatite has grown over albite and phlogopite. Sample RGM 421550 (96ZW009). (b) Subhedral emerald (dark) has grown over recrystallised albite; width of emerald 2.1 mm. Crossed nicols, polarised light. Sample RGM 421552 (96ZW011). (c) Rounded emerald grains (white) grew over phlogopite. The black grain with frayed edges is chromian ilmenorutile. Length of the phlogopite grain at the top is 0.9 mm. RGM 421550. All samples from Zeus underground mine, 200 ft. level, 26/28 stope.

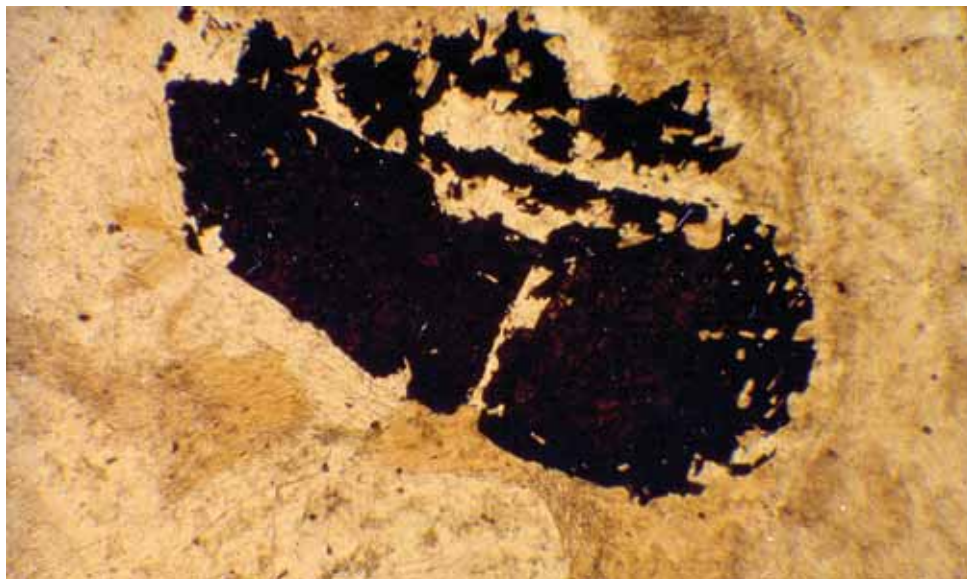


Fig. 19. Ilmenorutile is abundant in the ore zones at Sandawana. It often shows frayed edges; it crystallised later than phlogopite and just before emerald (white grains). Length of ilmenorutile 1.0 mm. Sample RGM 421545 (96ZW006a), Zeus underground mine, 200 ft. level, 26/28 stope.

2.4. Structural geology

At the southern border of the greenstone belt, just east of the Zeus mine, in the river, mylonitic gneisses trending 056 NE (dip of foliation: 146/72), show the presence of a shear-zone parallel to the Limpopo belt border (Fig. 20a). Further down the Mwenezi river, to the east-southeast, near location no. 421753 (Map 3), the contact between sheared porphyritic granite and granulite gneiss can be observed in the NMZ of the Limpopo Belt (Fig. 20b; compare Map 3 and Fig. 7). Within the MGB, microshearing has been observed in the ore-zones. At the studied ore-sections, where pegmatite bodies are concordant to the main foliation, oblique foliations and mica-fish-like structures consistently indicate reverse sense of movement with top-to-the north-northwest displacement.

Phases of folding and intrusion of pegmatites – Due to poor exposure, only one example of disharmonic tight folds on a centimetre scale within the banded ironstone formation could be observed in the southwestern part of the MGB (north of Zeus underground mine; Fig. 21). These folds are designated as F1 folds, folding the S_0 bedding. They are upright and the F1 axial plane trends 040 NE. At an outcrop 300 m to the west, the bedding dips 312/72, with no trace of folding. On top of the banded ironstone formation north of the main greenstones, occasionally loose boulders with folded bedding were found. These observations are not in contradiction with the interpretation of F1 folds as slump folds related to gravitational collapse on a slope prior to lithification (Fedo *et al.*, 1995). The position of F1 folds in a deeper water setting (in this case next to the ultramafic greenstones; see also Fedo & Eriksson, 1995, and Section 2.4.3) may indicate the ramp

slope where sediments became gravitationally unstable and were prone to slumping.

The main foliation in the greenstone belt (S_1 , metamorphic foliation) roughly trends N65E to N70E, and is steeply dipping to the northnorthwest and to the southsoutheast, commonly subvertical. Both the bedding in the ironstones and the foliation in the greenstones show similar orientations (Fig. 22). The mean orientation is 340/87. These orientations suggest a F2 axial trace trending 070 ENE. A satellite image of the Sandawana region confirms the existence of a large isoclinal to very tight fold with the same trend, showing a northnorthwest-southsoutheast shortening direction (Fig. 23; also compare Fig. 7), which could correspond to the F2 folding observed further to the northeast (Fedo *et al.*, 1995).

At the Zeus underground mine, but



Fig. 20. (a) At the southern border of the greenstone belt, just east of the Zeus mine, in the Mwenezi river, mylonitic gneisses show the presence of a shear-zone parallel to the Limpopo belt border. (b) At location no. 421753 (Map 3), a sheared porphyritic granite (below) in contact with a granulite gneiss.



Fig. 21. Upright F1-folds were only observed at one outcrop in the southwestern part of the MGB, north of the Zeus underground mine, in the banded ironstone formation. Axial planes trend 040 NE.

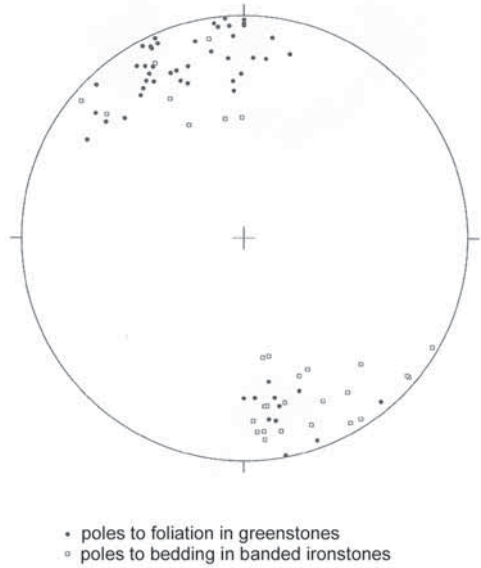


Fig. 22. Lower hemisphere, equal-area stereographic projection of poles to foliation (61 data points) in the greenstones and amphibolites in the Sandawana emerald mines region of the Mweza Greenstone Belt, and poles to bedding (32 data points) in the banded ironstone formations, same region.

also at the Orpheus mine, it could be observed that close to pegmatites the foliation does not follow the main trend, but tends to bend in the same direction as the folded pegmatite. Boudinaged and folded pegmatite clearly shows that, during deformation, pegmatite acted as a rigid body which forced the foliation of the greenstones to bend around it. At a section at the Orpheus Mine, a pegmatite was boudinaged in the direction of the main foliation and folded perpendicular to that direction, in the north-northwest-south-southeast shortening direction (Fig. 10). This would suggest that the pegmatites intruded prior to the main deformation (F2) event. However, the strike of many pegmatites appears to follow the main trend parallel to the NMZ (Map 1) and, for example, very close to the described folded pegmatite in the Orpheus Mine, pegmatite bodies exactly follow the main foliation, suggesting an emplacement during the main deformation (syn-F2). Therefore, it appears likely that intrusion of pegmatites in the MGB took place just prior to and/or during the main deformation event.

Near the Sandawana region, a F3 cross fold can be recognised in the MGB (Fig. 7). F3 folds are long-wavelength folds (> 40 km) that have axes orientated perpendicular to the orogenic strike of the NMZ. These cross folds were recognised by interpretation of regional-scale map patterns and noticing polarity reversals in the plunges of F2 folds.

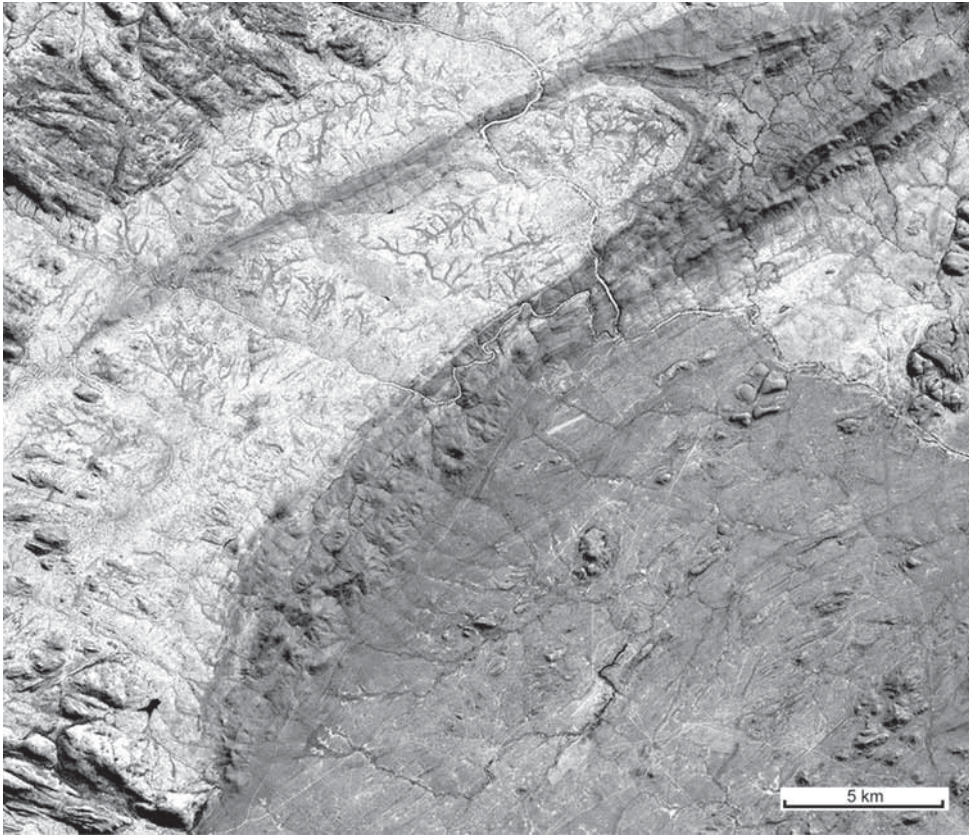
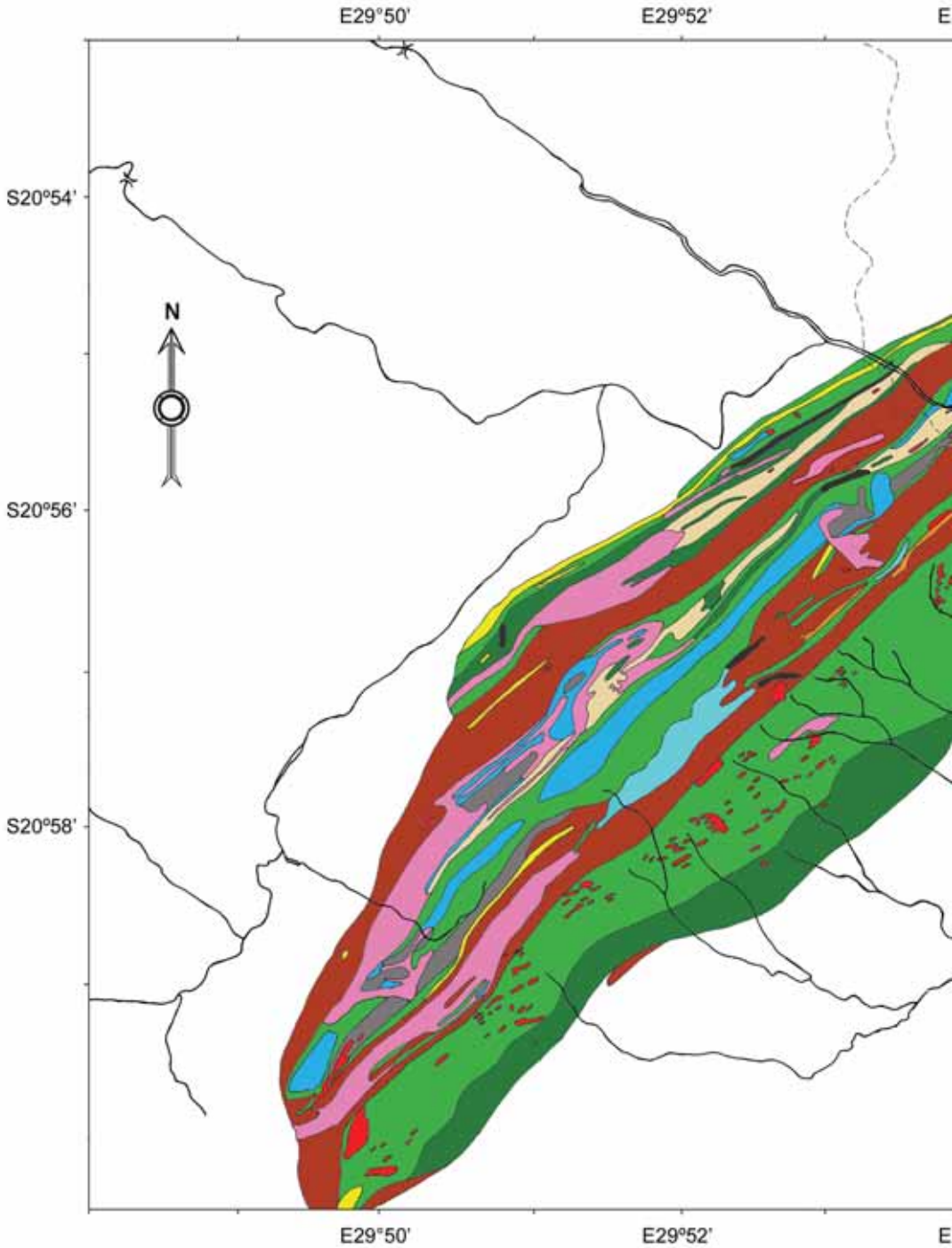


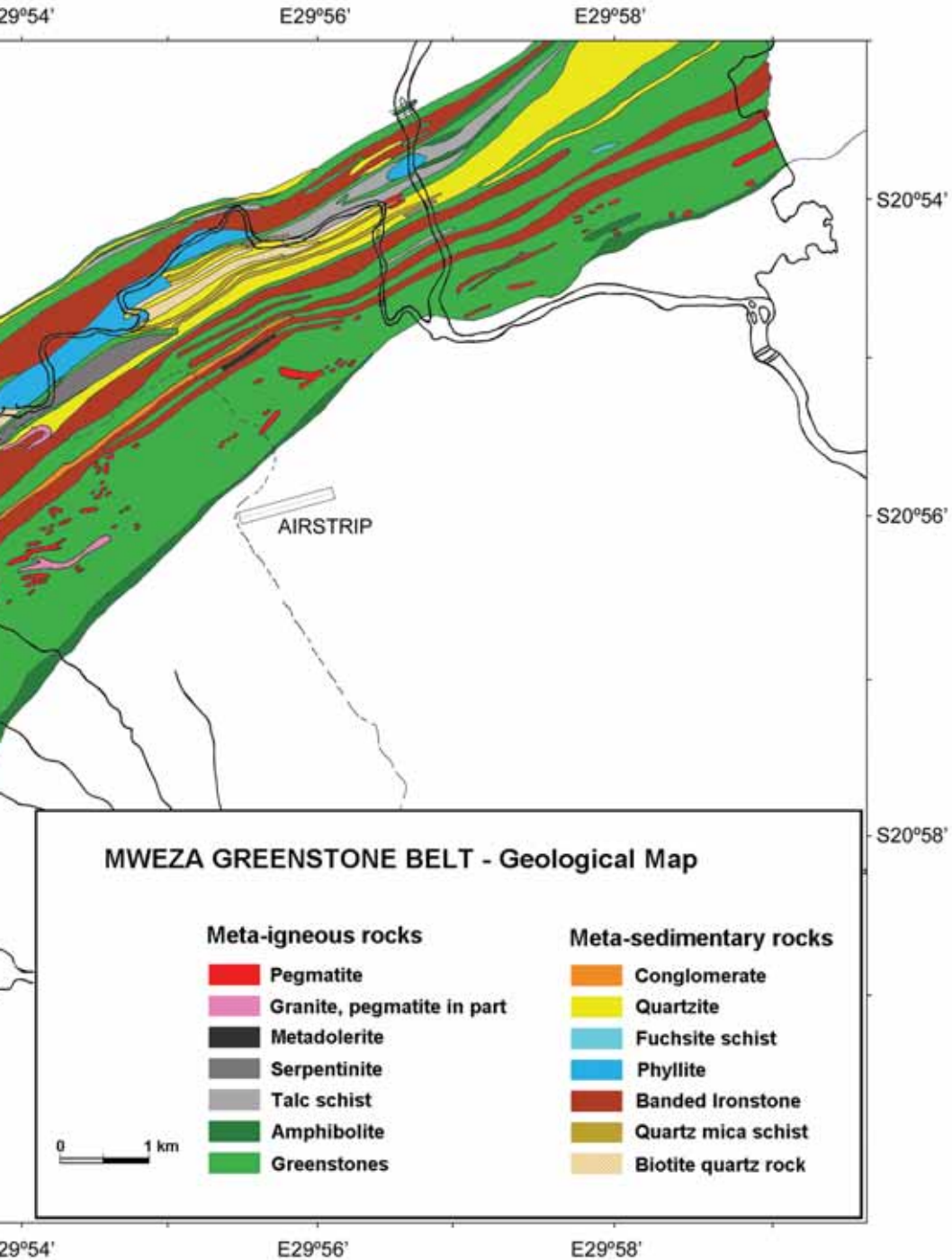
Fig. 23. Satellite image of the Mweza Greenstone Belt, showing a major very tight fold, of which the axial trace trends 070 ENE. This structure is in line with the F2 folding observed by others in the north-eastern continuation of the belt. The buildings of the Zeus mine, the major underground operation at Sandawana, are clearly visible in the MGB, north of the air-strip (visible as an eastnortheast-trending, thick white line).

Conclusion – Three successive phases of folding (F1, F2, F3) are identified in the Sandawana area. The first phase (F1) refolds the original bedding (S_0) and is assumed to be synsedimentary (slumping). The second phase (F2), which folds the major metamorphic schistosity (S_1), corresponds to the major structural event of the region. On a large scale, these F2 folds were refolded by F3 folds. A very comparable picture has been observed by Fedo *et al.* (1995) in the BGB, the northeastern continuation of the MGB. Thus, it seems that the MGB as a whole records a structural homogeneity.

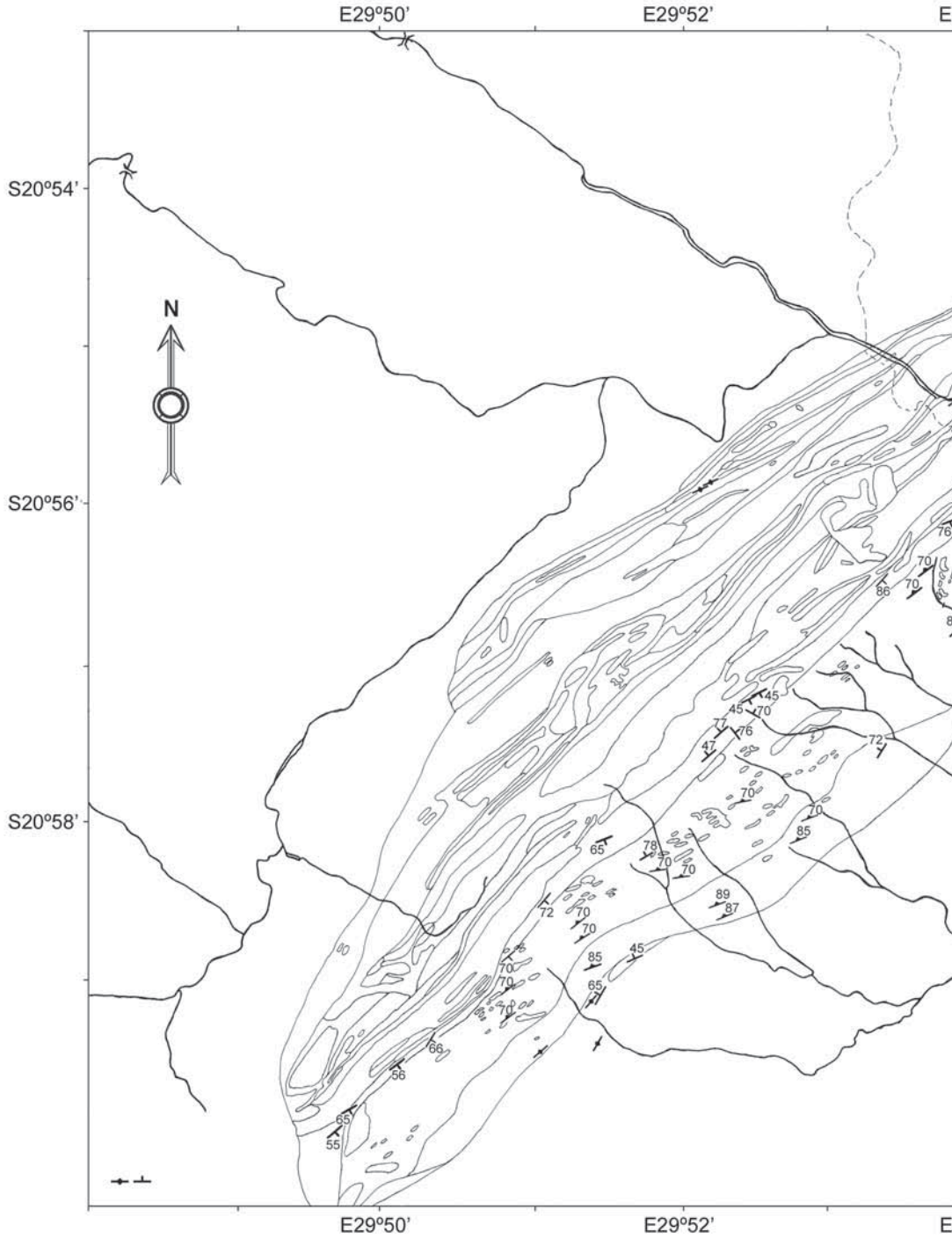
Note that, in the greenstones, possible older fabrics were obliterated by the main foliation (Section 2.3.2). Although not recognised, it can be expected that, during the large time span between 3.0 Ga, the deposition age, and 2.6 Ga (the main deformation event), the MGB underwent earlier regional metamorphism and deformation. It is likely that, during the emplacement of the tonalitic batholith around 2.9 Ga, the MGB was already severely deformed.



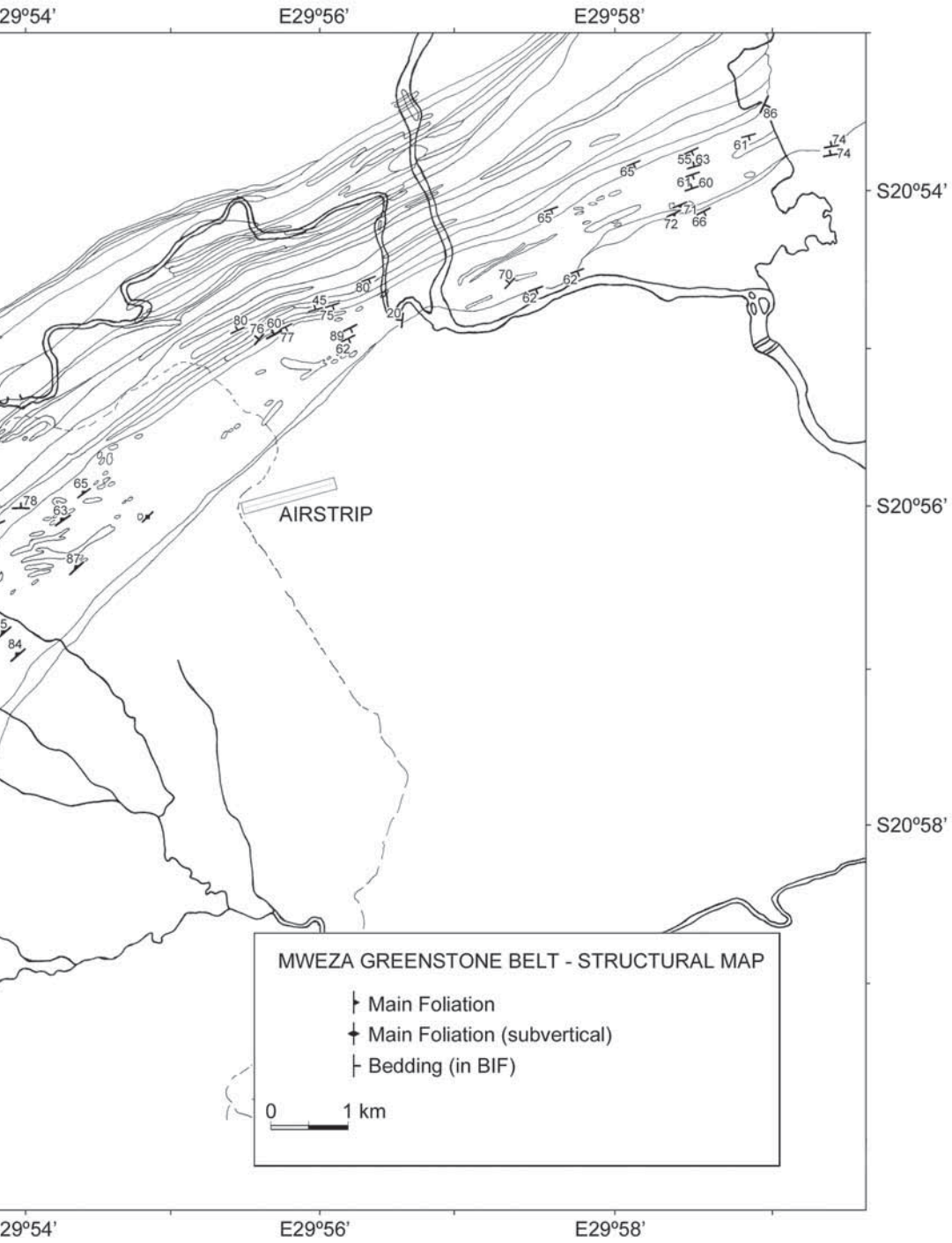
Map 1. Geological map of the southwestern part of the Mweza Greenstone Belt, where emerald deposits occur in association with the greenstone units. The map was compiled from the geological teams that have worked and still work at Sandawana Mines.

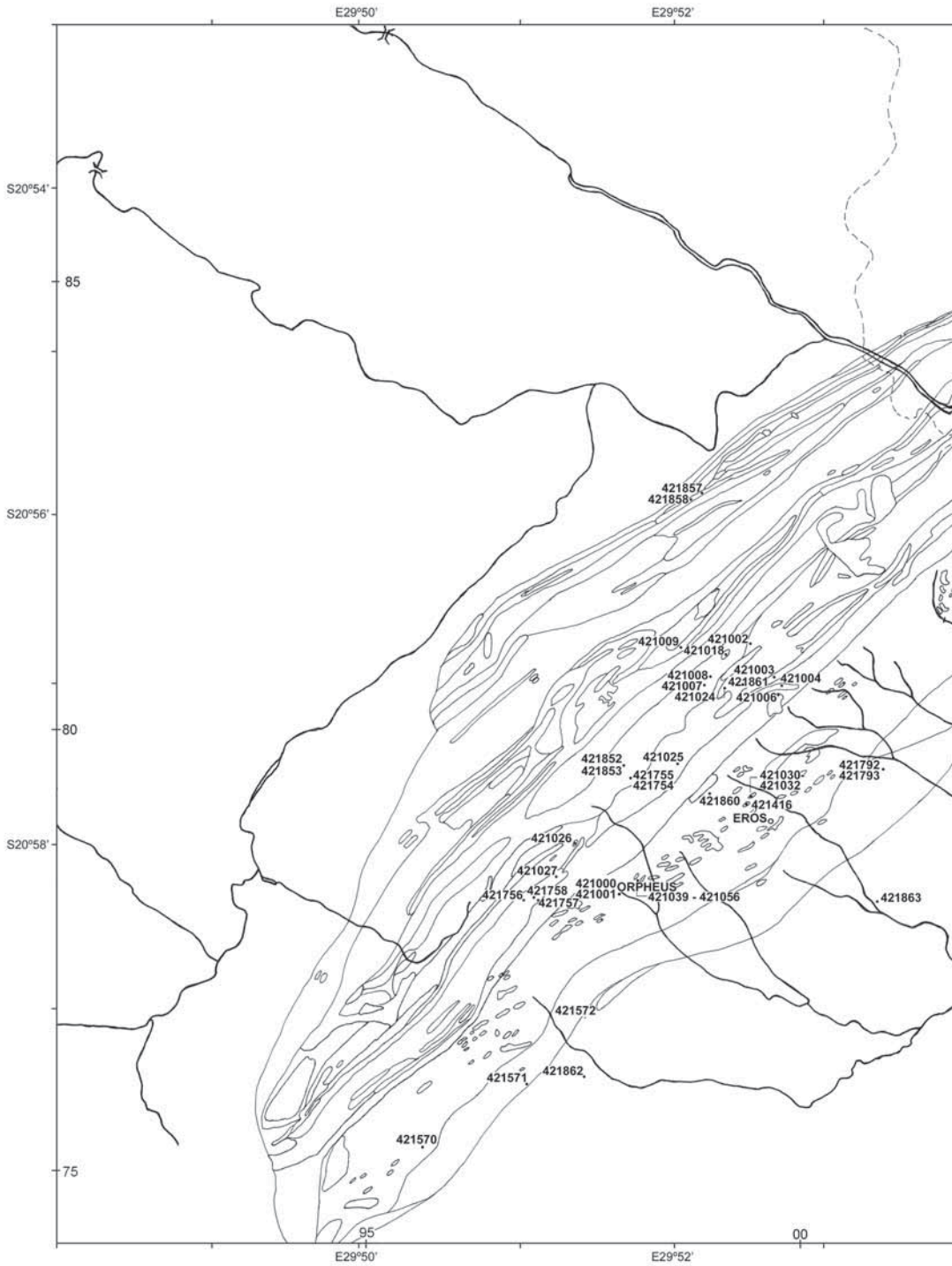


...ciation with pegmatite bodies, all the way along the southern flank. This map was compiled using own data, and data

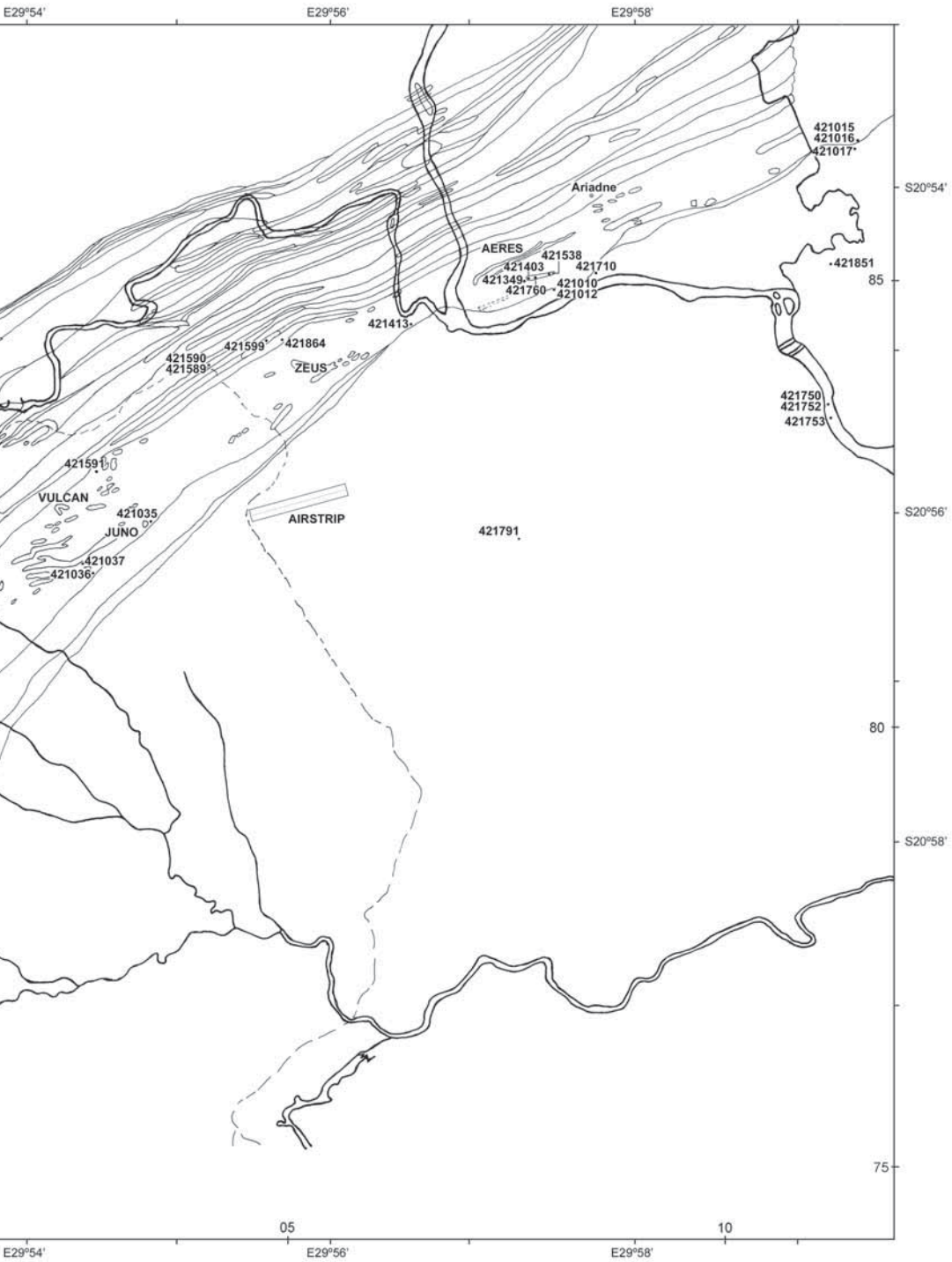


Map 2. Structural map of the southwestern part of the Mweza Greenstone Belt. Own data and data from the current ge





Map 3. Location map of the southwestern part of the Mweza Greenstone Belt. Samples that were taken from the Zeus u



underground mine are not shown on this map.

3. Gemmology of Sandawana emeralds

3.1. Introduction

It is believed by some that the area now known as Zimbabwe was the fabled land of Ophir, which produced gold for King Solomon's temple. By the middle of the 10th century, the discovery of ancient gold workings in different parts of the country had led Arab geographers to speculate on Ophir in their writings (Summers, 1969). Although gold, and even diamonds, stimulated exploration in the 20th century, for gemmologists the most important discovery in Zimbabwe was the large emerald deposit found in the mid-1950s at the area called Sandawana. For four decades, Sandawana has provided the jewellery industry with large quantities of fine, if typically small, emeralds. Production was sporadic for much of this period, but new ownership in the mid-1990s has brought renewed attention to exploration and mining, with excellent results in terms of both the quantity and quality of the stones produced.

Although the Sandawana mines have been known for some time now, until Zwaan *et al.* (1997) only short articles on the characteristics of Sandawana emeralds have been published. There has also been little information about the mining area, and the techniques used for exploration, mining and processing. This chapter, using Zwaan *et al.* (1997) and Zwaan & Burke (1998) as a basis, gives more and revised information on these topics.

3.2. Historical background

In 1868, German geologist Carl Mauch uncovered some of the ancient gold workings to which Arab geographers had referred, in the interior of what is now Zimbabwe, near Hartley (now Chegutu; Fig. 4). After Cecil Rhodes's British South Africa Company obtained a charter to promote commerce and colonization in Zimbabwe in 1889, prospecting for gold became a major industry. The simplest surface indicator was an ancient working. In the nine years between 1890 and the outbreak of the South African Boer War, which raged from 1899 to 1902, over 100,000 gold claims were pegged (Summers, 1969).

The search for gems in Zimbabwe appears to be more recent and dates from H.R. Moir's 1903 diamond find in the Somabula Forest (Mennell, 1906). Large-scale prospecting and mining for diamonds took place between 1905 and 1908, but these efforts faded as the results did not meet the expenses. Subsequently, several workers tried to make their fortunes in small mining operations, but interest waned and activity all but ceased (Wagner, 1914).

In 1923, Zimbabwe became a British colony under the name Southern Rhodesia. A sudden change in the fortunes of the nation's gemstone industry came in the mid-1950s, as a result of increased demand for beryllium and lithium minerals. On 7 October 1956, the first emerald was found in the Belingwe district by Laurence Contat and Cornelius Oosthuizen, two former civil servants who had relinquished their posts to take up full-time prospecting. This first stone was recovered in the Mweza hill range about 5 km westsouthwest of the confluence of the Nuanetsi (now Mwenezi) and Mutsime rivers. They called their first claim 'Vulcan' (Martin, 1962).

On 17 May 1957, after a rainstorm, a Vulcan worker named Chivaro found a deep green crystal protruding from a muddy footpath, some 2.5 km northeast of what eventually became the Vulcan mine. He reported the find to his employers, who rewarded him handsomely. Further investigation at the spot, which would later become known as the Zeus mine, revealed the presence of more such crystals in the 'black cotton' soil, the popular name for a dark calcareous soil, high in montmorillonitic clay, formed from rocks with a low silica content. Recognizing the superior quality of these crystals, Contat and Oosthuizen cautiously checked out the potential value through various renowned gemologists, including Dr Edward Gübelin, before revealing the discovery to government officials and seeking security protection. Late in 1957, Contat and Oosthuizen sent the first parcel of rough emeralds to the United States. By February 1958, suitable regulations to control the mining and marketing had been promulgated; shortly afterwards, the miners formally began production. The earliest processing consisted of simply washing wheelbarrow loads of soil (Böhmke, 1982).

When these rich green stones came on the world market, Zimbabwe quickly established itself as a source of fine emeralds. By late 1959, after washing a mere 70 m³ of soil, Contat and Oosthuizen had made their fortune and sold out to a subsidiary of the large mining company RTZ (Rio Tinto Zinc) that was owned jointly by RTZ (53%) and the Zimbabwean public (47%).

The name Sandawana, which refers to the mining area and the emeralds mined there, was derived from the name of a mythical 'red-haired animal'. According to local African folklore, this animal caused red flashes of rust on wet blades of grass; possession of one of its red hairs would result in life-long good fortune (Böhmke, 1982).



Fig. 24. The 'Bank of England' was the open pit of the original Zeus mine, which was extremely rich in emeralds. Buildings in the foreground are offices, workshop and processing plant. The village of the employees is visible in the background.



Fig. 25. The main production shaft at Zeus mine serving as haulage shaft down to 400 feet (122 m).



Fig. 26. Three-dimensional model of the underground mine workings at Zeus, showing all the tunnels and shafts that have been dug, and locations of pegmatites (marked in red) and emerald. The model is constantly revised.

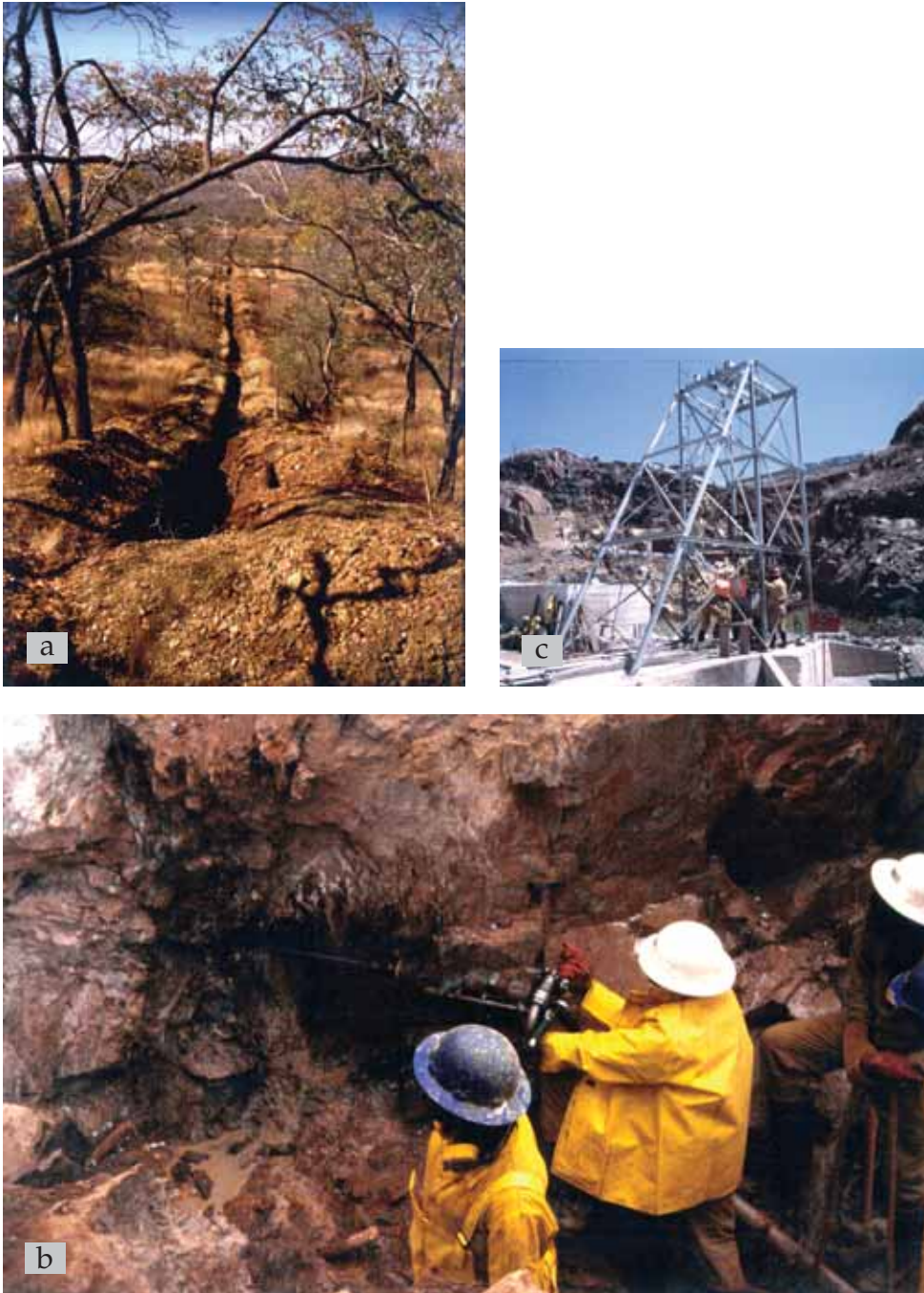


Fig. 27. Exploration activities; (a) cross-trenching at the Aeres-3 section in order to find new pegmatite bodies, (b) surface drilling at Orpheus in order to locate new ore zones and (c) an exploration shaft has been sunk at Orpheus after open pit mining.



Fig. 28. Dumps were left behind by Rio Tinto after extensive mining in the 1960s and 1970s. It was discovered that these dumps contain a lot of small emeralds and, for this reason, production was considerably improved during the last years.



Fig. 29. Until a few years ago, all ore fractions on the slow-moving conveyor belts were carefully checked for emeralds by hand-pickers. Gem-quality pieces were deposited in safety boxes by each sorter.



Fig. 30. The high-efficiency DMS (dense media separation) module is used at Sandawana to separate 'rich ore' (schist with emerald) from 'waste' material (usually pegmatite). A few hand-sorters are on the spot to 'save' the occasional emerald which occurs in the pegmatite.



Fig. 31. The Permanent Magnetic Roller separates slightly magnetic schist from emerald and remaining schist. The emeralds fall off the conveyor belt, whereas the magnetic schist particles remain adhered to it.



Fig. 32. In sorting rooms III and II the final ore is carefully checked by hand, and emeralds are sorted.



Fig. 33. Tungsten-tipped pliers are used to free the emeralds from their matrix.



Fig. 34. In the last sorting room all rough emeralds are sorted according to size, colour and clarity.



Fig. 35. Most of the emeralds seen *in situ* (here, in fine-grained, sugary albite) have been either euhedral or subhedral, with prominent prismatic faces.

The discovery of large quantities of fine emeralds at Sandawana sparked further interest in emerald prospecting. Within a few years, determined prospectors were rewarded with new finds in the Filabusi and Fort Victoria (now Masvingo) districts (see Fig. 4). Some of these occurrences have been described by Anderson (1976, 1978), Martin (1962) and Metson & Taylor (1977), e.g., Twin Star, Chikwanda, Novello, Mayfield, Popoteke and Renderd. A more recent (1984) discovery was at Machingwe (Kanis *et al.*, 1991), about 12 km northeast of the Sandawana area, also in the Mweza hills. Because RTZ insisted on strict secrecy, Dr Gübelin's initial article, published in 1958, was not followed by another paper until 24 years later; in 1982, resident geologist F.C. Böhmke published his lecture on 'Emeralds at Sandawana', given at the sixth annual commodity meeting in London at the Institution of Mining and Metallurgy (Böhmke, 1982).

In May 1993, RTZ sold the Sandawana company to a newly formed company, Sandawana Mines (Pvt.) Ltd., of which the Zimbabwean Government is a minor shareholder. Mr E.J. Petsch (Idar-Oberstein) was appointed chairman of the new board. He worked with a new technical team consisting of Mr P.J. Kitchen (Camborne School of Mines), Dr J. Kanis (consulting geologist), Dr A.N. Ncube (mineralogist and director of the company) and Mr A.H.F. Braunschweig (who continued as general manager of the mine) to revitalize all activities at the mine. Additional investment provided new mining equipment, transportation, housing, and important improvements to underground mining and ore processing.

In 1996, Mr D.B. Siroya of Dubai became the chairman. The company, which has its headquarters in Harare, employs about 400 workers at the mine, of which 60 are security officers. As is the case with most gem mines, security is a major concern.

3.3. Mining and Production

3.3.1. Mining – Since the discovery of the Sandawana deposits in 1956, an almost continuous exploration programme has been carried out within the 21 km-long claim holding. Over the years, systematic trenching and surface drilling of profiles for structural studies has led to the discovery of many emerald-bearing sites, including Eros, Juno, Aeres, Ariadne and, more recently, Orpheus. Nevertheless, since the earliest days, emerald exploitation has been concentrated mainly in the Zeus area (Fig. 7).

The Zeus mine was an open-cast operation until the pit reached 15 m. It was so rich in emeralds that the location was nicknamed 'The Bank of England' (Fig. 24). Subsequently, the Zeus mine was developed into a modern underground mine. Over a strike of 700 m, four vertical shafts have been sunk. The No. 3 shaft (Fig. 25) currently serves as the main production shaft, reaching levels as far down as 400 feet (122 m). Another subvertical shaft serves the mine from 400 feet (122 m) to the 500 feet (152 m) level. Levels and sublevels are 25 feet (7.6 m) apart vertically and are connected by raises. Drifts (horizontal tunnels) are mined along the hanging and footwall contacts of the pegmatites, and mining of the emerald-bearing shoots is done by stoping methods. Ore is removed via small tunnels called ore passes and transported in cocopans (ore carts) on rails to the haulage shaft. More than 40 km of tunnels and shafts have been dug at the Zeus mine. All underground survey data are plotted on a composite mine plan, scale 1:1000, and since its inception the survey department has maintained a three-dimensional model of the underground mine workings (Fig. 26).

After extensive trenching, surface drilling, sampling and some open-pit mining, exploration shafts were sunk recently at the Orpheus and Aeres-3 sections (Fig. 27). These prospects are 3 km northeast and 10 km southwest of the Zeus mine, respectively (Fig. 7; Aeres has been subdivided into 3 exploration-sections, Aeres-1, -2 and -3). Currently, small quantities of emerald are mined from these shafts.

Apart from the main production underground at the Zeus mine, production from the 'dumps' Rio Tinto left behind from their mining activities at earlier times has become more important during the last years (Fig. 28). Especially good quality small material has been recovered from these dumps. For instance, in 1998 the production from the dumps went from 25 to 75% of the total production in weight.

3.3.2. *Processing* – Waste rock loosened by the blasting is dumped near the haulage shaft, and rock with any 'green' in it taken from the (narrow) ore-zone is transported to the processing plant and batch processed. Exceptionally rich matrix with fine quality emeralds visible is hand cobbled underground and treated separately from the normal run-of-mine material. Some of these pieces are selected for sale as collectors' specimens.

The processing plant is a standard washing/screening trommel plant with a capacity of approximately 320 tons of ore per month at 8 hour shifts. About 42 people work at this plant, five days a week.

After the ore passes a grizzly-grid (24 cm), it is broken by a jaw crusher (although some emeralds might be slightly damaged by the jaw crusher, there is no alternative for large tonnages). The ore is then washed and sized with the largest (over 20 mm) and smallest (under 3 mm) pieces separated out in a rotating trommel. Additional vibrating screens further separate the material into specific size ranges, so that larger and smaller stones are not mixed (and the latter hidden by the former) during the next stage of sorting. Until a few years ago, the sorting of all ore fractions was continued on slow-moving conveyor belts. Under strict security, up to 30 hand-pickers scanned the material for emeralds (Fig. 29).

However, at the end of 1995, Sandawana introduced innovative processing technology based on gravity separation. This DMS module (dense media separation), as it is called, was originally designed for diamond processing. At first, this technology enabled the mine to recover smaller emeralds (from the 1.6 to 6.0 mm fraction) which were difficult to recover by hand sorting alone. Later, also fractions up to 12 mm were processed through the DMS plant.

After passing the crusher and the screens, the ore is only divided into various sizes, and basically consists of schist, emerald and pegmatite. The aim of the DMS plant is to separate the pegmatite material from the schist and emerald (most emeralds adhere to the schist). This is called the first run. Ferrosilicon is used as density liquid; as it is very expensive it is now mixed with magnetite. Operational density is kept at 2.15-2.20 (maximum is 2.50). In combination with the pressure and centrifugal forces the liquid obtains the right density to separate pegmatite from schist. This density should be very critical, as the pegmatite has a density close to 2.6, whereas the schist is around 2.9-3.0, and the emerald around 2.75. Hand-sorters inspect the 'waste' material, i.e., pegmatite, on the spot, in order to save the occasional emerald adhered to the pegmatite from going to the bin (Fig. 30). At this stage, two DMS computer controlled modules are in operation, with each a capacity of one ton of ore per hour.

After this run through DMS, the 'first concentrate', a mixture of schist and emerald, is separated. It appears that it is easier to separate the material from underground than the material that is processed from the dumps. The material from the dumps is more oxidised and higher densities are needed to separate this material.

During the second run, the first concentrate is further processed through the recently installed PERMROLL, the Permanent Magnetic Roller. The paramagnetic roller is a very powerful magnet, which separates slightly magnetic schist from emerald and remaining schist (Fig. 31). The schist only needs to contain very little slightly magnetic (usually opaque) material to be separated. This process effectively separates more waste from the final ore; the material is quickly checked by hand to make sure that no emeralds are left behind.

The use of DMS and PERMROLL reduced the amount of ore that finally has to be sorted by hand, by 40 to 60%. Consequently, labour costs were dramatically reduced.

After passing the first and second run, the final ore goes to sorting rooms III and II. Here any 'green' material is taken out by hand-sorters (Fig. 32). Subsequently, the selected emeralds go to sorting room I.

In sorting room I, 'cobbers' use tungsten-tipped pliers and chipping hammers to liberate the emeralds from their matrix with a minimum of damage (Fig. 33). Many emeralds still have a 'skin' of schist, which is removed against a polishing wheel. Some poor material needs additional tumbling for further cleaning. Finally, all the rough emeralds are sorted according to size, colour and clarity to prepare parcels for the international market (Fig. 34). The entire processing plant area is surrounded by a security fence, patrolled by security staff and monitored by security officers using closed circuit television.

3.3.3. The Sandawana Rough – The majority of the rough emeralds are recovered as crystal fragments, most of which show a few crystal faces. Also seen are well-formed, short-prismatic hexagonal crystals with pinacoidal terminations. Most of the emeralds seen *in situ* to date have been either euhedral or subhedral, with prominent prismatic faces (Fig. 35). Many of the crystals contain fractures filled with fine-grained albite, which represent very weak zones. Consequently, the emeralds break easily when they are removed from the host rock or processed.

Most of the emeralds are medium to dark green. Although pale green emeralds have occasionally been found, to date these have been seen only in the pegmatite, away from the contact with the schist.

Sandawana emerald crystals are typically small (most gem quality material is between 2 and 8 mm, although opaque crystals as large as 12 mm are frequently seen), but some larger crystals were found recently. The largest crystal that the author (JCZ) has seen was 1,021.5 ct, found at the Orpheus mine in 1995. It showed complex interpenetrating twinning and, in addition to the first-order prismatic faces, a small second-order bipyramidal face (Fig. 36). Some of the larger crystals from Orpheus (Fig. 37) were found in 'khaki'-coloured altered schist near a pegmatite at the surface. The crystals represent the more common crystal habit for this size, showing prismatic faces and rounded to somewhat irregular terminations, with pinacoidal faces only partly developed. Most of these crystals contain a substantial portion that is suitable for cutting, usually as cabochons. The average retention after cutting is 10-20% of the original weight.



Fig. 36. The largest emerald crystal seen by the author, here in the middle, weighing 1021.5 carats (height about 50 mm), found at Orpheus Mine in 1995.



Fig. 37. Note the crystal habits of these large emerald crystals found at Orpheus mine, 103.58 carats (left) and 64.95 carats (right). Both have translucent areas from which cabochons or beads could be cut.



Fig. 38. These stones, which range from 0.28 to 1.87 ct, are part of the group of 36 cut Sandawana emeralds examined for this study. Like most of the polished samples studied, they are medium to dark in tone.

The General Manager of the mines reported that larger crystals, about 25 to 100 ct each, are regularly extracted from the Zeus mine as well.

3.3.4. Production and distribution – Since 1993, when the mine changed management, monthly emerald production has improved considerably and become more consistent. As noted earlier, crystals in the 25-100 ct range are now produced fairly regularly (precise quantities are not available); a few exceptional crystal clusters, weighing around 500 ct, have also been found. Nevertheless, many polished stones weigh less than 0.25 ct, as previously described by Gübelin (1958), although a substantial number of polished stones weighing between 0.25 and 0.80 ct have entered the market. Additionally, stones weighing above 1 ct and even close to 2 ct are sometimes produced. Cut Sandawana emeralds of 1.50 ct or more are still rare.

Although the quantity of emeralds produced varies somewhat from month to month, figures over the last three years show a production of at least 60 kg of mixed grades of rough emeralds per month, of which 10% is usually transparent enough and of a sufficiently attractive colour to be faceted or cut *en cabochon*.

As regulated by the government, part of the production is cut locally for export from Zimbabwe. However, the greater part of the rough material is sold to traditional clients and, in recent years, also at regular invitation-only auctions. Sales of all gem materials (rough and cut) in Zimbabwe are monitored by the Mineral Marketing Corporation of Zimbabwe (MMCZ). For those emeralds cut officially in Harare, the fractures are not filled with an oil or an artificial resin. When fractures in these stones are filled, this happens at a later stage 'along the pipeline'. Although it is difficult to give a precise estimate of reserves, ongoing exploration in the Sandawana area indicates that current production can be maintained for many years to come.

3.4. Gemmological characteristics

3.4.1. Materials and methods – For this study, a total of 68 emerald specimens were examined, of which 36 were polished. Almost all of the rough material was transparent to translucent, suitable for cutting. Some of the material was collected *in situ* during fieldwork. The rest was obtained from the mine run, but from material that was kept separate for each stope, so that it could be identified from which mine or part of the mine it came. Most of the rough emeralds were found near the contact between pegmatite and schist, but I also studied one 25 mm pale green, gem-quality crystal that was recovered from the pegmatite 1.25 m from the contact.

A Rayner refractometer with an yttrium aluminum garnet (YAG) prism was used to measure the refractive indices and birefringence of all polished samples. Specific gravities were measured on all samples, except the eleven samples from which thin sections were made (see below), using the hydrostatic method with ethylene dibromide. Inclusions were identified using a standard gemmological (Super 60 Zoom Gemolite Mark VII) microscope, a polarizing (Leica DMRP Research) microscope and a laser Raman microspectrometer (Dilor S.A. model Microdil-28). For the detailed study of fluid inclusions, polished thin sections were made from eleven samples. Polarized absorption spectra of ten representative medium to dark green samples were taken with a Pye Unicam PU 8730 UV/VIS spectrometer under room-temperature conditions.

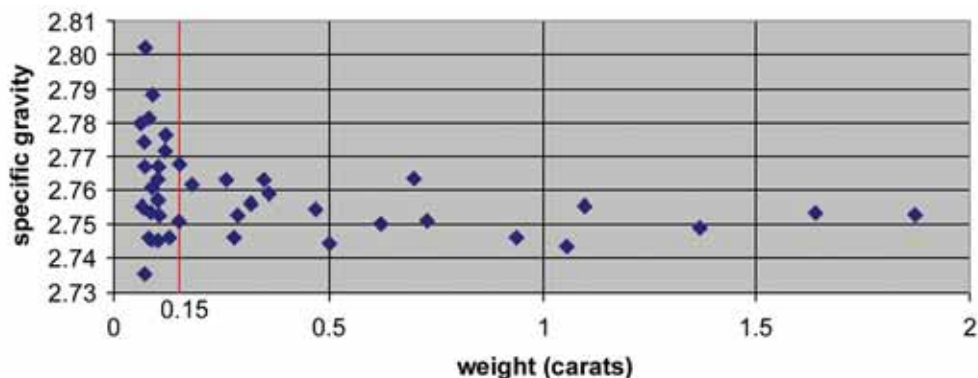


Fig. 39. Relation between specific gravity and weight. Most stones show values between 2.74 and 2.77. Only some stones weighing less than 0.15 carat give anomalous results, due to the small size of the stones and the greater influence of the inclusions at these sizes.

Table 7. Physical properties of 36 cut emeralds from Sandawana, Zimbabwe.

Colour	Saturated colours ranging from medium to dark green. Colour is evenly distributed; only weak colour zoning is seen in some crystals and polished stones.
Clarity	Slightly to heavily included.
Refractive indices	$n_e = 1.584-1.587$; $n_\omega = 1.590-1.594$.
Birefringence	0.006-0.007.
Optic character	Uniaxial negative.
Specific gravity (samples ≥ 0.15 ct.)	2.74-2.77.
Pleochroism	Dichroism: yellowish green (ω) and bluish green (ϵ).
Fluorescence	Usually inert to long- and short-wave ultraviolet radiation. Uncommonly faint green to long-wave UV.
Reaction to Chelsea filter	Light pink to pinkish red; the majority of the material shows pink.
Internal features	<ul style="list-style-type: none"> • Mineral inclusions: actinolite and cummingtonite needles and long-prismatic laths, randomly oriented; albite and apatite, both showing various crystal morphologies; phlogopite, calcite, dolomite, quartz, ilmenorutile. • Partially healed fissures. • Decrepitated primary fluid inclusions, typically rectangular in shape. • Weak, if any, colour zoning; complex zoning roughly parallel to the prismatic crystal faces is present in some clean crystals.

Quantitative chemical analyses were carried out on some emeralds and some inclusions with an electron microprobe (JEOL model JXA-8800M). In total, 40 spot analyses were performed on four gem-quality, medium to dark green rough emeralds and the one light green emerald extracted from a pegmatite, all from the Zeus mine, and one medium green emerald from the Orpheus mine; 23 were performed on amphibole inclusions; and 20 analyses were made of other inclusions. Trace element concentrations of 22 emeralds were measured with PIXE/PIGE, using an external 3 MeV proton micro-beam.

Both the Raman and microprobe analyses were performed at the Institute of Earth Sciences, Free University, Amsterdam (E.A.J. Burke and W. Lustenhouwer, analysts).



Fig. 40. The 'tremolite' needles and laths that are a well-known hallmark of emeralds from Sandawana were conclusively identified as actinolite and cummingtonite. Darkfield illumination, $\times 50$.

PIXE/PIGE analyses were carried out at the AGLAE IBA facility of the research laboratory of the Museums of France, Palais du Louvre, Paris.

3.4.2. Visual appearance – Fashioned Sandawana emeralds are known for their attractive colour. Most of the samples we examined were a vivid green with medium to dark tones (Fig. 38). It is striking that the darker tones are not restricted to the larger stones; for instance, one stone weighing only 0.10 ct had a medium dark tone. Sandawana emeralds typically show even colour distribution and are slightly to heavily included. Eye-visible internal features such as minerals or (partially healed) fractures are quite common.

3.4.3. Physical properties – The standard gemmological properties of the Sandawana emeralds tested are given in Table 7 and discussed below.

Refractive indices – The measured values fell within a somewhat narrower range than was indicated by Gübelin (1958; n_{ϵ} 1.581-1.588 and n_{ω} 1.588-1.595), which only confirms that small variations exist. More than 70% of the stones tested showed $n_{\epsilon} = 1.585$ -1.586 and $n_{\omega} = 1.592$ -1.593, and 90% showed a birefringence of 0.007.

Specific gravity – The measured values varied between 2.73 and 2.80 (Fig. 39). However, stones weighing 0.15 ct or more gave results between 2.74 and 2.77, and most stones (66%) showed values around 2.75-2.76. These numbers are consistent with ear-

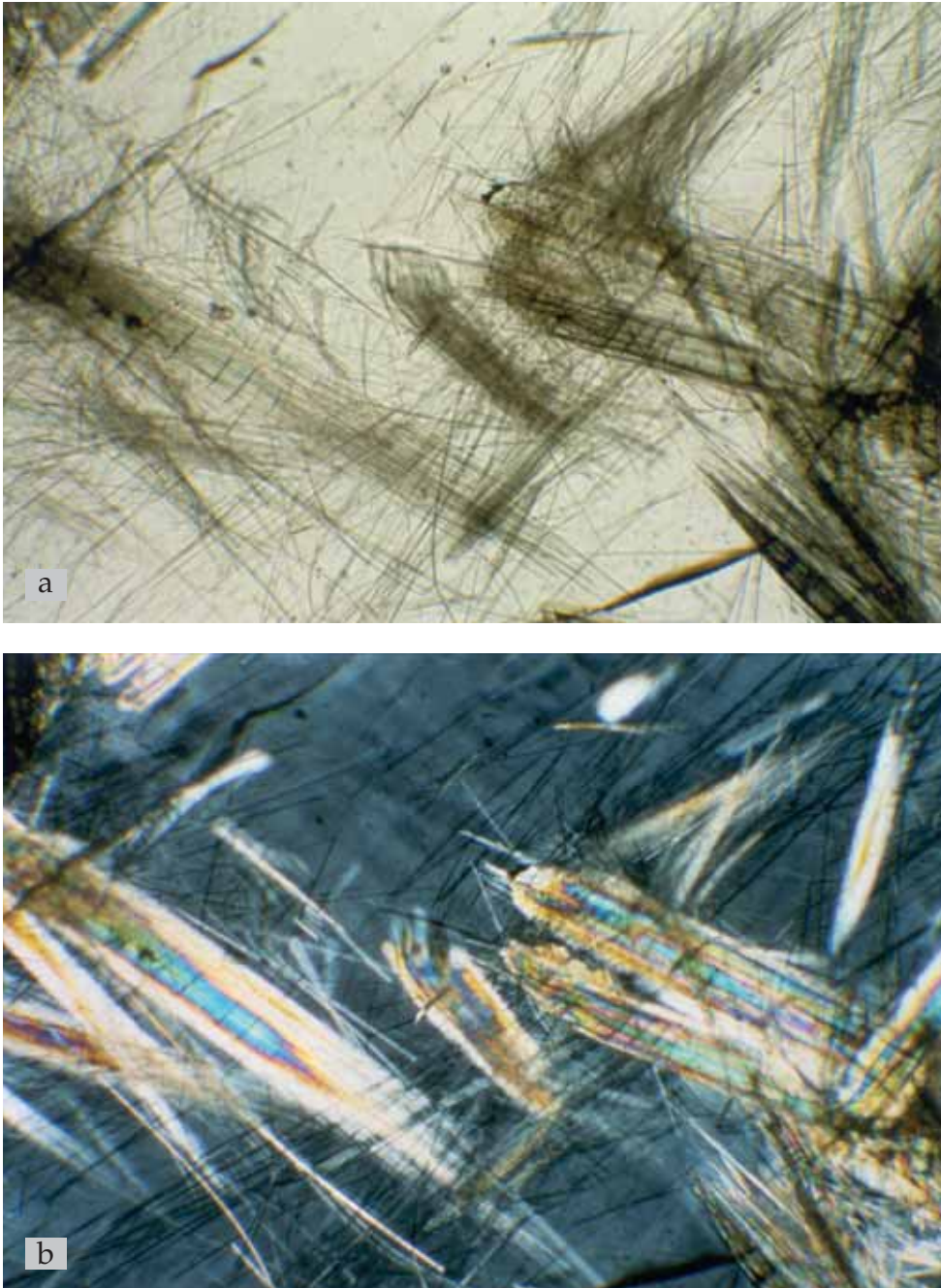


Fig. 41. Long-prismatic crystals of actinolite and cummingtonite were identified in the Sandawana emeralds studied. (a) In transmitted light, the cummingtonite laths (here, on the right of the photomicrograph) show a slightly higher relief. Between crossed polarizing filters (b), these same cummingtonite laths show lamellar twinning. $\times 35$.

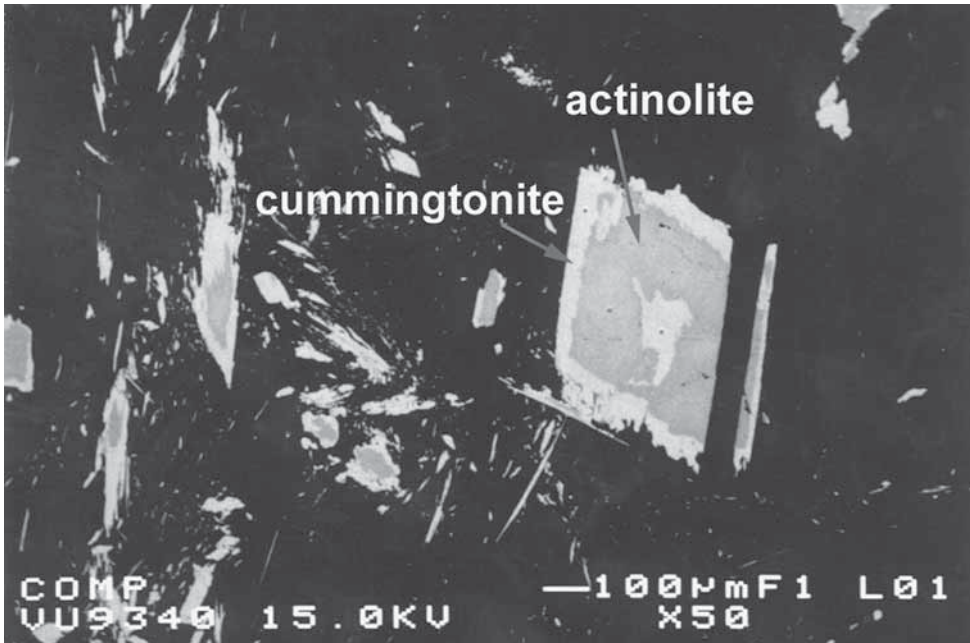


Fig. 42. Electron photomicrograph of thicker actinolite crystal, with cummingtonite rim, and thinner amphiboles, which also show actinolite intergrown with cummingtonite.

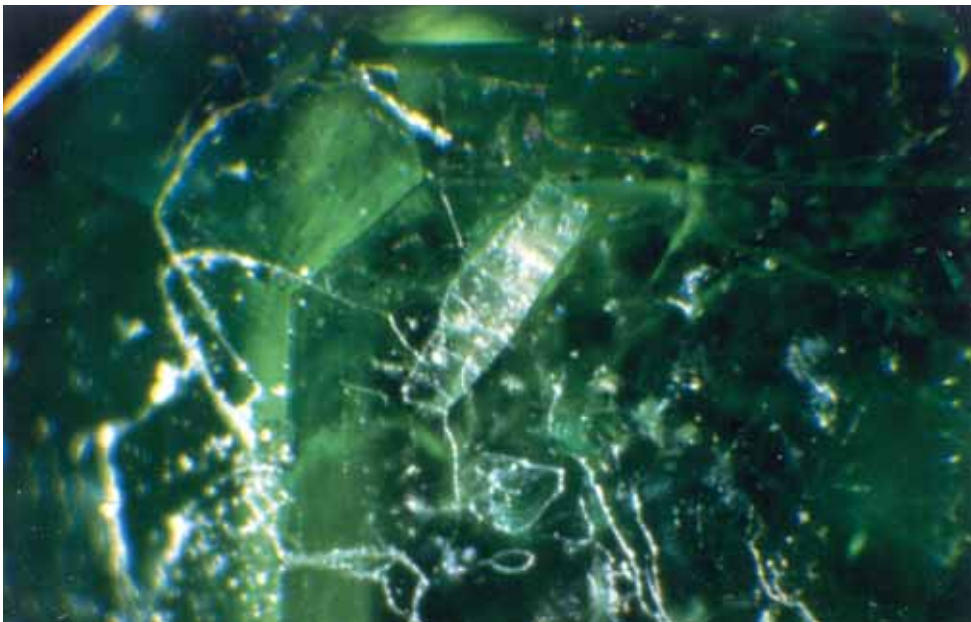


Fig. 43. Large colourless to milky white tabular albite crystals, such as the one shown here near the surface of the stone, frequently occur in Sandawana emeralds. Oblique illumination, $\times 60$.



Fig. 44. Many Sandawana emeralds of various qualities were also seen to contain small, rounded, colourless albite crystals. Transmitted light, $\times 125$.



Fig. 45. This albite crystal, which is surrounded by minute inclusions (probably also albite), looks like a snowball. Oblique illumination, $\times 60$.

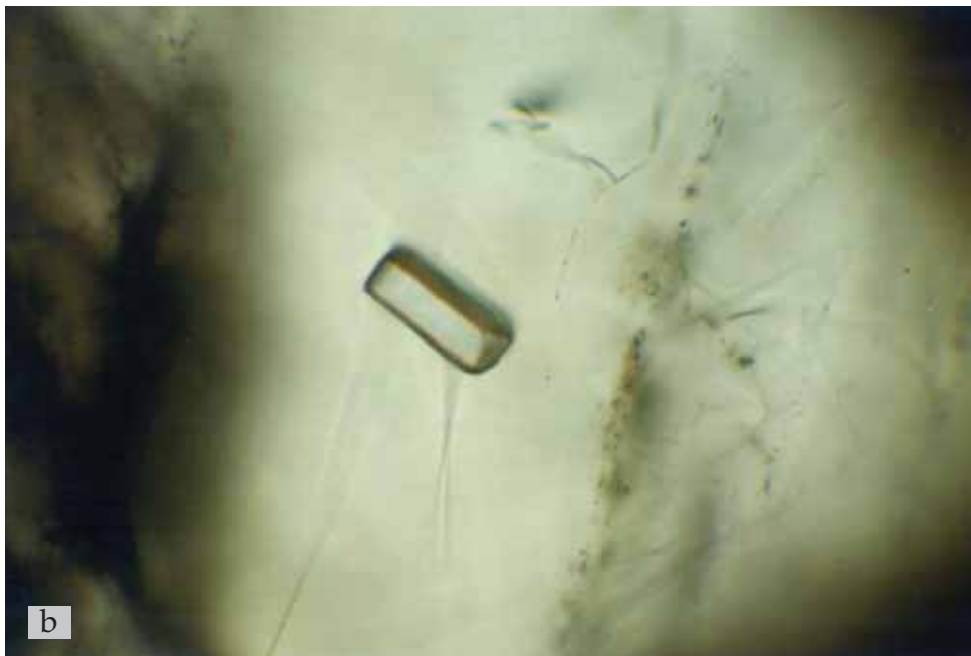
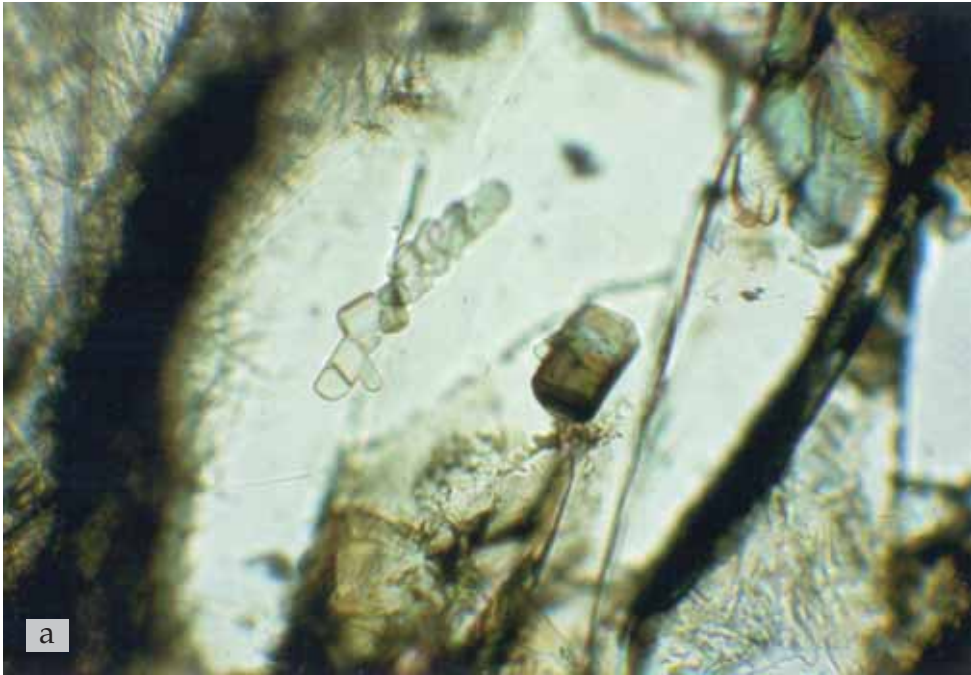


Fig. 46. (a) A cluster of small apatite crystals lies near a larger brownish green apatite in this Sandawana emerald. Transmitted light, $\times 100$. (b) An isolated idiomorphic apatite may also occur. Transmitted and conoscopic light, $\times 175$.

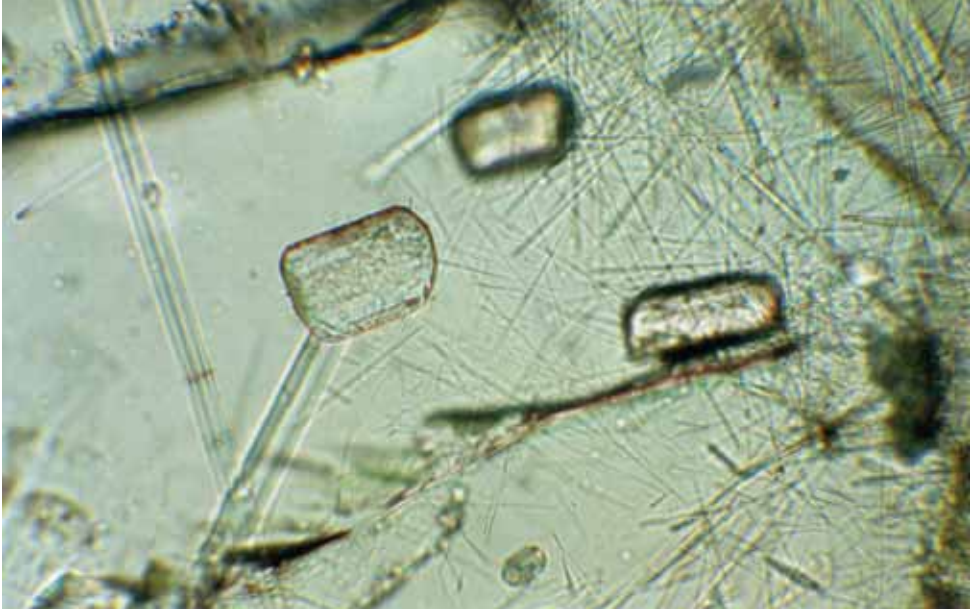


Fig. 47. In a classic 'Sandawana scene' of long actinolite and cummingtonite crystals and fibres, lie three small rounded apatite inclusions with slightly corroded surfaces, very different in appearance from those apatites shown in Figure 46. Transmitted light, $\times 160$.

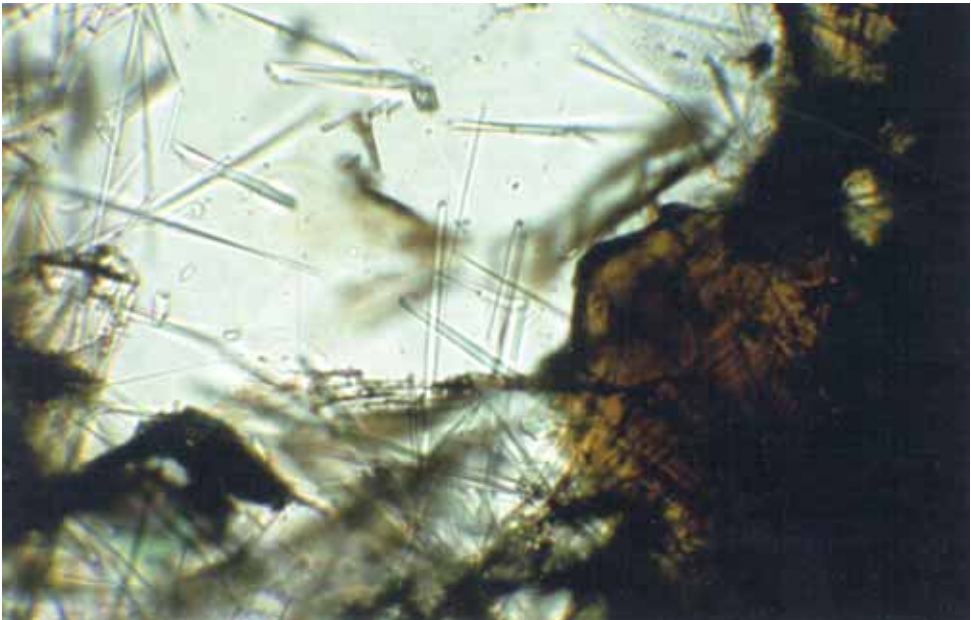


Fig. 48. Seen here at the edge of a gem-quality piece of rough, this orangy brown plate-like crystal is phlogopite, which is rare in Sandawana emerald. The black inclusion at the lower left was tentatively identified as a metamict zircon. Transmitted light, $\times 100$.

lier reports by Gübelin (1958) and Böhmke (1966). Note that the smaller stones with higher specific gravities contained many (predominantly amphibole) inclusions. Thus, the scattering of values between 2.73 and 2.80 can be attributed in part to inaccuracy due to the small size of the stones and the greater influence of the inclusions at these sizes.

3.4.4. Internal features

Mineral inclusions – The most abundant inclusions in the Sandawana emeralds examined are fibrous amphibole crystals, which were previously described by various authors (e.g., Gübelin, 1958; Böhmke, 1982) as tremolite needles or fibres (Fig. 40). In this study, two amphiboles were identified. Actinolite (a series with tremolite and ferro-actinolite) was identified by optical microscopy with transmitted light and by electron microprobe analyses (see Appendices). Tremolite and actinolite have the same basic chemical formula, $\text{Ca}_2(\text{Mg},\text{Fe}^{2+})_5\text{Si}_8\text{O}_{22}(\text{OH})_2$, but they have different $\text{Mg}/(\text{Mg} + \text{Fe}^{2+})$ ratios. Tremolite may have $\text{Mg}/(\text{Mg} + \text{Fe}^{2+}) = 1.0\text{-}0.9$, which means that it contains very little iron and is extremely rich in magnesium. Actinolite, however, may have $\text{Mg}/(\text{Mg} + \text{Fe}^{2+}) = 0.5\text{-}0.89$; thus, it contains significantly more iron (e.g., Leake, 1978; Leake *et al.*, 1997; Fleischer & Mandarino, 1995). The analyses gave a $\text{Mg}/(\text{Mg} + \text{Fe}^{2+})$ ratio of 0.69-0.79 (see discussion and appendices), which is well within the actinolite field.

The other amphibole identified is cummingtonite, which occurs both as fibres and as somewhat thicker prismatic crystals. It is as abundant as actinolite and may be dis-

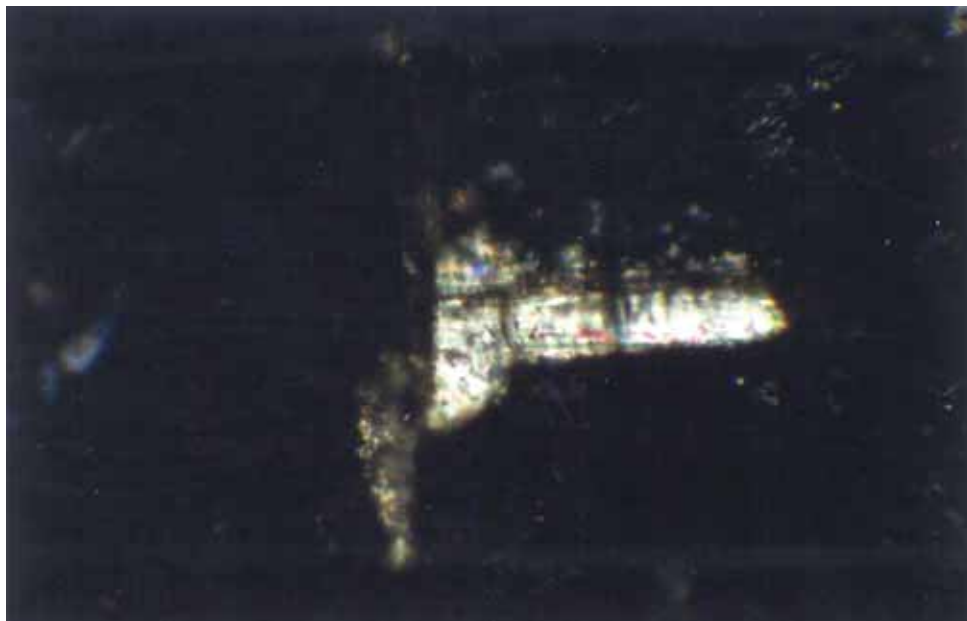


Fig. 49. Mn-Fe-bearing dolomite is a common carbonate in emeralds from Sandawana, normally as very small and irregular grains, but also as larger elongated grains, such as shown here. Between crossed polarising filters this grain shows high order interference colours, characteristic for a carbonate. $\times 100$.

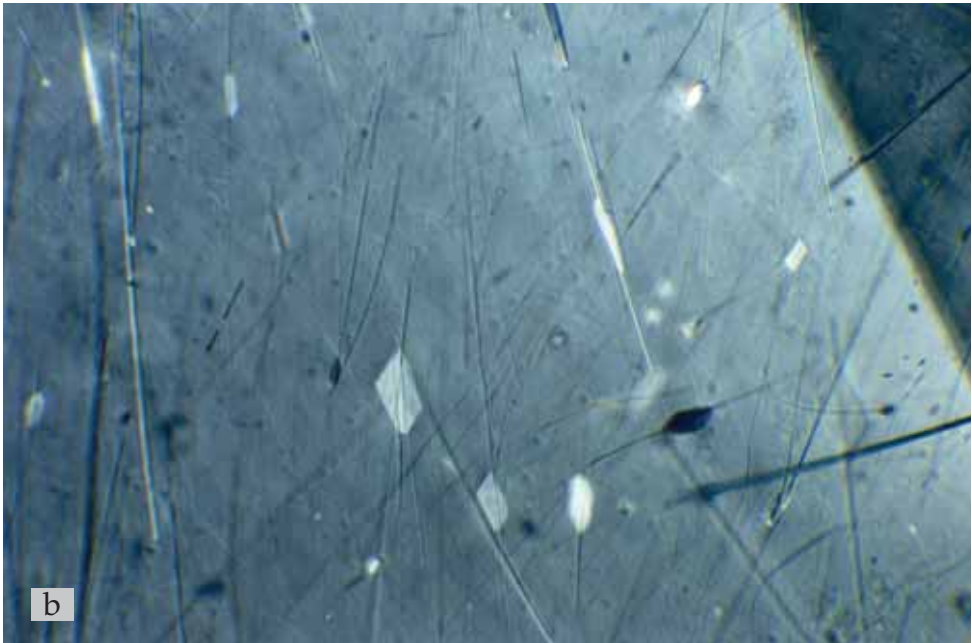
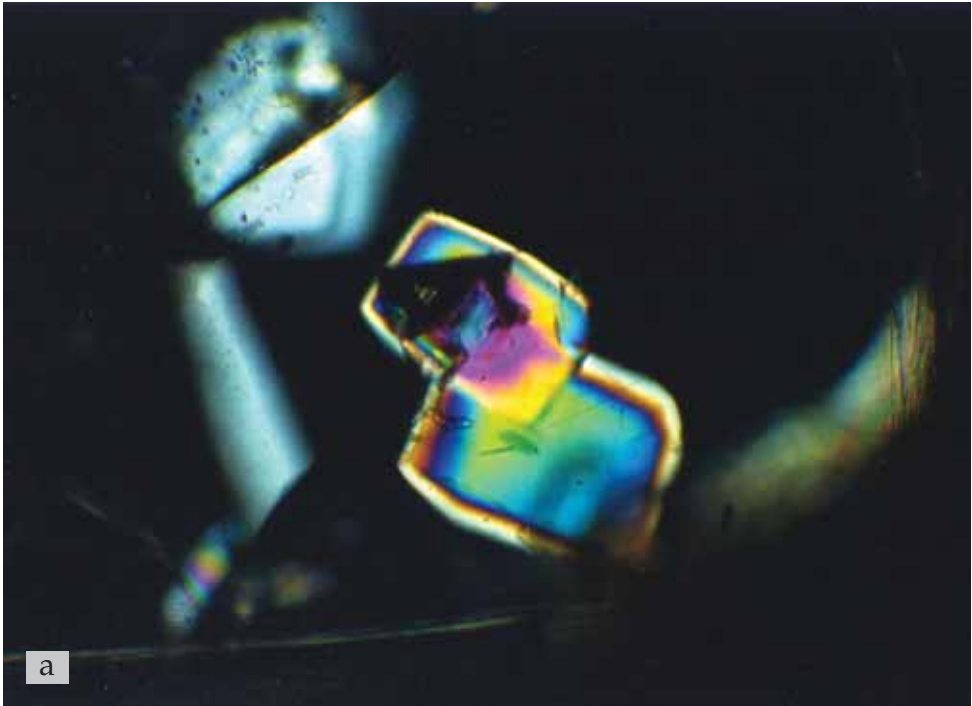


Fig. 50. (a) and (b). Emerald inclusions in emerald, in transmitted light between crossed polarising filters. $\times 100$.

tinguished from it by its slightly higher relief in transmitted light and the presence of lamellar twinning in polarized light (Fig. 41).

Using the electron microprobe, it became clear that the thicker actinolite crystals are zoned and often show a rim of cummingtonite; in contrast, the cummingtonite crystals are not zoned. In many thinner amphibole needles, actinolite is intergrown with cummingtonite (Fig. 42). Therefore, it will not come as a surprise that it is virtually impossible to distinguish between actinolite and cummingtonite with a normal gemmological microscope, using either transmitted or darkfield illumination.

Another fairly common mineral inclusion is albite. It most commonly occurs as large tabular fragments (Fig. 43) or as small, slightly rounded, colourless crystals (Fig. 44). It also occurs in the form of a whitish, rectangular crystal surrounded by minute grains of (probably) albite, which give it the appearance of a snowball (Fig. 45).

Apatite is a common inclusion, too, but the crystals are often very small and show various morphologies. Apatite may occur in clusters of small colourless to light green crystals or as isolated, idiomorphic crystals, sometimes brownish green, but also colourless (Fig. 46). In addition, apatite commonly occurs as rounded crystals with an irregular surface (Fig. 47). This illustrates that, in some gem materials, the same mineral can have a variety of appearances, which makes these inclusions difficult to identify by using only the microscope. In many cases, Raman spectroscopy helped reveal the true nature of an inclusion (see, e.g., Pinet *et al.*, 1992; Hänni *et al.*, 1997); in some, it easily distinguished between albite and apatite, which may look very similar.

Phlogopite is abundant in the ore zone where the emeralds are found, but it was only occasionally present in the samples that were studied. The distinctive orange-brown, plate-like crystals are easy to identify optically (Fig. 48; identification confirmed by microprobe, see Appendices).

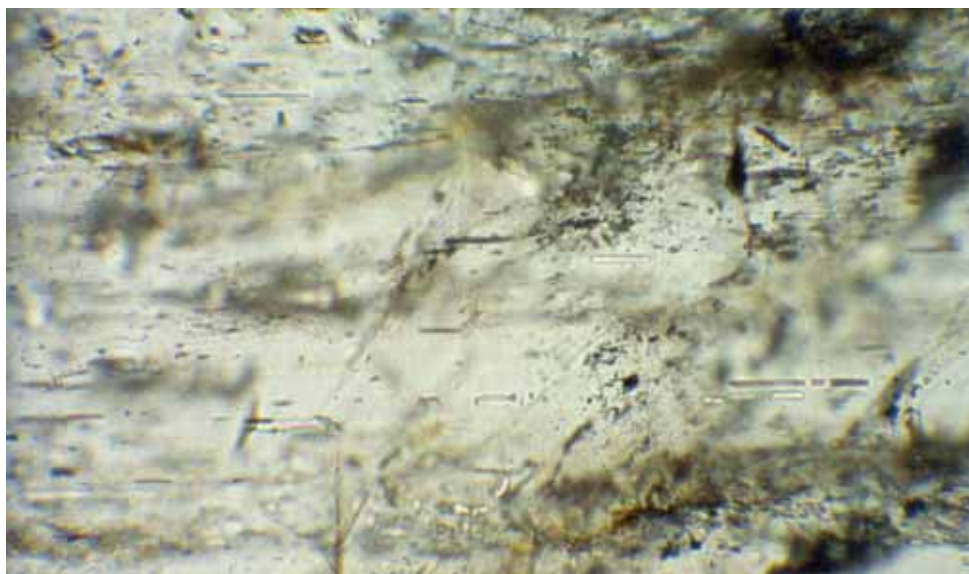


Fig. 51. Elongated and parallel quartz crystals occur in some emeralds from Sandawana. $\times 100$.



Fig. 52. Holmquistite frequently occurs in emeralds, which are formed in pegmatite. Length of this crystal is 300 μm .

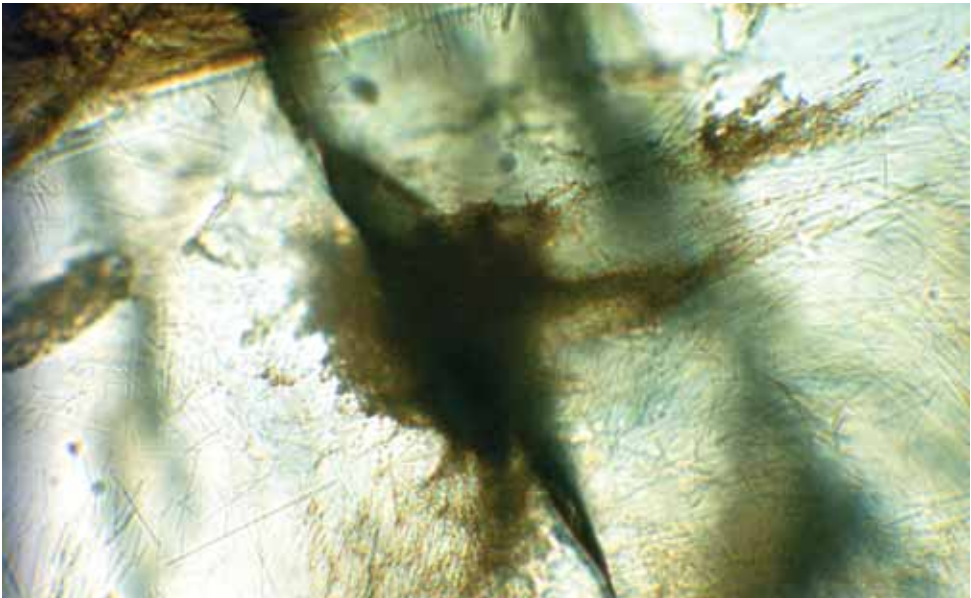


Fig. 53. Although similar in appearance to previously described garnet inclusions with brownish haloes, the inclusion shown here is probably a mixture of limonite (on the basis of visual appearance) and amphiboles (as identified by Raman spectroscopy). Garnets were not identified in any of the Sandawana emeralds studied for this thesis. Transmitted light, $\times 160$.

Two carbonate minerals were identified; calcite and Mn-Fe-bearing dolomite. Dolomites with similar chemical composition were regularly encountered in Sandawana emeralds, not only as small grains, like calcite, but also as larger, elongated grains (Fig. 49). Three dolomites which were chemically analysed contained on average 12.6 wt.% MgO, 7.70 wt.% FeO, and 3.35 wt.% MnO.

In some emeralds, emerald inclusions occur as crystals with a very low relief and a slightly different orientation, which can be viewed best between crossed polarising filters (Fig. 50). Their identity was confirmed by Raman analysis.

Quartz has been identified, but is not common in Sandawana emerald; it occurs as small isolated and rounded grains, and as elongated and tube-like crystals with low relief, which are orientated parallel to the c-axis (Fig. 51).

Zircon is very rare and only occurs as minute rounded crystals. Both the identity of quartz and zircon was confirmed by Raman analysis.

In emeralds that were found in the pegmatite, near streaks of amphibole schist, but a few or more cm away from the actual contact with the greenschist, the lithium amphibole holmquistite was identified (from electron microprobe analysis and calculation of the chemical formula). This was confirmed by optical microscopy; the amphiboles analyzed showed a violet/blue to violet/pink pleochroism (Fig. 52) and straight extinction under crossed polarising filters. As most cuttable emeralds are probably coming from the schist and not from the pegmatite (see Chapter 4), chances that holmquistite will be encountered in cut emeralds are slim.

I did not encounter any of the resorbed garnet inclusions that had been previously described (Gübelin, 1958; Gübelin & Koivula, 1992); similar-appearing inclusions (Fig. 53) were investigated with Raman spectroscopy, but could not be identified as garnet (which should be easily be identified by that method; Pinet *et al.*, 1992). Instead, amphiboles were present and, from appearance, some limonite.

Opaque minerals are rare in Sandawana emeralds, but black crystals with submetallic lustre up to 0.7 mm were present in one polished stone (Fig. 54). Chemical analysis proved these crystals to be a chromium-iron-niobium-tantalum-titanium oxide (chromium ilmenorutile). From Table 8 (spot analyses 1-5) and Figure 55 it can be seen that this analysed grain shows a rather homogeneous composition with a very high chromium content. The whitish area at the upper side of the grain shows even higher Cr, but also higher Nb, Ta, Fe and lower Ti (analysis 6). Based on analyses 1-5, the average chemical formula could be written as $(\text{Ti}_{0.804}\text{Sn}_{0.002}\text{Nb}_{0.062}\text{Ta}_{0.034}\text{Cr}_{0.081}\text{Fe}_{0.022})_{\Sigma 1.006}\text{O}_{2.00}$. For the whitish area in Figure 55 the formula would be: $(\text{Ti}_{0.745}\text{Sn}_{0.002}\text{Nb}_{0.078}\text{Ta}_{0.051}\text{Cr}_{0.092}\text{Fe}_{0.040})_{\Sigma 1.008}\text{O}_{2.00}$. The average atomic ratio Nb/Ta is 1.82 (whitish area: Nb/Ta = 1.53). Because the atomic ratio Nb/Ta > 1, this mineral may be called niobian rutile (preferred by Flinter, 1959; Cerný *et al.*, 1964) or ilmenorutile (Siivola, 1970), a name which has been used since its discovery in 1854 (if Nb/Ta < 1 the name would be tantalian rutile or strüverite). Other phases that were identified in the analysed grain (Fig. 55) are ilmenite and chromite; one grain of probable tantalite/columbite was too small for microprobe analysis. Another rare opaque mineral that was identified by microprobe analysis is gersdorffite, but it is only present as extremely small grains.

In conclusion, according to relative abundance the following mineral inclusions were encountered in Sandawana emeralds:

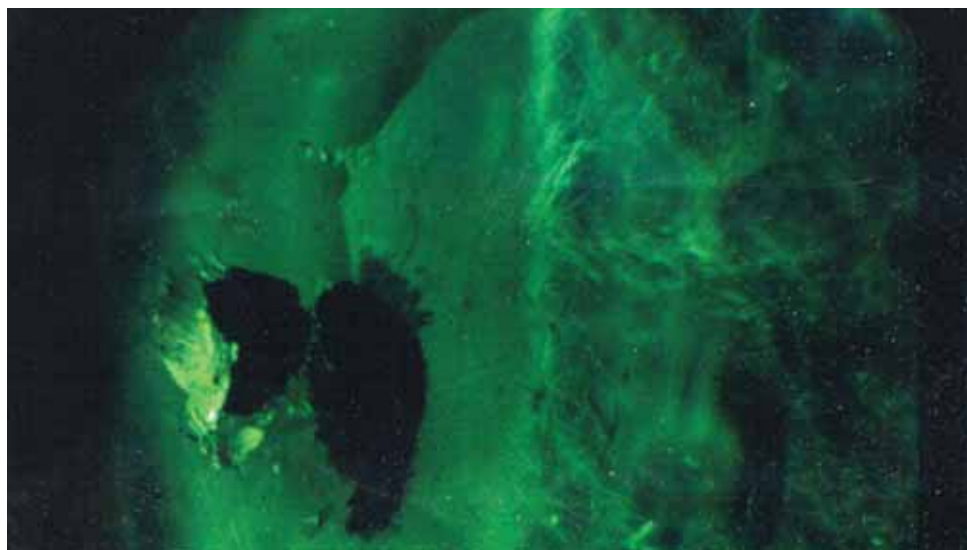


Fig. 54. Extremely rare crystals of chromian ilmenorutile were identified in a polished Sandawana emerald. $\times 60$.

Table 8. Spot chemical analyses of a chromium-rich ilmenorutile inclusion in emerald from Sandawana.

Oxides (wt.%)	1	2	3	4	5	6
TiO ₂	72.1	71.7	70.3	70.1	70.7	63.7
SiO ₂	0.07	0.07	0.07	0.08	0.07	0.09
SnO ₂	0.38	0.42	0.45	0.45	0.32	0.34
Nb ₂ O ₅	8.81	8.93	9.25	9.39	9.32	11.1
Ta ₂ O ₅	8.23	7.79	8.41	8.15	8.67	12.1
Al ₂ O ₃	0.05	0.04	0.05	0.05	0.05	0.06
Cr ₂ O ₃	6.64	6.85	7.03	6.83	6.62	7.45
FeO	1.80	1.53	1.66	1.75	2.05	3.07
MnO	-	-	-	-	-	-
MgO	-	-	-	-	-	-
CaO	0.02	0.03	0.03	0.03	0.02	0.01
Total*	98.10	97.36	97.25	96.83	97.83	97.92
Cations based on 2 O						
Ti ⁴⁺	0.810	0.810	0.800	0.800	0.801	0.745
Si ⁴⁺	0.001	0.001	0.001	0.001	0.001	0.002
Sn ⁴⁺	0.002	0.003	0.003	0.003	0.002	0.002
Nb ⁵⁺	0.060	0.061	0.063	0.064	0.063	0.078
Ta ⁵⁺	0.033	0.032	0.035	0.034	0.036	0.051
Al ³⁺	0.001	0.001	0.001	0.001	0.001	0.001
Cr ³⁺	0.078	0.081	0.084	0.082	0.079	0.092
Fe ²⁺	0.023	0.019	0.021	0.022	0.026	0.040
Ca ²⁺	-	-	0.001	0.001	-	-
Number of cations	1.008	1.008	1.009	1.008	1.009	1.011

- not detected

* low totals are due to conductivity which was not optimal

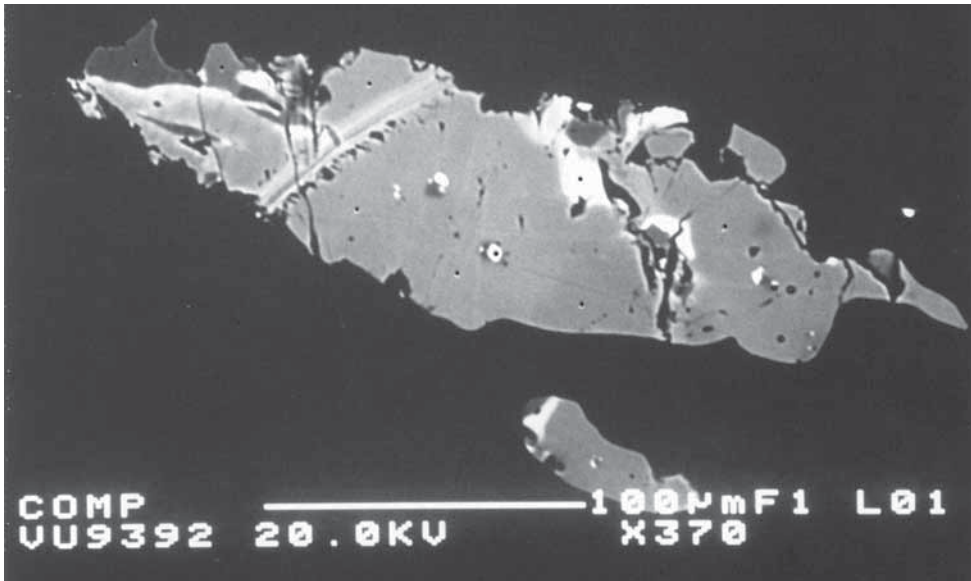


Fig. 55. Electron photomicrograph of a chromium-rich ilmenorutile grain in Sandawana emerald. The whitish area at the upper side of the grain indicates a lower Ti concentration (and higher Cr, Nb, Ta and Fe concentrations). Other phases include ilmenite (the very dark grey part on the upper left side), chromite (the dark grey part next to it) and tantalite/columbite (the small white speck in the middle of the grain). Photomicrograph by W.J. Lustenhouwer.



Fig. 56. Partially healed fractures containing minute inclusions were often present in the Sandawana emeralds examined. Darkfield illumination, $\times 60$.

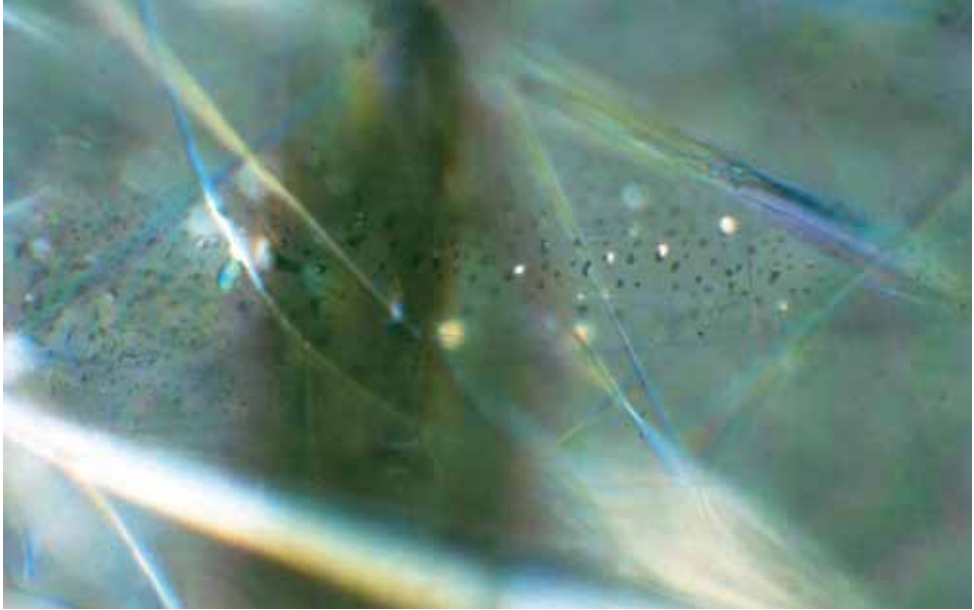


Fig. 57. A closer look at the minute inclusions in a partially healed fracture reveals that the doubly refractive minerals are carbonates. Transmitted light, crossed polarisers, $\times 175$.

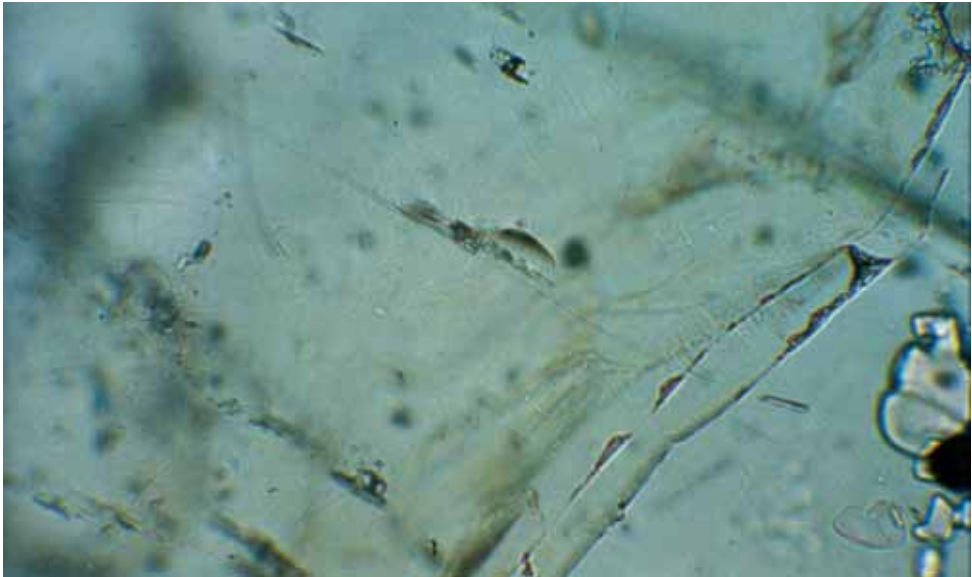


Fig. 58. Typical aspect of most fluid inclusion remnants found in Sandawana emeralds; decrepitated cavities, bounded by prominent micro fractures. All fractures are parallel for the three inclusions shown in the photo (centre, top to bottom). In the centre of the cavity are particles of whitish carbonates (some appearing black on the photo because of the high refractive index). Length of the lowest inclusion is about $30\ \mu\text{m}$. Transmitted light, $\times 200$ (width of view $450\ \mu\text{m}$).



Fig. 59. The trail with decrepitated inclusions on the left is a common feature in Sandawana emeralds; it indicates the earlier presence of fluids. Albite crystals are visible on the right. Transmitted light, $\times 125$.



Fig. 60. Exceptional primary 3-phase brine inclusion found in emerald from Zeus 200ft level, 26/28 stope. Large halite cube, two small unknown solids, large dark gas bubble, containing traces of CO_2 , remaining fluid = saturated liquid water. Length of the inclusion is about $20 \mu\text{m}$. (Width of view $120 \mu\text{m}$).

Very common: actinolite, cummingtonite
Common: albite, apatite
Rare: holmquistite, phlogopite, calcite, Mn-Fe-bearing dolomite, emerald, quartz
Exceptional: chromian ilmenorutile, ilmenite, chromite, gersdorffite, tantalite/columbite

Fluid inclusions – Much rarer and more difficult to investigate than the solid inclusions, the fluid inclusions seen in the samples are very different from the well-known brine inclusions present in, for example, Colombian emeralds. In the search for fluid inclusions, I did find partially healed fractures with minute inclusions to be quite common (Fig. 56). However, most of these were so small (less than 6 microns in diameter) that they could not be analyzed by Raman spectroscopy. Some of the slightly larger inclusions in a partially healed fracture were found to be empty and quite a few contained solids, which were identified as carbonates (Fig. 57).

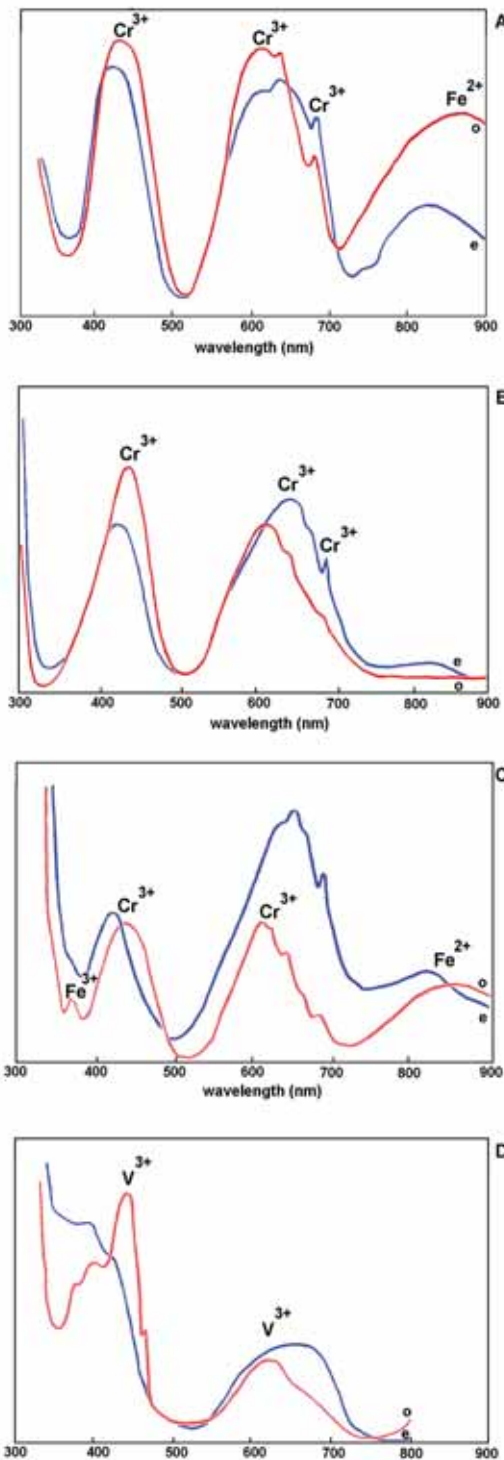
Slightly larger isolated inclusions (approximately 35 microns long) were seen to occur as small, dark, comma-like features oriented parallel to the c-axis (Fig. 58). These inclusions, too, were empty and carbonate has been identified near them. Carbonate is often found near decrepitated inclusions that may have contained CO₂ (J. Touret, pers. comm., 1996). These isolated inclusions thus can be interpreted as primary CO₂-rich inclusions. In addition to these partially healed fissures and isolated decrepitated inclusions, straight trails with decrepitated inclusions were also a common feature in the emeralds from Sandawana (Fig. 59).

Tube-like, two-phase, liquid and gas inclusions were seen in one sample, but they were difficult to identify with a standard gemmological microscope because there were so few of them and they were extremely small.

After having studied a great number of samples in vain, a small number of isolated, non-decrepitated (or at least not empty) inclusions have been found in five samples from different locations at the Zeus 200 ft. level, 26/28 stope (Fig. 60). They contain a typical hydrothermal, high-salinity aqueous brine (at least 50% wt. equivalent NaCl) and traces of CO₂. It is improbable that this fluid is exactly the same as the one initially present in the decrepitated inclusions, which from the size of the remaining carbonate must have been much more CO₂-rich. It is probable that this fluid was an immiscible gaseous-rich phase in the highly saline brines.

3.4.5. Absorption spectra – A typical absorption spectrum for Sandawana emeralds is shown in Figure 61. Broad absorption bands around 430 and 610 nm (for the ordinary ray), and the sharp peak at 683 nm, are reported to be caused by Cr³⁺, whereas the broad band around 810 nm is attributed to Fe²⁺ (Wood & Nassau, 1968; Schmetzer *et al.*, 1974). The spectrum is characteristic for a so-called 'Cr³⁺-emerald' (Schmetzer *et al.*, 1974), in which the colour is solely due to Cr³⁺-ions. The low absorption-minimum in the green and the steep slopes of the Cr³⁺ absorption bands produce the vivid green colour. Possible chromophores such as V³⁺ and Fe³⁺ are not present in sufficient quantities to contribute to the colour (see Section 3.4.6). Although present, Fe²⁺ does not influence the colour, because its peak lies outside the visible light region in the near-infrared.

The spectra of emeralds from Sandawana can be distinguished from the spectra of



'Cr³⁺-emeralds' from Colombia by the intensity of the Fe²⁺-absorption band in the former. Only the e-spectrum of Colombian emeralds may show a very weak, broad absorption band around 800 nm, but in most cases an iron spectrum can barely be detected (e.g., Bosshart, 1991; Henn & Bank, 1991). Emeralds from many other localities in which Fe³⁺ contributes to the colour show an additional (often low intensity) peak around 370 nm (e.g., Schmetzer *et al.*, 1974; Henn & Bank, 1991). Figure 61 provides examples of spectra caused by various chromophores.

3.4.6. *Chemical Analysis* – Table 9 gives the average quantitative results obtained with the electron microprobe and trace element concentrations measured with PIXE/PIGE. The Sandawana emeralds are characterized by extremely high chromium content. Average concentrations varied between 0.6 and 1.3 wt.%, but spot analyses revealed chemical zoning on a small scale within the samples, with concentrations varying from 0.38 to 1.48 wt.%. In one sample from the Zeus mine, the range was even greater, 0.13 to 3.05 wt.%. In those stones where weak colour zoning was observed, the slightly darker green zones revealed more chromium, but often no straightforward correlation between colour in-

Fig. 61. The absorption spectrum recorded in Sandawana emeralds (A) is comparable to that of Colombian emeralds (B), but has a strong absorption band in the near-infrared, due to Fe²⁺. A spectrum of a Brazilian emerald (C) shows an additional peak in the violet due to Fe³⁺. The spectrum of a chrome-free emerald from Salininha, Brazil (D), in which colour is due to V³⁺. Spectra (B) and (C) are from Henn & Bank (1991, fig. 2); spectrum (D) is from Wood & Nassau (1968, fig. 5). Red line = ordinary ray, blue line = extraordinary ray.

Table 9. EPMA and PIXE/PIGE analyses on emeralds from Sandawana, Zimbabwe.

Electron Microprobe results of analysed elements in four medium- to dark-green emeralds (range of average results) and one pale green emerald (the average for each element) from Sandawana.^a Data published in Zwaan *et al.* (1997).

	Medium to dark green emeralds from the Zeus and Orpheus mines	Pale green emerald from the Zeus mine
Oxide	Content (wt.%)	Content (wt.%)
SiO ₂	62.60 - 63.20	62.80
Al ₂ O ₃	13.00 - 13.70	14.30
Cr ₂ O ₃	0.61 - 1.33	0.16
V ₂ O ₃	0.04 - 0.07	0.04
FeO	0.45 - 0.82	0.71
MgO	2.52 - 2.75	2.38
Na ₂ O	2.07 - 2.41	2.30
K ₂ O	0.03 - 0.06	0.06
Cs ₂ O	0.06 - 0.10	0.09
Rb ₂ O ^b	≤ 0.04	bdl
CaO ^b	≤ 0.03	bdl
TiO ₂ ^b	≤ 0.05	bdl

^a MnO, Sc₂O₃, F and Cl were below the detection limits.

^b Most of the analyses gave values equal to or below the detection limit (bdl).

PIXE/PIGE analyses of trace elements in 22 emeralds from Sandawana. Mean elemental content in weight ppm. Standard deviations are given in parentheses. LOD is limit of detection. Data published in Calligaro *et al.* (2000).

Trace element	Content (ppm)	LOD
Li	800 (310)	50
Ti	120 (250)	30
V	210 (320)	10
Cr	5211 (2190)	10
Mn	180 (360)	20
Fe	6320 (3300)	3
Ni	20 (11)	2
Cu	1 (2)	2
Zn	66 (28)	2
Ga	30 (9)	2
Rb	350 (200)	2
Cs	710 (320)	100
F	34 (21)	60

tensity and chromium content could be found. From these analyses, it can be seen that the chromium content is partly consistent with the values given by Gübelin (1958), Martin (1962) and Hänni (1982), but it can also be substantially higher.

The Sandawana emeralds also show low Al₂O₃ content, but very high MgO and Na₂O contents. Using Schwarz's empirical subdivision of low, medium and high concentrations of elements in emerald (see, e.g., Schwarz, 1990b), it is concluded that the iron content is medium whereas the vanadium content is very low.

Notable is the presence of caesium. As observed by Bakakin & Belov (1962), Cs is present typically in Li-rich beryl. In fact, on the basis of very high Cs content, recently a new species of the beryl group, named pezzottaite, has been discovered (Laurs *et al.*, 2003). Lithium cannot be analyzed by microprobe, but its presence was indicated earlier by Gübelin (1958), Martin (1962) and Böhmke (1982), who gave Li₂O values ranging from 0.10 to 0.15%. Subsequent PIXE/PIGE analyses on 22 emeralds showed a very high Li content, between 490 and 1110 ppm.

Beryl may be considered as an isomorphous series of three end-members; Be₃Al₂Si₆O₁₈ (Na,Cs)Be₂Al₂AlLi₂Si₆O₁₈ and (Na, K, Cs)Be₃-R³⁺ R²⁺.Si₆O₁₈, of which the latter is called a 'femag beryl' with R³⁺ = Al, Fe³⁺, Cr and Sc, and R²⁺ = Fe²⁺, Mn and Mg (Schaller *et al.*, 1962; Deer *et al.*, 1986). The emeralds from Sandawana, with their high Cr, Mg and Na content, would contain around 45 percent of the femag beryl end-member.

The structure of beryl is characterised by hexagonal rings of six linked Si-O tetrahedra stacked one above another, resulting in a series of open channels

Table 10. Chemical analyses of the most magnesium-rich actinolite and a cummingtonite, as encountered in this study of Sandawana emeralds.

Oxides (wt.%)	Actinolite	Cummingtonite
SiO ₂	54.1	56.4
TiO ₂	0.05	-
Al ₂ O ₃	2.91	0.45
Cr ₂ O ₃	0.31	0.13
FeO	8.40	15.8
MnO	0.41	0.66
MgO	18.3	22.7
CaO	11.9	0.61
Na ₂ O	0.96	0.19
K ₂ O	0.06	-
H ₂ O*	2.01	2.11
F	0.13	-
Total	99.55	99.05

Cations based on 22 O and 2 (OH, F, Cl)	Min. Fe ³⁺	Max. Fe ³⁺	
Si	7.67	7.59	8.00
Al IV	0.33	0.41	0
T site	8.00	8.00	8.00
Al VI	0.16	0.08	0.07
Fe ³⁺	0	0.20	0
Ti	0.01	0.01	
Cr	0.04	0.04	0.01
Mg	3.87	3.83	4.79
Fe ²⁺	0.94	0.79	0.12
M1, 2, 3 sites	5.00	5.00	5.00
Fe ²⁺	0.06	0	1.75
Mn	0.05	0	0.08
Ca	1.81	1.79	0.09
Na	0.08	0.21	0.05
M4 site	2.00	2.00	1.97
Na	0.19	0.06	0
K ⁺	0.01	0.01	
A site	0.20	0.07	0
OH	1.90	1.90	2.00
F	0.10	0.10	
Anion	2.00	2.00	2.00

- not detected

* calculated

All ferrous formulas for both amphiboles are permitted, for cation sums are not too high. Thus, formulae were calculated based on a minimum Fe³⁺ estimate = 0.000 (compare Leake *et al.*, 1997). For an explanation of the actinolite formula based on a maximum Fe³⁺ estimate, see the text.

parallel to the c-axis of the mineral. The rings are connected by bonds between alternating Al and Be atoms. Each aluminium atom is surrounded and bonded to six oxygen atoms, while each beryllium atom is surrounded and bonded by four oxygen atoms. On the basis of structural refinements, Aurisicchio *et al.* (1988) proposed three types of beryls: 'octahedral', in which substitutions in the Al octahedral site by Me²⁺ (Fe²⁺ and Mg²⁺ plus Fe³⁺, Cr³⁺, V³⁺, Mn²⁺, Ti⁴⁺) represent the main isomorphous replacement; 'tetrahedral', in which the main substitution is Li in the Be tetrahedral site; and 'normal', in which the two substitutions occur together, but to a limited extent. In this model, a compositional gap exists between beryls with octahedral and tetrahedral substitutions. According to this model, the analysed emeralds from Sandawana would fall in the category of 'octahedral' beryls.

The open channels parallel to the c-axis are wide enough to incorporate molecules of volatiles such as H₂O, CO₂ and N₂, and alkalis (e.g., Na, Cs). Elements like Na and Cs compensate for negative charges in the lattice produced by the substitution of Fe²⁺ for Al³⁺ or by the omission of a Be²⁺ ion (Wood & Nassau, 1967).

3.5. Discussion

3.5.1. Actinolite and cummingtonite versus tremolite – The acicular amphibole crystals in the emeralds from Sandawana were previously described by various authors (e.g., Gübelin, 1958; Böhmke, 1982; Gübelin & Koivula, 1992) as tremolite needles or fibres. From results in our study, it became apparent that the amphiboles present are actinolite and cummingtonite, but not tremolite.

As reported in Section 3.4.4, the anal-

yses for actinolite gave a $\text{Mg}/(\text{Mg} + \text{Fe}^{2+})$ ratio of 0.69-0.79, which is well within the actinolite field. The particular actinolite with the highest measured Mg content is presented in Table 10, together with an analysis of cummingtonite. The analysis of this actinolite shows a $\text{Mg}/(\text{Mg} + \text{Fe}^{2+})$ ratio = 0.79, which is slightly higher than the maximum ratio of 0.74, which was previously indicated in Zwaan *et al.* (1997). The indicated ratio is based on a minimum ferric estimation. However, in order to define the range of possible formulae and possible names for this particular amphibole (as recommended by Leake *et al.*, 1997), also the formula for the maximum ferric estimate has been calculated (Table 10). From this calculation it was determined that the $\text{Mg}/(\text{Mg} + \text{Fe}^{2+})$ ratio = 0.83. Although close to the border with tremolite (which has $\text{Mg}/(\text{Mg} + \text{Fe}^{2+}) = 1.0-0.9$), this ratio is still of no consequence for the name actinolite.

3.5.2. *Chromian ilmenorutile* – The presence of ilmenorutile as a rare inclusion in Sandawana emerald was mentioned earlier by Böhmke (1982). While Mn-rich ilmenorutile is known from Uzumine, Japan (Kawai, 1960), a chromium-rich variety of ilmenorutile, such as described in this study and in Zwaan & Burke (1998), has not been reported before (see, e.g., Cerný *et al.*, 1964; Siivola, 1970). Chromium is not present in ilmenorutile from other localities. Only in ilmenorutile from the type locality in the Ilmen mountains, Urals, Russia, chromium is possibly present in concentrations of < 0.009% (Cerný *et al.*, 1964). While intergrowths of ilmenorutile with ilmenite and columbite are quite common (e.g., Sosedko, 1939; Ando & Nitta, 1941; Noll, 1949; Cerný *et al.*, 1964; Siivola, 1970), the association of ilmenorutile and chromite in Sandawana emerald is also the first of its kind.

3.5.3. *Identification of Sandawana emeralds relative to other occurrences* – In beryl, the larger alkali ions and water do not substitute isomorphously for other ions of similar ionic refractivity, but rather they occupy what would otherwise be empty spaces in the structure (e.g., Wood & Nassau, 1968; see also Sections 3.4.6, 4.1.1). Both substantially increase the refractive indices, with water having the greater effect (Deer *et al.*, 1986). The octahedral substitution of Al^{3+} by Mg^{2+} , Mn^{2+} , Ni^{2+} and Fe^{2+} also produces a steep increase in refractive indices (Cerný & Hawthorne, 1976). In Sandawana emeralds, the relatively low totals for chemical content indicate that at least 2% water probably is present. This high water content, together with the high magnesium and sodium content, thus contributes to the high refractive indices of Sandawana emeralds.

These higher R.I. values make them very easy to distinguish from their synthetic counterparts. The latter typically have lower refractive indices, roughly between 1.56 and 1.58, and lower specific gravities of 2.65-2.70 (see, e.g., Webster, 1994; Schrader, 1983; Liddicoat, 1989; Schmetzer *et al.*, 1997), although Russian hydrothermal synthetic emeralds may show R.I.s up to 1.584 and S.G.s up to 2.73 (Webster, 1994; Koivula *et al.*, 1996). Russian hydrothermal synthetics can usually be separated from natural emeralds by their distinctive chevron growth zoning (Koivula *et al.*, 1996).

On the basis of refractive index, birefringence and specific gravity values (see, e.g., Gübelin, 1989; Schwarz, 1990a, 1991a; Schwarz & Henn, 1992), emeralds from Sandawana resemble those from the Ural Mountains of Russia, the Habachtal region of Austria, the Santa Terezinha de Goiás deposits of Brazil, certain mines in Pakistan, the Mananjary region in Madagascar and the Kafubu area in Zambia. From Table 11, it can be

Table 11. Physical properties of emeralds from various localities.^a

Locality	Refractive indices		Birefringence	Specific gravity
	n_c	n_o		
Sandawana, Zimbabwe	1.584-1.587	1.590-1.594	0.006-0.007	2.74-2.77
Swat Mines, Pakistan	1.578-1.591	1.584-1.600	0.006-0.009	2.70-2.78
Makhad, Pakistan	1.579-1.587	1.586-1.595	0.007-0.008	2.74-2.76
Ural Mountains, Russia	1.575-1.584	1.581-1.591	0.007	2.72-2.75
Habachtal, Austria	1.574-1.590	1.582-1.597	0.005-0.007	2.70-2.77
Santa Terezinha de Goiás, Brazil	1.584-1.593	1.592-1.600	0.006-0.010	2.75-2.77
Mananjary Region, Madagascar	1.580-1.585	1.588-1.591	0.006-0.009	2.68-2.73
Kafubu area, Zambia	1.578-1.591	1.585-1.599	0.006-0.009	2.69-2.78

^a Pakistan data from Gübelin, 1989; Russia data from Schmetzer *et al.*, 1991, and Mumme, 1982; Austria data from Gübelin, 1956, and Schwarz, 1991a; Brazil data from Schwarz, 1990a, and Lind *et al.*, 1986; Madagascar data from Hänni & Klein, 1982, and Schwarz & Henn, 1992; Zambia data from Zwaan *et al.*, 2005.

seen that emeralds from these other localities show greater variation in properties than the Sandawana stones. Also, most emeralds from the Ural Mountains and from the Mananjary region have lower values than those recorded for the Sandawana stones.

A comparison of inclusions reveals that emeralds from the Swat and Makhad mines in Pakistan do not contain any amphibole fibres and needles, but commonly show black chromite and many two- (liquid-gas) and three-phase (liquid-gas-solid) inclusions (Gübelin, 1989); thus, they look quite different from Sandawana emeralds. Emeralds from the Charbagh and Khaltaro mines in Pakistan (not mentioned in Table 10 because most of the stones examined came from the Swat mines [the largest mines] and Makhad, and can be considered most representative of Pakistan emeralds) may contain brownish green to black actinolite rods, but certainly not thin fibres of amphibole; they also show slightly lower specific gravities and refractive indices (Gübelin, 1989).

Emeralds from the Ural Mountains may contain actinolite rods that closely resemble the long-prismatic actinolite and cummingtonite crystals observed in Sandawana emeralds. However, the thin and often curved fibres seen in Sandawana emeralds have not been reported in Uralian emeralds; in the latter, phlogopite is frequently present as rounded platelets or as large elongated tabular crystals (Schmetzer *et al.*, 1991; Gübelin & Koivula, 1992). Although phlogopite has been found in emeralds from Sandawana, it is uncommon. Like the Uralian emeralds, the emeralds from Habachtal contain actinolite rods and phlogopite platelets, but the Austrian stones also have apatite crystals (Gübelin & Koivula, 1992). However, these emeralds normally show an inhomogeneous, 'patchy' colour distribution (Morteani & Grundmann, 1977) that has not been seen in Sandawana emeralds.

Although amphibole has been identified in emeralds from Santa Terezinha, Brazil, these emeralds are characterized by abundant opaque inclusions such as black spinel (as small octahedra and larger irregular grains), hematite, rutile and pyrite. They also contain various pale brown to colourless carbonates, which are present as irregular grains, aggregates and fillings of fractures, but also as rhombohedra (Schwarz, 1990a). By contrast, opaque inclusions of distinguishable size are rare in Sandawana emeralds, so separation from these Brazilian emeralds should thus be relatively easy.

Inclusions in emeralds from Madagascar may look very similar to those in Sanda-

wana emeralds, because long prismatic amphibole rods are frequently found (Schwarz & Henn, 1992; Schwarz, 1994) as fibrous aggregates of talc which may resemble the amphibole fibres present in Sandawana emeralds. Feldspar crystals and carbonates were also identified, although feldspar is less common in Madagascar stones (Schwarz, 1994). Hänni & Klein (1982) identified apatite, too. However, in many Mananjary emeralds, transparent, somewhat rounded or 'pseudo-hexagonal' mica (most biotite/phlogopite) is the most common inclusion (Hänni & Klein, 1982; Schwarz & Henn, 1992; Schwarz, 1994). Fluid inclusions were observed in most Mananjary emeralds; the larger inclusions are often somewhat rectangular, negative crystals filled with gas and liquid (Hänni & Klein, 1982; Schwarz, 1994), but three-phase (solid-liquid-gas) inclusions may also occur (Schwarz & Henn, 1992). As mentioned above, neither mica nor fluid inclusions are commonly found in Sandawana emeralds.

Zambian emeralds are characterised by the presence of partially healed fissures with typically equant or rectangular two- and three-phase inclusions, platelets of phlogopite and randomly oriented actinolite needles (but no curved fibres), and may therefore look similar to emeralds from the Ural, Habachtal and Madagascar (Zwaan *et al.*, 2005). However, it is evident that their internal characteristics are usually very different from those of Sandawana emerald.

The chemistry of emeralds from the mentioned localities provides additional evidence (Table 12). The chromium content is distinctly lower for emeralds from the Ural Mountains, Habachtal and the Mananjary region, and in most cases lower for emerald from the Kafubu area. For the Uralian emeralds, this was confirmed by Laskovenkov & Zhernakov (1995), who gave typical chromium contents of 0.15-0.25 wt.%, with the content in some stones as high as 0.38 wt.%. In emeralds from Santa Terezinha, the chromium content can be very low, but also very high. However, the sodium content is lower, and, in most cases, the iron content is higher, than in emeralds from Sandawana.

Although trace elements may show considerable overlap, they may help eliminate some localities for a specific stone. For instance, relatively high K contents have been documented in emeralds from Kafubu and Mananjary. Note that emeralds from the Makhad mine and some emeralds from Kafubu were found to have appreciable Sc (Table 12), which was not detected in the Sandawana emeralds.

Additionally, if one has access to PIXE/PIGE, Li and Rb appear to be good provenance tracers, while Cs turned out to show more overlap. Comparing Li content of Sandawana emeralds (mean 800 ppm) with values published in Calligaro *et al.* (2000) for other localities, Habachtal, Mananjary and Pakistan emeralds show much lower values. While Rb content of most occurrences is very low, Sandawana emerald shows relatively high values, with only Kafubu and Mananjary emeralds showing some overlap (Table 12).

In conclusion, because of the relatively constant properties of Sandawana emeralds, these stones can be readily separated from emeralds from other localities on the basis of a combination of physical properties, inclusions and chemistry.

3.6. Conclusions

First discovered in 1956, Sandawana emeralds have become well known for their splendid vivid green colour and typically small size (0.05-0.25 ct). Since Sandawana

Table 12. Chemistry of emeralds with overlapping physical properties (wt.%).

Oxide	Electronmicroprobe data ^a									
	Sandawana, Zimbabwe	Swat mines, Pakistan	Makhad, Pakistan	Ural Mountains, Russia	Habachtal, Austria	Santa Terezinha, Brazil	Mananjary Region, Madagascar	Kafubu Area, Zambia		
SiO ₂	62.6-63.2	62.7-62.8	62.2-62.9	64.6-66.9	64.6-66.1	63.8-66.5	63.3-65.0	61.9-65.4		
Al ₂ O ₃	13.0-13.7	13.1-14.2	13.5-14.2	14.2-18.3	13.3-14.5	12.2-14.3	12.8-14.6	12.5-17.9		
Cr ₂ O ₃	0.61-1.33	0.39-1.17	0.23-1.26	0.01-0.50	0.01-0.44	0.06-1.54	0.08-0.34	≤ 0.84		
V ₂ O ₅	0.04-0.07	0.01-0.06	0.04-0.06	≤ 0.04	≤ 0.04	≤ 0.08	≤ 0.03	≤ 0.08		
FeO	0.45-0.82	0.52-0.91	0.44-0.67	0.10-1.16	0.61-1.87	0.77-1.82	0.91-1.46	0.06-1.75		
MnO	-	-	-	≤ 0.03	≤ 0.05	≤ 0.02	-	≤ 0.01		
MgO	2.52-2.75	2.46-2.50	2.37-2.68	0.29-2.23	2.33-2.92	2.48-3.09	1.71-3.00	0.27-2.90		
Nb ₂ O	2.07-2.41	2.06-2.11	1.64-2.05	0.61-1.72	1.54-2.24	1.46-1.73	1.28-2.16	0.16-1.99		
K ₂ O	0.03-0.06	- ^b	≤ 0.02	≤ 0.07	0.01-0.10	≤ 0.03	0.05-0.21	≤ 0.27		
Cs ₂ O	0.06-0.10	no data	no data	no data	no data	no data	no data	≤ 0.23		
Rb ₂ O	-	no data	no data	no data	no data	no data	no data	-		
CaO	-	-	-	≤ 0.03	0.02-0.04	no data	no data	≤ 0.12		
TiO ₂	≤ 0.05	-	0.01-0.02	≤ 0.05	≤ 0.03	no data	-	-		
Sc ₂ O ₃	-	no data	0.17-0.19	no data	no data	no data	no data	≤ 0.07		
Mo ₂ O ₃	-	no data	no data	no data	≤ 0.04	no data	no data	no data		
PIXE/PIGE data ^c										
Li	800 (310)	350 (130)	no data	720 (260)	190 (210)	170 (90)	130 (70)	580 (230)		
Cs	710 (320)	120 (80)		360 (230)	370 (390)	350 (300)	610 (580)	1150 (540)		
Rb	350 (200)	6 (3)		40 (60)	18 (13)	15 (2)	190 (70)	140 (60)		

^a Pakistan data from Hammarstrom (1989); Russia data from Schwarz (1991a) and Schmetzer *et al.* (1991); Austria data from Schwarz (1991a); Brazil data from Schwarz (1990a). Madagascar data from Schwarz & Henn (1992) and Hänni & Klein (1982); Zambia data from Zwaan *et al.* (2005).

^b - not detected

^c Data from Calligaro *et al.* (2000). Mean elemental content in weight ppm. Standard deviations are given in parentheses.

Mines Pvt. (Ltd.) assumed management of the mines in 1993, more stones up to 1.50 ct have been produced. Stones above 1.50 ct are still rare.

The emeralds from Sandawana show relatively constant physical properties, with high refractive indices and specific gravities. Unlike emeralds from many other localities, they are not characterized by abundant fluid inclusions, but rather by laths and fibres of amphibole, both actinolite and cummingtonite (previously reported to have been tremolite). Other common inclusions are albite and apatite. Inclusions of chromium-rich ilmenorutile have been identified. This variety of ilmenorutile has not been known and described before. The relative absence of fluid inclusions is due to decrepitation of these inclusions during the geological history. Nevertheless, remnants of fluid inclusion trails are common features.

The chemistry is characterized by very high contents of chromium, sodium, magnesium and lithium. Chromium contents in some samples were substantially higher than in specimens previously reported.

Although most emeralds from other localities with physical properties that overlap those for Sandawana emeralds also show solid inclusions, including actinolite rods (Russia, Brazil, Austria, Madagascar, Zambia), it is relatively easy to distinguish emeralds from Sandawana by their internal characteristics, especially by the presence of abundant amphibole fibres, which are seldom seen in stones from other localities. Although phlogopite and some opaque inclusions have been found, they are much less common in Sandawana emeralds, than in emeralds from the other localities. Although showing greater variation, the chemistry of emeralds from Zambia may appear to be closest to that recorded for Sandawana stones, but emeralds from the two localities can easily be distinguished by their different internal characteristics.

4. Key processes and conditions leading to emerald formation in the Mweza Greenstone Belt

4.1. Basic conditions of beryl formation

4.1.1. *Stability of beryl - pressure-temperature conditions* – The basic petrological conditions of emerald formation involve the presence of both beryllium and chromium (with or without vanadium) (see Chapter 1), and chemical and physical conditions that allow the formation of beryl as a stable mineral.

Beryl, $(\square, \text{Na}, \text{Cs}, \text{H}_2\text{O}, \text{CO}_2)(\text{Be}, \text{Li})_3(\text{Al}, \text{Sc}, \text{Fe}^{3+}, \text{Cr}, \text{Fe}^{2+}, \text{Mg})_2[\text{Si}_6\text{O}_{18}]$, has a wide stability field. Published studies on Be mineral stabilities focused on the $\text{BeO}-\text{Al}_2\text{O}_3-\text{SiO}_2-\text{H}_2\text{O}$ (BASH) system, and coexisting melts and aqueous fluids (e.g., Barton, 1986; Barton & Young, 2002). BASH phase equilibria provide some temperature constraints, but the assemblages are not distinctly pressure sensitive (Fig. 62). Hydrous beryllium minerals (e.g., behoite $(\text{Be}(\text{OH})_2)$, bertrandite $(\text{Be}_4\text{Si}_2\text{O}_7(\text{OH})_2)$ and euclase $(\text{BeAlSiO}_4(\text{OH}))$, but excepting beryl) are stable only at temperatures below 500°C. Bertrandite persists only up to about 300°C. The lower limit of beryl stability in the presence of water is between 200 and 350°C, depending on coexisting minerals and pressure (Fig. 62, inset). In quartz-bearing assemblages, chrysoberyl is restricted to (near-)magmatic temperatures, al-

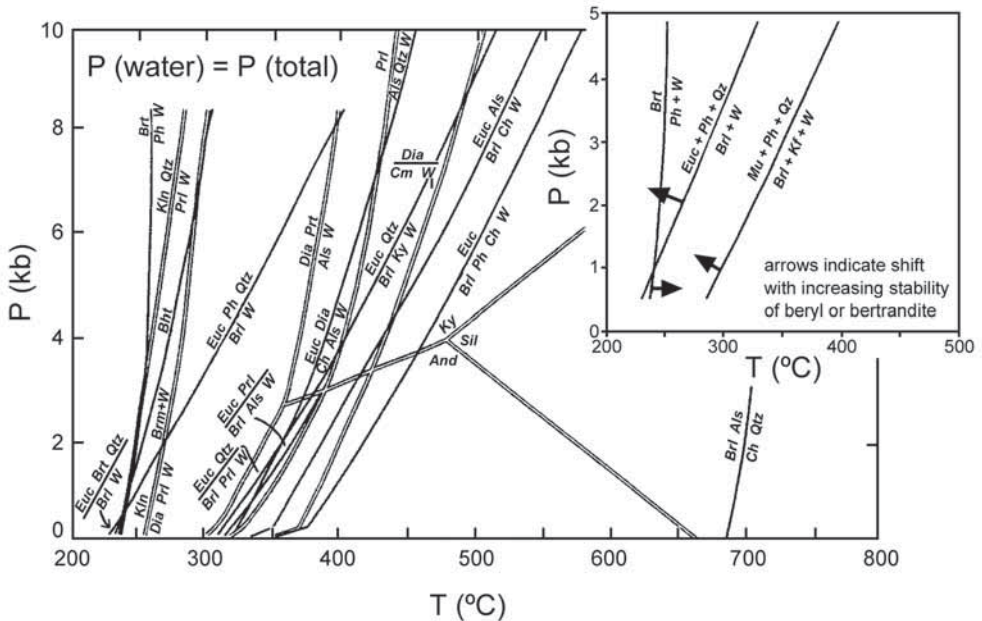


Fig. 62. Pressure-temperature projection of phase relationships in the $\text{BeO}-\text{Al}_2\text{O}_3-\text{SiO}_2-\text{H}_2\text{O}$ (BASH) system, from Barton & Young (2002, fig.10). Inset: limiting reactions for both bertrandite and beryl can depend on solid solution effects, F for OH in bertrandite, and multiple components in beryl. Abbreviations (consistent with Kretz, 1983): Als = aluminium silicate, And = andalusite, Bht = behoite, Brt = bertrandite, Brl = beryl, Brm = bromellite, Ch = chrysoberyl, Dia = diaspore, Euc = euclase, Kln = kaolinite, Ky = kyanite, Ph = phenakite, Prl = pyrophyllite, Qtz = quartz, Sil = sillimanite, W = water. Note that phases observed at Sandawana are beryl, phenakite, quartz and water.

though the position of the reaction chrysoberyl + quartz = beryl + aluminium silicate is sensitive to beryl composition and its position remains controversial (Barton & Young, 2002). Natural beryl contains up to several weight percent water occurring in the channels in the structure. The effect of channel water on the stability of beryl is pronounced; decreasing water pressure reduces the stability of beryl + aluminium silicate by several hundred degrees at moderate pressures (Fig. 63; Barton, 1986). The effect of other channel constituents such as CO_2 and alkalis has not been investigated, but is expected to be similar by analogy with cordierite (e.g., Carrington & Harley, 1996).

4.1.2. Activity relationships (mainly after Barton & Young, 2002)

Temperature-activity – Beside P-T projections, activity diagrams are useful in understanding the occurrence of beryl and other Be-minerals. The most useful independent variables are temperature and the activities of the major components, notably alumina and silica. Silica and alumina are crucial because they frame the thermodynamic conditions defined by many rock-forming minerals and, in addition, can be related to alkalinity of melts and fluids through reactions (1) and (2):

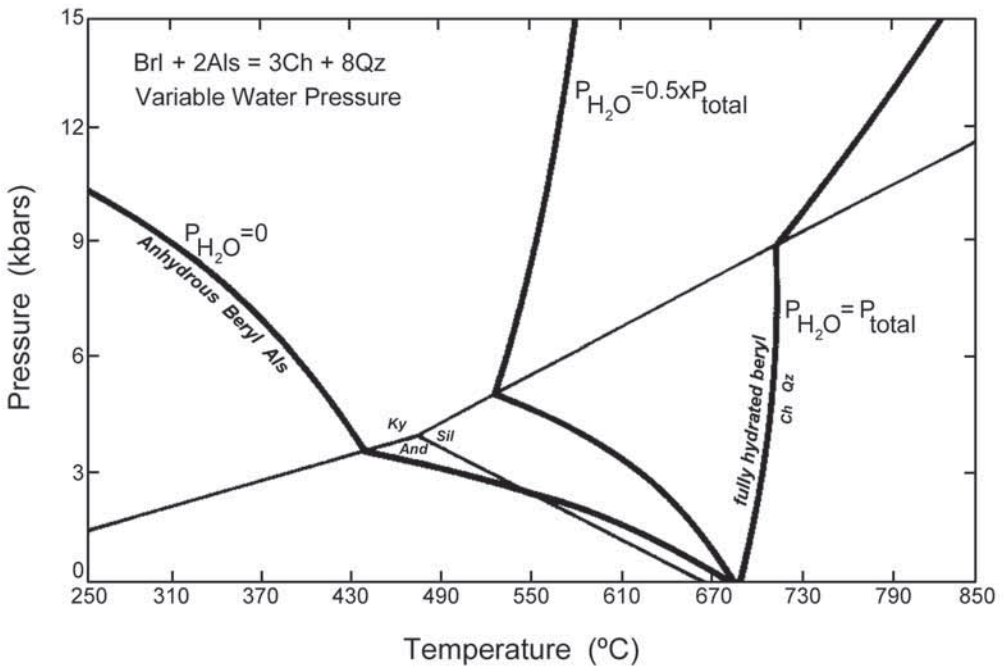
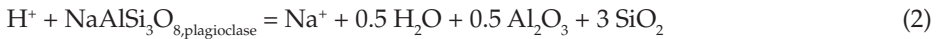
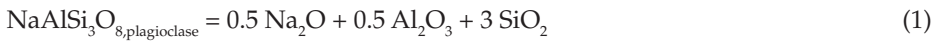


Fig. 63. The high-temperature stability limits of beryl + aluminium silicate are greatly reduced with decreasing water pressure, in favour of chrysoberyl + quartz. From Barton (1986, fig. 9). For abbreviations, see Figure 62.

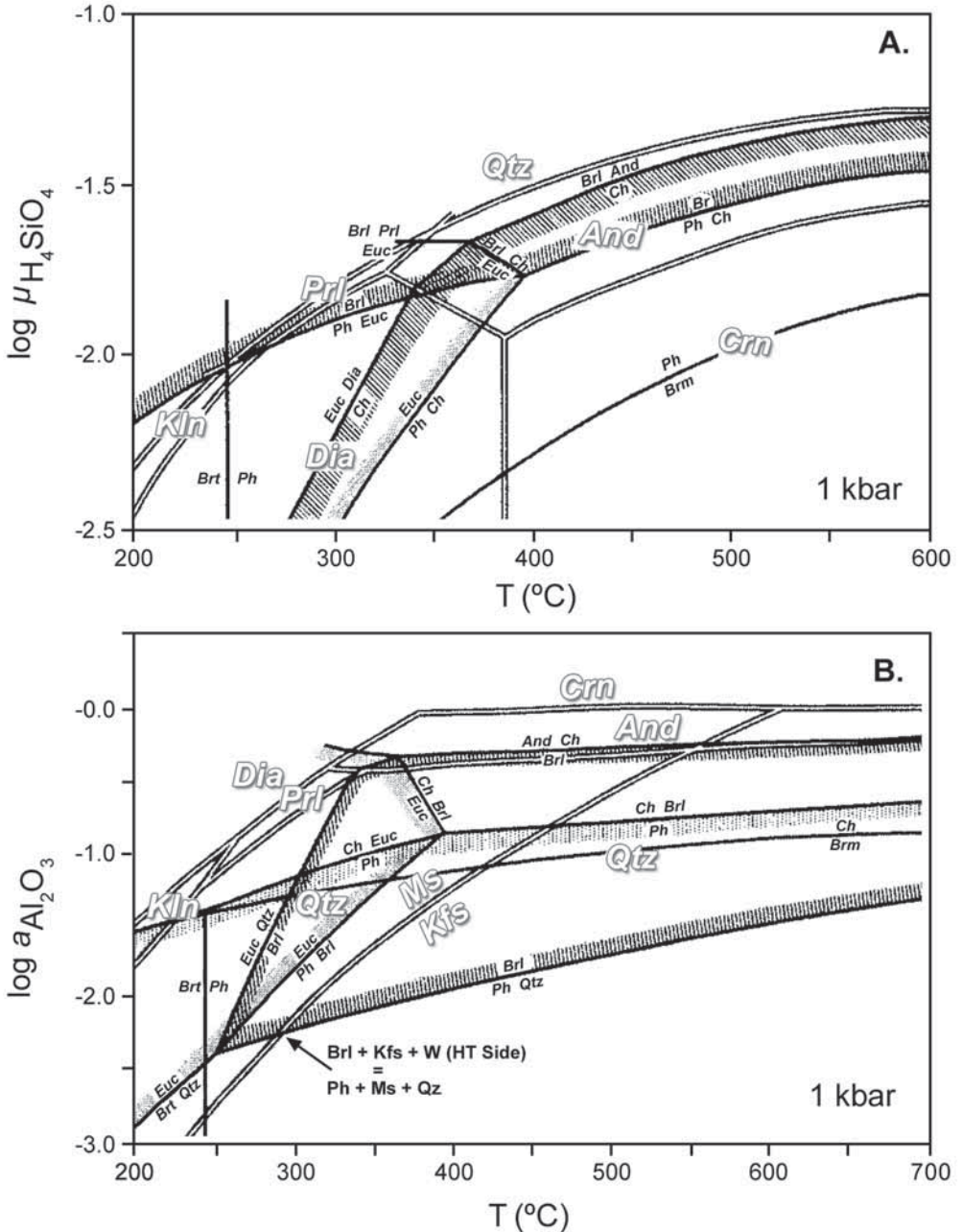


Fig. 64. (A) Beryllium mineral stability as a function of temperature and concentration of aqueous silica at 1000 bars. Shading outlines the upper a_{SiO_2} limit of chrysoberyl, the lower a_{SiO_2} limit of beryl and the upper thermal stability of euclase. (B) Beryllium mineral stability as a function of temperature and the activity of alumina at 1000 bars. Shading outlines stability limits of beryl, the upper $a_{Al_2O_3}$ limit for phenakite/bertrandite and the upper thermal stability of euclase. Note the arrow and label for the lower limit of stability for beryl in the presence of K-feldspar. Mineral abbreviations from Figure 62, with, in addition: Crn = corundum; Kfs = K-feldspar; Ms = muscovite. After Barton & Young (2002, fig. 11) and Barton (1986, fig. 11, 12).

Reaction (1) shows that alkalinity and alumina activity inversely correlate in feldspar-bearing rocks. Reaction (2) relates fluid acidity to alkalinity in the presence of plagioclase when $a_{\text{Al}_2\text{O}_3}$ and a_{SiO_2} are defined.

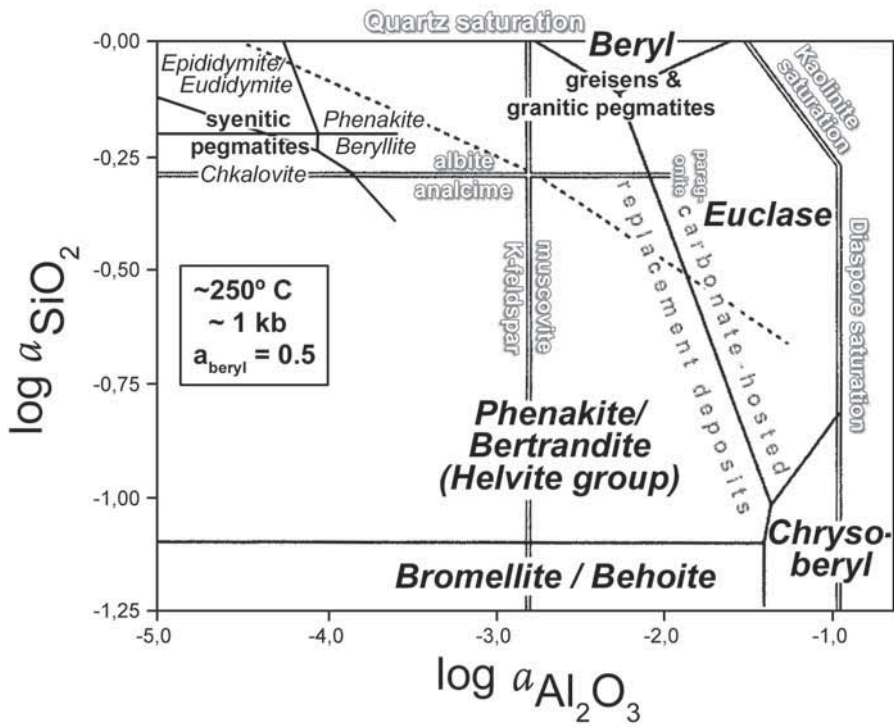
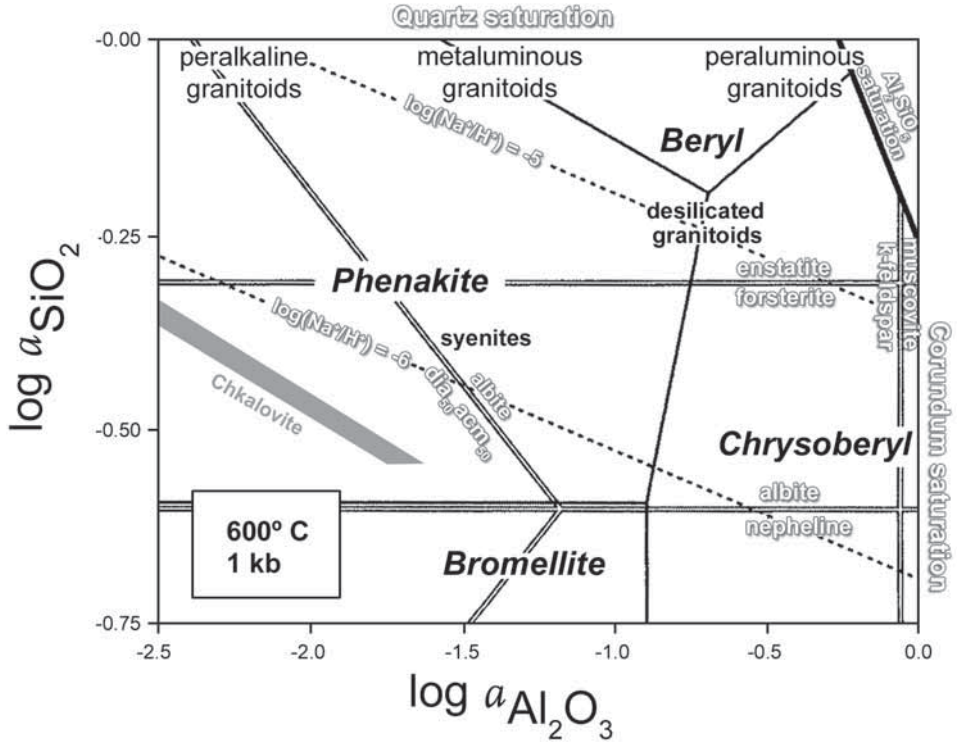
Figure 64 plots BASH mineral assemblages in terms of each a_{SiO_2} and $a_{\text{Al}_2\text{O}_3}$ as functions of temperature. At high temperature, beryl, phenakite and chrysoberyl ($T > 600^\circ\text{C}$) are stable at high silica activities (Fig. 64a). With decreasing silica activity beryl is replaced by chrysoberyl+phenakite and phenakite is ultimately replaced by bromellite. A similar progression occurs at lower temperatures except that chrysoberyl is strongly quartz undersaturated, and first euclase and then bertrandite become key phases.

The variable $a_{\text{Al}_2\text{O}_3}$ highlights differences between Al-rich and Al-poor assemblages (Fig. 64b). The saturation surface for the Al-only phases, corundum ($T > 360^\circ\text{C}$) and diaspore ($T < 360^\circ\text{C}$), neither of which is stable with quartz, bounds the top of the diagram. Quartz coexists with andalusite at high temperature, but then pyrophyllite followed by kaolinite form with decreasing temperature. Chrysoberyl and euclase are the characteristic minerals at high $a_{\text{Al}_2\text{O}_3}$, whereas beryl occupies an intermediate field (Fig. 64b). In contrast, phenakite and bertrandite are stable only at distinctly lower $a_{\text{Al}_2\text{O}_3}$ conditions until bertrandite and kaolinite become stable together at about 225°C . A key boundary is that between K-feldspar and muscovite which separates strongly peraluminous assemblages from others. On cooling in the presence of muscovite and K-feldspar, only below $T \approx 300^\circ\text{C}$ does beryl give way to phenakite + quartz (arrow in Fig. 64b). Solid solution will expand the beryl field to even lower temperatures (Fig. 62, inset). It shows why in most quartz-bearing rocks, beryl is the dominant Be-bearing silicate down to relatively low temperatures.

Activity-activity – Using the variables from Figure 64 in a $a_{\text{Al}_2\text{O}_3}$ versus a_{SiO_2} plot (Fig. 65) provides an overview of Be mineral assemblages in relation to major rock types that are separated by reactions among rock-forming minerals. Quartz-saturated rocks lie along the top of the diagrams, passing downward into undersaturated rocks, which are split by key reactions, such as forsterite + quartz = enstatite ($\text{Mg}_2\text{SiO}_4 + \text{SiO}_2 = \text{Mg}_2\text{Si}_2\text{O}_6$). Saturation with muscovite and andalusite occurs along the right boundary, defining strongly peraluminous rocks. Peralkaline rocks are located near the acmite-bearing reaction that passes diagonally across the left half of the diagram.

From the stability boundaries at 600°C (Fig. 65a), it is clear why beryl is typical of strongly peraluminous granitoids and rocks. Chrysoberyl has a large stability field, but only for unusual rocks that must be Al-rich and Si-poor (e.g., desilicated pegmatites). With decreasing temperature (Fig. 65b), the fields for euclase and, especially, the Al-free Be silicates expand at the expense of the beryl and chrysoberyl fields. The large phenakite/bertrandite field is consistent with widespread occurrence of these minerals in low-temperature deposits, particularly carbonate replacements.

Activity relationships in terms of other components, such as CaO, MgO and SiO_2 , can be used to visualize beryllium mineral parageneses in the Ca-Mg silicate assemblages of ultramafic and carbonate hosted deposits. For example, Figure 66 illustrates possible phase relationships and zoning paths in desilicated pegmatites or quartz-feldspar veins at 500°C and 3 kbar. As indicated by the arrows in Figure 66, starting with a granitic/vein assemblage on the high-silica side, rock composition can go into the actinolite field and, for instance, show zoning from beryl to chrysoberyl to phenakite or



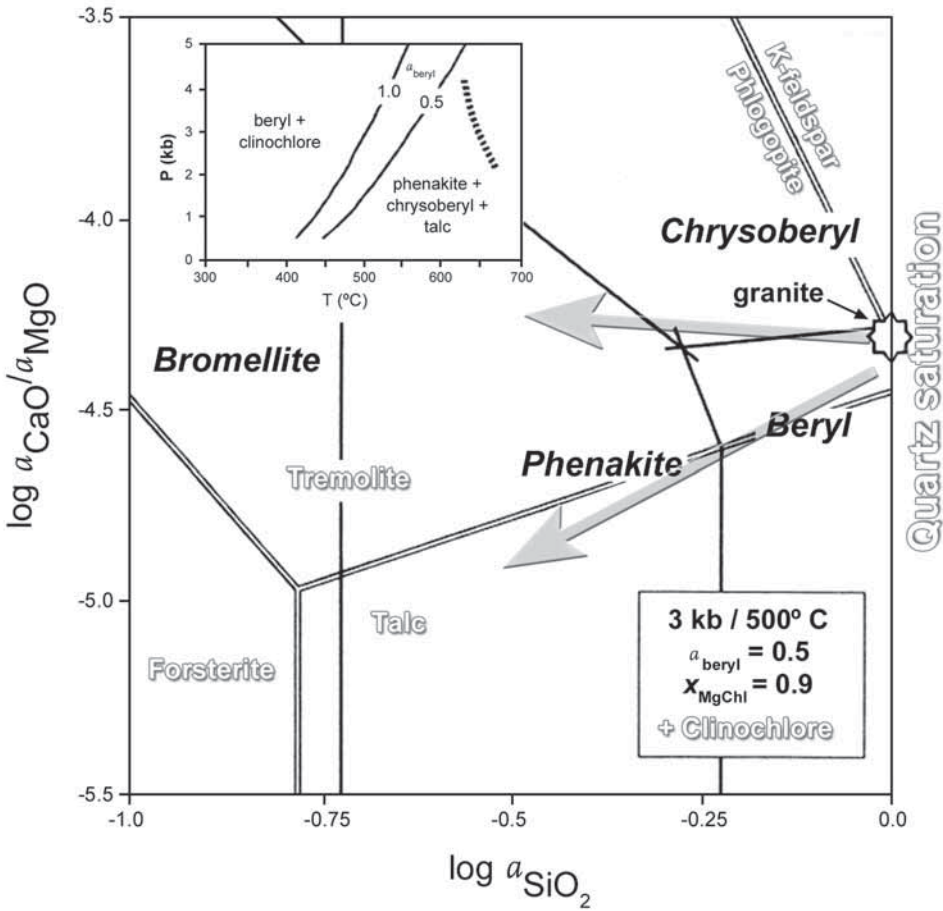


Fig. 66. Topology for phase relationships of Be minerals in ultramafic-hosted deposits at 500°C and 3 kbar. The arrows represent two alternative ranges of metasomatic zoning (see text). Chlorite is present throughout, and activities of beryl and clinocllore are reduced. The inset shows a schematic water-saturated granite solidus and the calculated position of the dehydration reaction beryl+chlorite = phenakite +chrysoberyl+talc (see text for explanation). From Barton & Young (2002, fig. 14).

◀ Fig. 65. Beryllium mineral stabilities as a function of silica and alumina activities. The diagrams illustrate the important control that these rock-defined variables have on mineral assemblages in Be-bearing pegmatitic/hydrothermal systems. (A) Phase relationships of Be minerals as a function of $a_{Al_2O_3}$ and a_{SiO_2} at 600°C and 1 kbar related to mineralogy in felsic rocks. (B). Phase relationships of Be minerals as a function of $a_{Al_2O_3}$ and a_{SiO_2} at 250°C and 1 kbar related to mineralogy in felsic rocks and some major groups of Be deposits. From Barton & Young (2002, fig. 12).

downward into phenakite and ultimately bromellite. Under these particular conditions, beryl is near its stability limit (Fig. 66, inset) and small differences in solid solution can have significant differences in the position of phase boundaries and, thus, paths. The inset of Figure 66 shows the calculated position of the dehydration reaction for beryl + chlorite = phenakite + chrysoberyl + talc, demonstrating that on the activity diagram the field of beryl will expand significantly at lower temperatures. It explains the scarcity of phenakite and chrysoberyl in ultramafic-hosted occurrences.

In terms of acidity versus alkalinity, beryl is replaced by phenakite with increasing HF as well as increasing alkalinity (e.g., K^+/H^+ ; Fig. 67). Burt (1975) used natural assemblages to derive topologies for activity diagrams involving P_2O_5 , CaO and F_2O_{-1} . In the system CaO-BeO-SiO₂-Al₂O₃-P₂O₅-F₂O₋₁-H₂O, the stability of beryl appears to be influenced by increasing ${}^{\mu}F_2O_{-1}$ and ${}^{\mu}P_2O_5$. At an unspecified pressure and temperature, Burt (1975) showed that when fluorite is stable, beryl will no longer be stable with increasing ${}^{\mu}F_2O_{-1}$, while in the fluorapatite stability field the assemblage beryl + fluorapatite will be broken down with increasing ${}^{\mu}F_2O_{-1}$ and ${}^{\mu}P_2O_5$.

4.1.3. *Concluding remarks* – The stability field of beryl needs to be determined in more detail. The high-temperature stability and melting relationships remain unclear. This is partly because beryl may incorporate up to 3 wt.% H₂O into the channels of its

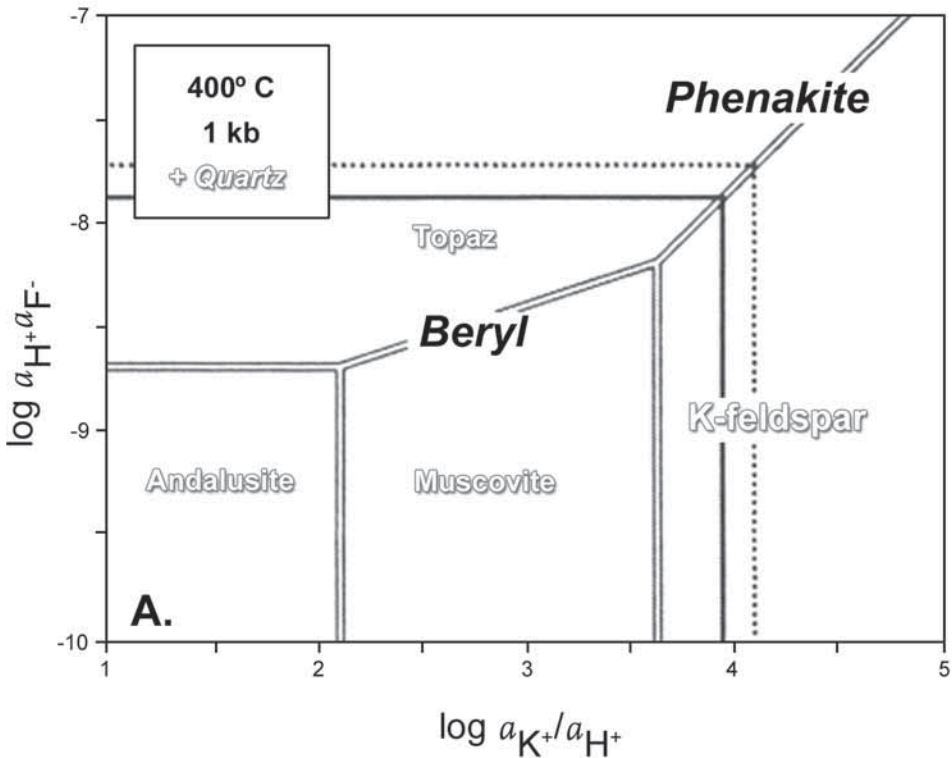


Fig. 67. Calculated Be mineral stability as a function of HF and K/H at 400°C and 1000 bars. From Barton & Young (2002, fig. 13).

structure and this water has a significant effect on its stability (Fig. 63). The effect of other channel constituents such as CO_2 and alkalis, most importantly Na, may be similar. Although the thermodynamic data of beryl are known, the lack of experimental investigations for systems more complex than the $\text{BeO-Al}_2\text{O}_3\text{-SiO}_2\text{-H}_2\text{O}$ system can be an obstacle for the explanation of natural occurrences (such as beryllium minerals in metamorphic rocks, e.g., Franz & Morteani, 2002).

Apart from the pressure-temperature-activity relationships, knowledge of the behaviour of beryllium (and chromium) in fluids is also important in understanding the formation of emerald. This behaviour is discussed below, describing the various processes that played a key role in the formation of Sandawana emerald.

4.2. Intrusion of rare-element granitic pegmatite

4.2.1. Characterisation of LCT rare element pegmatite – The intruded pegmatites at Sandawana did not retain their primary composition during hydrothermal reworking (Section 4.3). However, the presence of beryl, lepidolite and microcline in a less albitised section of pegmatite (see Section 2.3.3) and elevated concentrations of elements present in the ore-zones (Section 2.3.4; Table 13) indicate that these pegmatites were strongly fractionated. It further demonstrates that the melts and fluids involved contained high concentrations of K, Rb, Li, Be, F, P, Cs, Nb and Ta.

The pegmatites are related to the Bikita pegmatite (Chapter 2), which is known as one of the largest, highly differentiated pegmatites in the world (Norton, 1983). Cerny *et al.* (1985) and Cerny (1991) classified such pegmatites as extremely fractionated, rare-element, granitic pegmatites, belonging to the LCT (lithium, caesium, tantalum) association, as opposed to the NYF (niobium, yttrium, fluorine) association. Rare-element pegmatites of the LCT association comprise a broadly diversified spectrum of barren pegmatites, beryl \pm columbite-tantalite \pm phosphates bearing dykes, complex Li-rich to pollucite-bearing and other related types. Composition of these pegmatites is generally enriched in Li, Rb, Cs, Be, Sn, Nb \gtrsim Ta, B, P and F, whereas Ti, Zr, Y and REE are generally very low. In comparison, the NYF association is less widespread, shows a restricted variability in mineral paragenesis and contains accessory mineralisation with Nb > Ta, Y, REE, Ti, Zr, Be, U, Th and F; the contents of P, B and rare alkalis are commonly negligible.

The estimated average BeO content of Bikita pegmatites is around 500 ppm. It varies roughly between 100 and 700 ppm (Ackermann *et al.*, 1966; Gallagher, 1975), although it may locally increase to 4400 ppm, in parts where beryl is visible (Gallagher, 1975).

4.2.2. Rare metal behaviour in melt

Lithium and caesium – Pegmatite melts and fluids relatively low in $(\text{PO}_4)^{3-}$, but significantly enriched in F, precipitate most of their Li in the form of lithian muscovite and lepidolite. Besides extreme crystal-melt partition coefficients of some elements (such as Li, Rb, Cs), complexing plays an important role in the accumulation of others (e.g., Nb,

Table 13. Mobilised elements present in the ore-zones at Sandawana, Zimbabwe.

Elements present	Pegmatitic origin	Incorporated from greenstones
Mobilised by fluids	Na, K, Li, Be, F, P, Rb, Cs, Ta, Nb	Mg, Fe, Cr, Ca

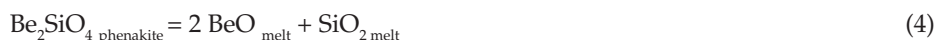
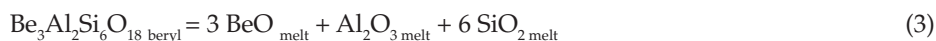
Ta, and probably also Li and Cs; Cerny *et al.*, 1985). Crystal /melt partitioning does not seem to be the only mechanism leading to the accumulation of elements like Li and Cs in late fractions of melt. Based on the general geochemical association, both Li and Cs are designated as 'fluorophile' elements by several authors (e.g., Hildreth, 1981; Cerny *et al.*, 1985), who suggested that complexing of Li and Cs with H₂O or F may assist their extraction from differentiating magmas into residual melts.

Additionally, thermodynamic data and calculations indicate that the stability fields of the lithium micas are governed not only by the activities of Li and F, but also to a considerable extent by the relation between the silica activity and the pH (Gordiyenko & Ponomareva, 1989). They show that higher alkalinity (pH > 5 at 400°C, 1 kbar) favours crystallisation of lepidolite micas rather than muscovite. Increasing pH (alkalinity), corresponding to an increase in silicic acid activity, expands the stability fields of the lithium micas, displacing them to lower Li and F activities. From experimental studies by Stewart (1978), it appears that melts must contain about ≥ 2 wt.% Li₂O, to attain saturation in lithium aluminosilicates.

Niobium and tantalum – Nb and Ta display a fractionation pattern opposite to that expected from ionic properties (Cerny *et al.*, 1985). The first marked increase of Nb and Ta is noted only in silicic leucogranites and pegmatitic granites, and the enrichment trend is extended into rare-element pegmatites. Enrichment in Nb and Ta is pronounced in F-rich magmas that are typical of pegmatite-generating granites, and also in Cl-dominant rhyolites (Hildreth, 1981). Maximum contents reach 550 ppm Nb and 4500 ppm Ta (Cerny *et al.*, 1985). Compared to a Nb/Ta ratio of ~ 11, in the main course of gabbro-to-granite differentiation, these increased abundances also indicate a dramatic change in the Nb/Ta ratio during the evolution of a pegmatite system. As shown by Wang *et al.* (1982), fluorine-based complexes of Nb and Ta have different thermal stabilities, the Ta-bearing ones being stable to lower temperatures. Thus, Nb becomes available for crystallisation of solid phases in early stages relative to the bulk of Ta, which may lead to extensive ranges of the Nb/Ta ratio even in a single body of pegmatite (Cerny *et al.*, 1985).

4.2.3. Beryllium behaviour in melt/fluid – The geochemical cycle of Be, because of its special ionic properties, is still poorly known (Beus, 1966; Charoy, 1999). The small size of the Be-ion (0.34 Å) results almost invariably in tetrahedral coordination in crystals, and it could be expected to substitute easily for Si, Al and P. However, because of the difference in charge, the strong disturbance of the local electrostatic equilibrium bonds is a major factor against such isomorphous substitution. Therefore, beryllium demonstrates an incompatible behaviour in felsic igneous magmas and their residual liquids, and is concentrated in extremely evolved liquids.

Beryllium solubility in felsic melts, and its partitioning with coexisting minerals and aqueous fluids, has been studied by London *et al.* (1988), Evensen *et al.* (1999) and London & Evensen (2002). The principal controls on Be solubility in felsic magmas are a_{SiO_2} and $a_{\text{Al}_2\text{O}_3}$:



Beryl saturation is determined as an activity product, i.e. (using equation 3):

$$[a_{\text{Be}_3\text{Al}_2\text{Si}_6\text{O}_{18}}]_{\text{beryl}} = [a_{\text{BeO}}]^3 [a_{\text{Al}_2\text{O}_3}]_{\text{melt}} [a_{\text{SiO}_2}]^6 \tag{5}$$

in which the activity of a beryl component in the melt is a function of the activities of its constituent oxides.

Reactions (3) and (4) were investigated by Evensen *et al.* (1999), who showed that, at constant bulk composition, Be mineral solubility is a strong function of temperature, increasing by factors of 2-10 from 650° to 850°C (Fig. 68), and that beryl is the saturating phase in metaluminous and peraluminous melts (compare Fig. 65). The effect of silica

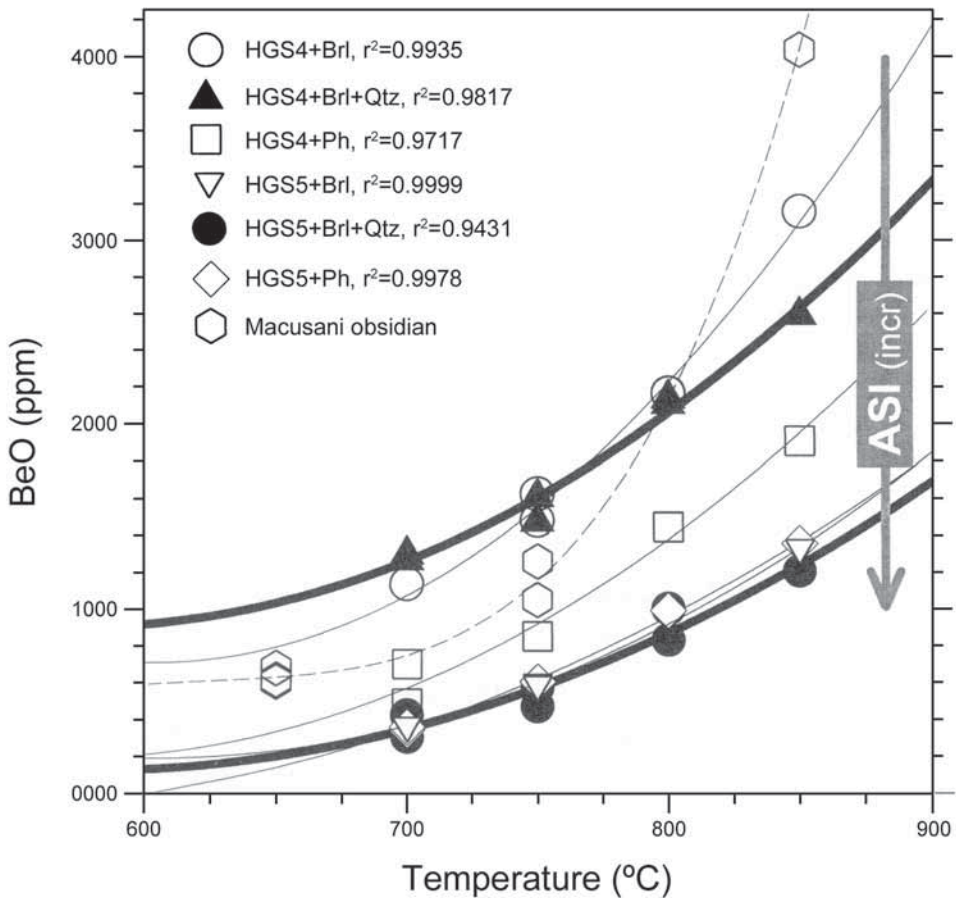


Fig. 68. BeO contents of granitic melts at beryl saturation from 650-850°C and $\text{P}_{\text{H}_2\text{O}} = 2$ kbar, from Evensen *et al.* (1999, fig. 5). The thick curves are for quartz-saturated experiments. The arrow shows the direction of increasing melt ASI from 1.00 in the simple metaluminous (HGS4) to 1.28 in the peraluminous (HGS5) melts. The experimental trend using the Macusani obsidian, with an ASI = 1.27, lies in the opposite direction of the arrow, at higher BeO contents of beryl-saturated melt, for reasons explained in the text.

activity on beryl saturation turned out to be negligible, because the activity of silica did not change appreciably over the range of temperature investigated and, additionally, beryl almost invariably occurs with quartz in natural systems, so the activity of silica in melt or vapour is normally buffered. In contrast to silica, however, the activity of alumina in melt varies considerably. Evensen *et al.* (1999) demonstrated that, in compositionally simple haplogranite (Ab-Or-Qtz) melts, the solubility of beryl decreases with increasing $a_{\text{Al}_2\text{O}_3}$ consistent with equation (3) and (5). The solubility of beryl is lowest in simple quartz-saturated peraluminous melt compositions; for instance, only ~200 ppm BeO (equivalent to ~70 ppm Be) was measured at 700°C (Fig. 68). Complexing of Be by other elements is implied by increased Be solubility in the Li-B-P-F-rich, but strongly peraluminous, Macusani rhyolite. The Aluminium Saturation Index, ASI (= mol Al_2O_3 / $[\text{Na}_2\text{O} + \text{K}_2\text{O} + \text{CaO}]$), of the Macusani glass = 1.27 (including Li, Rb and Cs in the total of alkalis), which is as high as the ASI value of the peraluminous haplogranite HGS5 (Fig. 68). In contrast to the experiments with granite HGS5, the Macusani obsidian yielded the highest BeO contents of any experiments. The disparity between Macusani obsidian and peraluminous haplogranite (HGS5) indicates that speciation reactions among the more numerous components of the Macusani glass and any or all of the beryl-forming components lead to a net reduction of activity for producing beryl. Among these components, F and P are believed to react with Al to form melt species (e.g., Manning *et al.*, 1980; Wolf & London, 1994, 1997). Thus, in reducing the activity of alumina, these components raise the BeO content of melts needed to achieve saturation in beryl (or chrysoberyl). Speciation reactions involving Be, F and P may also play a role (e.g., Wood, 1991; Charoy, 1999).

As the Macusani glass has a similar composition to many evolved Li-rich pegmatites, also these pegmatites will require higher BeO concentrations to achieve beryl saturation. Looking at the P-T crystallisation path of the Bikita pegmatite (Fig. 13), it appears that the primary consolidation of this pegmatite commenced around 650-675°C at comparable pressure with the experiments of Evensen *et al.* (1999). At $T = 650^\circ\text{C}$, the Macusani glass indicates that around 600 ppm BeO is needed for beryl saturation, which is in very good agreement with the estimated average BeO content (500 ppm, Section 4.2.1) of Bikita pegmatite. It is likely that at Sandawana, the primarily consolidated pegmatites contained comparable BeO concentrations (see Chapter 2), which has already been confirmed by Ackermann *et al.* (1966), who estimated BeO = 500 ppm for a Bikita type pegmatite body in the Mweza greenstone belt.

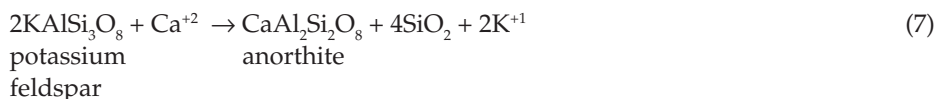
4.2.4. Concluding remarks – Based on a combination of field, fluid inclusion, and experimental data, London (1990) demonstrated that, in general, the primary consolidation of rare-element (Li-Be-Ta) pegmatites occurs in the range of 700° to 450°C at 4 to 2.5 kbar. Some studies indicate very low temperatures of crystallization (e.g., ~400°-450°C: Morgan & London, 1999; Webber *et al.*, 1999). As Cerny *et al.* (1985) stated earlier, it appears that selective extraction and transport in a volatile phase (by diffusion or in an exsolved hydrous fluid), complexing stable to relatively low late- to postmagmatic temperatures and crystallochemical preferences for specific mineral structures, operate in conjunction with crystal/melt fractionation.

The original pegmatite at Sandawana was a potassic, peraluminous, beryllium-rich granitic pegmatite, affiliated with the LCT family. It was formed out of a F and P

containing melt/solution (silica-rich hydrous fluid) with a substantial alumina activity, in which the various elements were easily transported by highly soluble compounds.

4.3. Metasomatic processes

4.3.1. *Albitisation of pegmatite* – The essential mineralogy of emerald occurrences at Sandawana is presented in Table 6. The omnipresence of albite in the pegmatite indicates intensive albitisation. The presence of microcline in a pegmatite section at Aeres, which at places hardly survived albitisation, and the abundant myrmekites, consisting of albite and quartz (see Section 2.3.3), indicate the former presence of K-feldspar in the pegmatite. The old K-feldspar was replaced by albite + quartz, releasing K⁺ in a surrounding fluid phase. This process can be written as follows:



Studying the myrmekites (see, e.g., Fig. 11), it becomes evident that quartz does not comprise more than 5 vol. % of the original K-feldspar grains (visual estimate). The volumes of vermicular quartz are directly proportional to the An content of the albite in the myrmekite. According to a theoretical curve of volume percent of vermicular quartz versus An content of plagioclase (Ashworth, 1972; Phillips & Ransom, 1968), 5 vol. % of quartz would roughly correspond to a maximum An content of 7%.

The pegmatite section at Aeres (Section 2.3.3) not only showed the presence of microcline, but also of quartz and oligoclase (An: 15-20%). The omnipresence of albite in the almost completely altered pegmatite, therefore, also indicates dissolution of quartz and oligoclase.

The significance of myrmekites – The spectacular quartz-feldspar intergrowth seen in many granitic rocks, called ‘myrmekite’ by Michel-Lévy (1874), has been debated over nearly a century. Becke (1908) was the first to suggest that it originates by metasomatic replacement of K-feldspar, but details of this process, as well as alternative mechanisms, were extensively discussed in the literature (e.g., Ashworth, 1972; Castle & Lindsley, 1993; Garcia *et al.*, 1996). Vernon (2004, p. 250) gave the most recent definition of myrmekite, ‘vermicular (worm-like, symplectic) intergrowth of quartz and sodic plagioclase (generally oligoclase) formed by replacement of K-feldspar, typically in deformed granitic rocks’, as well as a detailed description of major occurrences.

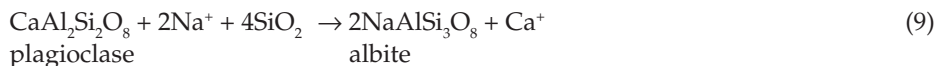
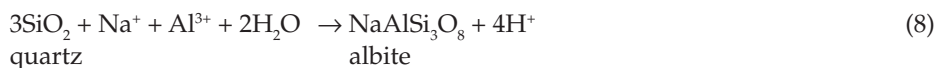
The lack of consensus about the origin of myrmekites is due to the fact that they usually occur scattered in apparently homogeneous rock masses and their volume percentage in a given sample remains very small. It is, thus, difficult to prove whether or not they were formed under open system conditions and to identify the force that drives

myrmekitisation. However, in the pegmatites at Sandawana, myrmekites commonly represent 5 to 30 vol. % of these rocks. In virtually all cases, K-feldspar was completely replaced. As in igneous enclaves of the Velay granite, Massif Central, France, which show abundant (5-20 vol. %) myrmekite-like textures (Garcia *et al.*, 1996), the replacement of K-feldspar is so intense that the process cannot be isochemical and fluid-rock exchange (K, Na) must be considered (see also Vernon, 2004).

A general relationship between deformation and myrmekite appears to be well established; it has been noticed that myrmekitisation preferentially develops in mylonitic zones. Simpson & Wintsch (1989) stated that the replacement of K-feldspar by plagioclase and quartz results in a volume decrease (7% in the case of pure albite; also compare with, e.g., Hippertt & Valarelli, 1998), and is favoured on high normal stress sites around the grains. They suggested that the ambient temperature, pressure and chemical activities were such that the replacement reaction was favoured, but the addition of extra strain energy along the high-pressure sides of the grains localized the reaction at these sites. On the contrary, Vernon (1991, 2004) argued that strain energy may not directly cause the formation of myrmekite, but probably contributes indirectly by facilitating access of fluids to growth sites, thereby altering the local chemical environment and so promoting development of myrmekite.

At Sandawana, the abundant presence of myrmekites and complete replacement of K-feldspar show that fluid flow must have been an important driving force. It indicates that albitisation of pegmatite was probably caused by a Na-rich fluid during shearing and folding. This timing is confirmed by the syntectonic growth of phlogopite in the wall-rock, during K-Na metasomatism (see Section 4.3.2).

Sodium-rich 'solution-melt' – Apart from the replacement of K-feldspar, a Na-rich fluid could also account for the mentioned dissolution of quartz and oligoclase. Possible reactions that could have been involved are:



Witt (1987) favoured Al transport as (alkali-)alumino-fluoride (e.g., NaAlF) complexes in high temperature Na- and F-rich fluids associated with feldspathic alteration. Also, NaF and AlPO_4 complexes have probably been involved (Mysen *et al.*, 2004; Wolf & London, 1994; Section 4.3.2).

The Na-rich fluid could be interpreted as a late stage 'solution-melt'¹ of pegmatitic origin, because as melt concentrations of B, F and P increase during the fractionation process, the liquidus fields of quartz and K-silicates (feldspar and mica) will be expanded

¹ 'Solution-melt' is a dense fluid with composition between a simple hydrothermal solution and silicate melt. This term was at first used by Soviet petrologists (e.g., Zakharchenko, 1976) and later taken over by London (1987).

(London, 1987, 1990). As a result, the residual melt eventually evolves toward silica-depleted, alkaline, Na-rich compositions in which H₂O, other fluxes and lithophile trace elements are highly concentrated. If this were a probable case, it would mean that intrusion of the pegmatites and subsequent albitisation during deformation are part of a continuous process and, thus, occurred almost contemporaneous. The few available case histories of cooling rates in complex pegmatite dykes (Chakoumakos & Lumpkin, 1990; Webber *et al.*, 1999; Morgan & London, 1999) are not in contradiction with this concept, because they indicate that these magmas would have cooled below their solidi quickly (in days to months), which means that primary consolidation of the rare element pegmatite could have taken place in a rather short time. Thus, albitisation of this pegmatite may as well have occurred shortly after its intrusion and may be seen as a late effect of pegmatite intrusion (auto-metasomatism). Emplacement of the pegmatite just before and/or during deformation is consistent with the field data presented in Chapter 2 and is also in agreement with Cerny (1991), who observed that there is some tendency toward syn- to late-orogenic origin of rare-element granitic pegmatites, belonging to the LCT (lithium, cesium, tantalum) association (see Section 4.2).

4.3.2. Wall-rock alterations

Mineral compositions – As described in Chapter 2, a narrow zone (up to 30 cm) in the greenstone next to the intruded pegmatite has been affected by the intrusion and subsequent metasomatic processes, at places where pegmatites show signs of intense folding and shearing. The mobilised elements that are present in the ore-zones are shown in Table 13. Average compositions of the minerals involved in the ore-zones are summarised in Table 14.

The growth of phlogopite at the contact of pegmatite and greenstone indicates a substantial enrichment of K and Rb (0.5 wt.%) in the Mg- and Cr-rich schist adjacent to the pegmatite, and was obviously related to the albitisation of the pegmatite and the consequent release of K. The abundant occurrence of fluorapatite and the substantial F content in phlogopite indicate the invasion of a relatively F- and P-rich fluid in the ore zones. Also, the amphiboles (especially actinolite) have taken up some F. The presence of emerald and phenakite correlates to gains of Be and Cs (to 0.1 wt.% in emerald), while holmquistite indicates enrichment in Li. Additionally, PIXE/PIGE analyses (Calligaro *et al.*, 2000; Table 9) also showed a very high Li content in emerald, between 490 and 1110 ppm. The low totals of phlogopite and the seemingly low occupation of the A-site suggest that Li might also be present in phlogopite. Increase of Nb and Ta is indicated by the presence of chromian ilmenorutile. Na was preferentially taken up by emerald and is present to a lesser extent in actinolite, followed by cummingtonite, phlogopite and holmquistite. As the mentioned elements K, Rb, F, P, Be, Cs, Li, Nb and Ta are all typical pegmatite elements, the nearby pegmatites most likely have been major fluid sources.

Additionally, from greenstones, Mg and Fe were incorporated in phlogopite, holmquistite and emerald; Fe went into chromian ilmenorutile as well. Ca was mainly incorporated in fluorapatite, while most chromium was incorporated into emerald (up to 2.12 wt.%), phlogopite (up to 1.25 wt.%) and chromian ilmenorutile. Also, amphiboles contain chromium; one core of actinolite shows 0.96 wt.% Cr, and one holmquistite at

Table 14. Average compositions of minerals present in the emerald-bearing zones. Minor minerals such as chlorite, chromite, phenakite, and manganese- and iron-bearing dolomite are not listed here. For details and representative analyses, including cation distributions, see appendix.

Emerald ¹		Phlogopite ³		Amphiboles				
Oxide	wt.%	Oxide	wt.%	Oxide	wt.%	Actinolite ⁴	Cummingtonite ⁵	Holmquistite ⁶
SiO ₂	62.76	SiO ₂	41.39	SiO ₂	55.10		56.17	61.31
TiO ₂	0.04	TiO ₂	0.45	TiO ₂	0.05		0.02	0.02
Al ₂ O ₃	13.27	Al ₂ O ₃	13.08	Al ₂ O ₃	2.53		0.55	11.17
Sc ₂ O ₃	0.01	V ₂ O ₃	0.06	Cr ₂ O ₃	0.15		0.06	0.15
V ₂ O ₃	0.06	Cr ₂ O ₃	0.50	FeO	8.22		17.64	9.32
Cr ₂ O ₃	1.07	FeO	10.14	MnO	0.75		2.44	0.15
BeO	13.00	MnO	0.11	MgO	19.10		19.55	11.26
FeO	0.68	MgO	19.59	Li ₂ O				3.50
MnO	0.01	ZnO	0.05	CaO	10.72		0.92	0.04
MgO	2.57	Na ₂ O	0.49	Na ₂ O	1.13		0.49	0.20
CaO	0.02	K ₂ O	6.82	K ₂ O	0.04		0.00	0.00
Na ₂ O	2.28	Rb ₂ O	0.46	F	0.32		0.13	0.08
K ₂ O	0.04	BaO	0.01	Cl	0.00		0.00	0.00
Rb ₂ O	0.04	F	0.77	O_F_Cl	0.14		0.06	0.03
Cs ₂ O	0.07	Cl	0.02					
Cl	0.01	O_F_Cl	0.33					
F	0.03							
Total	95.90	Total	93.62	Total	97.98		97.92	97.16
		H ₂ O_calc	3.74	H ₂ O_calc	1.99		2.04	2.24

Emerald ²		Fluorapatite ⁷		Chromian Ilmenorutile ⁸ Albite ⁹			
Trace elements (ppm)		Oxide	wt.%	Oxide	wt.%	Oxide	wt.%
Li	807	P ₂ O ₅	42.86	TiO ₂	69.8	SiO ₂	68.51
F	33	SiO ₂	0.05	SiO ₂	0.08	Al ₂ O ₃	19.69
Ti	123	FeO	0.07	SnO ₂	0.39	FeO	0.01
V	208	MnO	0.05	Nb ₂ O ₅	9.47	CaO	0.14
Cr	5198	CaO	55.49	Ta ₂ O ₅	8.89	SrO	0.02
Mn	173	SrO	0.08	Al ₂ O ₃	0.05	Na ₂ O	11.92
Fe	6254	F	3.07	Cr ₂ O ₃	6.90	K ₂ O	0.02
Ni	20	Cl	0.02	FeO	1.98		
Cu	1	O_F_Cl	1.30	CaO	0.02		
Zn	66	Total	100.39	Total*	97.55	Total	100.31
Ga	30						
Rb	342						
Cs	711						

¹ EPMA average of 36 analyses on 5 crystals; ² PIXE/PIGE average of 23 analyses (12 stones); ³ EPMA average of 11 analyses on 5 crystals; ⁴ EPMA average of 24 analyses on 9 crystals; ⁵ EPMA average of 14 analyses on 6 crystals; ⁶ EPMA average of 24 analyses on 9 crystals; ⁷ EPMA average of 6 analyses on 2 crystals; ⁸ EPMA average of 6 analyses on 1 crystal; ⁹ EPMA average of 10 analyses on 10 crystals.

* low totals are due to conductivity which was not optimal.

the contact between greenstone and pegmatite shows up to 0.58 wt.% Cr. Cummingtonite invariably has low Cr contents.

Emeralds from Sandawana show not only the highest Li content, compared to emeralds from other sources, but also have high sodium, magnesium and chromium contents (Chapter 3; Zwaan *et al.*, 1997).

Crystallisation order – Based on textures (Chapter 2), and inclusions encountered in emerald (Chapter 3), a relative crystallisation order of minerals associated with the emerald-bearing zones is presented in Figure 69. It emphasizes that the syntectonic formation of emerald basically occurred during albitisation of pegmatite and is closely linked to K-Na metasomatism between pegmatite and wall-rock.

Phenakite. In the wall-rock, the early formation of phenakite, which was only occasionally encountered within emerald, can be explained by higher temperatures at the beginning of metasomatism. In ultramafic host rocks, phenakite is stable at high temperatures (Fig. 66, inset). When temperatures decreased, emerald may have precipitated instead (see Section 4.4 for temperature calculations).

During the initial fluid-wall rock interaction, the release of high amounts of K^+ could also have resulted in stable conditions for phenakite instead of beryl, as might be expected from phase relations presented in Figure 67. Subsequently, the formation of phlogopite apparently equilibrated the a_{K^+}/a_{H^+} ratio in the fluid to a level at which emerald became the favourite beryllium phase that was allowed to form in the ore-bearing zones and not phenakite.

Fluorapatite and phlogopite. Although fluorapatite generally appears to have grown later than albite and phlogopite, inclusions of fluorapatite were encountered in emeralds that grew at an early stage. This confirms that fluorapatite and emerald were formed in the same time frame, and probably at the same time as, or not much later than, phlogopite.

Experimental studies of apatite dissolution and solubility in the peraluminous haplogranite system at 750°C and 2 kbar (Wolf & London, 1994) indicated that apatite solubility increases linearly with ASI to $P_2O_5 \sim 0.63$ wt.% in melt at $ASI = 1.3$ (strongly peraluminous composition, comparable to the compositions of evolved Li pegmatites, see Section 4.2.3 and Fig. 68). Their studies also indicated that, within an apatite dissolution aureole, P diffusion through the melt is accompanied by diffusion of Al towards the apatite, resulting in an increase of up to 2 wt.% Al_2O_3 in melt near the apatite. The gradient in Al_2O_3 is probably the result of increasing local Al solubility with apatite dissolution. Within the aureole, the melt contains one additional Al cation for every P cation, which is suggestive of an associated $AlPO_4$ complex. It is clear that the effects of P on Al and Al on P are interrelated.

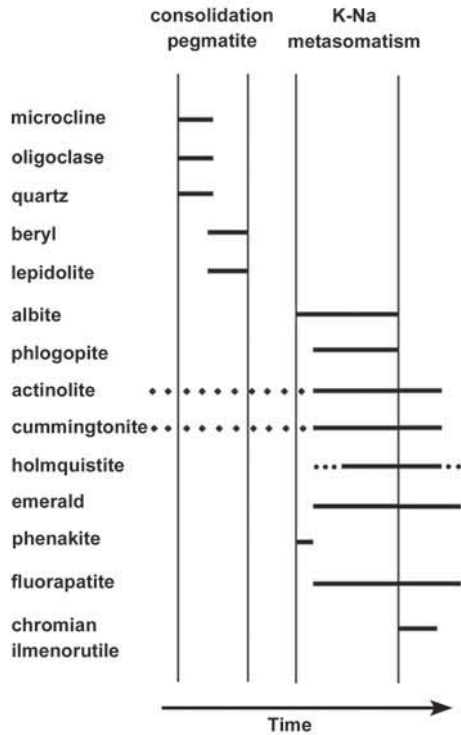


Fig. 69. Crystallisation order of minerals present in the ore zones at Sandawana, based on textural evidence and inclusions found in emerald. Emerald formation is closely linked to K-Na metasomatism.

Thus, at Sandawana, when a solution rich in P, F and K entered the metasomatic zone next to the pegmatite and during cooling, Al and K were consumed by the formation of phlogopite, and the aluminium content of the fluid was decreased, which meant less opportunity to form AlPO_4 complexes. Most likely, this factor, combined with increased $a_{\text{Ca}^{2+}}$ due to interaction of fluid and wall-rock, promoted the crystallisation of fluorapatite.

Emerald. As a result of phlogopite and fluorapatite crystallisation, the removal of P, F and Al from the fluid could also have had an effect on the solubility of emerald. Apart from cooling, the absence of P and F in an evolved melt strongly decreases the solubility of beryl at lower temperatures (see Section 4.2.3, Fig. 68). However, this effect could have been neutralised to some extent by decrease of Al, which would have promoted emerald solubility.

Data on beryllium concentrations in aqueous solutions are scarce, but F is implicated to be the complexing agent. Beus *et al.* (1963) found significant Be concentrations in F-bearing solutions that had reacted with beryl, alkali feldspar and quartz at 490-540°C. This is consistent with evidence from experiments on fluids equilibrated with Macusani rhyolite at 650°C and 2 kbar (London *et al.*, 1988; compare Fig. 68). Macusani rhyolite melt, containing 39 ppm Be and 1.3 wt.% F, furnishes only 6 ppm Be and 0.35 wt.% F to coexisting aqueous fluid (London *et al.*, 1988). Given these results and the fact that beryl solubility in Macusani melts is near 500 ppm Be (Evensen *et al.*, 1999), a plausible maximum Be concentration in a magmatically-derived aqueous fluid would be in the order of 100 ppm. One can speculate that, to a certain extent, this situation may be applicable to Sandawana, because of the similar chemistry of Bikita pegmatite and the Macusani rhyolite (Section 4.2.3), and the late stage pegmatitic/hydrothermal solutions (Section 4.3.1) involved in metasomatic reactions. In conclusion, the presence of sufficient beryllium in the invading solution-melt, in combination with decreasing temperature, decreasing F (and P) content and increasing water content, contributed to the formation of emerald in the chromium-bearing host rock. Thus, it appears that the formation of phlogopite and apatite catalysed emerald crystallisation, which is supported by the observation that emerald is only found near the contact with pegmatite, at places where phlogopite has been formed.

Chromian ilmenorutile. Decreasing acidity of the fluid would also be consistent with the simultaneous crystallisation of chromian ilmenorutile. Rutile is not very soluble at low temperatures (300-400°C) in fluids of near-neutral pH. However, it is most soluble in aqueous solutions with high fluoride and low pH, due to formation of complexes such as $\text{Ti}(\text{OH})_4\text{F}_2^{-2}$ and $\text{Ti}(\text{OH})_2\text{F}_4^{-2}$ (Barsukova *et al.*, 1979). The ionic character of F makes it a good complexing anion for Ti. Solubility also increases with increasing temperature at low pressure (Ayers & Watson, 1991, 1993), forming $\text{Ti}(\text{OH})_4$ by hydrolysis. Thus, a decrease in a_{F^-} , increase of pH, or drop in temperature might cause supersaturation of the fluid and subsequent precipitation of ilmenorutile. The metasomatic character of its crystallisation in the emerald-bearing zones is emphasised by the presence of Nb and Ta, and the concentration of large amounts of Cr and (less) Fe (Table 8, Chapter 3).

Mineral reaction and mass balance – As the formation of emerald and other minerals in the altered zones is clearly related to the alteration of the pegmatite and the resulting K-Na metasomatism, an attempt to calculate a mass balance, involving the phases that

were consumed and produced, and a Na-rich solution, may provide a better insight in what might have happened in terms of mineral reactions.

Criteria based on field observations. The calculations have to be in line with the observations and, therefore, have to fulfil the following basic conditions:

1. microcline, oligoclase (An: ~ 20) and quartz, present in the pegmatite, were consumed and replaced by albite;
2. chlorite is abundantly present in the greenstones, but virtually absent in the alteration zones next to pegmatite, therefore nearly all chlorite must have been consumed;
3. in the alteration zones, phlogopite, actinolite, cummingtonite, holmquistite, fluorapatite and emerald have been produced;
4. in terms of modal abundance, it is estimated that albite > phlogopite > holmquistite > fluorapatite > emerald; albite/phlogopite volume ratio is estimated to be around 2:1; fluorapatite/emerald volume ratio appears to vary and is roughly estimated in the order of 1:1 to around 3:1. Actinolite has been found as idiomorphic and long prismatic laths associated with, and also growing over, phlogopite. These can be interpreted as recrystallised grains or (partly) newly formed crystals.

Composition of the fluid. A largely unknown factor is the composition of the fluid that is involved. It is suspected that a late stage, residual Na-rich solution-melt/hydrothermal fluid altered the pegmatite and surrounding rocks (Section 4.3.1). This appears to be supported by minute fluid inclusions present in emerald (see Section 4.3.3). To investigate the effect of various melt and solution-melt compositions on the reactions that may have taken place, known compositions of Bikita pegmatite and various glasses, which

Table 15. Compositions of Bikita pegmatite and experimental melts.

	Melt 1		Melt 2		Melt 3		Melt 4		
	Bikita pegmatite		MAC run product		Na-F glass metaluminous		Na-F glass peralkaline		
	wt.%	norm. wt.%	wt.%	norm. wt.%	wt.%	norm. wt.%	wt.%	norm. wt.%	
SiO ₂	73.00	72.85	66.88	66.45	SiO ₂	76.01	67.54	79.71	71.38
Al ₂ O ₃	16.00	15.97	14.68	14.59	Al ₂ O ₃	15.56	13.83	4.14	3.71
Na ₂ O	4.50	4.49	3.46	3.44	Na ₂ O	6.93	6.16	14.58	13.06
K ₂ O	2.00	2.00	3.37	3.35	K ₂ O		0.00		0.00
P ₂ O ₅		0.66	0.66	0.66	P ₂ O ₅		0.59		0.59
CaO	0.00	0.00	0.22	0.22	CaO		0.00		0.00
F		1.00	1.39	1.38	NaF	2.59	2.30	1.79	1.60
H ₂ O	1.50	1.50	9.24	9.18	H ₂ O		8.21		8.27
BeO	0.05	0.05	0.06	0.06	BeO		0.04		0.04
Li ₂ O	1.50	1.50	0.68	0.68	Li ₂ O		1.33		1.34
Total	98.55	100.00	100.64	100.00	Total	101.09	100.00	100.22	100.00

Melt 1: data from Stewart (1978); assumed before normalisation: F=1 wt.% in rare element pegmatites (London, 1987); P₂O₅ = P₂O₅ Melt 2.

Melt 2: glass composition of MAC run product (experiment of beryl added to macusanite; Evensen *et al.*, 1999); Li content Macusani glass from London (1987).

Melt 3: composition of a Na- and F-rich meta-aluminous (Na=Al) experimental glass (Mysen *et al.*, 2004).

Melt 4: composition of a Na- and F-rich peralkaline (Na>Al) experimental glass (Mysen *et al.*, 2004).

For normalised melt 3 and 4 it was assumed that BeO and Li₂O are equal to the contents in Bikita pegmatite, and P₂O₅ and H₂O are equal to the contents in macusanite (melt 2). Explanation see text.

were produced as a result of experimental studies on melts, have been taken as a basis (Table 15). As discussed, the rare-element Bikita pegmatite is a late-stage product formed out of a strongly evolved melt. The MAC-run glass product reflects the composition of an experimental melt, equivalent to macusanite with added beryl. Macusanite is a peraluminous rhyolite obsidian from Macusani, Peru, which, as mentioned earlier, has a similar composition to many evolved Li-rich pegmatites. Additionally, compositions of Na- and F-rich experimental glasses were used, given by Mysen *et al.* (2004). These compositions do not contain H₂O. However, as it is expected that the solution involved in the alteration process at Sandawana did contain a significant amount of water; a minimum H₂O content equal to that of the experimental macusanite melt (9.24 wt.%) is assumed. In order to further approach the likely situation at Sandawana, it was also assumed that these melts contained BeO, Li₂O and P₂O₅ contents that are equal to those measured in Bikita pegmatite (Be- and Li-rich) and macusanite (P-rich), respectively (Table 15).

Mass balance method. Phases that are involved and their average molar compositions (simplified to a relevant chemical subsystem), together with the various solution melts that were successively used to take part in the reactions, are presented in Table 16. The reaction that occurs in the presence of a particular melt/solution was balanced using linear algebra on a spreadsheet. The reaction balances for each component, which in this case gives eleven equations that have to be solved. When normalising to one phase, in this case emerald (emerald = -1), the ratios of the eleven other unknown phases can be calculated by taking the inverse matrix of the dataset². The end results are presented

² For instance, a reaction involving all the phases and melt 1 (Table 16) would give the following equilibrium:

$$a \text{ Act} + b \text{ Chl} + c \text{ Fluap} + d \text{ Qtz} + e \text{ H}_2\text{O} + f \text{ An} + g \text{ Kfs} + h \text{ Alb} + i \text{ Phl} + j \text{ Hlm} + k \text{ Em} + l \text{ Melt} = 0.$$

This reaction balances for each component, which in this case gives 11 equations. For example, for Si the equation is (compare Table 16):

$$\text{Si: } 7.7a + 2.8b + 0 + d + 0 + 2f + 3g + 3h + 2.95i + 8j + 6k + 1.215l = 0.$$

For Al the equation is:

$$\text{Al: } 0.3a + 2.4b + 0 + 0 + 0 + 2f + g + h + 1.10i + 2j + 2k + 0.314l = 0.;$$

and so forth for the other 9 components.

Normalizing to emerald gives $k = -1$. Rearranging gives 11 equations and 11 unknowns, which can be presented in matrix notation (compare Table 16)

$$\begin{pmatrix} 7.70 & 2.80 & 0.00 & 1.00 & 0.00 & 2.00 & 3.00 & 3.00 & 2.95 & 8.00 & 1.215 \\ 2.00 & 0.00 & 5.00 & 0.00 & 0.00 & 1.00 & 0.00 & 0.00 & 0.00 & 0.00 & 0.000 \\ 5.00 & 4.80 & 0.00 & 0.00 & 0.00 & 0.00 & 0.00 & 0.00 & 2.95 & 3.00 & 0.000 \\ 0.30 & 2.40 & 0.00 & 0.00 & 0.00 & 2.00 & 1.00 & 1.00 & 1.10 & 2.00 & 0.314 \\ 0.00 & 0.00 & 3.00 & 0.00 & 0.00 & 0.00 & 0.00 & 0.00 & 0.00 & 0.00 & 0.009 \\ 0.00 & 0.00 & 0.80 & 0.00 & 0.00 & 0.00 & 0.00 & 0.00 & 0.14 & 0.00 & 0.053 \\ 2.00 & 8.00 & 0.20 & 0.00 & 2.00 & 0.00 & 0.00 & 0.00 & 1.86 & 2.00 & 0.167 \\ 0.00 & 0.00 & 0.00 & 0.00 & 0.00 & 0.00 & 1.00 & 0.00 & 1.00 & 0.00 & 0.042 \\ 0.30 & 0.00 & 0.00 & 0.00 & 0.00 & 0.00 & 0.00 & 1.00 & 0.00 & 0.00 & 0.145 \\ 0.00 & 0.00 & 0.00 & 0.00 & 0.00 & 0.00 & 0.00 & 0.00 & 0.00 & 0.00 & 0.002 \\ 0.00 & 0.00 & 0.00 & 0.00 & 0.00 & 0.00 & 0.00 & 0.00 & 0.00 & 2.00 & 0.100 \end{pmatrix} \cdot \begin{pmatrix} a \\ b \\ c \\ d \\ e \\ f \\ g \\ h \\ i \\ j \\ l \end{pmatrix} = \begin{pmatrix} 6.00 \\ 0.00 \\ 0.00 \\ 2.00 \\ 0.00 \\ 0.00 \\ 0.00 \\ 0.00 \\ 0.00 \\ 3.00 \\ 0.00 \end{pmatrix}$$

This can be solved for $a, b, c, \text{etc.}$, by taking the inverse matrix multiplied by the vector on the right-hand side (which simply represents the composition of emerald, the phase to which was normalized).

Table 16. Molar compositions of reacting phases and melts.

	Phases										Melts/solutions					
	act	chl	fluap	qtz	H ₂ O	an	kfs	alb	phl	hlm	em	1	2	3	4	4b
Si	7.70	2.80	0.00	1.00	0.00	2.00	3.00	3.00	2.95	8.00	6.00	1.215	1.113	1.124	1.188	0.666
Ca	2.00	0.00	5.00	0.00	0.00	1.00	0.00	0.00	0.00	0.00	0.00	0.000	0.004	0.000	0.000	0.000
(Mg, Fe)	5.00	4.80	0.00	0.00	0.00	0.00	0.00	0.00	2.95	3.00	0.00	0.000	0.000	0.000	0.000	0.000
Al	0.30	2.40	0.00	0.00	0.00	2.00	1.00	1.00	1.10	2.00	2.00	0.314	0.288	0.271	0.073	0.081
P	0.00	0.00	3.00	0.00	0.00	0.00	0.00	0.00	0.00	0.00	0.00	0.009	0.009	0.008	0.008	0.009
F	0.00	0.00	0.80	0.00	0.00	0.00	0.00	0.00	0.14	0.00	0.00	0.053	0.073	0.062	0.043	0.043
H	2.00	8.00	0.20	0.00	2.00	0.00	0.00	0.00	1.86	2.00	0.00	0.167	1.026	0.912	0.919	3.537
K	0.00	0.00	0.00	0.00	0.00	0.00	1.00	0.00	1.00	0.00	0.00	0.042	0.072	0.000	0.000	0.000
Na	0.30	0.00	0.00	0.00	0.00	0.00	0.00	1.00	0.00	0.00	0.00	0.145	0.112	0.286	0.464	0.688
Be	0.00	0.00	0.00	0.00	0.00	0.00	0.00	0.00	0.00	0.00	3.00	0.002	0.002	0.002	0.002	0.002
Li	0.00	0.00	0.00	0.00	0.00	0.00	0.00	0.00	0.00	2.00	0.00	0.100	0.046	0.089	0.090	0.100

act = actinolite; chl = chlorite; fluap = fluorapatite; qtz = quartz; an = anorthite; kfs = K-feldspar; alb = albite; phl = phlogopite; hlm = holmquistite; em = emerald. Melts 1 to 4 are introduced in Table 15. The composition of solution 4b was obtained by reducing the SiO₂ content of melt 4 to 40 wt.%, and increasing Na₂O to 20 wt.%. The other oxides were kept constant, resulting in an increase of H₂O to 31.86 wt.%.

Table 17. Resulting mass balances with various solutions.

	Melts/solutions					4b	
	1	2	3	4	4b	<i>mol. vol.</i>	<i>volume ratios</i>
	mole	mole	mole	mole	mole		
Actinolite	144.8	186.1	149.1	2.4	-48.1	273.88	
Chlorite	229.2	292.6	332.8	341.8	361.7	210.65	<i>albite/phlogopite</i> = 1.60
Solution/melt	1500.0	1500.0	1688.8	1675.8	1500.7		<i>anorthite/K-feldspar</i> = 0.26
Fluorapatite	-4.5	-4.5	-4.7	-4.7	-4.7	84.05	<i>(oligoclase/K-feldspar</i> = 1.28)
Quartz	-1494.4	-1970.7	-1274.1	-82.5	1762.6	23.05	<i>quartz/K-feldspar</i> = 0.87
Water	-607.2	-1387.5	-1506.7	-1613.8	-3576.5		<i>fluorapatite/emerald</i> = 3.54
Anorthite	-267.2	-355.8	-274.9	18.4	119.4	100.96	
K-feldspar	479.1	648.4	717.5	483.7	430.4	109.05	Reconstructed pegmatite
Albite	-261.0	-223.8	-527.1	-778.8	-1018.6	100.00	composition
Phlogopite	-542.1	-756.4	-717.5	-483.7	-430.4	148.25	<i>Oligoclase</i> = 40.8%
Holmquistite	-75.0	-34.5	-75.3	-75.3	-75.3	258.31	<i>K-feldspar</i> = 31.7%
Emerald	-1.0	-1.0	-1.0	-1.0	-1.0	110.47	<i>Quartz:</i> = 27.5%

in Table 17. Note that, in the calculations, reactant phases have positive reaction coefficients, while product phases have negative reaction coefficients. The physical reaction sense does not follow from this mass balance, but from textural constraints.

Results. Table 17 shows that melt 1, 2 and 3 do not give results that can be harmonised with the observations. In all three cases quartz and anorthite are produced instead of dissolved, as expected from the albitisation process (see Section 4.3.1). Both phases are absent in the emerald-bearing zones. Additionally, too much phlogopite is produced, relative to albite. In the cases of melt 1 and 2 this result could be expected, because they have compositions of late-stage, strongly evolved Li and Be-rich melts. At Sandawana they are considered to reflect the compositions of the primarily consolidated pegmatites, which could never have produced the amount of albite observed. Although melt 3 contains more Na and produces more albite, it also still produces considerable quartz.

The strongly peralkaline melt 4, containing much more Na than even melt 3, but with little Al, appears to go in the 'right direction', with anorthite being consumed, only some quartz produced, and production of more albite than phlogopite. Subsequently, using melt 4 with Al already low, Si content was gradually decreased and the high Na content was increased even more, to study the effects on the mass balance. All other elements were kept at the same concentration and as increased H₂O content was expected, H₂O was used to add up to 100 wt.%. A solution with Si down to 40 wt.%, Na up to 20 wt.%, with H₂O = 31.86 wt.% (solution 4b, Table 16), gave a result that largely fits the criteria from field observations, as laid out at the beginning of this section (Table 17). It can be seen that some new actinolite is formed, as well as the other expected phases. Chlorite is consumed, as well as microcline, oligoclase and quartz. Calculating the volume ratios, the original composition of the pegmatite consisting of the phases that were consumed can be estimated, taking An = 20 in the original oligoclase. This composition is in good agreement with the ratios estimated for the Al Hayat pegmatite, Bikita district, which did not experience severe albitisation; Oligoclase₃₆K-feldspar₃₁Quartz₃₃ (Gallagher, 1975), although it should be noted that Bikita-type pegmatites show considerable variation (compare Gallagher, 1975; Ackermann *et al.*, 1966).

For the original composition of the greenstones, actinolite and chlorite have been taken as a basis. As described, cummingtonite is also common, although not as regularly present. It was found that the addition of cummingtonite (as a combined actinolite-cummingtonite molecule) to the system did not have any noticeable effect on the results.

To evaluate the influence of H₂O in solution 4b, the H₂O value was increased to 80 wt.% (which corresponds to modelling a hydrous fluid) and concentrations subsequently normalised to 100%. The effect was only marginal for most phases, but the fluorapatite/emerald ratio increased to 4.78, which appears to be too high compared to the observations.

In conclusion, the results indicate that a Na- and F-rich hydrous fluid, somewhere in the transition between residual melt and a hydrothermal solution, was involved in the alterations that ultimately caused the formation of emerald. As Li, Be and P are more easily transported in melt than in an aqueous fluid (see, e.g., this section, under crystallisation order), it is expected that in reality their contents have been somewhat lower than the values obtained from the existing and experimental melts.

4.3.3. Fluid behaviour and composition

Data from inclusions – In contrast to the Colombian emeralds, which contain many fluid inclusions (multiphase inclusions consisting of H₂O, CO₂ (liquid and gas), and one or several daughter minerals like halite and sylvite), Sandawana emeralds typically contain solid inclusions (Chapter 3; Zwaan *et al.*, 1997; Zwaan & Burke, 1998; Zwaan & Touret, 1998). Apart from abundant acicular actinolite and cummingtonite crystals, clusters of small idiomorphic apatite crystals (Fig. 46) are commonly present. These clusters indicate rapid hydrothermal growth and, therefore, support a hydrothermal origin of the emeralds. An attempt was made to support this hypothesis by fluid inclusion data, but fluid inclusions in most Sandawana emeralds have not been preserved. Most samples contain only remnants of isolated, decrepitated cavities, many of them containing a whitish carbonate (Mn-Fe-bearing dolomite; Fig. 58). Also, trails of fluid inclusion remnants, also containing whitish carbonate, occur, usually oriented parallel

to each other (Fig. 57). These observations indicate that the inclusions must originally have contained some CO₂. A small number of isolated, non-decrepitated (or at least not empty) inclusions have been found in five samples from different locations at the Zeus 200 ft. level, 26/28 stope (Fig. 60). Indeed, they contain a typical hydrothermal fluid, high-salinity aqueous brine (at least 50% wt. equivalent NaCl) and traces of CO₂. It is improbable that this fluid is exactly the same as the one initially present in the decrepitated inclusion, which from the size of the remaining carbonate must have been much more CO₂-rich. It is possible that this fluid was an immiscible gaseous-rich phase in the highly saline brines.

The original presence of CO₂-rich inclusions in emerald deposits agrees with the conclusions of, for example, Barros (1986), Seal (1989), de Souza *et al.* (1992), Moroz & Vapnik (1999), Vapnik & Moroz (2002), Seifert *et al.* (2004) and Zwaan *et al.* (2005). These authors described and investigated fluid inclusions in emeralds from 'schist-type' deposits at, for example, Nova Era (Itabira district), Santa Terezinha and Carnaiba, Brazil, Pansjhir Valley, Afghanistan, Swat Valley, Pakistan, Sumbawanga and Lake Manyara, Tanzania, the Maria deposit, Mozambique, and the Kafubu area, Zambia. Moroz & Vapnik (1999) and Vapnik & Moroz (2002) stated that carbonate crystals and CO₂ are often present in these fluid inclusions, and indicate that carbonic acid brines may have played an important role during emerald growth. They argued that, as salt-undersaturated inclusions, indicating low-salinity chloride brines, tend to be related to the later stages of progressive crystallization of granitic magma (Shmonov *et al.*, 1986), the possibility of emerald growth during contact metasomatism may be restricted to the latest stages of felsic magma crystallization.

However, it should be noted that detailed fluid inclusion studies in schist-type deposits areas by, for example, Barros (1986), Seal (1989) and Nwe & Morteani (1993), often show complex growth histories of emerald, with fluids involved that show a wide range of salinities. Additionally, the minute, isolated, salt-oversaturated three-phase inclusions discovered in emeralds from Sandawana, as well as rare isolated three-phase inclusions in emeralds from the Chantete mine, Kafubu area, Zambia (Zwaan *et al.*, 2005), do suggest that highly saline brines have been involved (at least at some stage) during the growth of emerald in ultrabasic rocks, at the contact of intruded rare-element pegmatite. Notably, in Queensland, Australia, highly saline brines of supposedly (late) magmatic origin have been described in relation to sodium metasomatism and alteration of fluorine-rich granites and of tonalites, respectively (Witt, 1988; Charoy & Pollard, 1989; Mark, 1998).

Although it was seen from the presence of fluorapatite in the emerald-bearing zones that the fluid contained considerable amounts of fluorine (and phosphorus), natural hydrothermal fluids probably contain more Cl than F even when fluorite and topaz stability is reached (Charoy & Pollard, 1989). The relationship in the distribution of chlorine and fluorine between the hydrothermal fluid and the apatite solid solution is due to the difference in the ionic radii (Cl⁻ 1.81 Å, F⁻ 1.33 Å). F⁻ has an ionic radius very similar to OH⁻ and, therefore, fits perfectly into most hydrous minerals. Fluorine enters the apatite preferentially under these conditions, which appears to explain its predominance over chlorine in apatite although in general chlorides predominate in the hydrothermal fluid (Korzhinskiy, 1981).

Cerny (2000) stated that miarolitic vugs in pegmatites form in late stages of consolidation, in consequence of oversaturation of the residual pegmatite melt by volatile

ZEUS 200' level 26/28 stope (section 2)

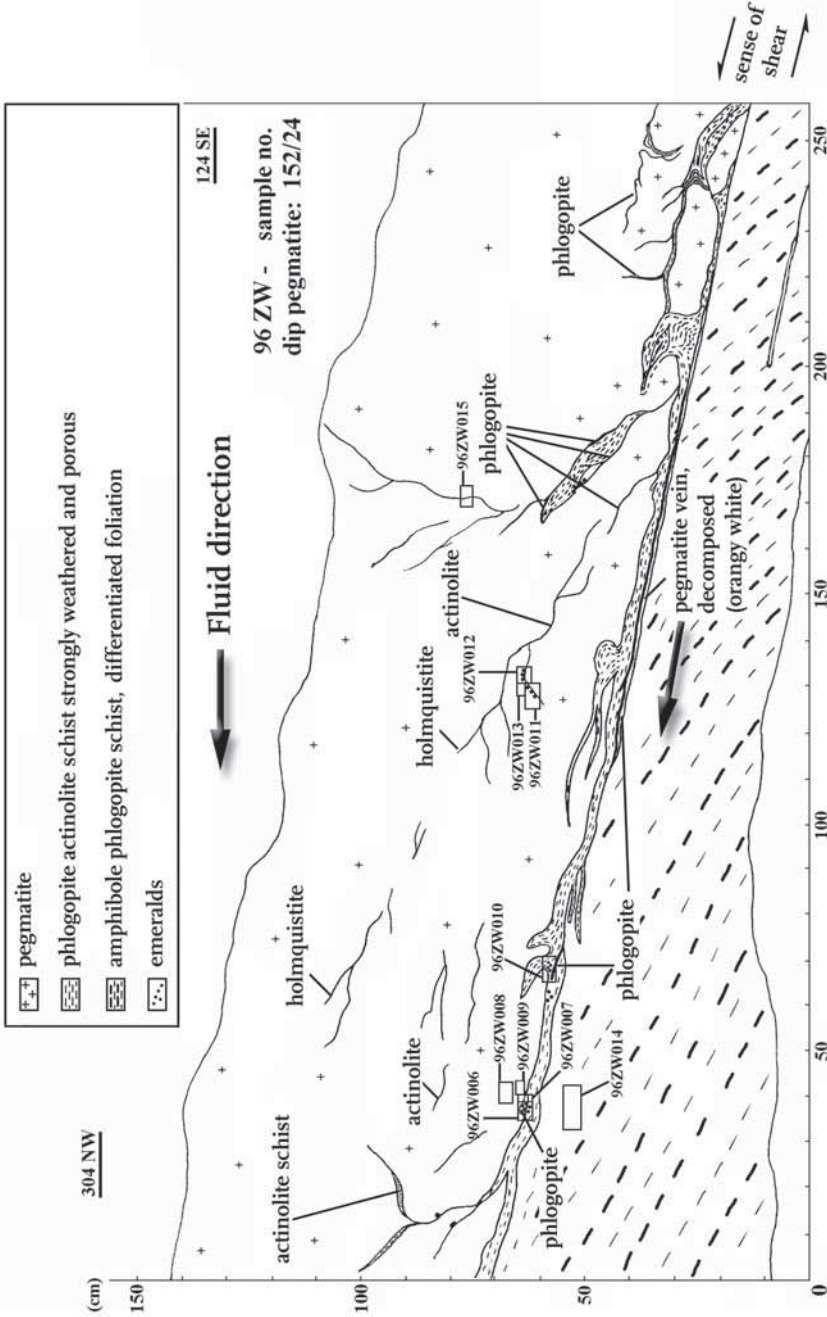


Fig. 70. Cross section taken at the Zeus underground mine, 200 ft. level, 26/28 stope (horizontal and vertical scales in cm). Fluids infiltrated along shear zones into the contact zone between pegmatite and greenstone, causing alterations and transport of elements. The direction of sheared contact and the foliation direction define the sense of shear. Dissolution of quartz increased the porosity in the pegmatite, allowing fluids to precipitate minerals like holmquistite and emerald.

components, in particular water. Exsolution of a hydrous supercritical fluid phase takes place and, if trapped inside the pegmatite, a segregated 'bubble' of the vapour-like fluid becomes the site of a vug. In geochemically evolved pegmatites (such as the LCT-family pegmatites, Section 4.2.1), the early lining of miarolitic cavities is commonly coated by minerals of rare and volatile components, such as beryl or fluorapatite, which are envisaged to have been precipitated from the supercritical aqueous fluid. In most cases, however, the evolving supercritical fluid can gradually escape from pegmatite to the host rocks. According to Cerny (2000), that is why miarolitic cavities are absent from most granitic pegmatites and why alterations in wall rocks are very common, generated by outflow of, for example, F, Be, CO₂ and Li-bearing fluids from the consolidating pegmatite bodies. This model appears to be supported by the presented inclusion data from Sandawana emeralds that clearly indicate the involvement of an aqueous fluid, and also with the observed wall rock alterations and produced minerals near the sheared pegmatites.

Fluid invasion at the contact between pegmatite and greenstone – At the Zeus mine, underground at a location (200 ft. level, stope 26/28) where many emeralds were recovered during the last years, a sheared contact between albitised pegmatite and phlogopite amphibole schist was observed (Fig. 70). At this section, the sense of shear could be recognised, based on the orientation of the contact and the foliation, which was formed during ductile deformation. It appears that a fluid invaded the contact zone, basically following this direction along the contact. Apatite and emerald mainly occur just along the contact, with phlogopite. Abundant holmquistite and locally emerald also crystallised in the amphibole schlieren in the pegmatite. Holmquistite was, indeed, found as an unusual inclusion in the emeralds that grew at this place. The spatial relations at this section appear to reflect the high 'relative reactivity' of K⁺ and higher 'relative mobility' of Li⁺ (e.g., Shearer & Papike, 1988). Phlogopite formation all along the footwall of the pegmatite resulted in depletion of K⁺ in the fluid relative to Li⁺. Consequently, the remaining fluid that was able to travel farther (i.e., into the pegmatite) was able to, almost exclusively, produce abundant holmquistite. In this respect, dissolution of quartz during albitisation probably provided greatly enhanced porosity for the invading fluids through the pegmatite (compare Charoy & Pollard, 1989).

Quartz with cleavage – A quartz inclusion that shows cleavage in two directions, virtually perpendicular to each other, was found in an emerald from a location close to the described section, Zeus Mine, 300 feet level, stope 23/7 (Fig. 71). Unusual and rare rhombohedral cleavage in quartz from St. Paul-la-Roche, Dordogne, France, has been described by Arbey (1975), who proposed two possible causes for the origin of this cleavage; directional tectonic stress or meteoritic shock. The second hypothesis is the most likely one, because Spray *et al.* (1998) identified the Rochechouart crater, close to St. Paul-la-Roche, as part of an impact chain. In addition, most metamorphic regions which underwent high directional stress do not show quartz grains with this rare cleavage, but, rather, many subgrains and/or complete recrystallisation. At Sandawana, there are no indications of impact of meteorite(s). It is also not likely that directional stress and fluid pressure were high enough to produce cleavage in quartz. Even an explosive nature of the fluids involved, causing shock-like events when entering shear-zones and

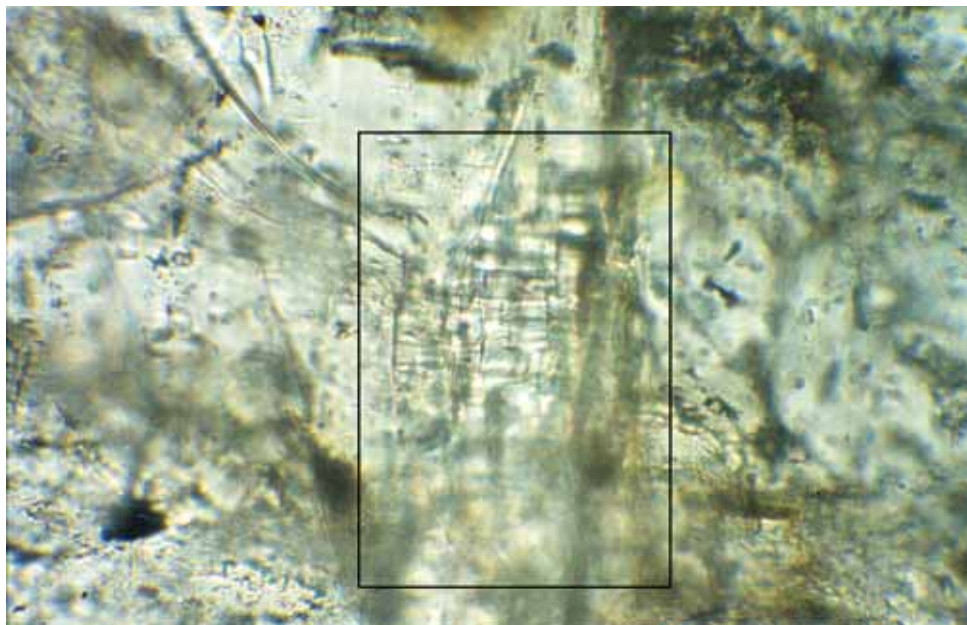


Fig. 71. Quartz inclusion in emerald, showing two cleavage directions; the cause of this rare cleavage remains unclear. Suggested causes of such a cleavage in the literature are high directional stress or meteoric shock. Neither of these explanations appear to be probable at Sandawana. Sample 421620 (thin section 96JCZ7), Zeus underground mine, 300 ft. level, 23/7 stope. The width of the quartz crystal is 115 μm .

releasing pressure, would not be powerful enough to cause this phenomenon.

Unfortunately, quartz is very rare as an inclusion in emerald (Section 3.4.4) and grains are usually very small. The inclusion in Figure 71 is the only (larger) one found with this peculiar cleavage. Also, the scarce quartz present in the pegmatites does not show this feature. In conclusion, the meaning of this inclusion, although remarkable, remains unclear.

Trapped fluids and the growth of gem-quality emerald – Idiomorphic, reasonably clean emerald often occurs in the schist away from the pegmatite, as shown in Figure 18a. A 'crust' of fine-grained emerald commonly occurs at the contact between pegmatite and schist. It appears that the cleaner idiomorphic emerald has been formed somewhat later than the finer grained sub- to anhedral crystals. In sub- to anhedral emeralds, often found exactly at the contact or in the pegmatite, trails of fluid inclusion remnants are commonly observed, which are usually parallel to each other. These secondary healed fractures suggest crystallization during shearing. The cleaner, idiomorphic emeralds in the schist were possibly formed shortly after shearing, as they do not show series of secondary healed fractures and are present in the low-pressure zone next to the pegmatite. Thus, it appears that the gem-quality crystals formed somewhat later than those of non-gem quality. The isolated decrepitated inclusions (Fig. 58), which are present in gem quality crystals, possibly indicate a later phase of fast regional decompression (block uplift).

From these observations, it becomes evident that gem-quality emeralds will probably always be recovered from the schist, at least 1 mm away from the pegmatite, and notably in relatively low pressure zones next to the pegmatite. This would possibly also explain the fact that the emeralds are not found all along the contact between pegmatite and schist, but always in areas where pegmatites are folded and sheared. These folds formed 'traps', areas of relatively lower pressure that the fluids were forced into and in which idiomorphic emeralds could grow. The emerald grains are usually small, but, sometimes, larger crystals are recovered in a trap like the one shown in Fig. 14 (marked areas). For instance, the author has seen emerald crystals up to 30 mm in size in this particular area.

Chromium solubility and mobility – Most studies of chromium solubility deal with the behaviour in basaltic melts. There is less known about the solubility of Cr in pegmatitic/hydrothermal solutions. The traditional view is that Cr is significantly less soluble than many of the other metals, although it was recognised by Treloar (1987) that, while Cr is immobile under metamorphic conditions, it may be mobile in hydrothermal systems. Recent analyses of the trace-element composition of vapour-rich fluid inclusions (e.g., Heinrich *et al.*, 1992, 1999) suggested that the vapour phase may play a far more important role in transporting the metals of ore-forming hydrothermal systems than was recognised hitherto. Experiments by Williams-Jones *et al.* (2003) on solubility of Cu, Ag, Au, Sn and Mo showed that the solubility of the metal in the vapour is orders of magnitude greater than that predicted theoretically from volatility calculations. This enhanced solubility is attributed to the ability of water to hydrate the metal in the vapour phase. Although the solubility of most metals in water vapour will reach a maximum at $T < 400^{\circ}\text{C}$, solubility increases with increasing vapour pressure and the critical pressure of aqueous fluids increases sharply with increasing salinity. Consequently, Williams-Jones *et al.* (2003) predicted that in highly saline systems solubility will be appreciable even at $T > 600^{\circ}\text{C}$.

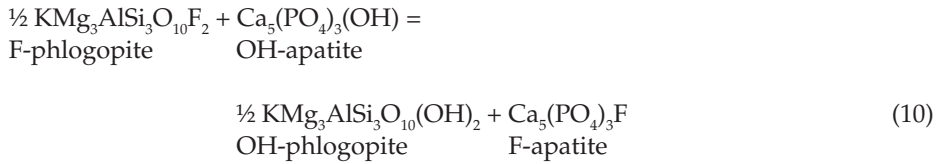
The observations at Sandawana are in line with these findings, indicating favourable conditions for Cr mobilisation. The evidence presented above suggests that there was indeed a link between emerald formation and a highly saline vapour-rich solution, with probably a high (initial) fluid pressure, which, therefore, should have been perfectly capable of dissolving and mobilising Cr. This is supported by the presence of chromite grains in the schist, showing frayed edges, suggesting dissolution. Additionally, the presence of metasomatic chromian ilmenorutile in the ore zone and the presence of emerald in the phlogopite schist, but also in holmquistite-bearing schlieren in the pegmatite (this section, fluid invasion), clearly indicates that chromium has been transported, even over a considerable distance.

4.4 Temperature (and pressure) conditions of emerald formation

4.4.1. *Apatite-phlogopite geothermometry* – As phlogopite, fluorapatite and emerald have grown syntectonically (Section 2.3.4), in close association, the temperature of emerald formation can be constrained by using a geothermometer that is based on the F-Cl-OH partitioning between apatite and phlogopite.

Basic principles – Zhu & Sverjensky (1992) formulated a revised and recalibrated apatite-biotite F-OH geothermometer, that yields temperatures in agreement with those

estimated from other independent geothermometers. F-OH exchange between apatite and phlogopite can be expressed in the following exchange reaction:



The corresponding equilibrium constant K is

$$K_d = \frac{(a_{\text{F-Ap}} / a_{\text{OH-Ap}})}{(a_{\text{F-Phl}} / a_{\text{OH-Phl}})^{1/2}} \quad (11)$$

where a_i represents the thermodynamic activity of the endmember i . The standard states for the solids are defined as the pure endmember components at the temperature and pressure of interest. Assuming ideal solution of F-OH-Cl in apatite, and applying definitions for $a_{\text{F-Phl}}$ and $a_{\text{OH-Phl}}$ given by Wood & Nicholls (1978), K_d can be written as

$$K_d = \frac{(X_{\text{F}}/X_{\text{OH}})^{\text{Apatite}}}{((X_{\text{F}}^2 X_{\text{Mg}}^3 \lambda_{\text{F-Phl}} / X_{\text{OH}}^2 X_{\text{Mg}}^3 \lambda_{\text{OH-Phl}})^{1/2})^{\text{Biotite}}} \quad (12)$$

where X is the mole fraction of the subscripted component in apatite or biotite, $X_{\text{Mg}} = 1 - X_{\text{Fe}}$, and $\lambda_{\text{F-Phl}}$ and $\lambda_{\text{OH-Phl}}$ are activity coefficients for fluorphlogopite and phlogopite, respectively. Subsequently we have

$$\ln K_d = \ln K_D + \frac{1}{2} \ln (\lambda_{\text{OH-Phl}} / \lambda_{\text{F-Phl}}) \quad (13)$$

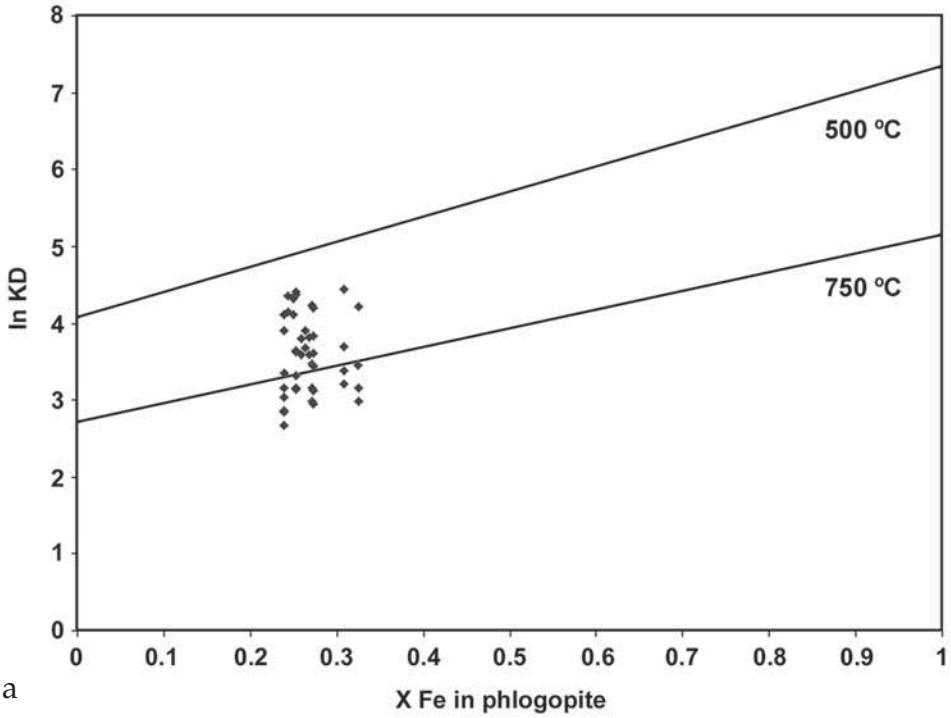
where

$$K_D = \frac{(X_{\text{F}}/X_{\text{OH}})^{\text{Apatite}}}{(X_{\text{F}}/X_{\text{OH}})^{\text{Biotite}}} \quad (14)$$

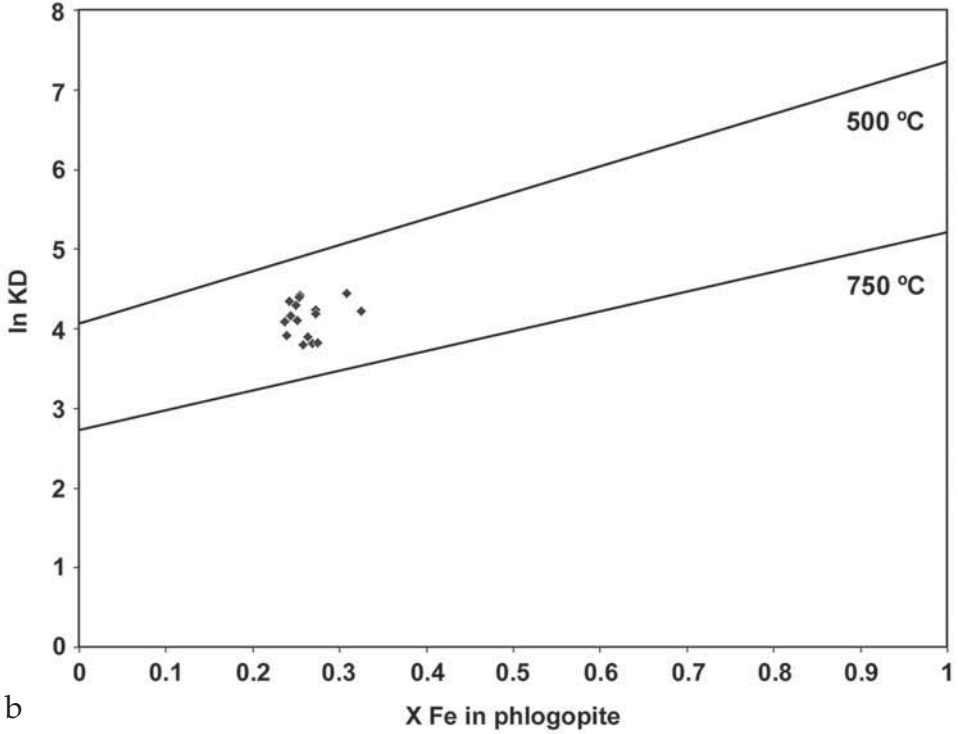
is the Henderson-Kracek partitioning coefficient (McIntire, 1963) for reaction 10.

F will be strongly preferentially partitioned into apatite with respect to biotite. The extent of the preference is dependent on the temperature and the Fe concentration of

Fig. 72. Partitioning of F-OH between apatite and biotite. The solid lines are calculated isotherms at the indicated temperatures, after Zhu & Sverjensky (1992). It reflects the notion that F preference for apatite is strongly dependent on temperature and the Fe concentration of biotite. (a) From Sandawana emerald deposits at the Zeus underground mine, from both the 200 ft. and 250 ft. level. Data from apatite and phlogopite, at both locations in close proximity (cm scale), but not necessarily in contact, show considerable scatter and indicate situations of disequilibrium between the two minerals. (b) At both locations, data of selected biotite and apatite grains that were in contact agree with the trends of the predicted isotherms. ▶



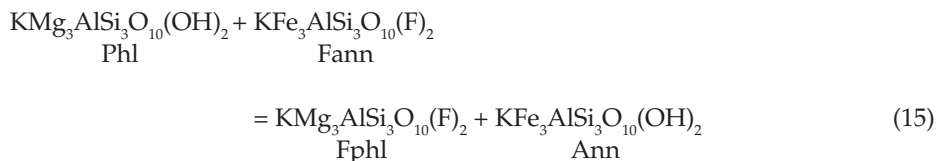
a



b

biotite. Increase of temperature and decrease of Fe concentration (or increase of Mg concentration) will reduce this preference (Fig. 72).

The thermodynamic properties of endmember biotite strongly support the positive correlation between Mg and F, and negative correlation between Fe and F, in biotite (Munoz & Ludington, 1974). The correlation can be depicted by the internal exchange reaction



The standard Gibbs free energy of reaction (15), calculated using the standard thermodynamic properties of Zhu & Sverjensky (1991), is about -10 kcal/mol for temperatures up to 1000°C and pressures between 1 and 5 kbar. This indicates that Mg will have a strong affinity for F and Fe will have a strong affinity for OH in biotite under crustal conditions.

A negative correlation of octahedral Al with F is found in experimental studies (Munoz & Ludington, 1974). However, the differences between log K for F-OH exchange reactions in annite and siderophyllite ($\text{KFe}_2\text{Al}(\text{Al}_2\text{Si}_2)\text{O}_{10}(\text{OH})_2$) are within experimental uncertainties. In the light of the lack of thermodynamic properties available for siderophyllite, it is assumed that octahedral Al has the same influence as Fe^{2+} (Munoz, 1984; Zhu & Sverjensky, 1992). Therefore, mole fractions of Fe of biotite are calculated as

$$X_{\text{Fe}} = \frac{\text{Fe} + \text{Al}^{\text{VI}}}{\text{Fe} + \text{Mg} + \text{Al}^{\text{VI}}} \quad (16)$$

to quantify the Mg- Fe^{2+} - Al^{VI} effects.

The isotherms in Figure 72 are predicted from the following equation:

$$\ln K_D = - \frac{\Delta G^0_{\text{R},10}}{RT} + \frac{1}{2} X_{\text{Fe}} \frac{\Delta G^0_{\text{R},15}}{RT} \quad (17)$$

where $\Delta G^0_{\text{R},10}$ and $\Delta G^0_{\text{R},15}$ are the standard Gibbs free energies of reaction (10) and reaction (15), respectively; R is the gas constant; and T is temperature in Kelvin. This equation shows that $\ln K_D$ should be a linear function of X_{Fe} at constant T.

Expressions like equation 17 can be obtained using the molecular mixing approach. As McIntire (1963) pointed out, this formulation works well for a number of liquid systems. Zhu & Sverjensky (1992) showed that the F-OH partitioning coefficients between natural apatite and biotite appear to be a linear function of X_{Fe} in biotite at constant temperature, as predicted from equation 17.

Therefore, Zhu & Sverjensky (1992) formulated the revised apatite-biotite geothermometer starting from equation (17). The Gibbs free energies, $\Delta G^0_{\text{R},10}$ and $\Delta G^0_{\text{R},15'}$ were

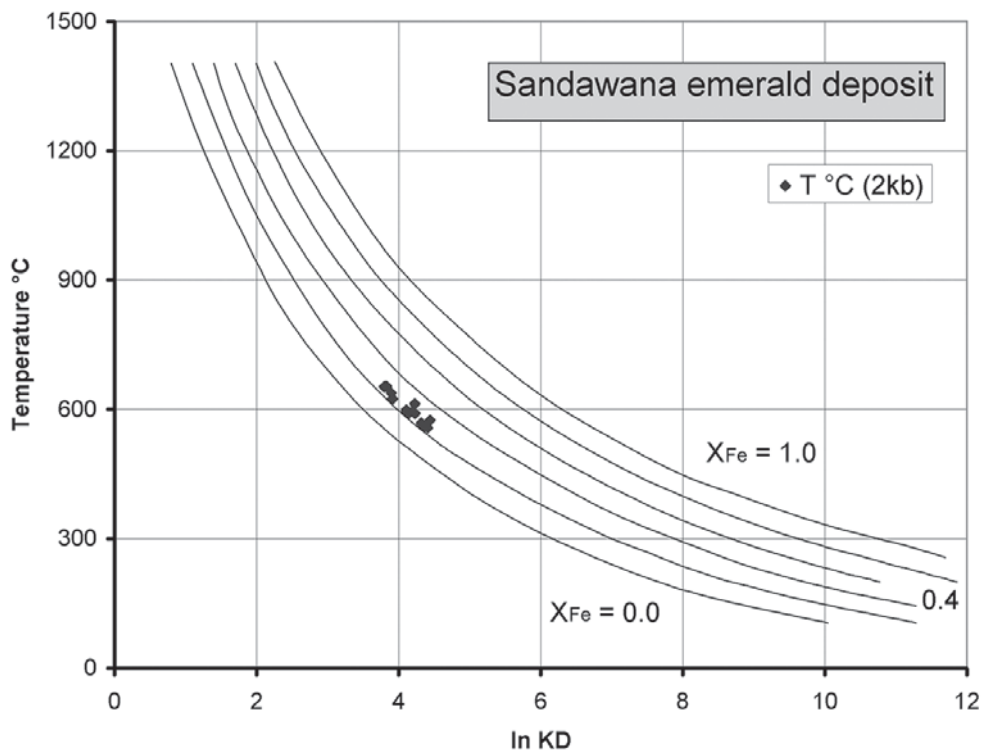


Fig. 73. Graphic presentation of calculated equilibrium temperatures using the apatite-biotite geothermometer of Zhu & Sverjensky (1992).

Table 18. Calculations of $\ln K_D$ s and temperatures for samples from the Zeus underground mine, according to the apatite-biotite geothermometer, as revised by Zhu & Sverjensky (1992).

Locality	Sample	Phlogopite	Apatite	K_D	$\ln K_D$	X_{Fe} phlog	T °C (2kb)	T °C (3kb)
Zeus mine, 200', 26/28 (2)	421551	2-ph.5	apa1rb	68.64	4.23	0.27	590	588
Zeus mine, 200', 26/28 (2)	421551	2-ph.5'	apa1rb	66.43	4.20	0.27	595	593
Zeus mine, 200', 26/28 (2)	421551	2-phl.E	apa1rb	49.93	3.91	0.24	625	622
Zeus mine, 200', 26/28 (2)	421551	2-phl.F	apa1rb	60.71	4.11	0.24	594	592
Zeus mine, 200', 26/28 (2)	421545	phlo1c	apa1rb	85.02	4.44	0.31	575	573
Zeus mine, 200', 26/28 (2)	421545	phlo1r	apa1rb	68.41	4.23	0.32	613	611
Zeus mine, 200', 26/28 (2)	421545	phlo2a	apa1rb	79.68	4.38	0.25	562	560
Zeus mine, 200', 26/28 (2)	421545	phlo2b	apa1rb	81.81	4.40	0.25	558	556
Zeus mine, 200', 26/28 (2)	421545	phlo2c	apa1rb	79.95	4.38	0.25	561	559
Zeus mine, 250', 17/16	421355	phl.Li1	apa 1a	62.96	4.14	0.24	591	589
Zeus mine, 250', 17/16	421355	phl.Li2	apa 1a	60.75	4.11	0.25	599	597
Zeus mine, 250', 17/16	421355	phl.Li1	apa 1b	77.63	4.35	0.24	561	559
Zeus mine, 250', 17/16	421355	phl.Li2	apa 1b	74.90	4.32	0.25	569	567
Zeus mine, 250', 17/16	421354	phl 1a	apa 1b	45.11	3.81	0.27	654	652
Zeus mine, 250', 17/16	421354	phl 1b	apa 1b	45.95	3.83	0.27	653	651
Zeus mine, 250', 17/16	421354	phl 2a	apa 1b	44.57	3.80	0.26	652	650
Zeus mine, 250', 17/16	421354	phl 2b	apa 1b	49.22	3.90	0.26	638	636

calculated from standard thermodynamic properties given by Zhu & Sverjensky (1991) to high temperature and pressure. Incorporating these results and rearranging equation (17) leads to the following equation for the apatite-biotite geothermometer:

$$T \text{ (}^\circ\text{C)} = \frac{8852 - 0.024 P \text{ (bars)} + 5000 X_{\text{Fe}}}{1.987 \ln K_D + 3.3666} - 273.15 \quad (18)$$

Equation (18) is valid for the T range 300-1100°C.

The partition coefficient and the mole fraction of Fe in biotite have been empirically calibrated and compiled by Zhu & Sverjensky (1992) into the graphical geothermometer shown in Figure 73.

Results – At Sandawana, fluorapatite and phlogopite were frequently found in association with emeralds (Chapter 2). Samples from two rich emerald-occurrences in the Zeus underground mine (the 26/28 stope at 200 ft level, and the 17/16 stope at 250 ft level), in which apatite and phlogopite coexist, were chosen for geothermometry. The apatite and phlogopite grains that were analysed occurred exactly at the contact of amphibole/phlogopite schist and pegmatite, or in the emerald bearing amphibole/phlogopite schist, only cm away from the pegmatite. Data from apatite and phlogopite in close proximity (same rock sample), but not necessarily in contact, showed considerable scatter and appear to indicate situations of disequilibrium (Fig. 72a). At both underground localities, data of selected biotite and apatite grains that were in contact give more consistent results and agree with the trends of the predicted isotherms (Fig. 72b). Calculated temperatures for those grains are shown in Table 18 and graphically presented in Figure 73. The temperatures range from 560 to 650°C, with an average $T = 600 \pm 30^\circ\text{C}$.

Alternative approach – An alternative apatite-biotite geothermometer was advocated by Sallet (2000). Zhu & Sverjensky (1992) recalibrated the apatite-biotite thermometer based on solid solution models. The version used by Sallet (2000) is based on biotite-fluid and apatite-fluid F-OH experimental data and equilibrium relations.

The following equation was deduced:

$$0.0085 T^2 - [13.25 - \text{IV (F)} - \log (X_{\text{F}}/X_{\text{OH}})_{\text{ap}}]T + 2100 = 0 \quad (19)$$

where T is in Kelvin and IV (F) is the fluorine intercept value of biotite, which corrects for the Mg/Fe control on F contents of biotite:

$$\text{IV (F)} = 1.52 X_{\text{Mg}} + 0.42 X_{\text{An}} + 0.20 X_{\text{Sid}} - \log (X_{\text{F}}/X_{\text{OH}}) \quad (20)$$

and

$$\begin{aligned} X_{\text{Mg}} &= \text{Mg} / \Sigma \text{Octahedral cations,} \\ X_{\text{Sid}} &= [(3 - \text{Si} / \text{Al}) / 1.75][1 - X_{\text{Mg}}], \\ X_{\text{An}} &= 1 - (X_{\text{Mg}} + X_{\text{Sid}}). \end{aligned}$$

Solving equation (19), only one set of results shows coherent temperatures. The other set is close to zero or even produces negative values.

It is emphasised that the proposed thermometer should strictly be used in agreement with the experimental conditions for which it is formulated; P and T range and, particularly, crystal-vapour equilibrium. Unfortunately, the author does not specify these conditions. The method is especially applied to describe the conditions in various (quartz-bearing) magmatic associations, rather than in mineralised bodies formed during metasomatism. The temperatures Sallet (2000) generated appear to be relatively high compared to other methods; many examples show a difference in the order of 50-70°C. Comparing the results for Sandawana (Table 19), the temperatures generated by the Sallet (2000) method produced slightly higher temperatures as well, up to 680°C, with differences from 30° up to 90°. Such temperatures, above the granite solidus, are deemed unrealistic.

Zhu & Sverjensky (1992) showed that temperatures calculated by using equation (18) for apatite-biotite pairs from a variety of igneous and metamorphic environments agree with temperatures independently estimated from other geothermometers. Therefore, in the case of Sandawana, the values calculated by this method will be used. Unfortunately, these values cannot be verified, because no other independent geothermometer can be applied with regard to the emerald-bearing zone. Actinolite-phlogopite thermometry could be useful as an independent method, but is not available at present.

4.4.2. *Discussion* – Although apatite-biotite geothermometry gives an indication of the temperature, no independent pressure indicators can be used for the mineralised zones at Sandawana. Looking at the mineral assemblage, the only theoretical possibility to constrain the pressure would, perhaps, be the use of aluminium in hornblende. How-

Table 19. Comparison of apatite-biotite geothermometers by Zhu & Sverjensky (1992) and Sallet (2000).

Locality	Sample	Phlogopite	Apatite	Application		
				Sallet (2000) T (°C)	Zhu & Sverjensky (1992) T (°C), 2 kb	Δ T
Zeus mine, 200', 26/28 (2)	421551	2-ph.5	apa1rb	667	590	77
Zeus mine, 200', 26/28 (2)	421551	2-ph.5'	apa1rb	670	595	75
Zeus mine, 200', 26/28 (2)	421551	2-phl.E	apa1rb	683	625	58
Zeus mine, 200', 26/28 (2)	421551	2-phl.F	apa1rb	670	594	76
Zeus mine, 200', 26/28 (2)	421545	phlo1c	apa1rb	655	575	80
Zeus mine, 200', 26/28 (2)	421545	phlo1r	apa1rb	674	613	61
Zeus mine, 200', 26/28 (2)	421545	phlo2a	apa1rb	652	562	90
Zeus mine, 200', 26/28 (2)	421545	phlo2b	apa1rb	650	558	92
Zeus mine, 200', 26/28 (2)	421545	phlo2c	apa1rb	652	561	91
Zeus mine, 250', 17/16	421355	phl.Li1	apa 1a	640	591	49
Zeus mine, 250', 17/16	421355	phl.Li2	apa 1a	645	599	46
Zeus mine, 250', 17/16	421355	phl.Li1	apa 1b	640	561	79
Zeus mine, 250', 17/16	421355	phl.Li2	apa 1b	645	569	76
Zeus mine, 250', 17/16	421354	phl 1a	apa 1b	686	654	32
Zeus mine, 250', 17/16	421354	phl 1b	apa 1b	686	653	33
Zeus mine, 250', 17/16	421354	phl 2a	apa 1b	685	652	33
Zeus mine, 250', 17/16	421354	phl 2b	apa 1b	679	638	41

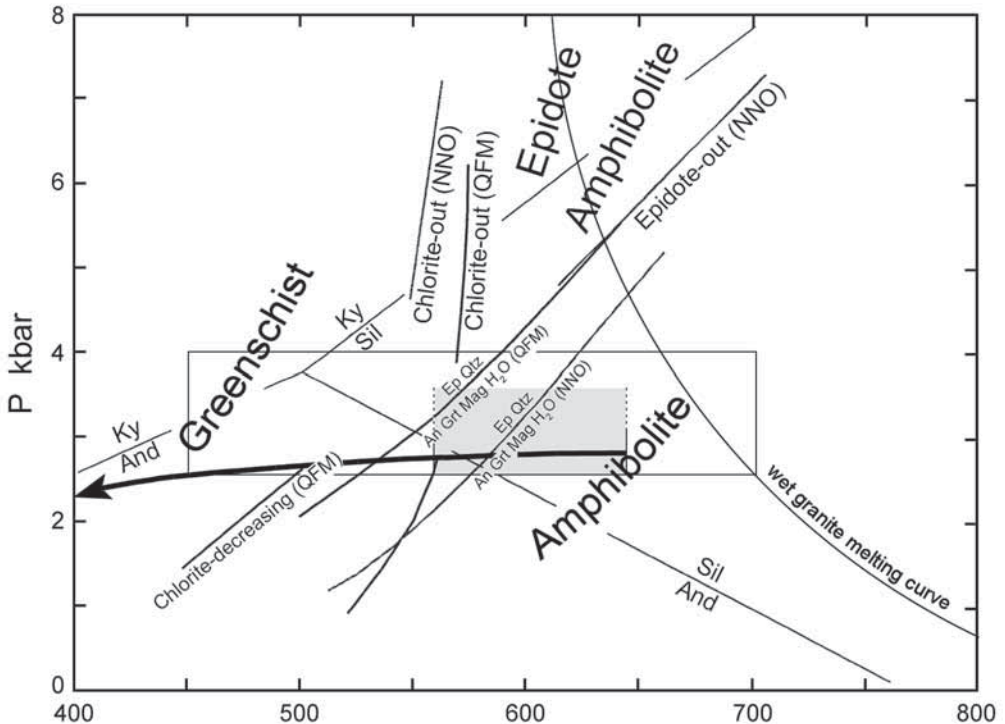


Fig. 74. P-T diagram showing the experimental results of Liou (1973), Liou *et al.* (1974) and Apter & Liou (1983) relevant to the greenschist to amphibolite facies transition (after Spear, 1993, fig. 11.16). Curves are experiments performed with oxygen fugacity defined by the quartz-fayalite-magnetite (QFM) buffer and the nickel-nickel oxide (NNO) buffer, respectively. The inferred crystallisation path of the Bikita pegmatite is indicated (after London, 1990), as well as the temperatures and pressures at which primary consolidation of rare-element pegmatites takes place (rectangular box; after London, 1984). The grey box indicates the estimated conditions of emerald formation at Sandawana; dashed lines show uncertainty about pressure conditions.

ever, the Al-in-hornblende barometer was constructed for estimating crystallisation pressure for plutonic complexes (e.g., Hammerstrom & Zen, 1986; Johnson & Rutherford, 1989; Anderson & Smith, 1995). So far, it has been common practice to apply the barometer to restricted magmatic mineral assemblages (plagioclase, hornblende, biotite, K-feldspar, quartz, sphene, magnetite or ilmenite, ± epidote) and plagioclase compositions ($\sim \text{An}_{25-35}$). Amphiboles with compositions other than 'igneous' hornblende (which shows $\text{Si} \leq 7.5$ and $\text{Ca} \geq 1.6$) were screened out and cannot be used when applying this barometer. Thus, at Sandawana, the metasomatic mineralised zones with actinolites, virtually all showing $\text{Si} > 7.5$, up to 7.95, and Al content lower than that calibrated for barometry, clearly disqualify for this method.

Nevertheless, without having a direct pressure estimate, it is clear that metamorphic grade and strain increase from the core of the MGB towards the southern margin, where greenstone belt lithologies are in contact with gneisses of the NMZ (Section 2.3.2; Map 1). A narrow band of amphibolite-facies rocks developed in response to regional

thrusting of granulite-facies rocks over the Zimbabwe Craton, south of the Zeus underground mine, which indicates higher temperatures there ($> 750^{\circ}\text{C}$; Section 2.3.2). In the emerald bearing zones, the edenite cores in idiomorphic actinolites (Section 2.3.4) also suggest relatively high formation temperatures, at the border of upper greenschist/amphibolite facies conditions, with peak conditions even in the amphibolite facies. Temperature can greatly increase Al^{IV} in hornblende at constant pressure by operation of the edenite-forming exchange mechanism (e.g., Spear, 1981a, b). These textures are in agreement with the calculated temperatures of associated apatite and phlogopite, which are in the amphibolite facies field, overlapping the boundary with upper greenschist facies conditions (Fig. 74). Because emerald was formed synkinematically, and was found to have grown at the same time as apatite and phlogopite, the indicated temperature range ($T = 560\text{--}650^{\circ}\text{C}$) should give a rough estimate of temperatures at which emerald was formed.

Taking into consideration the rather shallow intrusion level of the closely related Bikita pegmatite and its inferred crystallisation path on the basis of lithium aluminosilicate + quartz assemblages (London, 1984; see also Fig. 13), and the fact that, in general, primary consolidation of rare-element (Li-Be-Ta) pegmatites occurs in the range of 700° to 450°C at 4 to 2.5 kbar, a tentative P-T box for emerald formation is presented in Figure 74. The crystallization path of the Bikita pegmatite suggests low pressures under 3 kbar at the indicated temperatures. However, at Sandawana, the intruded rare-element pegmatites are situated at the southern edge of the MGB, which is virtually at the tectonic break between the Zimbabwe craton and the Limpopo NMZ (compare with Bikita, Figs. 6, 7), and just north of the amphibolites, which indicate a much higher metamorphic grade (see Map 1). This could mean that pressure conditions at Sandawana are somewhat different, but, as indicated earlier, independent pressure estimates cannot be made.

In conclusion, it is estimated that at Sandawana emeralds were formed under temperatures of around $650\text{--}550^{\circ}\text{C}$ and pressures around 2.5 to 3 kbar. This would be well within the stability limits of beryl, provided that the channel sites of emerald are saturated with water (compare Section 4.1.1 and Fig. 63). As indicated in Section 3.5.3, the high refractive indices of Sandawana emerald appear to indicate a high H_2O content. The low totals (Table 14) indicate that volatiles up to 4.1 wt.% may be present in the emeralds. As the maximum measured H_2O content in emerald is around 2.7 wt.% (Banerjee, 1995), it may be presumed that the channels of Sandawana emerald are full of water. From the high concentration of volatiles, it is probable that not only H_2O , but also CO_2 (heavier), are present in the channels. This probability appears to be confirmed by the presence of decrepitated inclusions with carbonate in emerald.

The temperatures at the contact of altered pegmatite and greenstone are relatively high, compared to the regional metamorphic conditions of the surrounding rocks. In addition to the indications for infiltration metasomatism (Section 4.3), it implies that the association of minerals at the pegmatite-greenstone contact represent contact metamorphic rather than regional metamorphic assemblages, which is a strong indication for a direct relation between emerald formation and the synkinematic intrusion of the pegmatites.

5. Oxygen isotopes and Ar-Ar dating: implications for the origin and timing of emerald formation at Sandawana

5.1. Tracing the emerald origin by oxygen isotope data – (After Zwaan *et al.*, 2004)

5.1.1. Introduction – Emeralds from around the world exhibit a wide range of oxygen isotope composition ($\delta^{18}\text{O} = 6.2$ to 24.7‰). Therefore, stable oxygen isotopic analysis of emeralds was recently promoted as a way to establish the country of origin of cut emeralds that are sold on the commercial market (Giuliani *et al.*, 1998; Giuliani *et al.*, 2000a). In these studies only two measurements were done on emeralds from Sandawana, Zimbabwe, which seemed to indicate relatively small variations in oxygen isotope composition. The present study presents additional data on precisely located emeralds from the Zeus underground mine and the Orpheus mine in the Sandawana district. There is no doubt that oxygen isotope data bring useful elements to the knowledge of emerald origin. However, relying only on this technique can be ambiguous if different occurrences show overlapping values. In this respect, the emeralds from Sandawana will be used to test this method in comparison with the traditional, non-destructive techniques, such as measuring the physical properties, characterising the inclusions and chemical analysis.

5.1.2. Oxygen isotope studies

Basic principles – Oxygen is the most abundant element of the Earth's crust and the main component of emerald. It is composed of three stable isotopes, ^{16}O , ^{17}O , ^{18}O . The relative abundances of these isotopes in air oxygen are 99.759%, 0.0374% and 0.2039%, respectively (Nier, 1950). The ratio of the most abundant oxygen isotopes ^{18}O to ^{16}O in air is thus about 1 to 489, but in nature this ratio may vary by as much as 10%, or from about 1:475 to 1:525 (Taylor, 1967).

The isotope data are reported as $\delta^{18}\text{O}$ in per mil (Taylor, 1979), where

$$\delta^{18}\text{O} = \left(\frac{{}^{18}\text{O}/{}^{16}\text{O}_{\text{sample}}}{{}^{18}\text{O}/{}^{16}\text{O}_{\text{standard}}} - 1 \right) 1000$$

Consequently, we are only concerned with relative deviations from a standard material, not with absolute ratios. The most convenient standard is ocean water. A particular set of ocean water values, designated Standard Mean Ocean Water (SMOW) by Craig (1961), is the most common standard. Thus, a $\delta^{18}\text{O}$ value = + 10 means that the sample is 10‰ or 1% richer in ^{18}O than SMOW. Negative numbers indicate relative depletion in the heavy oxygen isotope.

Materials – Four emeralds from Sandawana, Zimbabwe, were used for analysis. Three emeralds were chosen from the largest underground operation at Sandawana, the Zeus Mine. Samples were taken on the 200, 225, and 300 feet levels, corresponding to depths below surface of approximately 61.0, 68.6 and 91.4 m, respectively. The ore zones are all very narrow, normally up to only 15 cm width, sometimes to a maximum of 30 cm width, with gem-quality emerald production from the actinolite-cummingtonite-

Table 20. Results of $\delta^{18}\text{O}$ measurements in Sandawana Emeralds. Values of $\delta^{18}\text{O}$ have an overall reproducibility of c. 0.2‰.

This study		
Locality at Sandawana	Sample no.	$\delta^{18}\text{O}$ ‰
Zeus mine, 200' level, 25/28 stope	RGM 421629	+ 6.6
Zeus mine, 225' level, 25/27 stope	RGM 466002	+ 7.2
Zeus mine, 300' level, 23/7 stope	RGM 421620	+ 6.9
Orpheus mine	RGM 421622	+ 7.4
Previous work (Giuliani <i>et al.</i> , 1998)		
Locality at Sandawana	Sample no.	$\delta^{18}\text{O}$ ‰
Unknown	SAND-1	+ 8.0
Unknown	SAND-2	+ 6.9

phlogopite schist at the contact with pegmatite. At the Orpheus mine, located 11 km southwest of the Zeus mine (Fig. 7), the emeralds are mined from an open pit. The chosen sample from this occurrence was mined from a weathered zone, close to the surface, from essentially the same amphibole-phlogopite schist found in close contact with pegmatite in the Zeus mine. For comparison, one emerald each from the Belmont mine, Minas Gerais, Brazil, and Habachtal, Austria, were also analysed.

Analytical technique – Oxygen isotope analysis was carried out at the Geological Survey of Canada, Ottawa, on powdered aliquots of pure, hand-picked emerald using conventional methods of fluorination employing BrF_5 in externally-heated nickel vessels (Clayton & Mayeda, 1963). The released oxygen extracted from the framework of emerald was converted to CO_2 in a graphite furnace. Mass spectrometry was performed on CO_2 using standard IRMS procedures in a FinniganMAT 252 spectrometer. Data are reported in the usual δ -notation (permil, ‰), on the normalized V-SMOW - SLAP scale. Values of $\delta^{18}\text{O}$ reported for emerald have an overall reproducibility of c. 0.2‰. Our value of $\delta^{18}\text{O}$ for NBS-28 (African Glass Sand; IAEA-RM 8546) is 9.6‰.

Results – $\delta^{18}\text{O}$ values for the four Sandawana emeralds are given in Table 20 and compared with previous measurements by Giuliani *et al.* (1998), using the ion microprobe technique (Fig. 3). Our results are very homogeneous ($\pm 0.8\%$ variation range, $\delta^{18}\text{O} = 7.0 \pm 0.4\%$), slightly lower, but within the same error range, than the $\delta^{18}\text{O}$ values given by Giuliani *et al.* (1998); $\delta^{18}\text{O} = 7.5 \pm 0.5\%$. Considering these two studies, the mean value for the Sandawana emerald is $\delta^{18}\text{O} = 7.3 \pm 0.7\%$.

Comparable $\delta^{18}\text{O}$ values are found in various other deposits in the world (Fig. 75). Similar values were measured for emeralds from Habachtal, Austria ($\delta^{18}\text{O} = 7.1 \pm 0.1\%$; Giuliani *et al.*, 1998; $\delta^{18}\text{O} = 7.0\%$; Zwaan *et al.*, 2004), Poona, Australia ($\delta^{18}\text{O} = 7.25 \pm 0.25\%$; Giuliani *et al.*, 1998) and various other non-economic deposits in Brazil (Juca: $\delta^{18}\text{O} = 6.8\%$; Pombos: $\delta^{18}\text{O} = 7.5\%$; Santana dos Ferros, $\delta^{18}\text{O} = 7.9\%$; all three by Giuliani *et al.*, 1998). Also, a single oxygen isotope value from the Maria deposit, Mozambique ($\delta^{18}\text{O} = 8.2 \pm 0.2\%$; Giuliani *et al.*, 1998) is indistinguishable from the Sandawana SAND-1 value ($\delta^{18}\text{O} = 8.0 \pm 0.2\%$; Giuliani *et al.*, 1998; Table 20).

The economically important deposits of the Quadrilatero Ferrifero, Minas Gerais, Brazil, comprise a range of values (Capoeirana: $\delta^{18}\text{O} = 6.2 \pm 0.3\%$; Fallick *et al.*, 1994;

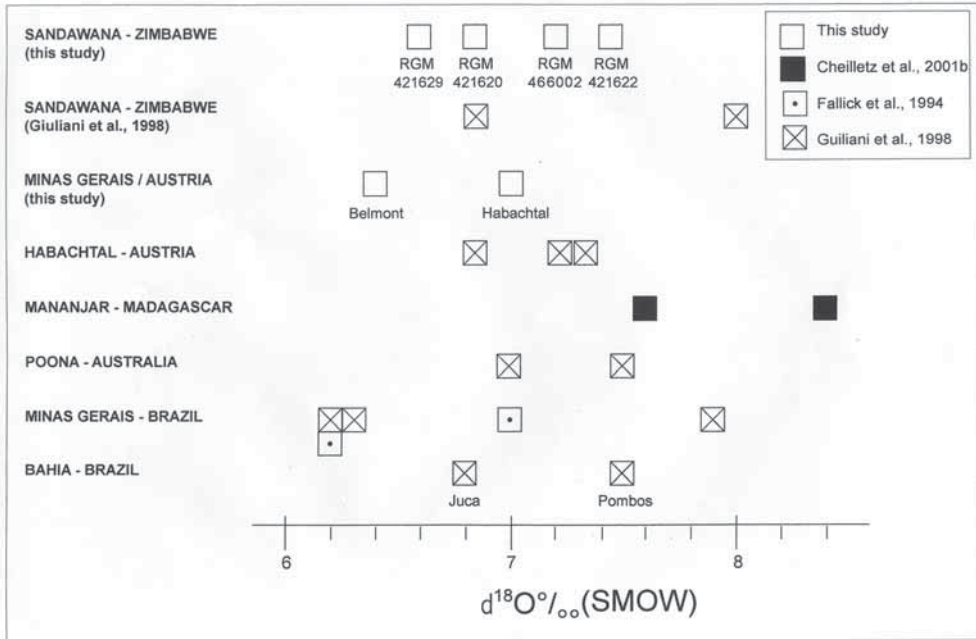


Fig. 75. $\delta^{18}\text{O}$ values of emerald from different deposits in the world compared to new $\delta^{18}\text{O}$ values obtained for the Sandawana-Zimbabwe deposit, Belmont mine (Minas Gerais, Brazil) and Habachtal (Austria), showing close correspondence.

Giuliani *et al.*, 1998; Belmont: $\delta^{18}\text{O} = 6.4\text{‰}$; Zwaan *et al.*, 2004; Itabira $\delta^{18}\text{O} = 7.0 \pm 0.3\text{‰}$; Fallick *et al.*, 1994) with some overlapping (within error range) the Sandawana emerald $\delta^{18}\text{O}$ values ($\delta^{18}\text{O} = 7.3 \pm 0.7\text{‰}$). Emeralds from the Mananjar deposit in Madagascar have $\delta^{18}\text{O}$ values ranging from 7.6 to 8.7‰ (Cheilietz *et al.*, 2001b), which partly overlap the Sandawana values. Relative to the wide range of oxygen isotopic composition of emerald in the world (between 6.2 and 24.7‰; Giuliani *et al.*, 1998), the $\delta^{18}\text{O}$ values of emeralds from the Sandawana mines are among the lowest measured. Only emeralds from Capoeirana and Belmont (Minas Gerais, Brazil) have lower values of $\delta^{18}\text{O} = 6.2$ and 6.4‰, respectively.

5.1.3. Discussion

Oxygen isotope signature of Sandawana emeralds – The very narrow ore zone (most commonly only 15 cm wide) in both the Orpheus and Zeus mines at the contact of greenstones with pegmatite is representative of the whole emerald-bearing belt. All gem-quality emeralds from the Sandawana area come from exactly the same rock-type, i.e., an actinolite-cummingtonite-phlogopite schist, representing a metasomatized greenstone, corresponding to a series of metamorphosed komatiites.

As pointed out by Fallick *et al.* (1994), Fallick & Barros (1987) and Cheilietz *et al.* (2001a), host-rock buffering plays an important role in establishing the oxygen isotope composition of emerald. The range of $\delta^{18}\text{O}$ values in metamorphosed komatiites, including young komatiites from Gorgona, is relatively narrow, between + 5 and + 8‰

(Kyser, 1986). Komatiites from the nearby Belingwe greenstone belt, for example, have $\delta^{18}\text{O}$ values between 5.5 and 7.0, somewhat higher than values of komatiites from Barberton ($\delta^{18}\text{O} = 5.5 \pm 0.25\%$). The range in $\delta^{18}\text{O}$ values of the oceanic mantle, as sampled by xenoliths from Hawaii, and of peridotite nodules from continental areas are quite similar, ranging from about 5 to 7. The only exception to this rule are extreme $\delta^{18}\text{O}$ values of continental eclogites, ranging from 2.8 to 8.2 (Kyser, 1986).

The other rocks involved in the genesis of emeralds, namely pegmatitic lenses, have a more variable and significantly higher $\delta^{18}\text{O}$ signature (Taylor *et al.*, 1979; Taylor, 1982; Sheppard, 1986; Taylor *et al.*, 1992). However, the narrow range of oxygen isotopic composition in Sandawana emeralds, which overlaps with the komatiite field, shows no influence of the metasomatised pegmatite, in line with the very low volume of these rocks compared to the greenstones. Entire isotopic homogenisation took place through fluid-rock buffering during regional metamorphism, but the signature was imprinted by the mantle-derived original protolith (komatiite). Similar conclusions can be drawn for the Habachtal deposit in Austria, which is thought to have involved interaction with serpentinites (Grundmann & Morteani, 1989; Nwe & Grundmann, 1990). However, these serpentinites are much younger than those in Sandawana. Peak metamorphism occurred during the Middle Alpine 'Tauernkristallisation', between 65 and 35 Ma (Grundmann, 1989), and were derived from deep-seated (plutonic) ultrabasics (harzburgites or lherzolites). Yet the oxygen isotope signature ($\delta^{18}\text{O}\text{‰} = +7.1 \pm 0.1$) of Habachtal emeralds exactly matches that from Sandawana (Fig. 75), suggesting that the $\delta^{18}\text{O}$ composition of emerald is a reliable indicator of the geological environment, independent of age.

Oxygen isotope and chemical analysis: limits to distinction of the origin of cut emeralds – The traditional method of oxygen isotope analysis, as used in this study, is a destructive technique, not applicable to expensive, gem-quality cut emeralds. Spot analysis by ion microprobe, however, produces craters of only 10 to 20 micron in diameter and a few angstroms deep (invisible to the unaided eye). Ion microprobe analysis could, therefore, be done on emeralds of any commercial or historical value (Giuliani *et al.*, 2000a). Oxygen isotope analyses by the ion microprobe are less accurate than those by traditional method; the 1σ analytical precision using the ion microprobe is $\pm 0.6\%$, instead of $\pm 0.2\%$ by traditional methods. Nevertheless, it would be wrong to assert that oxygen isotope analysis, alone, is a 'miracle tool', able to identify the origin of any emerald without ambiguity and without considering other criteria. Emeralds from the commercially mined occurrences, at Sandawana (Zimbabwe), Habachtal (Austria), Minas Gerais (Brazil) and, partly, Mananjar (Madagascar), show overlapping $\delta^{18}\text{O}$ values. Thus, in these cases, oxygen isotope analysis alone cannot be used to establish their origin.

Emeralds from the above occurrences can be identified relatively easily, using other, more traditional gem testing techniques. Refractive indices and densities are not very useful either in these particular cases, because they all fall in the same range (refractive indices 1.574-1.597, birefringence 0.005-0.009, densities 2.68-2.77; Zwaan *et al.*, 1997; Hänni *et al.*, 1987). Except for Habachtal emeralds with the lower values, they are useful, however, to discriminate between emeralds from these localities and emeralds from the most important commercial sources in Colombia (refractive indices 1.569-1.580, birefringence 0.005-0.007, 2.69-2.70; Gübelin, 1989; Webster, 1994). Colombian emeralds can be distinguished from the other sources noted (including Habachtal) by their om-

nipresent, highly diagnostic, irregularly shaped, three phase brine inclusions. Among commercially available emeralds, only those from central Nigeria and Afghan emeralds from the Panshijir Valley are known to also contain three phase or multiphase brine inclusions, which in some cases may appear similar to the inclusions in Colombian emeralds (Henn & Bank, 1991; Bowersox *et al.*, 1991).

In contrast to those in Sandawana emeralds, fluid inclusions are abundant in emeralds from Minas Gerais (Hänni *et al.*, 1987; Zwaan, 2001), which feature narrow growth tubes, orientated parallel to the c-axis, that produce the well-known 'rain effect', often seen in aquamarine. Other characteristic inclusions are rectangular to almost square-shaped cavities, filled with CO₂-rich fluids. Thus, whereas fluid inclusions in emeralds from some localities have unique characteristics, such properties must be used in conjunction with other features to confirm an emerald's geographic locality.

Solid inclusions in emeralds may also vary from locality to locality. For example, Habachtal emeralds typically contain amphibole rods, apatite crystals and phlogopite platelets, like Sandawana emeralds, but exhibit an inhomogeneous 'patchy' colour (Morteani & Grundmann, 1977) that has not been observed in Sandawana emeralds. Also, unlike Habachtal emeralds, phlogopite is uncommon as an inclusion in Sandawana emeralds.

With respect to chemical composition, emeralds from Sandawana contain high MgO (2.5-2.8 wt.%) and Na₂O content (2.1-2.4 wt.%; Zwaan *et al.*, 1997; Chapter 3), compared to the emeralds from Itabira, Minas Gerais (MgO: 0.5-1.9; Na₂O: 0.3-1.3; Hänni *et al.*, 1987). Additionally, various analyses (electron microprobe, PIXE) of cut and rough Habachtal emeralds show distinctly lower chromium content (Cr₂O₃ 0.01-0.44 wt.%; Schwarz, 1991a; Cr₂O₃ 1390 ± 720 ppm; Calligaro *et al.*, 2000) than Sandawana emeralds (Cr₂O₃ 0.61-1.33 wt.%; Zwaan *et al.*, 1997; Cr₂O₃ 5211 ± 2190 ppm; Calligaro *et al.*, 2000). It should be noted, however, that at the rim of Habachtal emerald crystals Cr₂O₃ up to 0.91 wt.% was measured (Grundmann & Morteani, 1989) and, according to Grundmann (pers. comm.), in some cases their chromium content can even go up to 1.14 wt.%.

There are situations in which oxygen isotopic compositions can be effectively used as an additional diagnostic tool. Emeralds from Rajasthan (India) enclose 'tremolite' fibres (Fernandes, 2001), which clearly resemble the actinolite/cummingtonite fibres in Sandawana emeralds. Other inclusions may be very different, though; rectangular multiphase fluid inclusions are frequently encountered in emeralds from Rajasthan, whereas fluid inclusions are virtually absent in Sandawana emeralds. Refractive indices and densities of Rajasthan and Sandawana emeralds are very similar (e.g., compare Gübelin, 1989, and Zwaan *et al.*, 1997), and, consequently, a somewhat ambiguous picture might arise when examining a cut stone with an unknown origin. Oxygen isotopic compositions of these two localities are very different and can give a conclusive answer; δ¹⁸O = 7.3 ± 0.7‰ (Sandawana) versus 10.8 (Rajasthan; Giuliani *et al.*, 1998). Furthermore, long-prismatic amphibole rods and fibrous aggregates of talc occasionally found in emeralds from Mananjar (Madagascar) may also look very similar to the amphibole fibres found in Sandawana emeralds (Schwarz, 1994). However, in many Mananjar emeralds, phlogopite is the most common inclusion and fluid inclusions also occur. δ¹⁸O values of Mananjar emeralds have a larger range (7.6 to 9.5‰; Cheillett *et al.*, 2001b), but partly overlapping with those of the Sandawana emeralds (Fig. 75), making oxygen isotope discrimination not totally secure as the distinguishing diagnostic tool for these two

deposits. Thus, distinguishing source localities among emeralds is generally best approached by comparison of many features.

5.1.4. Conclusion – The relatively low $\delta^{18}\text{O}$ values of emeralds from the Sandawana mines, Zimbabwe, reflect the buffering of the isotopic system by metasomatised ultramafic host rocks during the metamorphism-driven formation of these emeralds. The $\delta^{18}\text{O}$ value of the fluid was controlled by the ultramafic nature of the greenstones, and the intensity of the fluid-rock interactions at the sheared and porous schist at the contact with the pegmatite. At any time during Earth's history, emeralds formed in a comparable geological (lithological) environment can readily have comparable oxygen isotope compositions. Therefore, traditional gem testing techniques can often better fingerprint the locality of origin of commercially available emeralds. In cases of overlapping physical and chemical properties, and ambiguous inclusion characteristics, as for the deposits of Sandawana (Zimbabwe) and Rajasthan (India), the use of oxygen isotopes may be helpful.

5.2. Geochronology

5.2.1. Introduction – There is a great deal of published data on regional radiometric dating by a variety of techniques such as U/Pb, Rb/Sr, Pb/Pb, Sm/Nd and Ar/Ar. A number of these data give contradictory indications, which need a careful analysis and synthesis into a regional framework (Section 5.2.3). This framework can be used to interpret the results that are obtained by this study, in relation to the timing of emerald formation.

Looking at the minerals that were found in emerald-bearing zones at Sandawana (Table 6), the $^{40}\text{Ar}/^{39}\text{Ar}$ dating method appeared to be most appropriate in attempting to get a reliable age of emerald formation. The basics of this method are introduced in Section 5.2.2.

In low-grade metamorphic rocks, the $^{40}\text{Ar}/^{39}\text{Ar}$ method, applied on individual minerals, can directly date tectonic or metamorphic events, which, in the case of Sandawana, is very useful, because emerald formation is associated with deformation, shearing and regional metamorphism (Chapters 2, 4). Therefore, $^{40}\text{Ar}/^{39}\text{Ar}$ were performed on single grains of amphibole and phlogopite, extracted from three metasomatised rocks, which were present at three different emerald-bearing zones, at the contact between deformed pegmatite and greenstone. The locations were chosen at the Zeus and Aeres mines, respectively. Grain size for single grain analyses are in the order of 400-600 μm . These relatively larger amphiboles and phlogopite are considered to have grown simultaneously with emerald (Section 2.3.4; Chapter 4), and can, therefore, indirectly give the age of emerald formation.

In comparison, direct $^{87}\text{Rb}/^{87}\text{Sr}$ dating on emerald has not been applied, because of the low rubidium contents in the Sandawana emeralds, which would give 'model ages' that are not precise enough. Besides, Vidal *et al.* (1992) showed that emeralds are even more sensitive to radiogenic strontium loss than associated micas, which probably causes a spread of model ages beyond analytical error.

5.2.2. Basic principles of the $^{40}\text{Ar}/^{39}\text{Ar}$ technique (mainly after Lips, 1998) – Recent summaries of the principles of the $^{40}\text{Ar}/^{39}\text{Ar}$ dating technique were given by Dickin (1995)

and Lips (1998). This technique was firstly applied and introduced by Merrihue & Turner (1966) and Mitchell (1968), respectively. It is now the most commonly used variant of the conventional K-Ar method and is based on the natural decay of ^{40}K to ^{40}Ar . There are three naturally-occurring isotopes of potassium (abundances after Lips, 1998); ^{39}K (c. 93.2581%), ^{40}K (c. 0.01167%) and ^{41}K (c. 6.7302%). ^{40}K is radioactive and decays to two daughter isotopes, namely to ^{40}Ca and ^{40}Ar . As ^{40}Ca is the most abundant of all Ca isotopes and ^{40}K is the least abundant of all K isotopes, it implies that the isotopic variations of Ca produced by decay of ^{40}K are negligible, in most cases. This is why the decay of ^{40}K to ^{40}Ca is not widely used in geochronology studies. The parent isotope ^{40}K decays to the daughter isotope ^{40}Ar with an half-life time of 1.72×10^{10} years (Steiger & Jäger, 1977). The decay to ^{40}Ar occurs mainly because an electron of the K-shell is captured by the nucleus and a neutron is created at the expense of a proton. The argon atom is in an excited state and rapidly decays to the ground state by emitting gamma photons.

As is the case with other radioactive systems, an age can be calculated when the quantities of daughter and parent isotope are precisely known. The following equation for the age of a sample forms the basis for the K-Ar and $^{40}\text{Ar}/^{39}\text{Ar}$ dating method:

$$t = 1/\lambda \ln \{^{40}\text{Ar}^*/^{40}\text{K} (\lambda/\lambda_{\text{Ar}}) + 1\} \quad (1)$$

t is the duration of decay

$^{40}\text{Ar}^*$ is the amount of ^{40}Ar produced by the *in situ* decay of ^{40}K in a closed system

λ is the total decay constant of ^{40}K , i.e., $5.543 \times 10^{-10} \text{ yr}^{-1}$ ($\lambda = \lambda_{\text{Ar}} + \lambda_{\text{Ca}}$)

λ_{Ar} the partial decay constant that refers to the decay of ^{40}K to ^{40}Ar , i.e. $0.581 \times 10^{-10} \text{ yr}^{-1}$

λ_{Ca} the partial decay constant that refers to the decay of ^{40}K to ^{40}Ca , i.e. $4.962 \times 10^{-10} \text{ yr}^{-1}$

In the conventional K-Ar method, the ^{40}Ar and ^{40}K contents are measured on separate aliquots of the sample to be dated. Because of the need to measure absolute contents of K and Ar from two separate aliquots, it is important that the sample is as homogeneous as possible. The $^{40}\text{Ar}/^{39}\text{Ar}$ technique has significant advantages over the K-Ar method. The sample does not need to be split into two aliquots, so problems of sample heterogeneity can be avoided. The date is determined by the mass-spectrometric measurement of the ratio of the argon isotopes, which is more precise than measuring absolute concentrations of ^{40}K and ^{40}Ar .

The $^{40}\text{Ar}/^{39}\text{Ar}$ method is based on the measurement of the ^{40}K in the sample by a neutron activation procedure involving the conversion of a fraction of ^{39}K , the main naturally occurring K isotope (which occurs in a constant ratio to ^{40}K), to ^{39}Ar by irradiation of the sample with fast neutrons in a nuclear reactor. ^{39}Ar is itself radioactive, but its half-life of 265 years is sufficiently long for any error in a mass spectrometry measurement to be very small. Following this irradiation, the sample is fused in an ultra high vacuum system (UHV) and the purified Ar gas is measured isotopically by noble gas mass spectrometry. After the mass intensities have been corrected for atmospheric argon and mass interference, due to production of additional Ar isotopes derived from irradiated K, Ca and Cl in the analysed material, the $^{40}\text{Ar}/^{39}\text{Ar}$ ratio can be obtained. Apart from the higher analytical precision, the effect of the production of an Ar isotopic ratio in the sample allows stepwise extraction and analysis of the argon isotopes (incremental heating experiment) to investigate the presence of a heterogeneous or homo-

geneous Ar distribution in the sample. A single spectrometric analysis is sufficient to determine the K/Ar ratio, which is a parameter of the age equation, because the quantity of ^{39}Ar is a function of the quantity of total K and, thus, ^{40}K . A sample with known K-Ar ratio (a standard) is required to establish a precise knowledge of the ^{39}Ar production during irradiation. The standard is irradiated simultaneously with the unknown samples and analysed to obtain its $^{40}\text{Ar}^*/^{39}\text{Ar}_k$ ratio. An irradiation parameter, J, is defined that is appropriate for both the standard and the unknown samples:

$$J = (e^{\lambda t} - 1) / ({}^{40}\text{Ar}^* / {}^{39}\text{Ar}_k) \quad (2)$$

t is age of standard

${}^{39}\text{Ar}_k$ is the amount of ^{39}Ar derived from irradiation of ^{39}K

The variation in neutron fluency is mapped out to establish the exact irradiation parameter per sample. Once J is known, ages can be calculated:

$$t = 1/\lambda \ln\{J ({}^{40}\text{Ar}^* / {}^{39}\text{Ar}_k) + 1\} \quad (3)$$

The closure temperature concept – When the absolute age of a sample has been determined, it is important to interpret the obtained numerical ‘age’ value in terms of its geological relevance. Given the case of a stable mineral, the most important process of controlling the isotopic composition of a crystal is thermally activated volume diffusion. At low temperatures, diffusion is slow and radiogenic Ar may be retained quantitatively after it has formed (closed system). At high temperatures, diffusion is rapid and radiogenic Ar may be lost by diffusion from the crystal after it has formed (open system). There is a critical temperature range over which the mineral goes from completely open to being a completely closed system to argon loss during cooling, which is called the closure temperature range. The closure temperature is mostly dependent on the activation energy for diffusion, but also on the geometry and size of the diffusion domain, and the cooling rate (Dodson, 1973). The generally accepted closure temperature ranges for the K-bearing minerals that were used for this study are presented in Table 21.

Apatite/phlogopite thermometry (Section 4.4) indicates temperatures around 600°C. Amphiboles present in the emerald-bearing zone at Sandawana also appear to indicate that peak metamorphism occurred at upper-greenschist/amphibolite conditions (Section 2.3.4), which means they may have crystallised slightly above or at their closure temperatures. Therefore, the amphiboles provide the potential to almost directly date the events during which they were formed.

Biotite or phlogopite do not crystallize below their closure temperatures, so micas buried at moderate depths may lose radiogenic Ar continuously until uplift, erosion and consequent cooling reduce their temperature rapidly to a level at which ^{40}Ar can

Table 21. Average argon closure temperatures of K-bearing minerals used in this study.

K-bearing mineral	Closure temperature	References
Hornblende	500 ± 50°C	McDougall & Harrison (1999)
	~ 580°C	Kamber <i>et al.</i> (1995b); Willigers <i>et al.</i> (2001)
Biotite	300 ± 30°C	Villa (1998)

accumulate. Dates measured on phlogopite will then give the time of cooling, which, in the case of Precambrian areas would represent the point at which they became stable shield areas.

Age spectra – The $^{40}\text{Ar}/^{39}\text{Ar}$ laserprobe incremental heating experiments (IHE) are most effective for samples that might have a heterogeneous distribution of ^{40}Ar . In the IHE a sample is heated by a defocussed laserbeam and the argon that is released by degassing of the sample is collected. After cleaning of the released gas, the argon isotopes are measured, the corrections are applied and an age is calculated using equations 1 to 3 (above). The laserpower is then increased and the process is repeated. The final result is an argon release spectrum (age spectrum). If it is assumed that gas is evolved from the sample during IHE by thermally activated volume diffusion, then the successively higher-temperature steps are sampling gas from progressively deeper in the crystals. In the case of a rapidly cooled mineral that has not lost Ar since it passed through its closure temperature or a mineral that has crystallised rapidly below its relevant closure temperature range, there should be a uniform distribution of Ar throughout the crystal given that it has not been affected by other factors which might control argon loss (e.g., recrystallisation, chemical alteration, *etc.*) Theoretically, all ages obtained in a IHE of such a sample will be within uncertainty and the age spectrum will be flat. Such a flat spectrum (plateau age) is taken to indicate that the sample has remained a closed system to argon (loss or gain) and that the date represents an age of geological significance. However, when argon from grain edges and grain centres evolves at the same time during step-heating, a meaningless plateau date can be the result. Therefore, a plateau spectrum is generally a necessary, but not sufficient, indication, that a mineral has not partially lost argon since it last passed through its closure temperature.

5.2.3. Geochronological data, Zimbabwe craton-Limpopo belt (NMZ) boundary – A summary of relevant dating results in the literature, regarding the Zimbabwe craton/Limpopo NMZ boundary, the area in which the Sandawana emerald occurrence is located, is presented in Table 22. As described in Chapter 2, there are many indications, including geochronological data, that a major tectonic event took place in this area at *c.* 2.6 Ga (Hawkesworth *et al.*, 1979; Berger *et al.*, 1995; Mkweli *et al.*, 1995). Northnorthwest directed crustal shortening, which caused folding of the MGB and regional greenschist metamorphism, occurred in response to uplift of the NMZ over the Zimbabwe Craton. This uplift took place along parallel shear zones which form the tectonic break between the Zimbabwe Craton and the NMZ. Two suites of potassic granites were emplaced north and south of the greenstone belt towards the end of thrusting.

Other data (Table 22) confirm the existence of a major event at 2.6 Ga, but also indicate a major tectonic event (strike-slip/transpression movement) in the Triangle Shear Zone (TSZ), Limpopo Belt, at 2.0 Ga. This event affected the whole of the Limpopo Belt, including the northern boundary with the Zimbabwe Craton. This interpretation is based on the following evidence.

1. Van Breemen & Dodson (1972) indicated that the average of 20 biotite and K-feldspar Rb/Sr ages confirm a strong thermal event at 2000 ± 70 Ma. They stated that equilibration of Sr isotopes at 2000 Ma in the Limpopo Belt can be related to intrusive events

in South Africa. A granitic phase of a migmatite, in the NMZ of the Limpopo Belt, just south of the boundary with the Mweza Greenstone Belt, gave a Rb-Sr isochron age of 2010 ± 60 Ma, based on K-feldspar, plagioclase and whole-rock data. The biotite-whole rock result is slightly lower, 1940 ± 50 Ma. Also, a 'remobilised' granitic gneiss 'near the Mweza schist belt' gave a date of 1900 ± 50 Ma, based on biotite-plagioclase, which is slightly lower than the corresponding feldspar age. Van Breemen & Dodson (1972) argued that the huge time gap between the major stage of the metamorphic and structural evolution of the (NMZ of) the Limpopo Belt (around 2.6 Ga, see Table 22 and below) and the mineral ages can be explained either by uplift and cooling 2000 Ma ago, after a long period of fairly deep burial, or overprinting by a 2000 Ma metamorphic episode.

As explained for radiogenic Ar in Section 5.2.2, the uplift/cooling hypothesis is based on the idea that micas buried at moderate depths may lose radiogenic Sr continuously until uplift, erosion and consequent cooling reduce their temperature rapidly to a level ('blocking temperature') at which ^{87}Sr can accumulate; dates measured on these minerals will then give the time of cooling. However, van Breemen & Dodson (1972) considered that it would be doubtful that isotopes of strontium could migrate through feldspars without intense reheating. Therefore, they stated that a low-grade metamorphic overprint would be necessary to explain the uniformity of the 2000 Ma mineral ages.

2. Wilson (1990) and Wilson *et al.* (1987) pointed out that the Mashonaland Igneous Event (2000-1800 Ma) is seen as one affecting the whole Zimbabwe craton and, marginally, the NMZ of the Limpopo Province. The intrusions of the Mashonaland Igneous Event would have accompanied a widespread reactivation of the Great Dyke fracture pattern that resulted from the dextral shear couple imposed by the westward (west-southwest) movement of the CZ of the Limpopo Belt across the NMZ and the Zimbabwe Province. Wilson (1990) argued that temperature rise due to burial and subsequent cooling would explain the c. 2000 Ma mineral ages in the southern part of the Zimbabwe craton and the magnetic resetting of the Great Dyke main satellite to the near Mashonaland direction. The fracture pattern followed by the Mashonaland intrusions may have been the brittle response of the Zimbabwe block (Zimbabwe craton and the NMZ) to the dextral shear couple, which would be imposed upon it by this movement of the CZ of the Limpopo Belt.

3. Kamber *et al.* (1995a) stressed that in nearly all tectonic models of continent-continent collision between the Zimbabwe and Kaapvaal cratons, the metamorphic events documented by mineral parageneses throughout the Limpopo belt have been regarded as coeval with the Late Archean thrusting events in the Marginal Zones (~2.6 Ga). The age of tectonism both in the Southern Marginal Zone (SMZ) – Kaapvaal Craton boundary and on the NMZ – Zimbabwe Craton boundary were determined by dating syn- and post-tectonic plutons. Because the authors noticed a common prior dismissal of all ~ 2.0 Ga ages, their study focused on unravelling the significance of the existing 2.0 Ga dates.

They argued that Triangle Shear Zone (TSZ) mylonites in the Limpopo belt (Fig. 76) equilibrated at 2.0 Ga, under high-temperature conditions (700-850°C) and pressures between 5 and 9 kilobar. Pb-Pb dates obtained for syn-deformational garnets are grouped closely around 2040 Ma and can be considered as the age of strike-slip movement during high temperature metamorphism (M_{TSZ}).

Garnets from re-metamorphosed leucosomes are closely clustered around 2220 Ma. This age is interpreted as dating the time of migmatization, which clearly predates the

Table 22. Summary of dates and events reported in the literature, of relevance to the Sandawana area, Mweza greenstone belt, Zimbabwe.

Date (Ma)	Method	Mineral, rock	Area	Significance of result	Authors
1838 ± 230	Rb-Sr whole rock	Mafic sills	Zimbabwe Craton	Mashonaland igneous event	Wilson <i>et al.</i> , 1987
1875 ± 6	Rb-Sr isochron	Biotite from enderbite	Limpopo NMZ s.s., Renco Mine	Cooling age of a postgranulite facies tectono-thermal overprint	Blenkinsop & Frei, 1996
1900 ± 50	Rb-Sr isochron	Biotite and plagioclase, granitic gneiss	Limpopo NMZ, s.s., very near Mweza belt	Low grade metamorphic episode	Van Breemen & Dodson, 1972
1933 ± 25	Ar-Ar	Hornblende from amphibolites	Limpopo NMZ s.s.	Cooling age metamorphism related to TSZ shearing event	Kamber <i>et al.</i> , 1995b
1940 ± 50	Rb-Sr isochron	Biotite and whole rock data	Limpopo NMZ s.s.	Low grade metamorphic episode	Van Breemen & Dodson, 1972
1954.9 ± 8.2	Ar-Ar	Hornblende from amphibolites	Limpopo NMZ s.s.	Cooling age metamorphism related to TSZ shearing event	Kamber <i>et al.</i> , 1995b
1955.0 ± 3.3	Ar-Ar	Hornblende from amphibolites	Limpopo NMZ s.s.	Cooling age metamorphism related to TSZ shearing event	Kamber <i>et al.</i> , 1995b
1959 ± 17	Pb-Pb isochron	Sphene, biotite, from charnockite	Limpopo NMZ s.s.	Age of sphene growth during low T recrystallisation	Kamber <i>et al.</i> , 1996
1969 ± 28	Ar-Ar errorchron	Hornblende data from metabasite	Limpopo NMZ s.s.	Age of retrograde mineral growth	Kamber <i>et al.</i> , 1996
1971 ± 11	Pb-Pb isochron	Sphene, biotite, epidote from charnockite	Limpopo NMZ s.s.	Age of sphene growth during low T recrystallisation	Kamber <i>et al.</i> , 1996
1978 ± 31	Sm-Nd isochron	Garnet	Limpopo TSZ	Minimum age strike-slip movement	Kamber <i>et al.</i> , 1995a
1999 ± 14	Ar-Ar	Hornblende from amphibolites	Limpopo NMZ s.s.	Peak age metamorphism related to TSZ shearing event	Kamber <i>et al.</i> , 1995b
2000 ± 70	Rb-Sr isochron	Biotite and K-feldspar (average of 20)	Limpopo Belt	Low grade metamorphic episode	Van Breemen & Dodson, 1972
2001 ± 11	Ar-Ar	Hornblende from amphibolites	Limpopo NMZ s.s.	Peak age metamorphism related to TSZ shearing event	Kamber <i>et al.</i> , 1995b
2010 ± 60	Rb-Sr isochron	K-feldspar, plagioclase and whole rock data, granitic phase of migmatite	Limpopo NMZ s.s.	Low grade metamorphic episode	Van Breemen & Dodson, 1972
2040 ± 15	Ar-Ar	Hornblende	Limpopo NMZ s.s.	Reflects shearing event TSZ	Kamber <i>et al.</i> , 1995a
~2040	Pb-Pb	Syn-deformational garnets	Limpopo TSZ	Shearing (strike-slip movement) in TSZ	Kamber <i>et al.</i> , 1995a
2155 ± 21	Ar-Ar	Hornblende	Limpopo NMZ s.s.	Reflects TSZ shearing event	Kamber <i>et al.</i> , 1995a
2514 ± 16					
(2451 ± 15)	Rb-Sr whole rock	Layered ultramafics	Zimbabwe craton	Intrusion Great Dyke	Hamilton, 1977 (Kamber <i>et al.</i> , 1996, recalculated)

2520 ± 44	Rb-Sr whole rock isochron	Granite	Zimbabwe craton	Intrusion age Chibi granite	Hawkesworth <i>et al.</i> , 1979
2544 ± 39	Pb-Pb isochron	Pyroxene in enderbite	Limpopo NMZ <i>s.s.</i>	Formation age pyroxene during granulite facies metamorphism	Blenkinsop & Frei, 1996
2571 ± 5	U-Pb isochron	Zircon in enderbite	Limpopo NMZ <i>s.s.</i>	Intrusion age enderbite	Blenkinsop & Frei, 1996
2583 ± 52	Rb-Sr whole rock isochron	Composite sample suite of intrusive charnockite, granites, enderbites, retrogressive zones in enderbite	Limpopo NMZ <i>s.s.</i>	Indication of preceding crustal residence time	Mwkweli <i>et al.</i> , 1995, Berger <i>et al.</i> , 1995
2591 ± 4	U-Pb	Zircon in charnockite intrusion	Limpopo NMZ, <i>s.s.</i> , northernmost part	Peak HT-LP granulite facies metamorphism	Kamber <i>et al.</i> , 1996
2601 ± 5	Pb-Pb isochron	Syn- to postkinematic garnet of a protomylonite	Limpopo NMZ <i>s.s.</i>	Dates waning of tectonic activity in shear zone south of Renco	Blenkinsop & Frei, 1996
2603 ± 64	U-Pb	Zircon in enderbite	Limpopo NMZ <i>s.s.</i>	Intrusion age enderbite	Berger <i>et al.</i> , 1995
2620 ± 22	Rb-Sr whole rock isochron	Granite	Zimbabwe craton	Intrusion age Chibi granite	Hawkesworth <i>et al.</i> , 1979
2627 ± 7	U-Pb	Zircon in late-kinematic micro-granite, cutting porphyritic granite	Limpopo NMZ <i>s.s.</i>	Intrusion age Razi granite, minimum age reverse shearing NMZ on Zimbabwe craton	Mkweli <i>et al.</i> , 1995
2637 ± 19	U-Pb	Zircon in enderbite	Limpopo NMZ <i>s.s.</i>	Intrusion age enderbite	Berger <i>et al.</i> , 1995
2710 ± 38	U-Pb	Zircon in enderbite	Limpopo NMZ <i>s.s.</i>	Intrusion age enderbite	Berger <i>et al.</i> , 1995
2880 ± 47	Rb-Sr whole rock errorchron	Charnoenderbite and migmatite	Limpopo NMZ central part	Age of granulite facies metamorphism	Rollinson & Blenkinsop, 1995

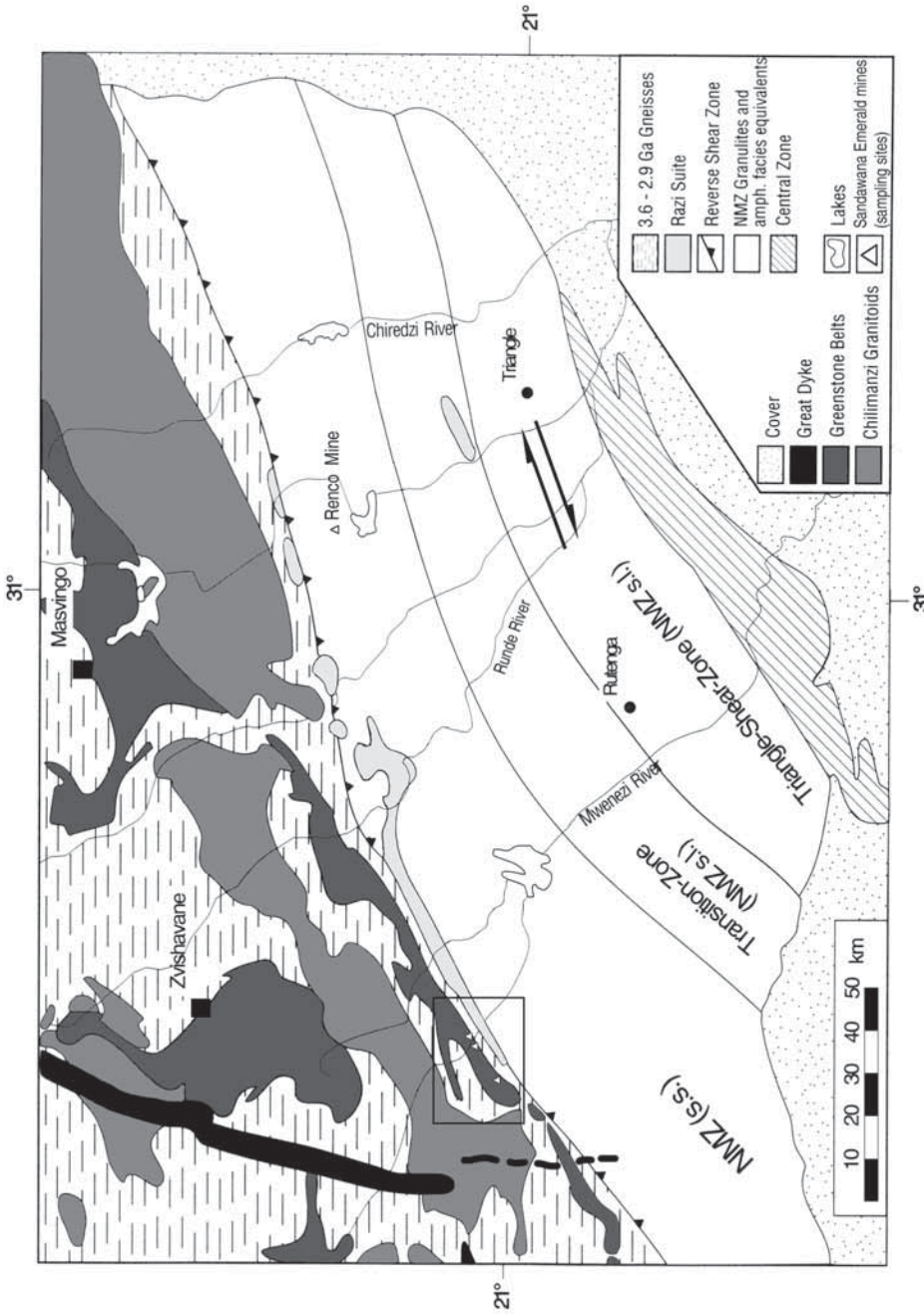


Fig. 76. Geological sketch map of the Limpopo belt (Northern Marginal Zone) and the southern margin of the Zimbabwe craton (redrawn after Berger *et al.*, 1995, fig. 2; Kamber *et al.*, 1995a, fig. 1; Blenkinsop & Frei, 1996, fig. 1).

strike-slip movement in the TSZ. Sm-Nd garnet data can be fitted to an isochron of broadly similar age as the Pb-Pb ages on syn-deformational garnet. Assuming total equilibration the isochron yields an age of 1978 ± 31 Ma. Kamber *et al.* (1995a) interpreted these as prograde ages, but due to incomplete isotopic homogenization during metamorphic reactions they must be regarded as minimum ages for the timing of M_{TSZ} . Kamber *et al.* (1995a) also presented Ar-Ar dating results on two hornblende samples from the NMZ, which yielded ages (2040 ± 15 and 2155 ± 21 Ma) that cannot be attributed to the 2.6 Ga Limpopo orogeny, but seem to reflect M_{TSZ} .

In conclusion, right-lateral strike-slip movement along the TSZ appears to have happened around 2000 Ma. The high geothermal gradient produced by rapid uplift (isothermal decompression) quickly evolved towards a more normal continental geotherm. In this concept, the mentioned Ar-Ar ages, as well as the 1950-2000 Ma Rb-Sr biotite ages obtained by Van Breemen & Dodson (1972), may be seen as dating the cooling through their blocking temperatures. The geographic extent of such ages, covering not only the whole Limpopo Belt, but also parts of the cratons, is noteworthy.

While the evidence that thrusting of NMZ rocks over the Zimbabwe Craton and of SMZ rocks over the Kaapvaal Craton around 2.60 and 2.67 Ga ago, respectively, clearly remains, Kamber *et al.* (1995a) believed that the 2.0 Ga event in the TSZ with its high-pressure, high-grade metamorphism cannot be described as a mere reactivation. It must be tied to a major tectonic episode. Thus, the southern and northern parts of the Limpopo Belt, with their respective Late Archaean tectonism, are separated from each other by a very major strike-slip structure which is 600 Ma younger. In addition, according to Kamber *et al.* (1995a), it is very uncertain to which event the various metamorphic PT paths obtained in the NMZ and SMZ may be assigned. For these reasons they stated that there is no basis for tectonic models in which the entire Limpopo Belt is seen as the product of a Late Archaean collision between the Zimbabwe and the Kaapvaal Craton.

The postulation of a step isothermal decompression path is in agreement with the observation that the Proterozoic tectono-metamorphism, unlike the Archaean evolution, has not been accompanied by widespread magmatism. The absence of voluminous magmatism enables delay of the extension of overthickened crust, which is needed to produce the path observed.

4. Kamber *et al.* (1995b) elaborated on the shearing event at the TSZ, affecting the southern half of the NMZ Zone at 2.0 Ga. The NMZ can be subdivided into the TSZ, a Transition Zone and the Northern Marginal Zone *s.s.* (Fig. 76). A structural profile through the Transition Zone well into the TSZ reveals deformation patterns which indicate that a single deformation occurred. This event consisted of subvertical extension and dextral shear, and can therefore be called transpression.

The authors argued that the NMZ *s.s.*, adjacent to the southern margin of the Zimbabwe craton, has only been weakly affected by the Proterozoic metamorphism, associated with the TSZ transpression, only inasmuch as the Rb/Sr system in biotite became reset. This view is consistent with data and interpretation of Van Breemen & Dodson (1972).

Kamber *et al.* (1995b) obtained five near-plateau ages between 2.00 and 1.93 Ga in chemically diverse hornblendes from various amphibolites. The spread in age of 68 m.y. can neither be attributed to the geographic distribution of the samples nor to the lineation they define. The authors argued that the best explanation for this range of age is

that there was a single event that occurred at 2.0 Ga. Two hornblendes give a peak age in agreement with the ages from the TSZ, whereas a sphene (Pb/Pb: 1.97 Ga) and three hornblendes give cooling ages. This interpretation presumes no geographic or structural control of the age range and, further, pure diffusional Ar loss during uniform slow cooling. The proximity of the amphibole samples justifies this interpretation. Kamber *et al.* (1995b) stated that the lack of microstructural/mineralogical recrystallization or phyllosilicate alteration of the hornblendes suggests that they cooled in a fluid-absent, deformationally static environment, such that volume-diffusion most likely governed post-2.00 Ga ^{40}Ar loss from minerals. The five near-plateau, 2.00-1.93 Ga ages are inversely correlated with 'ionic porosity' Z. This parameter (Dowty, 1980; Fortier & Giletti, 1989), defined as the percentage of unit cell not occupied by ions, is a first-order approximation for the overall length and strength of the ionic bonds in a crystal and is thus a good proxy for the resistance that a given lattice will exert on the diffusion of Ar. A quantitative model using the concept of 'ionic porosity' Z (Dahl, 1994, 1996) shows that Z ranges from 36.7 to 37.8%; these values correspond to a 41 ± 9 K difference in the model closure temperature. This translates into a model cooling rate which is consistent with an independent cooling rate of 1.0 ± 0.5 K/ m.y. from garnet, sphene and biotite.

5. Kamber *et al.* (1996) dated the peak of granulite facies metamorphism in the northernmost part of the NMZ at 2591 ± 4 Ma using conventional U-Pb zircon geochronology on a syntectonic charnockite intrusion. The thermal peak was reached during compressional deformation (= horizontal shortening) and coincided with vast granite intrusion into the overlying craton (compare Sections 2.2.1, 2.2.2 and Table 22: Hawkesworth *et al.*, 1979; Mkweli *et al.*, 1995). According to Kamber *et al.* (1996), after initial exhumation and cooling, the granulite facies rocks resided at a comparatively shallow depth (~ 10 km) for 620 Ma. They also stated that field, microstructural and geochronological investigation of a low-temperature overprint established that reworking and final exhumation occurred at 1.97 Ga along discrete greenschist facies thrusts. Early Proterozoic deformation would have lasted 10 to 20 Ma.

Retrogression of granulites in the NMZ *s.s.* is macroscopically confined to dm to m wide shear zones, which appear to have acted as pathways for fluid during retrogression. Samples taken from low-grade thrusts are characterized by a mylonitic fabric, and a mineral assemblage consisting of epidote, green-brown biotite, Fe-rich dark green amphibole and sphene, indicating lowermost amphibolite facies conditions and the presence of an H_2O -rich fluid. In the northernmost mylonites, no amphibole was found. Here, chlorite, epidote and biotite prevail. The local growth of new garnet in biotite-rich layers (pelitic composition) requires T of $\geq 420^\circ\text{C}$ (Yardley, 1989). Feldspar clasts record brittle behaviour, which constrains the upper T limit for retrograde recrystallization to $\leq 500^\circ\text{C}$.

Mafic rocks generally show much less evidence for retrogression. Hornblendes from a particular mafic granulite, 50 km eastsoutheast of Sandawana, scatter in age from 3.7 down to 2.05 Ga. No unambiguous age information can be extracted. It is, however, interesting to note that the early Proterozoic event, which did not exceed 500°C , has led to substantial loss of radiogenic Ar. The partial resetting of old (>2.6 Ga) hornblende did not produce a simple core(old)-rim(young) relationship. This may indicate that recrystallisation, even if minor, was able to dominate diffusion processes.

Biotite defines a narrow age cluster around 1.97 Ga. Textural observations confirmed

that biotite is a late phase, related to a new fabric forming event. It has Ar ages that are identical to Pb-Pb sphene ages.

Kamber *et al.* (1996) equated the time of the latest low-grade overprint with a north-northwest thrusting within the NMZ *s.s.* and the NMZ *s.s.* as a unit over the Zimbabwe craton. In spite of the comparatively low T (<500°C), the Ar systematics of granulite grade amphibole became partially reset during this event in contrast to the behaviour of amphiboles in the dryer Transition Zone, which retained Ar around 580°C (Kamber *et al.*, 1995b; Table 21 herein). This underlines that thermal diffusion is an intrinsically slow process and that temperature alone is not the rate-controlling parameter whenever fluids are present.

The NMZ *s.s.* is 80 km away from the centre of the early Proterozoic orogenic units further to the south, and the area in between records a decrease in metamorphic grade and a change in structural style. According to Kamber *et al.* (1996), the NMZ *s.s.* does show internal shortening during this event, but only at 1.97 Ga, clearly resolved from their postulated peak of metamorphism at 2.0 Ga in the Central Zone and the Triangle Shear Zone. They stated that deformation thus took place while the central part of the orogen was rapidly exhumed and, indeed, cooling ages from the Central Zone match with peak ages in the NMZ *s.s.* The low-grade 1.97 Ga deformation in the NMZ *s.s.* is interpreted to reflect a foreland response, partially reactivating older structures, to rapid tectonic unroofing further south.

Thus, Kamber *et al.* (1996) argued that the jump in metamorphic P between craton and Limpopo belt encompasses the effects of both Proterozoic and Archaean thrusting. In the western portion of the NMZ *s.s.* (close to Sandawana), early Proterozoic thrusting may be called in question because the 2.45 Ga Great Dyke extends relatively undisturbed over the craton-belt boundary. However, Kamber *et al.* (1996) argued that remagnetisation of the extension of the Great Dyke into the NMZ *s.s.*, and sinistral displacement of each of the five segments, are compatible with a 1.97 Ga compression and resulting exhumation of the NMZ *s.s.*

6. On the contrary, Blenkinsop & Frei (1996) confirmed that the major reverse movement in the shear zone between the NMZ and the Zimbabwe craton has been dated at ~2.6 Ga, and that the NMZ had been exhumed to crustal levels corresponding to greenschist facies by this time. They argued that a major part of the exhumation of NMZ granulites, at least to lower greenschist facies conditions, occurred within a time span of < 200 m.y. and, thus, possibly within the same orogenic cycle, after peak metamorphism. This is based on the intrusion age of high level, undeformed pyroxenite dykes (cutting through the Zimbabwe craton – NMZ boundary), bracketed by a minimum Pb-Pb age of 2399 Ma obtained from garnet and by the host enderbite date of 2571 Ma. The intrusion age, the northnortheast orientation and undeformed nature of these dykes suggest a relationship to the Great Dyke and its satellites.

However, the major gold mineralization at the Renco Mine (Fig. 76) occurred under greenschist facies conditions (< 400°C) at 2.0 Ga. The *c.* 2.0 Ga age of the mineralization (Blenkinsop & Frei, 1996) implies a link with the Early Proterozoic tectono-thermal event in the Limpopo Mobile Belt. Chlorite, epidote and calcite are associated with cataclastic deformation, and document the prevalence of greenschist facies metamorphic conditions. Granitic pegmatites intruded the shear zones during brittle conditions and are only weakly deformed. Biotite is confined to high strain zones with higher fluid circula-

tion. A biotite Rb-Sr age of 1875 ± 6 Ma is interpreted as a cooling age of a later, post-granulite facies tectono-thermal overprint in the Renco area, during which K-rich solutions invaded pre-existing high strain zones in the course of brittle deformation.

Contrary to the conclusions of Blenkinsop & Frei (1996), Kisters *et al.* (1997) attempted to show that deformation and fluid flow (i.e., mineralization and alteration) at the Renco mine occurred under mid-amphibolite facies conditions at temperatures around 600°C in a high-temperature ductile shear zone system that formed as a second-order splay during the northnorthwest-directed regional scale thrusting of the NMZ onto the Zimbabwe craton during the Late Archean. According to them, the Middle Proterozoic greenschist facies alteration and brittle deformation postdate the gold mineralization. Although in their reply Blenkinsop & Frei (1997) stressed that one of the difficulties in recognizing the existence of Proterozoic deformation throughout the NMZ is that it could have very similar kinematics to those of the Late Archean deformation, as shown farther south in the NMZ by Kamber *et al.* (1995b), the two parties seem to agree on the brittle nature of the Proterozoic deformation.

In conclusion, the diverse geochronological data basically reflect three types of event (Fig. 77); regional metamorphism (peak and/or cooling age), intrusion and local deformation (shearing). These different ages indeed cluster around 2600 and 2000 Ma, which indicate two major events, affecting the Limpopo NMZ/Zimbabwe craton

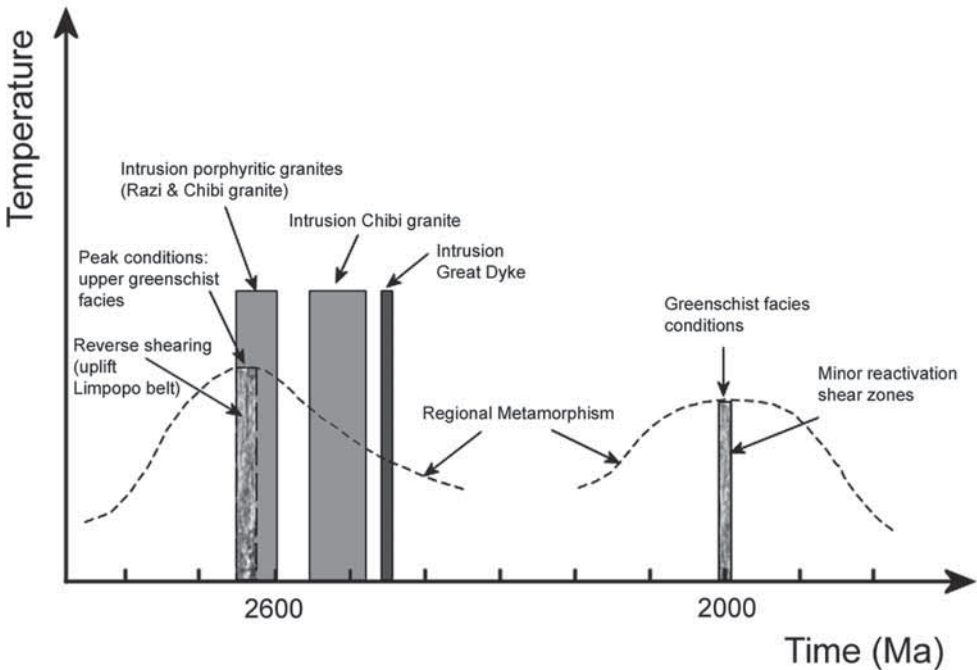


Fig. 77. Framework of important events affecting the Sandawana area in the Mweza Greenstone Belt, at the Zimbabwe craton – Limpopo belt (NMZ) boundary. Major uplift of the Limpopo Belt relative to the Zimbabwe craton took place around 2.6 Ga. Hawkesworth *et al.* (1979) generated two Rb-Sr whole-rock isochrons for 15 samples of Chibi Granite, one at 2520 Ma and the other at 2620 Ma.

boundary, and thus the Sandawana area. At 2600 Ma, the 3.0 Ga old greenstones of the Mweza belt were folded and underwent greenschist facies metamorphism, during uplift of the NMZ against the Zimbabwe craton, along a series of parallel shear-zones. At the same time, porphyritic granites intruded into the shear-zone and also the pegmatites found within the MGB were intruded just prior and/or during folding and shearing of the greenstones (Section 2.4). At c. 1970 Ma, the shear-zones could have been re-activated to some extent, which was interpreted by Kamber *et al.* (1996) as a result of internal shortening of the NMZ *s.s.*, in response to the 2.0 Ga shear event in the TSZ, and the subsequent rapid exhumation of the central part of the Limpopo orogen. The associated low-grade thermal overprint took place at greenschist facies conditions. This Proterozoic event was not accompanied by major magmatic activity.

5.2.4. $^{40}\text{Ar}/^{39}\text{Ar}$ on amphibole and phlogopite

Materials and analytical method – The argon isotope analyses were performed at Nice (UMR Géosciences Azur) by Alain Cheilletz (CRPG-CNRS). As already mentioned in Section 5.2.1, $^{40}\text{Ar}/^{39}\text{Ar}$ were performed on single grains of amphibole and biotite extracted from three metasomatised rocks, which were present at three different emerald-bearing zones (Aeres mine and two locations at the Zeus mine), at the contact between deformed pegmatite and greenstone. Grain size for single grain analyses are in the order of 400-600 μm . The samples were irradiated in the nuclear reactor at McMaster University in Hamilton, Canada. The irradiation flux was calculated using the Hb3gr hornblende (1072 Ma; Roddick, 1983) as irradiation monitor. The analytical procedures for single grain analyses are described in detail by Féraud *et al.* (1982), Ruffet *et al.* (1991) and Alexandrov *et al.* (2002). The gas extraction of single grains was carried out by a Coherent Innova 70-4 continuous argon-ion laser. The laser beam was approximately 2.5 times larger than the analysed grain to obtain homogeneous heating. The purified gases were introduced into a VG3600 mass spectrometer and analysed in static mode with a Daly photomultiplier system.

The argon isotopes and the background baselines were measured in eleven cycles in peak-jumping mode. Blanks were performed routinely each first or third run and subtracted from the subsequent sample gas fractions. All isotope measurements were corrected for K and Ca isotope interferences, mass discrimination and atmospheric argon contamination. All errors are quoted at the 1σ level. To define a plateau age, at least three consecutive steps are necessary, corresponding to a minimum of 70% of the total $^{39}\text{Ar}_k$ released, and the ages of the individual fractions must agree with the mean age of the plateau segment within 2σ error. In addition, pseudo-plateau ages were defined with less than 70% of the total $^{39}\text{Ar}_k$ released.

Results – The results of the respective analyses are given in Table 23. The plateau and pseudo-plateau ages that came out are presented in Figures 78 to 81 and summarised in Table 24.

Two phlogopites and one amphibole display good plateau ages. Amphibole 421759 yields a plateau age at 1935.4 \pm 6.7 Ma, corresponding to 75.06% $^{39}\text{Ar}_k$ released. Phlogopites 421372 and 421594 yield two identical plateau ages at 1903.8 \pm 8.0 Ma (70.02% $^{39}\text{Ar}_k$ released), and 1901.7 \pm 2.2 (72.57% $^{39}\text{Ar}_k$ released), respectively. The biotite ages are therefore \sim 30 Ma younger than the amphibole age.

Table 23. $^{40}\text{Ar}/^{39}\text{Ar}$ laserprobe analyses of amphibole and phlogopite from the Sandawana emerald mines, Mweza Greenstone Belt, Zimbabwe.

Step n°	Atmospheric contamination (%)	^{39}Ar (%)	$^{37}\text{Ar}_{\text{Ca}}/^{39}\text{Ar}_{\text{K}}$	$^{40}\text{Ar}^*/^{39}\text{Ar}_{\text{K}}$	Age (Ma)		
421 759 amphibole single grain (G918)							
406	30.765	0.68	2.575	104.784	1785.7	±	65.6
482	3.550	9.30	10.898	136.057	2095.8	±	10.0
492	0.000	4.61	27.119	120.865	1951.8	±	14.5
511	0.144	7.18	23.374	117.727	1920.5	±	12.4
521	0.292	9.57	32.094	120.648	1949.6	±	9.6
530	0.230	10.09	34.541	119.628	1939.5	±	9.3
540	0.152	36.01	34.422	118.683	1930.1	±	4.3
545	0.000	13.81	34.767	119.992	1943.1	±	7.7
561	0.280	5.58	34.967	119.226	1935.5	±	15.0
1111	0.000	3.18	42.110	121.792	1960.9	±	24.4
						Integrated age = 1951.4 ± 2.9 Ma	
421 759 phlogopite single grain (H120)							
330	72.438	0.71	0.000	90.064	1619.0	±	99.4
351	40.562	5.64	0.000	135.290	2088.8	±	9.8
356	4.339	14.45	0.002	160.149	2302.9	±	4.2
361	2.658	21.55	0.000	160.341	2304.4	±	2.9
370	1.897	15.99	0.001	162.293	2320.2	±	3.8
373	1.310	5.75	0.006	152.940	2243.4	±	6.5
382	1.160	13.15	0.004	155.687	2266.3	±	3.6
392	0.545	11.21	0.001	153.195	2245.5	±	4.8
402	0.686	4.12	0.007	146.847	2191.4	±	6.8
416	0.469	3.45	0.006	143.077	2158.6	±	9.8
431	0.000	1.51	0.010	136.420	2099.1	±	18.4
461	1.186	1.12	0.003	130.711	2046.4	±	21.8
520	0.000	0.73	0.044	137.733	2111.0	±	26.2
1111	1.944	0.62	0.032	141.065	2140.8	±	34.6
						Integrated age = 2258.5 ± 1.6 Ma	
421 759 phlogopite single grain (G915)							
320	47.965	0.17	0.363	58.726	1202.5	±	125.4
339	32.113	1.48	0.063	112.162	1863.8	±	16.8
360	9.861	10.36	0.010	138.132	2114.6	±	3.6
365	3.441	10.39	0.003	154.821	2259.1	±	3.2
367	2.850	7.16	0.007	156.731	2274.9	±	5.0
369	2.186	8.30	0.011	156.938	2276.6	±	3.5
362	2.063	4.82	0.022	158.601	2290.3	±	5.1
364	3.717	1.02	0.112	158.430	2288.9	±	16.4
368	1.698	1.49	0.023	160.084	2302.4	±	8.6
373	1.712	5.30	0.010	157.913	2284.6	±	5.9
378	1.893	9.18	0.010	161.614	2314.7	±	3.0
382	1.792	8.09	0.014	160.893	2308.9	±	4.6
386	1.759	15.32	0.015	161.756	2315.9	±	4.2
388	1.032	4.90	0.011	153.179	2245.4	±	5.3
392	0.947	2.73	0.037	149.728	2216.2	±	7.6
401	1.034	2.69	0.031	149.596	2215.1	±	4.6
416	1.081	1.93	0.034	153.139	2245.0	±	10.4
440	1.351	2.30	0.025	166.496	2353.7	±	8.3
500	0.000	1.20	0.000	158.055	2285.8	±	10.5
777	0.229	1.17	0.000	146.820	2191.2	±	14.4
						Integrated age = 2261 ± 1 Ma	

(Table 23 continued)

Step n°	Atmospheric contamination (%)	³⁹ Ar (%)	³⁷ Ar _{Ca} / ³⁹ Ar _K	⁴⁰ Ar*/ ³⁹ Ar _K	Age (Ma)		
421 594 phlogopite single grain (G920)							
318	61.626	0.13	0.000	42.697	945.5	±	63.1
338	42.746	0.24	0.016	56.466	1168.5	±	34.4
360	76.368	2.27	0.006	108.676	1827.3	±	23.7
363	48.649	2.83	0.010	112.935	1871.8	±	10.2
365	23.059	1.99	0.016	113.175	1874.2	±	5.4
368	19.088	1.92	0.021	113.069	1873.2	±	5.9
373	15.419	2.34	0.003	114.093	1883.7	±	5.8
380	10.589	6.64	0.001	114.839	1891.3	±	3.9
383	4.845	5.01	0.004	115.382	1896.8	±	3.1
398	2.933	10.77	0.005	115.433	1897.4	±	2.3
401	1.636	7.84	0.004	115.395	1897.0	±	3.3
404	1.340	3.28	0.013	116.046	1903.6	±	2.7
410	1.196	6.61	0.001	115.404	1897.1	±	3.3
418	0.900	9.46	0.003	116.238	1905.5	±	2.7
425	0.847	10.77	0.005	116.167	1904.8	±	2.8
429	0.832	9.79	0.008	116.235	1906.0	±	2.3
431	0.705	5.33	0.000	116.114	1904.3	±	2.9
434	0.683	3.72	0.010	116.213	1905.3	±	4.2
435	0.778	2.60	0.012	117.091	1914.1	±	4.0
440	0.435	1.54	0.000	117.038	1913.6	±	7.2
451	0.949	1.22	0.010	115.585	1898.9	±	7.8
490	0.739	2.84	0.014	116.502	1908.2	±	4.1
563	1.823	0.68	0.154	116.821	1911.4	±	10.8
1111	0.519	0.19	0.056	117.814	1921.4	±	25.4
					Integrated age = 1895.4 ± 1.0 Ma		
421 594 amphibole single grain (H119)							
365	5.400	2.05	0.807	81.196	1572.1	±	22.1
412	0.952	22.18	0.254	109.185	1901.8	±	4.2
424	0.043	14.09	0.231	106.463	1872.2	±	5.3
435	0.409	14.65	1.137	109.762	1907.9	±	3.8
446	0.359	13.41	2.517	109.240	1902.3	±	4.3
458	0.000	8.09	6.488	113.853	1951.3	±	5.6
473	0.000	6.05	12.069	111.458	1926.0	±	9.8
505	0.000	15.83	49.967	118.461	1998.9	±	5.7
521	0.000	2.27	41.567	107.944	1888.3	±	24.6
1111	1.993	1.38	91.671	118.850	2002.9	±	27.5
					Integrated age = 1914.9 ± 2.0 Ma		
421 372 phlogopite single grain (G919)							
320	84.743	0.02	1.971	53.284	1119.3	±	456.9
340	53.058	0.19	0.345	62.691	1260.9	±	54.7
378	70.548	4.49	0.021	109.218	1833.0	±	17.1
381	37.264	4.84	0.004	112.918	1871.6	±	7.1
384	19.144	6.89	0.007	114.574	1888.6	±	4.8
387	9.986	3.85	0.014	114.103	1883.8	±	4.9
388	4.161	9.71	0.000	115.239	1895.4	±	3.6
399	1.563	15.52	0.001	115.925	1902.4	±	2.5
403	1.039	16.12	0.000	116.034	1903.5	±	3.3
405	0.917	12.20	0.006	116.197	1905.1	±	3.0
407	0.689	8.80	0.002	116.312	1906.3	±	2.7
410	0.747	4.61	0.012	115.324	1896.3	±	3.5
417	1.223	2.42	0.031	115.449	1898.0	±	6.3

(Table 23. continued)

Step n°	Atmospheric contamination (%)	³⁹ Ar (%)	³⁷ Ar _{Ca} / ³⁹ Ar _K	⁴⁰ Ar*/ ³⁹ Ar _K	Age (Ma)		
430	1.165	3.28	0.033	115.585	1898.9	±	7.3
455	0.328	3.25	0.016	116.870	1911.9	±	7.0
499	0.190	1.30	0.053	116.391	1907.1	±	12.8
1111	0.253	2.52	0.016	117.155	1914.8	±	5.1
Integrated age = 1895.4 ± 1.3 Ma							
421 372 amphibole single grain (H118)							
381	8.693	1.02	2.415	166.671	2433.8	±	65.5
483	1.201	19.34	1.778	203.226	2705.3	±	7.5
493	1.233	5.81	2.887	138.139	2189.3	±	14.5
505	0.393	22.64	46.401	185.227	2576.7	±	7.1
515	0.000	9.57	33.348	195.279	2649.7	±	11.0
525	0.000	20.33	68.944	139.053	2197.6	±	7.3
535	1.378	7.50	48.262	127.556	2089.4	±	17.1
550	0.957	9.84	54.720	143.925	2241.6	±	14.9
571	5.328	1.18	15.619	124.633	2060.8	±	64.6
630	0.099	1.35	47.475	145.221	2253.1	±	66.1
1111	2.774	1.40	54.647	227.857	2867.6	±	48.1
Integrated age = 2446.9 ± 3.8 Ma							

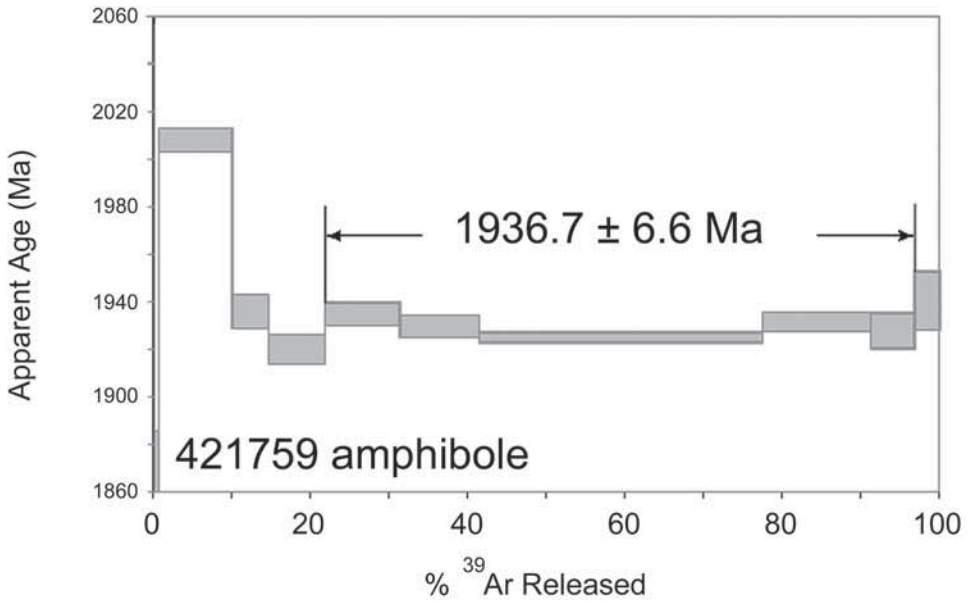


Fig. 78. Cumulative proportion of ³⁹Ar versus age (Ma) for amphibole 421759, from an amphibole phlogopite schist, close to pegmatite and emerald mineralisation, Aeres mine, Sandawana, Zimbabwe.

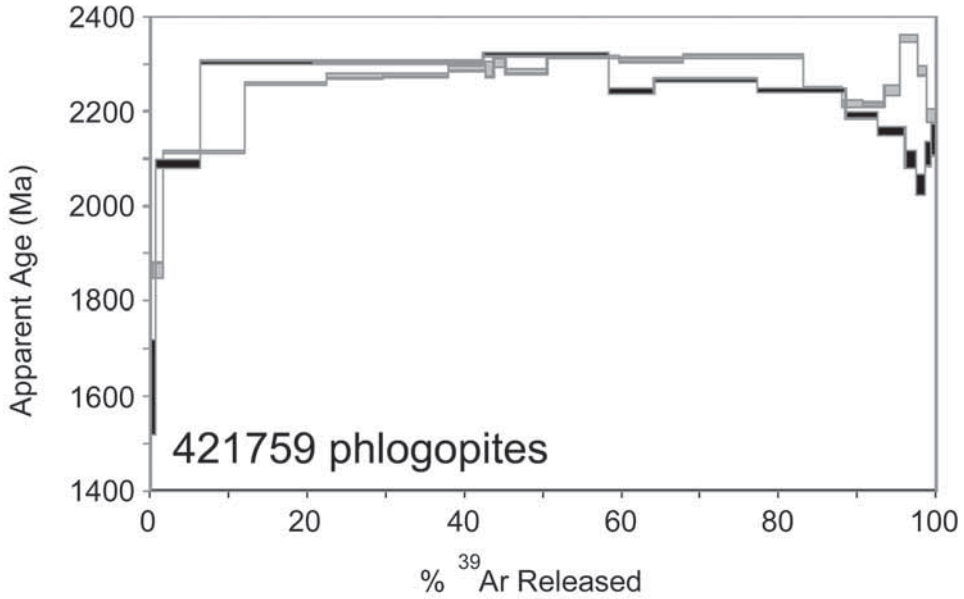


Fig. 79. Cumulative proportion of ³⁹Ar versus age (Ma) for two phlogopites (G918 – grey spectrum, and H120 – black spectrum) from sample 421759, taken from an amphibole phlogopite schist, close to pegmatite and emerald mineralisation, Aeres mine, Sandawana, Zimbabwe.

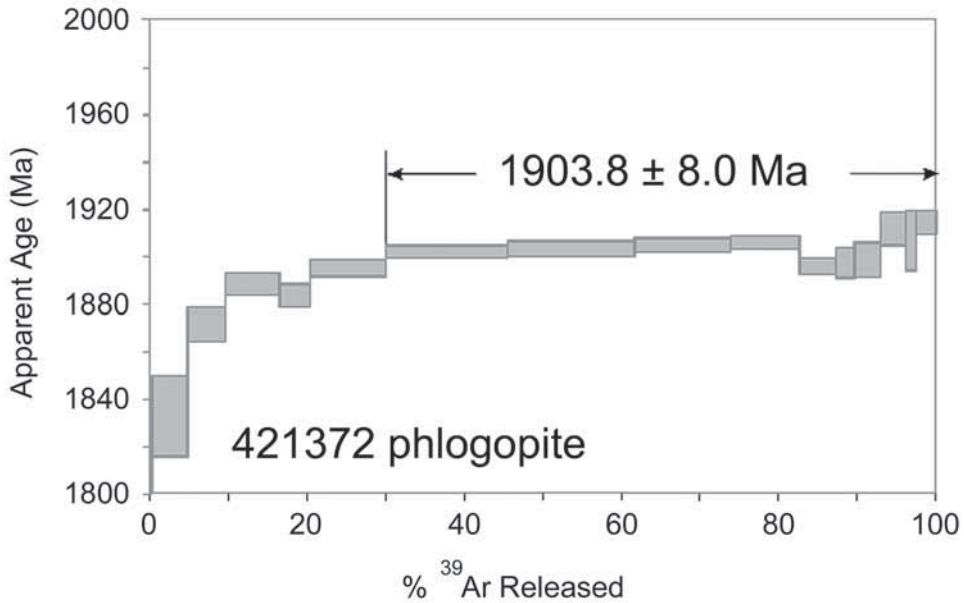


Fig. 80. Cumulative proportion of ³⁹Ar versus age (Ma) for phlogopite 421372, from an amphibole phlogopite schist, close to pegmatite and emerald mineralisation, Zeus mine, 300 ft. underground level, stope 23/7, Sandawana Zimbabwe.

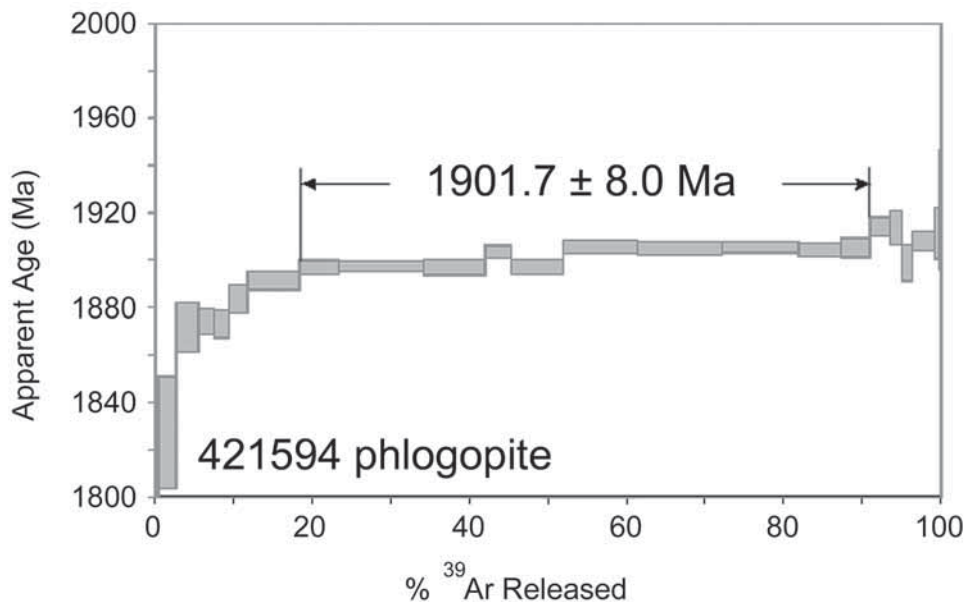


Fig. 81. Cumulative proportion of ^{39}Ar versus age (Ma) for phlogopite 421594, from an amphibole phlogopite schist, close to pegmatite and emerald mineralisation, Zeus mine, 200 ft. underground level, stope 26/28, Sandawana Zimbabwe.

Phlogopites from sample 421759 show a disturbed $^{40}\text{Ar}/^{39}\text{Ar}$ spectrum. For example, grain G915 is characterized by three degassing domains (Fig. 79): a low- to intermediate-temperature domain (0 to 50 % $^{39}\text{Ar}_k$ released) corresponding to a staircase shape; an intermediate temperature domain yielding a pseudo-plateau age at 2313.8 Ma \pm 5.0 (32.6 % $^{39}\text{Ar}_k$ released); and a high-temperature domain characterised by a very irregular shape (83 to 100% $^{39}\text{Ar}_k$ released). The integrated age of phlogopite 421759 (grain G915) is 2261.1 Ma \pm 1.2. The other analysed phlogopite grain from the same sample (Grain H120) shows a similar pseudo-plateau age around 2310 Ma, with a integrated age of 2258.5 \pm 1.6 Ma.

It is interesting to note that the pseudo-plateau age displayed by phlogopites from sample 421759 is \sim 380 Ma older than the plateau age of amphibole from the same sample. Amphiboles 421372 and 421594 give highly disturbed $^{40}\text{Ar}/^{39}\text{Ar}$ spectra, not even showing pseudo-plateau ages. The integrated ages are 2446.9 Ma \pm 3.8 Ma and 1914.9 \pm 2.0 Ma, respectively.

Table 24. Summary of Ar/Ar data based on amphibole and phlogopite.

Locality	RGM no.	Mineral	Ar-Ar plateau age
Aeres mine	421759	Amphibole	1936.7 \pm 6.6 Ma
Aeres mine	421759	Phlogopite	2313.8 \pm 5.0 Ma (pseudo-plateau)
Zeus mine, 300 ft., stope 23/7	421372	Phlogopite	1903.8 \pm 8.0 Ma
Zeus mine, 200 ft., stope 26/28	421594	Phlogopite	1901.7 \pm 8.0 Ma

5.2.5. *Significance of dating results* – Two different phlogopite grains from two different samples (421372 and 421594) give similar ages at ~ 1902 Ma. This age is ~ 35 Ma younger than the amphibole 421759 age at 1937 Ma. The difference in age between amphibole and these phlogopites is best interpreted in a cooling model of the crust after the closure of the isotopic system of the amphiboles; the difference in blocking temperature of amphibole and biotite (200°C) implies a cooling rate of about 6°C/Ma.

Although the older pseudo-plateau ages of phlogopites from sample 421759 do not appear to be reliable, the irregular patterns could indicate partial resetting of the phlogopite grains (Dickin, 1995), which means that they kept some memory of an older event. Old apparent pseudo-plateau ages can also be the result of ^{39}Ar recoil; that is, a significant fraction of ^{39}Ar is lost from the irradiated sample, its $^{40}\text{Ar}/^{39}\text{Ar}$ ratio is increased and its total-release date would be older than its geological age. ^{39}Ar recoil is often related to incipient chloritisation (e.g., Ruffet *et al.*, 1991; McDougall & Harrison, 1999). However, in this case, although they may be strongly folded, the phlogopite grains appear to be fresh and no sign of chloritisation was observed.

Amphibole 421372 and 421594 produced highly disturbed spectra; therefore, the integrated ages can be considered as meaningless. However, it is peculiar that, like the phlogopites showing older pseudo-plateau ages, amphibole 421372 shows older values as well, between 2.1 and 2.9 Ga, perhaps also indicating some memory of an older event (Table 23).

The amphibole and phlogopite plateau ages are in good agreement with $^{40}\text{Ar}/^{39}\text{Ar}$ ages on biotites by van Breemen & Dodson (1972) and Kamber *et al.* (1995b). The only biotites van Breemen & Dodson (1972) dated in the northern part of the Limpopo belt, that are more than 70 Ma away from the mean age of 2000 Ma (Section 5.2.3), come from the Zimbabwe Craton, just north of the NMZ, 'very near the Mweza belt' (Rb-Sr isochron: 1900 ± 50 Ma; Table 22). Kamber *et al.* (1995b) established an Ar/Ar age of 1933 ± 25 Ma, on hornblende from an amphibolite, just south of the Razi porphyritic granite, in the Mwenezi River, very close to the Sandawana mines (Fig. 76). This age may reflect a cooling age of regional metamorphism, related to the TSZ shearing event at 2.0 Ga (Section 5.2.3).

The amphibole age (1936.7 ± 6.6 Ma) obtained at the Aeres mine can also be interpreted as a cooling age, related to the postulated low grade regional metamorphism around 1.97-2.0 Ga (also compare Kamber *et al.*, 1996). As no clear signs of microstructural/mineralogical recrystallization or phyllosilicate alteration of amphiboles are present, the difference between the obtained amphibole age, and other cooling ages and peak ages of amphiboles in the NMZ *s.s.* (varying between 1.93 and 2.00 Ga; Table 22), could be explained by the difference in 'ionic porosity' of various amphiboles, as showed by Kamber *et al.* (1995b) (see Section 5.2.3). The more 'porous' samples (more ^{40}Ar loss by volume diffusion) yield lower ages (1.93-1.95 Ga). In their study, the maximum difference in ionic porosity can correspond to a 41 ± 9 K difference in the model closure temperature. Taking into account that the maximum difference in measured ages is around 70 m.y., according to Kamber *et al.* (1995b) the model cooling rate in this period of time would be around 0.7 (+0.9/-0.3) K/m.y. This is consistent with an independent slow cooling rate of around 1.0 ± 0.5 K/m.y. from garnet, sphene and biotite, as given by Kamber *et al.* (1995b). As indicated at the beginning of this section, from the results presented in this study, it appears that the cooling rate could have been 6°C/m.y. in the period between 1.93 and 1.90 Ga.

5.2.6. *Age of emerald formation at Sandawana* – Zwaan & Touret (2000) stated that isolated decrepitated inclusions, which are present in gem-quality emerald crystals, could indicate a later phase of fast regional decompression (block uplift) after the initial formation of the emeralds. This would imply that the emeralds were formed before the episode of isothermal decompression of the Limpopo-Zimbabwe block and thus well before 1935 Ma, the amphibole Ar-Ar age, interpreted as a cooling age (compare Section 5.2.5).

As the Ar-Ar data on amphibole and phlogopite from the Sandawana area cluster around the 2.0 Ga event, one could draw a straightforward conclusion that the formation of emerald should have occurred during that time. However, as explained in Section 5.2.3., the Sandawana area appears to have been only weakly effected by Proterozoic metamorphism. The 2.0 Ga event caused a thermal overprint and possibly reactivation of shear-zones, which were already in place and were formed during the older 2.6 Ga event. In this case, the Ar-Ar ages could just reflect a resetting of the isotopic system in minerals that were formed long before 2.0 Ga. Therefore, it appears that there are two possibilities regarding the age of emerald formation:

1. Emeralds were formed during the late Archean 2.6 Ga age event, shortly after the intrusion of pegmatites, during the main folding of the greenstone belt, and shearing due to the uplift of the NMZ of the Limpopo belt relative to the Zimbabwe Craton. As a result of metasomatic exchange between an evolving residual melt and greenstones, the emeralds formed in pockets, under structural control, close to the pegmatites. The Ar-systematics of amphibole and biotite became reset during the 2.0 Ga low grade metamorphism.

2. Emeralds were formed later, during the Proterozoic tectono-metamorphism at 2.0 Ga which affected the whole of the Limpopo Belt and the southern margin of the Zimbabwe craton. Sodium-rich fluids were channelled through the reactivated shear zones, and concentrated the necessary elements of pegmatitic and greenstone origin to form emerald. The cooling ages of amphibole and phlogopite give a lower age limit of the formation age and thus an indication of the formation age of emerald.

It is questionable whether there was any major reverse movement along the shear-zone between NMZ *s.s.* and the MGB during the Proterozoic event (Section 5.2.3). In the late Archean, the granulite facies Limpopo rocks were already juxtaposed to the greenschist-facies supracrustal rocks of the Zimbabwe craton. Although Kamber *et al.* (1996) demonstrated movement along shear zones in the eastern part of the NMZ at ~ 2.0 Ga and a low grade overprint, and also suggested a sinistral displacement of Great Dyke segments, there are no clear indications for significant relative movement in the major shear zone nearest to the Sandawana mines during the Proterozoic event. Intrusions which are a continuation of The Great Dyke extend undisturbed over the craton-belt boundary. The minimum intrusion age of these high level, undeformed pyroxenite dykes is 2.4 Ga (Blenkinsop & Frei, 1996), which indicates that after that time no major tectonics occurred in this area.

Thus, while there is strong evidence for a 2.0 Ga thermal overprint covering a large area, by uniform amphibole and biotite ages throughout the Limpopo NMZ and the adjacent Zimbabwe Craton boundary, there is little evidence for major reactivation of shear-zones in the Mweza greenstone belt. This would be an argument in favour of a resetting of the Ar systematics in amphibole and biotite at that time. In support of this view, the older pseudo-plateau ages of phlogopite from the Aeres mine possibly show that they kept some memory of an older event.

Other arguments against emerald formation around 2.0 Ga are:

- The nature of deformation in the Mweza greenstone belt. The emerald bearing zones are characterised by ductile deformation. The association of minerals indicate that emerald formation is closely related to K-metasomatism between pegmatite and greenstone, and simultaneous fluid activity during ductile shearing and deformation (Chapter 4). This is not in agreement with Proterozoic weak deformation under brittle conditions, such as observed at, e.g., the Renco Mine (see Section 5.2.3).
- From field evidence it appears safe to presume that the Li- and Be-rich pegmatites were emplaced just prior to and/or during major (ductile) deformation (Chapter 2). This is supported by a U-Pb age on monazite of about 2640 Ma, in the Bikita pegmatite, located further to the eastnortheast (Holmes, 1954), a Pb-Pb age on microcline of 2600 ± 100 Ma (Holmes, 1954) and a K-Ar age on lepidolite of about 2660 Ma (Wilson *et al.*, 1954; corrected by Jamieson & Schreiner, 1957), also on pegmatites from the same Bikita district. K-metasomatism was caused by a Na-rich fluid, which is interpreted as a late stage 'solution-melt' of pegmatitic origin (Chapter 4). This means that intrusion of pegmatites, subsequent albitisation of the pegmatite and K-metasomatism in the adjacent greenstone during deformation, accompanied and/or followed by hydrothermal activity, resulting in the formation of emerald, are part of a continuous process and thus occurred almost contemporaneously. In this scenario, emerald formation is closely related to magmatic activity, and, thus, to the 2.6 Ga event.
- According to apatite-phlogopite thermometry, emerald formation occurred at temperatures around 600°C. This clearly indicates higher temperatures than the low greenschist facies metamorphism ($T < 400^\circ\text{C}$, Blenkinsop & Frei, 1996; $420 \leq T \leq 500^\circ\text{C}$, Kamber *et al.*, 1996) characteristic of the Proterozoic event.

An argument in favour of an emerald formation around 2.0 Ga would be that, in theory, amphibole needs at least 500°C (Kamber *et al.*, 1995b; Willigers *et al.*, 2001, even indicate a hornblende closure temperature of 580°C) to be totally reset and to be able to produce a plateau age through Ar/Ar dating. The temperature is less for phlogopite, but in agreement with younger plateau ages for this mineral. At 500°C, emerald-bearing zones can easily be affected by ductile deformation, shearing and fluid activity, and apparent fresh amphibole and biotite could therefore indicate approximate formation temperatures. As stated earlier, some authors reason that it is very difficult to recognize Proterozoic deformation in the NMZ *s.s.*, because it could have very similar kinematics to those of the Late Archean deformation; especially, the mafic granulites generally lack any indication of recrystallization (Kamber *et al.*, 1995b; Kamber *et al.* 1996). Thus, also in the MGB, one could consider the possibility of emerald formation connected to re-activation of major and associated shear zones at 2.0 Ga. In that case, albitisation of the pegmatite and subsequent crystallisation of the various phases occurred 600 m.y. later than the intrusion and ductile deformation of the pegmatites. Albitisation of pegmatite would have been caused by a Na-rich fluid of unknown origin, and an associated F- and P-rich fluid, which would be responsible for emerald growth in pre-existing structures.

However, the characterisation of the Na-F-P rich solution involved (Section 4.3.2) strongly suggests associated (very late stage) magmatic activity, which does not appear

to be compatible with the Proterozoic event. As mentioned before, the formation temperatures also appear to be too high for the Proterozoic event; thus, even at 500°C (the upper temperature limit of this event) resetting of amphibole still appears to be a valid option. In addition, it is known that also at lower temperatures ($T < 500^\circ\text{C}$) amphibole can be reset by even minor recrystallisation, but especially whenever fluids are present (compare Kamber *et al.* 1995b, 1996). While at first sight amphibole and phlogopite appeared fresh, a reinvestigation locally showed subtle signs of chloritisation in amphiboles. Also locally, some feldspars in the pegmatite, showing subgrains and signs of brittle deformation, appear to indicate some influence of a low-grade event.

In conclusion, most geological data and observations appear to be compatible with a Late Archean formation of emerald. This would mean that the emeralds are 600 m.y. older than the dates on amphibole and biotite indicate. In this scenario, the Ar systematics of both amphibole and biotite became reset during a Proterozoic thermal overprint.

The deduced 2.6 Ga age of Sandawana emeralds means that compared to all other commercially available emeralds, namely from Colombia (Late Eocene-Early Oligocene; e.g., Cheilletz *et al.*, 1994), Brazil (Proterozoic and Palaeozoic; Giuliani *et al.*, 1997a; Schwarz *et al.*, 2001), Zambia (Pan-African, ~ 450 Ma; Seifert *et al.*, 2004), Madagascar (younger than 550 Ma; Kanis & Schwarz, 2001), Afghanistan (Mesozoic; Kazmi & Snee, 1989), Pakistan (Tertiary; Laurs *et al.*, 1996) and Russia (younger than Palaeozoic; e.g., Schmetzer *et al.*, 1991; Gavrilenko *et al.*, 2001), the Sandawana emeralds are by far the oldest.

6. Conclusions and model of emerald formation

6.1 Results and conclusions

As a result of this study the following conclusions can be drawn:

1. The emeralds from Sandawana show relatively constant physical properties, with high refractive indices and specific gravities. Unlike emeralds from many other localities, they are not characterized by fluid inclusions, but, rather, by laths and fibres of amphibole, both actinolite and cummingtonite (previously reported to have been tremolite). Other common inclusions are albite and apatite. The relative absence of fluid inclusions is due to decrepitation of these inclusions during rapid block uplift.
2. Inclusions of chromium-rich ilmenorutile have been identified. This variety of ilmenorutile, with an average chemical formula that can be written as $(\text{Ti}_{0.804}\text{Sn}_{0.002}\text{Nb}_{0.062}\text{Ta}_{0.034}\text{Cr}_{0.081}\text{Fe}_{0.022})_{\Sigma 1.006}\text{O}_{2.00}$, has not been described before and can be considered as extremely rare.
3. Sandawana emeralds have very high contents of chromium, sodium, magnesium and lithium, and high caesium content. Chromium contents in some samples were substantially higher than in specimens previously reported.
4. Sandawana emeralds can be readily separated from those from other localities by using traditional gem testing techniques, on the basis of a combination of physical properties, inclusions and chemistry.
5. Stable oxygen isotopic analysis was recently promoted as a way to establish the country of origin of cut emeralds that are sold on the commercial market. However, emeralds from the commercially-mined occurrences, at Sandawana (Zimbabwe), Habachtal (Austria), Minas Gerais (Brazil) and, partly, Mananjar (Madagascar), show overlapping $\delta^{18}\text{O}$ values, rendering this technique inconclusive. In cases of not only overlapping physical and chemical properties, but also ambiguous inclusion characteristics, as, for instance, for the deposits of Sandawana (Zimbabwe) and Rajasthan (India), the use of oxygen isotopes may be helpful.
6. The original pegmatite at Sandawana was a potassic, peraluminous, Be-rich granitic pegmatite, affiliated with the Li-Cs-Ta (LCT) family of rare-element pegmatites. Intrusion of pegmatites into metamorphosed komatiites of the Mweza Greenstone Belt occurred just prior to and/or during the main deformation event. These pegmatites are probably related to the K-feldspar granites that intruded the major break between the MGB and the Limpopo NMZ.
7. At Sandawana, ductile deformation is indicated by boudinage, pinch-and-swell and folded pegmatites; by differentiated layering in associated amphibole phlogopite schist; and by the presence of (micro)shear zones.
8. The abundant presence of myrmekites in pegmatite, and almost complete replacement of K-feldspar by albite, show that fluid flow must have been an important driving force for albitisation. Syntectonic growth of phlogopite next to the pegmatite confirms K-Na metasomatism at the contact of pegmatite and greenstone during shearing and folding.
9. Synkinematic growth of emerald, phlogopite, fluorapatite, holmquistite and chromian ilmenorutile testifies to enrichment of Na, K, Li, Be, F, P, Rb, Cs, Ta and Nb in the emerald bearing shear zone, and suggests that emerald formation is closely related to syntectonic K-Na metasomatism.

10. The occurrence of emerald is structurally controlled; it is closely related to phlogopite amphibole schist next to albitised pegmatite, showing pronounced differentiated layering. The gem-quality emeralds are restricted to low-stress domains, such as pockets which are present in (micro)shear zones, zones related to folded pegmatite (e.g., fold hinges) or pinch zones at the contact of pegmatites showing pinch-and-swell structures.
11. Mass balance calculations, involving the phases that were consumed and produced, and various melts and solutions, indicate that a Na- and F-rich hydrous fluid, somewhere in the transition between residual melt and a hydrothermal solution, must have been involved in the alterations that ultimately caused the formation of emerald. The presence of small, isolated, highly saline brine inclusions in emerald supports this result.
12. From experimental studies on solubility effects in melt solutions, related to Be, F, P and Al, it can be deduced that the formation of phlogopite and apatite probably catalysed emerald formation.
13. Apatite-phlogopite thermometry gives $T = 560\text{--}650^\circ\text{C}$, interpreted as the temperature range at which emerald was formed. From the general conditions of primary consolidation of rare element pegmatites, and from the inferred crystallisation path of the Bikita pegmatite, a pressure of around 2.5-3 kbar appears plausible at Sandawana.
14. The relatively high temperatures at the contact of altered pegmatite and greenstone compared to the regional metamorphic conditions of the surrounding rocks imply contact metamorphic rather than regional metamorphic conditions. This evidence, together with the indicated pegmatitic/hydrothermal nature of the involved fluid (see 11), provide strong indications for a direct relation between emerald formation and the synkinematic intrusion of the pegmatites. The Na- and F-rich fluid involved in the mineral reactions can, therefore, be interpreted as a very late stage 'solution-melt' of pegmatitic origin; a residual melt which evolved toward a silica-depleted, alkaline, Na-rich composition, in which H_2O , other fluxes and lithophile trace elements are highly concentrated. It may be seen as a late effect of pegmatite intrusion (auto-metasomatism) along the pathways created by reverse shearing in the area. It means that intrusion of the pegmatites, and subsequent albitisation and metasomatism during deformation, have been part of a continuous process and, thus, occurred almost contemporaneous.
15. From geological data and observations, it is deduced that Sandawana emerald was formed in the Late Archaean, around 2.6 Ga. In this scenario, the Ar systematics of both amphibole and biotite (indicating $^{40}\text{Ar}/^{39}\text{Ar}$ dates of 1937, 1904 and 1902 Ma, respectively) became reset during a Proterozoic thermal overprint. Older pseudo-plateau ages of phlogopites (2314 Ma) could indicate partial resetting, which means that they kept some memory of an older event.
16. The deduced age of around 2.6 Ga means that, compared to all other commercially available emeralds, the Sandawana emeralds are by far the oldest.

6.2. Model of emerald formation at Sandawana

From the results and conclusions, a model of emerald formation at Sandawana can be presented (Fig. 82). Firstly, rare-element granitic pegmatites intruded into the Mweza

Greenstone Belt (MGB) just prior and/or during the main deformation event at 2.6 Ga. In a continuing process during folding and shearing, late stage Na-rich 'solution-melt', which was able to transport and dissolve elements like F, P, Li, Be and Cr, was injected along shear zones, causing albitisation of the pegmatite and phlogopitization in the greenstone wallrock. Microcline, oligoclase, quartz (from the pegmatite) and chlorite (from the greenstones) were consumed, in favour of albite (in the pegmatite), phlogopite, some new actinolite and cummingtonite, holmquistite, fluorapatite and emerald (at the contact and in the greenstone). Formation of emerald occurred in regions of relatively lower pressure, such as (micro) shear-zones, 'traps' under folded pegmatite or pinch areas near pegmatites with pinch-and-swell or boudin structures, where clean, gem-quality crystals could grow.

There is evidence that, apart from the intrusion of rare-element pegmatites into the MGB, granites rich in K intruded into the major break between the Zimbabwe craton and the NMZ, just south of the MGB. It is therefore emphasised that a magmatic source for the Na-rich fluids, possibly mixed with metamorphic waters, appears very likely, because of the intimate spatial and temporal relationship with magmatic activity, and the near magmatic temperatures of phlogopite and apatite formation as a result of metasomatism caused by the Na-rich fluids. The high temperatures (around 550-650°C) imply a late-magmatic or very early post-magmatic origin of emerald formation.

In conclusion, intense ductile deformation played a key role in the formation of emerald, in terms of channelling reactive fluids along shear zones and creating low-stress traps near deformed pegmatite where good quality emerald could grow. Additionally, however, at Sandawana, emerald formation has also been directly linked to magmatic activity.

6.3. Comparison with other models

As discussed in Chapter 1, several theories exist on the formation of emerald. The situation outlined above represents yet another model of emerald formation. At first sight the case of the Sandawana emerald deposit appears to be largely in line with the conclusions reached by Grundmann & Morteani (1989), namely that schist-type emerald deposits in metamorphic rocks are the product of metasomatism during a deformation event accompanied or followed by regional metamorphism. However, in this model, Grundmann & Morteani (1989) emphasized and advocated the non-pegmatitic nature of emerald growth (see Chapter 1), and the importance of regional metamorphism in providing energy for continued metasomatic exchanges and emerald growth over a longer period of time. On the contrary, at Sandawana, although emeralds have grown during a major deformation event, causing intense deformation and shearing, and accompanied by regional metamorphism, their formation is also closely related to magmatic activity along a major shear-zone. Thus, in this case, emerald formation cannot be disconnected from magmatic activity. In answering the questions raised by Barton & Young (2002), as to which mechanisms of metasomatism are involved and which mechanism was dominating in schist-type emerald deposits (Section 1.3.5), the Sandawana emerald occurrence did not originate through metasomatic exchange by intergranular diffusion over a relatively long time, which is available during regional metamorphism, but by infiltration/diffusion metasomatism generated during a shorter lived magmatic/

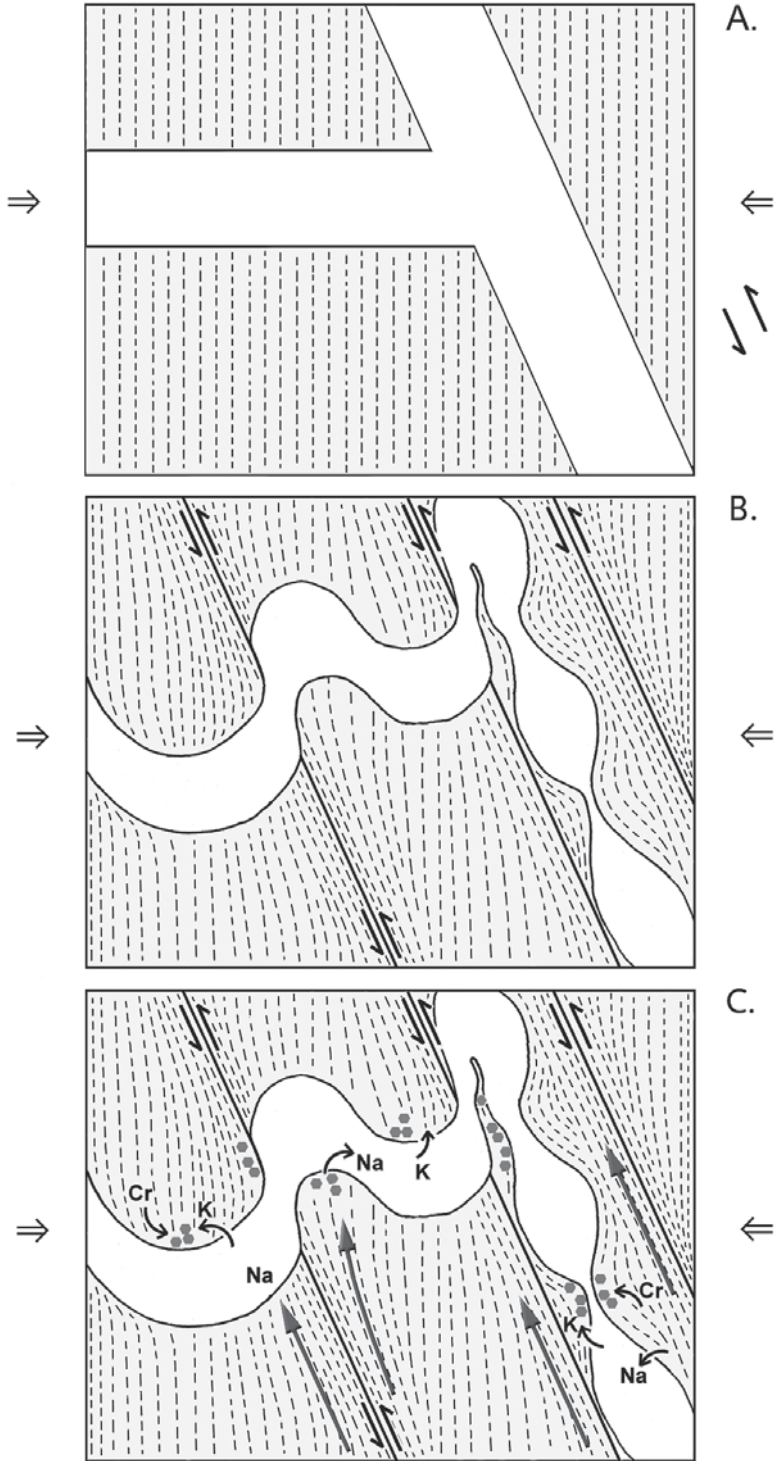


Table 25. Schist-type emerald deposits and various models of emerald formation.

No.	Model – Emerald is the product of:	Reference
1	Single-stage contact metamorphism at the border of magmatic intrusive bodies and (ultra)mafic rocks ('classic' model).	Fersman, 1929
2	Syn- to post-tectonic reactions during a deformation event accompanied or followed by regional metamorphism.	Grundmann & Morteani, 1989
3	Circulation of hydrothermal fluids, causing metasomatism in mafic to ultramafic rocks around pegmatite veins altered to plagioclase.	Giuliani <i>et al.</i> , 1997a, b
4	Interaction between metamorphic fluids and mafic to ultramafic rocks in ductile shear zones.	Giuliani <i>et al.</i> , 1997a, b
5	Contact metasomatism at the border of ultramafic rocks and rare-element pegmatites during a deformation event, involving late stage magmatic/hydrothermal activity focused by shearing.	This study

hydrothermal event. Apart from the evidence presented above, this view is supported by the absence of evidence that would indicate polystage growth in Sandawana emerald.

Thus, for schist-type deposits, a new mode of emerald formation is proposed, next to the other theories that have been presented in Chapter 1 and summarised in Table 25, namely emerald formation as a product of contact metasomatism at the border of ultramafic rocks and rare-element pegmatites during a deformation event, involving late stage magmatic/hydrothermal activity channelled by shearing. At Sandawana, this took place at the border of a major Late Archaean suture zone.

The model does not fit into any of the genetic classification schemes presented in Chapter 1. This study underscores that no single theory or model can be applied to all schist-type deposits, as earlier suggested by Grundmann & Morteani (1989). Emeralds of gem quality can be formed in very different geological settings (compare also the extreme case of Colombia). Basic conditions need to be fulfilled, namely availability of beryllium and chromium (\pm vanadium), means of transport to bring the elements together, i.e., magmatic, hydrothermal, metamorphic or a combination of these fluids, chemical and physical conditions in which emerald may form as a stable mineral (formation temperatures generally from around 600 down to 300°C), and sufficient space to grow transparent and well-formed crystals.

◀ Fig. 82. Emerald formation at Sandawana has been related to both magmatic and tectonic activity. The process is illustrated by (A) intrusion of rare-element pegmatites, just prior and/or during the main deformation event; (B) simultaneous compression and shearing, causing folding of pegmatites and pinch-and-swell and boudinage of pegmatites depending on the starting orientation; (C) invasion of late stage Na-rich solution melt along shear-zones, causing auto-metasomatism of pegmatites and alterations at the contact with greenstone, resulting in growth of emerald in zones of relatively low pressure: porous (micro)shear zones, traps created by folded and pinched pegmatite. Phases A, B and C are envisaged to be part of a continuous process.

Acknowledgements

I thank my 'promotor', Professor Jacques Touret, for all the input, for critically reading the manuscript, and also for his enthusiasm and patience on this long and unusual trial. Also, Professor Leo Kriegsman is thanked for his valuable contributions and suggestions to improve the manuscript, and for his great support especially during the last year. The members of the dissertation committee, Professor Gareth Davies, Professor Henry Hänni, Dr Dietmar Schwarz, Dr Wijbrans and Frank Beunk are thanked for taking the time to look at this work, and for their useful comments and suggestions.

I am very grateful to Dr Jan Kanis and Eckehard Petsch who introduced me to the Sandawana Mines, and gave me the unique opportunity to do fieldwork in and around the mines. Without their support, this project would not have been possible. Also at the mines, I received great assistance from many people. I want to especially thank Dr Abel Ncube (former director of the company), Mr D.B. Siroya, Arthur Braunschick, Peter Kitchen, Ernie Rice, Jim Dryburgh, Howard Ross, Ananias Mutsvanga (mine geologist), Tenashe, Calvin, Herbert and John.

Ernst Burke and Wim Lustenhouwer are thanked for helping with Raman spectroscopy and microprobe analyses. Facilities for Raman spectroscopy and microprobe analyses were provided by the Free University of Amsterdam and by NWO, the Netherlands Organisation for Scientific Research. Wynanda Koot is thanked for making superb polished thin sections. Dr Piet Maaskant is thanked for his support in the early stage of this project and for visiting Sandawana mines once, during my fieldwork.

The Geological Survey of Canada, Ottawa, provided analytical facilities for work on oxygen isotopes. Professor Bruce Taylor and Adrian Timbal (Ottawa) are thanked for their careful assistance. Professor Alain Cheilletz of CRPG-CNRS, Vandoeuvre-lès-Nancy cedex, France, is greatly thanked for his contributions to the Ar-Ar dating. Facilities for argon isotope analyses were provided by UMR Géosciences Azur, Nice, France. I am also grateful to Dr Thomas Calligaro, who guided the PIXE/PIGE analytical work at the AGLAE IBA facility of the research laboratory of the Museums of France, Palais du Louvre, Paris.

Most of the gem material was kindly provided by Sandawana Mines (Pvt.) Ltd., Zimbabwe. The late Mr A.G. Bode, of Bodes & Bode, The Netherlands, and Dr Jan Kanis, Veitsrodt, Germany, are thanked for loaning some of the polished material.

Dirk van der Marel, technician at Naturalis, is greatly thanked for his tireless assistance with preparation and modification of photographs and drawings, and also for polishing emerald samples. Peter Wittekoek made many thin sections, which is much appreciated. Professor Steve Donovan and Niko Korenhof are thanked for helping efficiently with editing and putting everything in the right format for publication. Jan Krikken and Charles Arps are thanked for their general support during this project.

The financial support of the Foundation Stichting Dr Schürmannfonds is gratefully acknowledged.

Finally, I owe much to my late father Professor Pieter Zwaan, for introducing me into the field of gemmology, and for his general support and wisdom. I cannot thank Ike Zwaan-Kruijs Voorberge enough for her love, endless understanding and patience during the last years.

References

- Abaa, S.I. 1991. Hydrothermal fluids responsible for the formation of precious minerals in the Nigerian Younger Granite Province. *Mineralium Deposita*, **26**: 34-39.
- Abdalla, H.M. & Mohamed, F.H. 1999. Mineralogical and geochemical investigation of emerald and beryl mineralisation, Pan-African Belt of Egypt; genetic and exploration aspects. *Journal of African Earth Sciences*, **28**: 581-598.
- Ackermann, K.J., Branscombe, K.C., Hawkes, J.R. & Tidy, A.J.L. 1966. The geology of some beryl pegmatites in Southern Rhodesia. *Transactions of the Geological Society of South Africa*, **69**: 1-38.
- Alexandrov, P., Ruffet, G. & Cheilletz, A. 2002. Muscovite recrystallization and saddle-shaped $^{40}\text{Ar}/^{39}\text{Ar}$ age spectra: example from the Blond granite (Massif Central, France). *Geochimica et Cosmochimica Acta*, **66**: 1793-1807.
- Anderson, J.L. & Smith, D.R. 1995. The effects of temperature and $f\text{O}_2$ on the Al-in-hornblende barometer. *American Mineralogist*, **80**: 549-559.
- Anderson, S.M. 1976. A note on the occurrence of emerald at Mayfield Farm, Fort Victoria, Rhodesia. *Journal of Gemmology*, **15**: 80-82.
- Anderson, S.M. 1978. Notes on the occurrence and mineralogy of emeralds in Rhodesia. *Journal of Gemmology*, **16**: 177-185.
- Ando, R. & Nitta, I. 1941. X-ray study of some Japanese minerals. II. Ilmenorutile at Tesirogi, Hukushima Prefecture. *Journal of the Chemical Society of Japan*, **62**: 978-983.
- Apted, M.J. & Liou, J.G. 1983. Phase relations among greenschist, epidote-amphibolite, and amphibolite in a basaltic system. *American Journal of Sciences*, **283-A**: 328-354.
- Arbey, F. 1975. Le quartz de St.-Paul-la-Roche (Dordogne). *Minéraux et Fossiles*, **1(7)**: 17-24.
- Arif, M., Fallick, A.F. & Moon, C.J., 1996. The genesis of emeralds and their host rocks from Swat, north-western Pakistan: a stable-isotope investigation. *Mineralium Deposita*, **31**: 255-268.
- Ashworth, J.R. 1972. Myrmekites of exsolution and replacement origins. *Geological Magazine*, **109**: 45-62.
- Aurischio, C., Fioravanti, G., Grubessi, O. & Zanazzi, P.F. 1988. Reappraisal of the crystal chemistry of beryl. *American Mineralogist*, **73**: 826-837.
- Ayers, J.C. & Watson, E.B. 1991. Solubility of apatite, monazite, zircon, and rutile in supercritical aqueous fluids with implications for subduction zone geochemistry. *Philosophical Transactions of the Royal Society London*, **A335**: 365-375.
- Ayers, J.C. & Watson, E.B. 1993. Rutile solubility and mobility in supercritical aqueous fluids. *Contributions to Mineralogy and Petrology*, **114**: 321-330.
- Bakakin, V.V. & Belov, N.V., 1962. Crystal chemistry of beryl. *Geokhimiya*, **5**: 420-433.
- Baker, D.R. 1998. The escape of pegmatite dikes from granitic plutons: constraints from new models of viscosity and dike propagation. *Canadian Mineralogist*, **36**: 255-263.
- Banerjee, A. 1995. Investigation of fluid inclusion in emeralds of different geological origins by microchemical analysis and IR-reflexion-spectroscopy. *Boletín de la Sociedad Española de Mineralogía*, **18**: 18-19.
- Barros, J.C. 1986. Fluid inclusions, genetic models and exploration strategies for emerald deposits: cases from Brazil. *Terra Cognita*, **6**: 509.
- Barsukova, M.L., Kuznetov, V.A., Dorofeyeva, V.A. & Khodakovskiy, L.I. 1979. Measurement of the solubility of rutile TiO_2 in fluoride solutions at elevated temperatures. *Geokhimiya*, **7**: 1017-1027.
- Barton, M.D. 1986. Phase equilibria and thermodynamic properties of minerals in the $\text{BeO-Al}_2\text{O}_3\text{-SiO}_2\text{-H}_2\text{O}$ (BASH) system, with petrologic applications. *American Mineralogist*, **71**: 277-300.
- Barton, M.D. & Young, S. 2002. Non-pegmatitic deposits of beryllium: mineralogy, geology, phase equilibria and origin. In: Grew, E.S. (ed.), *Beryllium: Mineralogy, Petrology and Geochemistry. Reviews in Mineralogy & Geochemistry*: 591-691. Mineralogical Society of America, Washington, D.C.
- Becke, F. 1908. Ueber Myrmekite. *Schweizerische Mineralogische und Petrographische Mitteilungen*, **27**: 377-390.
- Berger, M., Kramers, J.D. & Nägler, T.F. 1995. Geochemistry and geochronology of charnoenderbites in the Northern Marginal Zone of the Limpopo Belt, Southern Africa, and genetic models. *Schweizerische Mineralogische und Petrographische Mitteilungen*, **75**: 17-42.
- Beus, A.A. 1966. *Geochemistry of Beryllium and Genetic types of Beryllium Deposits*. Freeman & Co., San Francisco: 401 pp.

- Beus, A.A., Sobolev, B.P. & Dikov, Y.P. 1963. Geochemistry of beryllium in high temperature post-magmatic mineralization. *Geokhimiya*, **3**: 316-323. [In Russian.]
- Bickle, M.J. & Nisbet, E.G. 1993. *The Geology of the Belingwe Greenstone Belt, Zimbabwe - a Study of the Evolution of Archaean Continental Crust*. Geological Society of Zimbabwe Special Publication No. 2. A.A. Balkema, Rotterdam: 239 pp.
- Blenkinsop, T.G. & Frei, R. 1996. Archean and Proterozoic mineralization and tectonics at the Renco Mine (Northern Marginal Zone, Limpopo Belt, Zimbabwe). *Economic Geology*, **91**: 1225-1238.
- Blenkinsop, T.G. & Frei, R. 1997. Archean and Proterozoic mineralization and tectonics at the Renco Mine (Northern Marginal Zone, Limpopo Belt, Zimbabwe) - a reply. *Economic Geology*, **92**: 747-748.
- Böhme, F.C. 1966. *The Geology of the Sandawana Mines*. Sandawana Mines, RTZ, Harare: 20 pp.
- Böhme, F.C. 1982. Emeralds at Sandawana. In: *Gemstones, Report of the Sixth Annual Commodity Meeting: A110-A122*. Institution of Mining and Metallurgy, London.
- Bosshart, G. 1991. Emeralds from Colombia (part 2). *Journal of Gemmology*, **22**: 409-425.
- Bowersox, G., Snee, L.W., Foord, E.E. & Seal II, R.R. 1991. Emeralds of the Panjshir Valley, Afghanistan. *Gems & Gemology*, **27**: 26-39.
- Branquet, Y., Laumonier, B., Cheilletz, A. & Giuliani, G. 1999. Emeralds in the Eastern Cordillera of Colombia: two tectonic settings for one mineralization. *Geology*, **27**: 597-600.
- Breemen, O. van & Dodson, H. 1972. Metamorphic chronology of the Limpopo Belt, Southern Africa. *Geological Society of America Bulletin*, **83**: 2005-2018.
- Burt, D.M. 1975. Beryllium mineral stabilities in the model system $\text{CaO-BeO-SiO}_2\text{-P}_2\text{O}_5\text{-F}_2\text{O}_{-1}$ and the breakdown of beryl. *Economic Geology*, **70**: 1279-1292.
- Calligaro, T., Dran, J.C., Poirrot, J.P., Querré, G., Salomon, J. & Zwaan, J.C. 2000. PIXE/PIGE characterisation of emeralds using an external micro-beam. *Nuclear Instruments and Methods in Physics Research B*, **161-163**: 769-774.
- Carrington, D.P. & Harley, S.L. 1996. Cordierite as a monitor of fluid and melt H_2O contents in lower crust; an experimental calibration. *Geology*, **24**: 647-650.
- Castle, R.O. & Lindsley, D.H. 1993. An exsolution silica-pump model for the origin of myrmekite. *Contributions to Mineralogy and Petrology*, **115**: 58-65.
- Cerny, P. 2000. Constitution, petrology, affiliations and categories of mirolitic pegmatites. *Memorie della Società Italiana di Scienze Naturali e del Museo Civico di Storia Naturale di Milano*, **30**: 5-12.
- Cerny, P. 1991. Fertile granites of Precambrian rare-element pegmatite fields: is geochemistry controlled by tectonic setting or source lithologies? *Precambrian Research*, **51**: 429-468.
- Cerny, P., Cech, F. & Povondra, P. 1964. Review of ilmenorutile-strüverite minerals. *Neues Jahrbuch für Mineralogie, Abhandlungen*, **101**: 142-172.
- Cerný, P. & Hawthorne, F.C. 1976. Refractive indices versus alkali contents in beryl: general limitations and applications to some pegmatitic types. *Canadian Mineralogist*, **14**: 491-497.
- Cerny, P., Meintzer, R.E. & Anderson, A.J. 1985. Extreme fractionation in rare-element granitic pegmatites: selected examples of data and mechanisms. *Canadian Mineralogist*, **23**: 381-421.
- Chakoumakos, B.C. & Lumpkin, G.R. 1990. Pressure-temperature constraints on the crystallization of the Harding pegmatite, Taos County, New Mexico. *Canadian Mineralogist*, **28**: 287-298.
- Charoy, B. 1999. Beryllium speciation in evolved granitic magmas: phosphates versus silicates. *European Journal of Mineralogy*, **11**: 135-148.
- Charoy, B. & Pollard, P.J. 1989. Albite-rich, silica-depleted metasomatic rocks at Emuford, northeast Queensland; mineralogical, geochemical, and fluid inclusion constraints on hydrothermal evolution and tin mineralization. *Economic Geology*, **84**: 1850-1874.
- Cheilletz, A., Donato, P. de & Barrès, O. 2001a. La traçabilité des émeraudes: une avancée décisive obtenue par microscopie infrarouge (μIRTF). *Revue de Gemmologie*, **141/142**: 81-83.
- Cheilletz, A., Féraud, G., Giuliani, G. & Rodriguez, C.T. 1994. Time-pressure and temperature constraints on the formation of Colombian emeralds: an $^{40}\text{Ar}/^{39}\text{Ar}$ laser microprobe and fluid inclusion study. *Economic Geology*, **89**: 361-380.
- Cheilletz, A. & Giuliani, G. 1996. The genesis of Colombian emeralds: a restatement. *Mineralium Deposita*, **31**: 359-364.

- Cheilletz, A., Sabot, B., Marchand, P., Donato, P. de, Taylor, B., Archibald, D., Barrès, O. & Andrianjaffy, J. 2001b. Emerald deposits in Madagascar: two different types for one mineralising event. *In: Borg, G. & Schmid, S. (eds), EUG XI: 547. Strasbourg.*
- Clayton, R.N. & Mayeda, T.K. 1963. The use of bromine pentafluoride in the extraction of oxygen from oxides and silicates for isotopic analysis. *Geochimica et Cosmochimica Acta*, **27**: 43-52.
- Coats, J.S., Mosley, P.N., Mankelov, J.M., Mwale, M., Chikambwe, E.M., Muibeya, B., Ndhlovu, K.C. & Nzabara, F. 2001. *The Geology and Mineral Resources of Zambia. Geological Survey Department Memoir 6.* Ministry of Mines and Minerals Development, Lusaka, Zambia.
- Cosi, M., Bonis, A. De, Gosso, G., Hunziker, J., Martinotti, G., Moratto, S., Robert, J.P. & Ruhlman, F. 1992. Late Proterozoic thrust tectonics, high-pressure metamorphism and uranium mineralization in the Domes area, Lufilian Arc, northwestern Zambia. *Precambrian Research*, **58**: 215-240.
- Craig, H. 1961. Isotopic variations in meteoric waters. *Science*, **133**: 1702-1703.
- Dahl, P.S. 1994. Closing in on argon closure temperatures? An extended 'ionic porosity' model for thermochronometric minerals, with application to amphiboles. *U.S. Geological Survey Circular*, **1107**: 72.
- Dahl, P.S. 1996. The effects of composition on retentivity of argon and oxygen in hornblende and related amphiboles: a field-tested empirical model. *Geochimica et Cosmochimica Acta*, **60**: 3687-3700.
- Daly, M.C. & Unrug, R. 1983. The Muva Supergroup in Zambia – a craton to mobile belt sedimentary sequences. *Transactions of the Geological Society of South Africa*, **85**: 155-165.
- Deer, W.A., Howie, R.A. & Zussman, J. 1982. *Rock-forming Minerals, Orthosilicates.* Longman, New York: 919 pp.
- Deer, W.A., Howie, R.A. & Zussman, J. 1986. *Rock-forming Minerals, Disilicates and Ring Silicates.* Longman, New York: 629 pp.
- Dickin, A.P. 1995. *Radiogenic Isotope Geology.* Cambridge University Press, Cambridge.
- Dodson, M.H. 1973. Closure temperature in cooling geochronological and petrological systems. *Contributions to Mineralogy and Petrology*, **40**: 259-274.
- Dodson, M.H. Compston, W., Williams, I.S. & Wilson, J.F. 1988. A search for ancient detrital zircons in Zimbabwean sediments. *Journal of the Geological Society, London*, **145**: 977-983.
- Dowty, E. 1980. Crystal-chemical factors affecting the mobility of ions in minerals. *American Mineralogist*, **65**: 174-182.
- Dymek, R.F., Boak, J.L. & Brothers, S.C. 1988. Titanian chondrodite- and titanian clinohumite-bearing metadunite from the 3800 Ma Isua supracrustal belt, West Greenland: chemistry, petrology, and origin. *American Mineralogist*, **73**: 547-558.
- Emsley, J. 2001. *Nature's Building Blocks. An A-Z Guide to the Elements.* Oxford University Press, Oxford: 448 pp.
- Eriksson, K.A. & Fedo, C.M. 1994. Archean synrift and stable-shelf sedimentary successions. *In: Condie, K.C. (ed.), Archean Crustal Evolution: 171-204.* Elsevier, Amsterdam.
- Evensen, J.M., London, D. & Wendlandt, R.F. 1999. Solubility and stability of beryl in granitic melts. *American Mineralogist*, **84**: 733-745.
- Fallick, A.E. & Barros, J.G. 1987. A stable-isotope investigation into the origin of beryl and emerald from the Porangatu deposits, Goiás State, Brazil. *Chemical Geology*, **66**: 293-300.
- Fallick, A.E., Schorscher, H.D., Machado, G.A.A., Monteiro, M.M.G. & Ellam, R.M. 1994. A review of stable isotope ($\delta^{18}\text{O}$, δD) studies of emerald deposits in Brasil. *In: Annual Meeting, Mineral Deposit Study Group: 411.* Exeter.
- Fedo, C.M., Eriksson, A. & Blenkinsop, T.G. 1995. Geologic history of the Archean Buhwa greenstone belt and surrounding granite-gneiss terrane, Zimbabwe, with implications for the evolution of the Limpopo belt. *Canadian Journal of Earth Sciences*, **32**: 1977-1990.
- Fedo, C.M. & Eriksson, K.A. 1995. Geologic setting and ideas concerning the origin of the iron-ore deposits at Buhwa, Zimbabwe. *In: Blenkinsop, T. G. & Tromp, P. L. (eds), Sub-Saharan Economic Geology: 43-53.* Geological Society of Zimbabwe, Special Publication. A.A. Balkema, Rotterdam.
- Fedo, C.M. & Eriksson, K.A. 1996. Stratigraphic framework of the ~3.0 Ga Buhwa Greenstone Belt: a unique stable-shelf succession in the Zimbabwe Archean Craton. *Precambrian Research*, **77**: 161-178.
- Féraud, G., Gastaud, J., Suzende, J.M., Olivet, J.L. & Cornen, G. 1982. $^{40}\text{Ar}/^{39}\text{Ar}$ ages for the alkaline volcanism and the basement of Gorrington Bank, North Atlantic Ocean. *Earth and Planetary Science Letters*, **57**: 211-226.

- Fernandes, S. 2001. Emerald deposits of Rajasthan. In: *XXVIII International Gemmological Conference, Extended Abstracts*: 110-116. Madrid.
- Fersman, A.E. 1929. Geochemische Migration der Elemente: III. Smaragdgruben im Uralgebirge. *Abhandlungen zur praktischen Geologie und Bergwirtschaftslehre*, **18** (Halle (Saale): Wilhelm Knapp.): 74-116.
- Fleischer, J.A. & Mandarino, J.A. 1995. *Glossary of Mineral Species 1995*. Mineralogical Record Inc., Tucson, Arizona: 280 pp.
- Flinter, B.H. 1959. Re-examination of 'strüverite' from Salak North, Malaya. *American Mineralogist*, **44**: 620-632.
- Fortier, S.M. & Giletti, B.J. 1989. An empirical model for predicting diffusion coefficients in silicate minerals. *Science*, **245**: 1481-1484.
- Franz, G. & Morteani, G. 2002. Be-minerals: synthesis, stability, and occurrence in metamorphic rocks. In: Grew, E.S. (ed.), *Beryllium - Mineralogy, Petrology and Geochemistry. Reviews in Mineralogy & Geochemistry*: 551-589. Mineralogical Society of America, Washington, D.C.
- Gallagher, M.J. 1975. Composition of some Rhodesian lithium-bearing pegmatites. *Transactions of the Geological Society of South Africa*, **78**: 35-41.
- Garcia, D., Pascal, M.L. & Roux, J. 1996. Hydrothermal replacement of feldspars in igneous inclusions of the Velay and the genesis of myrmekites. *European Journal of Mineralogy*, **8**: 703-717.
- Gaspar, J.C. 1992. Titanian clinohumite in the carbonatites of the Jacupiranga Complex, Brazil: mineral chemistry and comparison with titanian clinohumite from other environments. *American Mineralogist*, **77**: 168-178.
- Gavrilenko, E., Giuliani, G., Popov, M. & France-Lanord, C. 2001. Emeralds of the Ural Mountains (Russia): geology, fluid inclusions and oxygen isotopes. In: *XXVIII International Gemmological Conference, Extended Abstracts*: 36-40. Madrid.
- Giuliani, G., Chaussidon, M., Schubnel, H.J., Piat, D.H., Rollion-Bard, C., France-Lanord, C., Giard, D., Narvaez, D.D. & Rondeau, B. 2000a. Oxygen isotopes and emerald trade routes since antiquity. *Science*, **287**: 631-633.
- Giuliani, G., Cheilletz, A., Arboleda, C., Carrillo, V., Rueda, F. & Baker, J.H. 1995. An evaporitic origin of the parent brines of Colombian emeralds: fluid inclusion and sulphur isotope evidence. *European Journal of Mineralogy*, **7**: 151-165.
- Giuliani, G., Cheilletz, A., Zimmermann, J.L., Ribeiro-Althoff, A.M., France-Lanord, C. & Feraud, G. 1997a. Les gisements d'émeraude du Brésil: genèse et typologie. *Chronique de la Recherche Minière*, **526**: 17-61.
- Giuliani, G., France-Lanord, C., Cheilletz, A., Coget, P., Branquet, Y. & Laumonnier, B. 2000b. Sulfate reduction by organic matter in Colombian emerald deposits: chemical and stable isotope (C,O,H) evidence. *Economic Geology*, **95**: 1129-1153.
- Giuliani, G., France-Lanord, C., Coget, P., Schwarz, D., Cheilletz, A., Branquet, Y., Girard, D., Martin-Izard, A., Alexandrov, P. & Piat, D.H. 1998. Oxygen isotope systematics of emerald: relevance for its origin and geological significance. *Mineralium Deposita*, **33**: 513-519.
- Giuliani, G., France-Lanord, C., Zimmermann, J.L., Cheilletz, A., Arboleda, C., Charoy, B., Coget, P., Fontan, F. & Giard, D. 1997b. Fluid composition, δD of channel H₂O, and $\delta^{18}O$ of lattice oxygen in beryls: genetic implications for Brazilian, Colombian, and Afghanistani emerald deposits. *International Geology Review*, **39**: 400-424.
- Giuliani, G., Sheppard, S.M.F., Cheilletz, A. & Rodriguez, C. 1992. Contribution de l'étude des phases fluides et de la géochimie isotopique $^{18}O/^{16}O$, $^{13}C/^{12}C$ à la genèse des gisements d'émeraude de la Cordillère orientale de la Colombie. *Compte Rendue de l'Académie des Sciences, Paris*, **314**(II): 269-274.
- Giuliani, G., Silva, L.J.H.D. & Couto, P. 1990. Origin of emerald deposits of Brazil. *Mineralium Deposita*, **25**: 57-64.
- Gole, M.J., Barnes, S.J. & Hill, R.E.T. 1987. The role of fluids in the metamorphism of komatiites, Agnew nickel deposit, Western Australia. *Contributions to Mineralogy and Petrology*, **96**: 151-162.
- Gordiyenko, V.V. & Ponomareva, N.T. 1989. Stability conditions for lithium micas of the lepidolite series. *International Geology Review*, **31**: 253-257.

- Grew, E.S. 2002. Mineralogy, Petrology and Geochemistry of Beryllium: an introduction and list of beryllium minerals. In: Grew, E. S. (ed.), *Beryllium - Mineralogy, Petrology and Geochemistry. Reviews in Mineralogy & Geochemistry*: 1-76. Mineralogical Society of America, Washington, D.C.
- Groat, L.A., Marshall, D.D., Giuliani, G., Murphy, D.C., Piercy, S.J., Jambor, J.L., Mortensen, J.K., Ercit, T.S., Gault, R.A., Matthey, D.P., Schwarz, D., Maluski, H., Wise, M.A., Wengzynowski, W. & Eaton, D.W. 2002. Mineralogical and geochemical study of the Regal Ridge emerald showing, southeastern Yukon. *Canadian Mineralogist*, **40**: 1313-1338.
- Grubb, P.L.C. 1973. Paragenesis of spodumene and other lithium minerals in some Rhodesian pegmatites. In: Lister, L. A. (ed.), *Symposium on Granites, Gneisses and related rocks*: 201-216. Geological Society of South Africa, Salisbury.
- Grundmann, G. 1989. Metamorphic evolution of the Habach formation: a review. *Mitteilungen der Österreichische Geologische Gesellschaft*, **81** (for 1988): 133-149.
- Grundmann, G. 2001. Die Smaragde der Welt. In: Schwarz, D. & Hochleitner, R. (eds), *Smaragd, der kostbarste Beryll, der teuerste Edelstein. Extra Lapis*: 26-37. Weise Verlag, München.
- Grundmann, G. & Morteani, G. 1982. Die Geologie des Smaragdorkommens im Habachtal (Land Salzburg, Österreich). *Archiv für Lagerstättenforschung Geologische Bundesanstalt, Wien*, **2**: 71-107.
- Grundmann, G. & Morteani, G. 1989. Emerald mineralization during regional metamorphism: the Habachtal (Austria) and Leydsdorp (Transvaal, South Africa) deposits. *Economic Geology*, **84**: 1835-1849.
- Grundmann, G. & Morteani, G. 1998. Alexandrite, emerald, ruby, sapphire, and topaz in a biotite-phlogopite fels from Poona, Cue district, Western Australia. *Australian Gemmologist*, **20**: 159-167.
- Gübelin, E.J. 1958. Emeralds from Sandawana. *Journal of Gemmology*, **6**(8): 340-354.
- Gübelin, E.J. 1989. Gemological characteristics of Pakistani emeralds. In: Kazmi, H. & Snee, L.W. (eds), *Emeralds of Pakistan: Geology, Gemology and Genesis*: 75-92. Van Nostrand Reinhold, New York.
- Gübelin, E.J. & Koivula, J.I. 1992. *Photoatlas of Inclusions in Gemstones*. ABC Edition, Zürich: 532 pp.
- Guilbert, J.M. & Park, C.F. 1986. *The Geology of Ore Deposits*. Freeman, New York: 985 pp.
- Hamilton, P.J. 1977. Sr isotope and trace element studies of the Great Dyke and Bushveld Mafic Phase and their relation to early Proterozoic magma genesis in southern Africa. *Journal of Petrology*, **18**: 24-52.
- Hammerstrom, J.M. 1989. Mineral chemistry of emeralds and some associated minerals from Pakistan and Afghanistan: an electron microprobe study. In: Kazmi, H. & Snee, L.W. (eds), *Emeralds of Pakistan: Geology, Gemology and Genesis*: 125-150. Van Nostrand Reinhold, New York.
- Hammerstrom, J.M. & Zen, E.A. 1986. Aluminium in hornblende: an empirical igneous geobarometer. *American Mineralogist*, **71**: 1297-1313.
- Hänni, H.A. 1982. A contribution to the separability of natural and synthetic emeralds. *Journal of Gemmology*, **18**: 138-144.
- Hänni, H.A., Kiefert, L. & Chalain, J.P. 1997. A Raman microscope in the gemmological laboratory: first experiences of application. *Journal of Gemmology*, **25**: 394-406.
- Hänni, H.A. & Klein, H.H. 1982. Ein Smaragdorkommen in Madagaskar. *Zeitschrift der Deutschen Gemmologischen Gesellschaft*, **31**: 71-77.
- Hänni, H.A., Schwarz, D. & Fischer, M. 1987. The emeralds of the Belmont Mine, Minas Gerais, Brazil. *Journal of Gemmology*, **20**: 446-456.
- Hawkesworth, C.J., Bickle, M.J., Gledhill, A.R., Wilson, J.F. & Orpen, J.L. 1979. A 2.9 b.y. event in the Rhodesian Archaean. *Earth & Planetary Science Letters*, **43**: 285-297.
- Heinrich, C.A., Guenther, D., Audetat, A., Ulrich, T. & Frischknecht, R. 1999. Metal fractionation between magmatic brine and vapor, determined by microanalysis of fluid inclusions. *Geology*, **27**: 755-758.
- Heinrich, C.A., Ryan, C.G., Mernagh, T.P. & Eadington, P.J. 1992. Segregation of ore metals between magmatic brine and vapor; a fluid inclusion study using PIXE microanalysis. *Economic Geology*, **87**: 1566-1583.
- Henn, U. & Bank, H. 1991. Aussergewöhnliche Smaragde aus Nigeria. *Zeitschrift der Deutschen Gemmologischen Gesellschaft*, **40**: 181-187.
- Hickman, A.C.J. 1973. The geology of the Luanshya area. *Report of the Geological Survey of Zambia*, **46**: 32 pp.

- Hickman, M.H. 1984. Rb-Sr chemical and isotopic response of gneisses in Late Archean shear zones of the Limpopo Belt, Southern Africa. *Precambrian Research*, **24**: 123-130.
- Hildreth, W. 1981. Gradients in silicic magma chambers: implications for lithospheric magmatism. *Journal of Geophysical Research*, **86**: 10153-10192.
- Hippertt, J.F. & Valarelli, V. 1998. Myrmekite: constraints on the available models and a new hypothesis for its formation. *European Journal of Mineralogy*, **10**: 317-331.
- Holmes, A. 1954. The oldest dated minerals of the Rhodesian Shield. *Nature*, **173**: 612-614.
- Jamieson, R.T. & Schreiner, G.D.L. 1957. The ages of some African lepidolites determined from the ^{87}Rb - ^{87}Sr decay. *Proceedings of the Royal Society of London*, **146**: 257-269.
- John, T., Schenk, V., Mezger, K. & Tembo, F. 2004. Timing and PT evolution of whiteschist metamorphism in the Lufilian Arc - Zambezi Belt Orogen (Zambia): implications for assembly of Gondwana. *Journal of Geology*, **112**: 71-90.
- Johnson, M.C. & Rutherford, M.J. 1989. Experimental calibration of the aluminum-in-hornblende geobarometer with application to Long Valley caldera (California) volcanic rocks. *Geology*, **17**: 837-841.
- Jolly, W.T. 1982. Progressive metamorphism of komatiites and related Archean lavas of the Abitibi area, Canada. In: Arndt, N.A.N.E.G. (ed.), *Komatiites*: 247-266. Allen & Unwin, London.
- Kamber, B.S., Biino, G.G., Wijbrans, J.R., Davies, G.R. & Villa, I.M. 1996. Archean granulites of the Limpopo Belt, Zimbabwe: one slow exhumation or two rapid events? *Tectonics*, **15**: 1414-1430.
- Kamber, B.S., Blenkinsop, T.G., Villa, I.M. & Dahl, P.S. 1995b. Proterozoic transpressive deformation in the Northern Marginal Zone, Limpopo Belt, Zimbabwe. *Journal of Geology*, **103**: 493-508.
- Kamber, B.S., Kramers, J.D., Napier, R., Cliff, R.A. & Rollinson, H.R. 1995a. The Triangle Shearzone, Zimbabwe, revisited: new data document an important event at 2.0 Ga in the Limpopo Belt. *Precambrian Research*, **70**: 191-213.
- Kanis, J., Arps, C.E.S. & Zwaan, P.C. 1991. 'Machingwe': a new emerald deposit in Zimbabwe. *Journal of Gemmology*, **22**: 264-272.
- Kanis, J. & Schwarz, D. 2001. Die Smaragd-Vorkommen der Welt: Afrika. In: Schwarz, D. & Hochleitner, R. (eds), *Smaragd, der kostbarste Beryll, der teuerste Edelstein*. Extra Lapis: 56-63. Weise Verlag, München.
- Kawai, T. 1960. Chemical studies on minerals containing rare elements from the Far East (Rept. 49): ilmenorutile from Uzumine, Sukagawa-shi, Fukushima Prefecture. *Journal of the Chemical Society Japan (Pure Chemistry Section)*, **81**: 1059.
- Kazmi, A.H. & Snee, L.W. 1989. Geology of World emerald deposits: a brief review. In: Kazmi, H. & Snee, L. (eds), *Emeralds of Pakistan: Geology, Gemology and Genesis*: 165-228. Van Nostrand Reinhold, New York.
- Kisters, A.F.M., Kolb, J. & Meyer, F.M. 1997. Archean and Proterozoic mineralization and tectonics at the Renco Mine (Northern Marginal Zone, Limpopo Belt, Zimbabwe) - a discussion. *Economic Geology*, **92**: 745-752.
- Klein, C. 1978. Regional metamorphism of Proterozoic iron-formation, Labrador Trough, Canada. *American Mineralogist*, **63**: 898-912.
- Koivula, J.I., Kammerling, R.C., Ghionno, D. De, Reinitz, I., Fritsch, E. & Johnson, M.L. 1996. Gemological investigation of a new type of Russian hydrothermal synthetic emerald. *Gems & Gemology*, **32**: 32-39.
- Korzhinskiy, M.A. 1981. Apatite solid solutions as indicators of the fugacity of HCl^0 and HF^0 in hydrothermal fluids. *Geochemistry International*, **18**(3): 44-60.
- Kozłowski, A., Metz, P. & Estrada Jaramillo, H.A. 1988. Emeralds from Somondoco, Colombia: chemical composition, fluid inclusions and origin. *Neues Jahrbuch für Mineralogie Mitteilungen*, **159**: 23-49.
- Kretz, R. 1983. Symbols for rock-forming minerals. *American Mineralogist*, **68**: 277-279.
- Kyser, T.K. 1986. Stable isotope variations in the mantle. In: *Reviews in Mineralogy*: 141-164. Mineralogical Society of America, Washington, D.C.
- Laskovenkov, A.F. & Zhernakov, V.I. 1995. An update on the Ural emerald mines. *Gems & Gemology*, **31**: 106-113.
- Laurs, B.M., Dilles, J.H. & Snee, L.W. 1996. Emerald mineralization and metasomatism of amphibolite, Khaltaro granitic pegmatite - hydrothermal vein system, Haramosh mountains, northern Pakistan. *Canadian Mineralogist*, **34**: 1253-1286.

- Laurs, B.M., Simmons, W.B., Rossmann, G.R., Quinn, E.P., McClure, S.F., Peretti, A., Armbruster, T., Hawthorne, F.C., Falster, A.U., Günther, D., Cooper, M.A. & Grobóty, B. 2003. Pezzottaite from Ambatovita, Madagascar: a new gem mineral. *Gems & Gemology*, **39**: 284-301.
- Leake, B.E. 1978. Nomenclature of amphiboles. *American Mineralogist*, **63**: 1023-1052.
- Leake, B.E., Woolley, A.R., Arps, C.E.S., Birch, W.D., Gilbert, M.C., Grice, J.D., Hawthorne, F.C., Kato, A., Kisch, H.J., Krivovichev, V.G., Linthout, K., Laird, J., Mandarino, J., Maresch, W.V., Nickel, E.H., Rock, N.M.S., Schumacher, J.C., Smith, D.C., Stephenson, N.C.N., Ungaretti, L., Whittaker, E.J.W. & Youzhi, G. 1997. Nomenclature of amphiboles: report of the Subcommittee on Amphiboles of the International Mineralogical Association Commission on New Minerals and Mineral Names. *Mineralogical Magazine*, **61**: 295-321.
- Liddicoat, R.T. 1989. *Handbook of Gem Identification*. Gemological Institute of America, Santa Monica, CA: 440 pp.
- Lind, T., Henn, U. & Bank, H. 1986. Smaragde von Sta. Terezinha de Goias, Brasilien, mit relativ hoher Lichtbrechung. *Zeitschrift der Deutschen Gemmologischen Gesellschaft*, **35**: 186-187.
- Liou, J.G. 1973. Synthesis and stability relations of epidote, $\text{Ca}_2\text{Al}_2\text{FeSi}_3\text{O}_{12}(\text{OH})$. *Journal of Petrology*, **14**: 381-413.
- Liou, J.G., Kuniyoshi, S. & Ito, K. 1974. Experimental studies of the phase relations between greenschist and amphibolite in a basaltic system. *American Journal of Science*, **274**: 613-632.
- Lips, A.L.W. 1998. *Temporal constraints on the Kinematics of the Destabilization of an Orogen; Syn- to Post-Orogenic extensional collapse of the Northern Aegean Region*. Unpublished Ph.D. thesis, Rijksuniversiteit Utrecht, Geologica Ultraiectina, no. 166 Thesis, University of Utrecht, Utrecht: 224 pp.
- London, D. 1984. Experimental phase equilibria in the system $\text{LiAlSi}_4\text{O}_4\text{-SiO}_2\text{-H}_2\text{O}$: a petrogenetic grid for lithium-rich pegmatites. *American Mineralogist*, **69**: 995-1004.
- London, D. 1986. The magmatic-hydrothermal transition in the Tanco rare-element pegmatite: evidence from fluid inclusions and phase equilibrium experiments. *American Mineralogist*, **71**: 376-395.
- London, D. 1987. Internal differentiation of rare-element pegmatites: effects of boron, phosphorus, and fluorine. *Geochimica et Cosmochimica Acta*, **51**: 403-420.
- London, D. 1990. Internal differentiation of rare-element pegmatites; a synthesis of recent research. In: Stein, H.J. & Hannah, J.L. (eds), *Ore-bearing Granite Systems; Petrogenesis and Mineralizing Processes*: 35-47. Geological Society of America, Boulder.
- London, D. 1996. Granitic pegmatites. *Transactions of the Royal Society of Edinburgh: Earth Sciences*, **87**: 305-319.
- London, D. & Evensen, J.M. 2002. Beryllium in silicic magmas: origin of beryl-bearing pegmatites. In: Grew, E.S. (ed.), *Beryllium - Mineralogy, Petrology, and Geochemistry. Reviews in Mineralogy and Geochemistry*: 445-486. Mineralogical Society of America, Washington, D.C.
- London, D., Hervig, R.L. & Morgan, G.B. 1988. Vapor-undersaturated experiments with Macusani glass + H_2O at 200 MPa, and the internal differentiation of granitic pegmatites. *Contributions to Mineralogy and Petrology*, **102**: 360-373.
- Longstaffe, F.J. 1982. Stable isotopes in the study of granitic pegmatites and related rocks. In: Cerný, P. (ed.), *Granitic Pegmatites in Science and Industry*: 373-404. Mineralogical Association of Canada, Short-Course Handbook.
- Manning, D.A.C., Hamilton, D.L., Henderson, C.M.B. & Dempsey, M.J. 1980. The probable occurrence of interstitial Al in hydrous, F-bearing and F-free aluminosilicate melts. *Contributions to Mineralogy and Petrology*, **75**: 257-262.
- Mark, G. 1998. Albitite formation by selective pervasive sodic alteration of tonalite plutons in the Cloncurry district, Queensland. *Australian Journal of Earth Sciences*, **45**: 765-774.
- Martin, A., Nisbet, E.G., Bickle, M.J. & Orpen, J.L. 1993. Rock units and stratigraphy of the Belingwe Greenstone Belt: the complexity of the tectonic setting. In: Bickle, M.J. & Nisbet, E.G. (eds), *The Geology of the Belingwe Greenstone Belt, Zimbabwe*. Geological Society of Zimbabwe, Special Publication: 13-38. A.A. Balkema, Rotterdam.
- Martin, H.J. 1962. Some observations on Southern Rhodesian emeralds and chrysoberyl. *Chamber of Mines Journal*, **4**(10): 34-38.

- McDougall, M. & Harrison, T.M. 1999. *Geochronology and Thermochronology by the $^{39}\text{Ar}/^{40}\text{Ar}$ Method*. Oxford University Press, New York.
- McIntire, W.L. 1963. Trace element partition coefficients - a review of theory and applications to geology. *Geochimica et Cosmochimica Acta*, **27**: 1209-1264.
- Mennell, F.P. 1906. Somabula diamond field of Rhodesia. *Geological Magazine*, **43**: 459-462.
- Merrihue, C. & Turner, G. 1966. Potassium-argon dating by activation with fast neutrons. *Journal of Geophysical Research*, **71**: 2852-2857.
- Metson, N.A. & Taylor, A.M. 1977. Observations on some Rhodesian emerald occurrences. *Journal of Gemmology*, **15**: 422-434.
- Michel-Lévy, A.M. 1874. Structure microscopique des roches acides anciennes. *Bulletin de la Société Minéralogie-Cristallographie*, **3**: 201-222.
- Mitchell, J.G. 1968. The argon-40/argon-39 method for potassium-argon age determination. *Geochimica et Cosmochimica Acta*, **32**: 781-790.
- Mkweli, S., Kamber, B. & Berger, M. 1995. Westward continuation of the craton-Limpopo belt tectonic break in Zimbabwe and new age constraints on the timing of the thrusting. *Journal of the Geological Society, London*, **152**: 77-83.
- Morgan, G.B.V. & London, D. 1999. Crystallization of the Little Three layered pegmatite-aplite dike, Ramona District, California. *Contributions to Mineralogy and Petrology*, **136**: 310-330.
- Moroz, I. & Vapnik, Y. 1999. Fluid inclusions in emeralds from schist-type deposits. *Canadian Gemmologist*, **20**: 8-14.
- Morteani, G. & Grundmann, G. 1977. The emerald porphyroblasts in the penninic rocks of the central Tauern Window. *Neues Jahrbuch für Mineralogie Mitteilungen*, **11**: 509-516.
- Mumme, I. 1982. *The Emerald*. Mumme Publications, Port Hacking, N.S.W.
- Munoz, J.L. 1984. F-OH and Cl-OH exchange in micas with applications to hydrothermal ore deposits. In: Bailey, S.W. (ed.), *Micas. Reviews in Mineralogy*: 469-493. Mineralogical Society of America, Washington, D.C.
- Munoz, J.L. & Ludington, S.D. 1974. Fluorine-hydroxyl exchange in biotite. *American Journal of Science*, **274**: 396-413.
- Mysen, B.O., Cody, G.D. & Smith, A. 2004. Solubility mechanisms of fluorine in peralkaline and meta-aluminous silicate glasses and in melts to magmatic temperatures. *Geochimica et Cosmochimica Acta*, **68**: 2745-2769.
- Nier, A.O. 1950. A redetermination of the relative abundances of the isotopes of carbon, nitrogen, oxygen, argon, and potassium. *Physics Reviews*, **77**: 789-793.
- Noll, W. 1949. Zur Kristallchemie des Zinnsteins (Kassiterit). *Heidelberger Beiträge zur Mineralogie und Petrographie*, **1**: 593-625.
- Norton, J.J. 1983. Sequence of mineral assemblages in differentiated granitic pegmatites. *Economic Geology*, **78**: 854-874.
- Nwe, Y.Y. & Grundmann, G. 1990. Evolution of metamorphic fluids in shear zones: the record from the emeralds of Habachtal, Tauern Window, Austria. *Lithos*, **25**: 281-304.
- Nwe, Y.Y. & Morteani, G. 1993. Fluid evolution in the $\text{H}_2\text{O}-\text{CH}_4-\text{CO}_2-\text{NaCl}$ system during emerald mineralization at Gravelotte, Murchison Greenstone Belt, northeast Transvaal, South Africa. *Geochimica et Cosmochimica Acta*, **57**: 89-103.
- Ottaway, T.L., Wicks, F.J., Bryndzia, L.T., Kyser, T.K. & Spooner, E.T.C. 1994. Formation of the Muzo hydrothermal emerald deposit in Colombia. *Nature*, **369**: 552-554.
- Parkin, J. 2000. *Geology of the St. Francis Mission and Musakazhi River Areas. Explanation of Degree Sheet 1226 NE and SE Quarters and Part of 1126 SE Quarter*. Geological Survey Department, Lusaka, Zambia: 49 pp.
- Phillips, E.R. & Ransom, D.M. 1968. The proportionality in myrmekite. *American Mineralogist*, **54**: 1411-1413.
- Pichavant, M. 1987. Effects of B and H_2O on liquidus phase relations in the haplogranite system at 1 kbar. *American Mineralogist*, **72**: 1056-1070.
- Pinet, M., Smith, D. & Lasnier, B. 1992. Utilité de la microsonde Raman pour l'identification non destructive des gemmes. In: *La Microsonde Raman en Gemmologie Revue de Gemmologie a.f.g.*: 11-61.

- Pyke, D.R., Naldrett, A.J. & Eckstrand, O.R. 1973. Archaean ultramafic flows in Munro Township, Ontario. *Geological Society of America Bulletin*, **84**: 955-978.
- Ridley, J. 1992. On the origins and tectonic significance of the charnockite suite of the Archaean Limpopo Belt, Northern Marginal Zone, Zimbabwe. *Precambrian Research*, **55**: 407-427.
- Robertson, I.D.M. 1973. Potash granites of the southern edge of the Rhodesian craton and the northern granulite zone of the Limpopo mobile belt. In: Lister, L. A. (ed.), *Symposium on Granites, Gneisses and Related Rocks*: 265-276. Geological Society of South Africa, Salisbury.
- Roddick, J.C. 1983. High precision intercalibration of ^{40}Ar - ^{39}Ar standards. *Geochimica et Cosmochimica Acta*, **47**: 887-898.
- Roedder, E. 1984. Fluid Inclusions. *Reviews in Mineralogy*, **12**: 1-644. Mineralogical Society of America, Washington, D.C.
- Rollinson, H. & Blenkinsop, T. 1995. The magmatic, metamorphic and tectonic evolution of the Northern Marginal Zone of the Limpopo belt in Zimbabwe. *Journal of the Geological Society, London*, **152**: 65-75.
- Ruffet, G., Féraud, G. & Amouric, M. 1991. Comparison of $^{40}\text{Ar}/^{39}\text{Ar}$ conventional and laser dating of biotites from the North Tregor Batholith. *Geochimica et Cosmochimica Acta*, **55**: 1675-1688.
- Russell, A. 1988. Bikita Minerals, 35 years on and still further potential. *Industrial Minerals*, **249**: 63-71.
- Sallet, R. 2000. Fluorine as a tool in the petrogenesis of quartz-bearing magmatic associations: applications of an improved F-OH biotite-apatite thermometer grid. *Lithos*, **50**: 241-253.
- Satir, M. 1974. Rb-Sr-Altersbestimmungen und Glimmern der westlichen Hohen Tauern; interpretation und geologische Bedeutung. *Schweizerische Mineralogische und Petrographische Mitteilungen*, **54**: 214-228.
- Schäfer, W. 2002. *Geologische, mineralogische und geochemische Untersuchungen an zwei Smaragdorkommen in der Neuhof-Formation SW-Namibia*. Unpublished Diplomarbeit Thesis, Ludwig-Maximilian-Universität, München: 106 pp.
- Shaller, W.T., Stevens, R.E. & Jahns, R.H. 1962. An unusual beryl from Arizona. *American Mineralogist*, **47**: 672-699.
- Schmetzer, K., Berdesinski, W. & Bank, H. 1974. Über die Mineralart beryll, ihre farben und Absorptionsspektren. *Zeitschrift der Deutschen Gemmologischen Gesellschaft*, **23**: 5-39.
- Schmetzer, K., Bernhardt, H. & Biehler, R. 1991. Emeralds from the Ural Mountains, USSR. *Gems & Gemology*, **27**: 86-99.
- Schmetzer, K., Kiefert, L., Bernhardt, H.-J. & Zhang, B. 1997. Characterization of Chinese hydrothermal synthetic emerald. *Gems & Gemology*, **33**: 276-291.
- Schrader, H.W. 1983. Contributions to the study of the distinction of natural and synthetic emeralds. *Journal of Gemmology*, **18**: 530-543.
- Schulz, B., Siegesmund, S., Steenken, A., Schoenhofer, R. & Heinrichs, T. 2001. Geologie des ostalpinen Kristallins südlich des Tauernfensters zwischen Virgental und Pustertal. *Zeitschrift der Deutschen Geologischen Gesellschaft*, **152**: 261-307.
- Schwarz, D. 1990a. Die brasilianischen Smaragde und ihre Vorkommen: Santa Terezinha de Goias/Go. *Zeitschrift der Deutschen Gemmologischen Gesellschaft*, **39**: 13-44.
- Schwarz, D. 1990b. The Brazilian emeralds and their occurrences: Socotó, Bahia. *Journal of Gemmology*, **22**: 147-163.
- Schwarz, D. 1991a. Die chemischen Eigenschaften der Smaragde III. Habachtal/Österreich und Uralgebirge/UdSSR. *Zeitschrift der Deutschen Gemmologischen Gesellschaft*, **39**: 13-44.
- Schwarz, D. 1991b. Australian emerald. *Australian Gemmologist*, **17**: 488-497.
- Schwarz, D. 1994. Emeralds from the Mananjary Region, Madagascar: Internal features. *Gems & Gemology*, **30**: 88-101.
- Schwarz, D. & Giuliani, G. 2001. Emerald deposits - a review. *Australian Gemmologist*, **21**: 17-23.
- Schwarz, D., Giuliani, G., Grundmann, G. & Glas, M. 2001. Die Entstehung der Smaragde, ein viel diskutiertes Thema. In: Schwarz, D. & Hochleitner, R. (eds), *Smaragd, der kostbarste Beryll, der teuerste Edelstein, ExtraLapis*: 68-73. Weise Verlag, München.
- Schwarz, D. & Henn, U. 1992. Emeralds from Madagascar. *Journal of Gemmology*, **23**: 140-149.
- Schwarz, D., Kanis, J. & Kinnaird, J. 1996. Emerald and green beryl from central Nigeria. *Journal of Gemmology*, **25**: 117-141.

- Seal II, R.R. 1989. A reconnaissance study of the fluid inclusion geochemistry of the emerald deposits of Pakistan and Afghanistan. In: Kazmi, A.H. & Snee, L.W. (eds), *Emeralds of Pakistan*: 151-164. Van Nostrand Reinhold, New York.
- Seifert, A.V., Žáček, V., Vrána, S., Pecina, V., Zachariáš, J. & Zwaan, J.C. 2004. Emerald mineralization in the Kafubu area, Zambia. *Bulletin of Geosciences*, **79**: 1-40.
- Shearer, C.K. & Papike, J.J. 1988. Pegmatite-wallrock interaction: Holmquistite-bearing amphibolite, Edison pegmatite, Black Hills, South Dakota. *American Mineralogist*, **73**: 324-337.
- Sheppard, S.M.F. 1986. Characterization and isotopic variations in natural waters. *Reviews in Mineralogy*, **16**: 165-183.
- Shmonov, V.M., Acsyuk, A.M. & Alyokhin, Y.V. 1986. Hydrothermal solutions and skarn-formation. In: Zharikov, V.A. (ed.), *Experiment in the Solving of the Actual Geological Problems*: 278-306. Nauka, Moscow. [In Russian.]
- Siivola, J. 1970. Ilmenorutile and strüverite from Penikvoja, Somero, SW Finland. *Bulletin of the Geological Society of Finland*, **42**, 33-36.
- Simpson, C. & Wintsch, R.P. 1989. Evidence for deformation-induced K-feldspar replacement by myrmekite. *Journal of Metamorphic Geology*, **7**: 261-275.
- Sinkankas, J. 1981. *Emerald and other Beryls*. Chilton Book Co., Pennsylvania & Nelson Canada Ltd., Ontario: 665 pp.
- Sliwa, A.S. & Nguluwe, C.A. 1984. Geological setting of Zambian emerald deposits. *Precambrian Research*, **25**: 213-228.
- Smith, D. 1979. Hydrous minerals and carbonates in peridotite intrusions from the Green Knobs and Buell Park kimberlitic diatremes on the Colorado Plateau. In: Boyd, F.R. & Meyer, H.O.A (eds), *The Mantle Sample: Inclusions in Kimberlites and other Volcanics*: 345-356. American Geophysical Union, Washington, D.C.
- Snee, L.W. & Kazmi, A.H. 1989. Origin and classification of Pakistani and world emerald deposits. In: Kazmi, A.H. & Snee, L.W. (eds), *Emeralds of Pakistan*: 229-236. Van Nostrand Reinhold, Karachi.
- Sosedko, A.F. 1939. New data on the mineralogy of the Ilmen Mountains. *Doklady Akademii Nauk Soyuzha Sovetskikh Sotsialisticheskikh respublik*, **22**: 596-598. [In Russian.]
- Souza, J. L. de, Mendes, J.C., Silveira Bello, R.M. da, Svisero, D.P. & Valarelli, J.V. 1992. Petrographic and microthermometrical studies of emeralds in the 'Garimpo' of Capoeirana, Nova Era, Minas Geras State, Brazil. *Mineralium Deposita*, **27**: 161-168.
- Spear, F.S. 1981a. An experimental study of hornblende stability and compositional variability in amphibolite. *American Journal of Sciences*, **281**: 697-734.
- Spear, F.S. 1981b. Amphibole-plagioclase equilibria: an empirical model for the reaction albite + tremolite = edenite + 4 quartz. *Contributions to Mineralogy and Petrology*, **77**: 355-364.
- Spear, F.S. 1993. *Metamorphic Phase Equilibria and Pressure-Temperature-Time Paths*. Mineralogical Society of America - Monograph, Washington, D.C.: 799 pp.
- Spray, J.G., Kelley, S.P., Rowley, D.B. 1998. Evidence for a Late Triassic multiple impact event on Earth. *Nature*, **392**: 171-173.
- Steiger, R.H. & Jäger, E. 1977. Subcommittee on geochronology: convention on the use of decay constants in geo- and cosmochronology. *Earth & Planetary Science Letters*, **36**: 359-362.
- Stewart, D.B. 1978. Petrogenesis of lithium-rich pegmatites. *American Mineralogist*, **63**: 970-980.
- Summers, R. 1969. *Ancient Mining in Rhodesia*. Mardon Printers, Salisbury: 236 pp.
- Taylor, B.E. 1982. Light stable isotope geochemistry of granitic gem- and non-gem-bearing pegmatites. In: Brown-Gordon, E. J. (ed.), *The Mineralogy of Pegmatites*: 185. Mineralogical Society of America, Washington, D.C.
- Taylor, B.E., Foord, E.E. & Friedrichsen, H. 1979. Stable isotope and fluid inclusion studies of gem-bearing granitic pegmatite-aplite dikes, San Diego Co., California. *Contributions to Mineralogy and Petrology*, **68**: 187-205.
- Taylor, H.P. 1967. Oxygen isotope studies of hydrothermal mineral deposits. In: Barnes, H.L. (ed.), *Geochemistry of Hydrothermal Ore Deposits*: 109-142. Wiley, New York.
- Taylor, H.P. 1979. Oxygen and hydrogen isotope relationships in hydrothermal mineral deposits. In: Barnes, H.L. (ed.), *Geochemistry of Hydrothermal Ore Deposits*: 236-277. Wiley, New York.

- Taylor, R.P., Fallick, A.E. & Breaks, F.W. 1992. Volatile evolution in Archean rare-element granitic pegmatites; evidence from the hydrogen isotopic composition of channel H₂O in beryl. *Canadian Mineralogist*, **30**: 877-893.
- Tracy, R.J. & Frost, B.R. 1991. Phase equilibria and thermobarometry of calcareous, ultramafic and mafic rocks, and iron formations. In: Kerrick, D.M., *Contact Metamorphism, Reviews in Mineralogy*: 207-289. Mineralogical Society of America, Washington, D.C.
- Treloar, P.J. 1987. The Cr-minerals of Outokumpu - their chemistry and significance. *Journal of Petrology*, **28**: 867-886.
- Tsunogae, T., Miyano, T. & Ridley, J. 1992. Metamorphic P-T profiles from the Zimbabwe Craton to the Limpopo Belt, Zimbabwe. *Precambrian Research*, **55**: 259-277.
- Vapnik, Y. & Moroz, I. 2002. Compositions and formation conditions of fluid inclusions in emerald from the Maria deposit (Mozambique). *Mineralogical Magazine*, **66**: 201-213.
- Vernon, R.H. 1991. Questions about myrmekite in deformed rocks. *Journal of Structural Geology*, **13**: 979-985.
- Vernon, R.H. 2004. *A Practical Guide to Rock Microstructure*. Cambridge University Press, Cambridge: 594 pp.
- Vidal, P., Lasnier, B. & Poirot, J.P. 1992. Determination of the age and origin of emeralds using rubidium-strontium analysis. *Journal of Gemmology*, **23**: 198-200.
- Villa, I.M. 1998. Isotopic closure. *Terra Nova*, **10**: 42-47.
- Waele, B. de, Wingate, M.T.D., Fitzsimons, I.C.W. & Mapani, B. 2003. Untying the Kibaran Knot: a re-assessment of Mesoproterozoic correlations in southern Africa based on SHRIMP U-Pb data from the Irumide belt. *Geology*, **31**: 509-512.
- Wagner, P.A. 1914. *The Diamond fields of Southern Africa*. Struik, Cape Town.
- Wang, Y., Li, J., Lu, J. & Fan, W. 1982. Geochemical mechanism of Nb, Ta-mineralisation during the late stage of granite crystallisation. *Geochemistry Beijing*, **1**: 175-185.
- Webber, K.L., Simmons, W.B., Falster, A.U. & Foord, E.E. 1999. Cooling rates and crystallization dynamics of shallow level pegmatite-aplite dikes, San Diego County, California. *American Mineralogist*, **84**: 708-717.
- Webster, R. 1994. *Gems*. Butterworth-Heinemann, Oxford: 1024 pp.
- Williams-Jones, A.E., Migdisov, A.A. & Archibald, S.M. 2003. Vapor transport of ore metals in hydrothermal systems. *Geological Society of America, Abstracts with Programs*, **35**(6): 356.
- Willigers, B.J.A., Krogstad, E.J. & Wijbrans, J.R. 2001. Comparison of thermochronometers in a slowly cooled granulite terrain: Nagssugtoqidian Orogen, West Greenland. *Journal of Petrology*, **42**: 1729-1749.
- Wilson, A.H. & Versfeld, J.A. 1994. The early Archaean Nondweni greenstone belt, southern Kaapvaal Craton, South Africa, part II. Characteristics of the volcanic rocks and constraints on magma genesis. *Precambrian Research*, **67**: 227-320.
- Wilson, A.H., Versfeld, J.A. & Hunter, D.R. 1989. Emplacement, crystallization and alteration of spinifex-textured komatiitic basalt flows in the Archaean Nondweni greenstone belt, southern Kaapvaal Craton, South Africa. *Contributions to Mineralogy and Petrology*, **101**: 301-317.
- Wilson, J.F. 1990. A craton and its cracks: some of the behaviour of the Zimbabwe block from the Late Archaean to the Mesozoic in response to horizontal movements, and the significance of some of its mafic dyke fracture patterns. *Journal of African Earth Sciences*, **10**: 483-501.
- Wilson, J.F., Bickle, M.J., Hawkesworth, C.J., Martin, A., Nisbet, E.G. & Orpen, J.L. 1978. Granite-greenstone terrains of the Rhodesian Archaean craton. *Nature*, **271**: 23-27.
- Wilson, J.F., Jones, D.L. & Kramers, J.D. 1987. Mafic dyke swarms in Zimbabwe. In: Halls, H.C. & Fahrig, W.F. (eds), *Mafic Dyke Swarms*: 433-444. Geological Association of Canada, Toronto.
- Wilson, J.T., Farquhar, R.M., Gretener, P., Russell, R.D. & Shillibeer, H.A. 1954. Estimates of age for some African minerals. *Nature*, **174**: 1006-1007.
- Witt, W.K. 1987. Fracture-controlled feldspathic alteration in granites associated with tin mineralization in the Irvinebank-Emuford area, northeast Queensland. *Australian Journal of Earth Sciences*, **34**: 447-462.
- Witt, W.K. 1988. Evolution of high-temperature hydrothermal fluids associated with greisenization and feldspathic alteration of a tin-mineralized granite, northeast Queensland. *Economic Geology*, **83**: 310-334.

- Wolf, M.B. & London, D. 1994. Apatite dissolution into peraluminous haplogranitic melts: An experimental study of solubilities and mechanisms. *Geochimica et Cosmochimica Acta*, **58**: 4127-4145.
- Wolf, M.B. & London, D. 1997. Boron in granitic magmas: stability of tourmaline in equilibrium with biotite and cordierite. *Contributions to Mineralogy and Petrology*, **130**: 12-30.
- Wood, B.J. & Nicholls, J. 1978. The thermodynamic properties of reciprocal solid solutions. *Contributions to Mineralogy and Petrology*, **66**: 389-400.
- Wood, D.L. & Nassau, K. 1967. Infrared spectra of foreign molecules in beryl. *Journal of Chemical Physics*, **47**: 2220-2228.
- Wood, D.L. & Nassau, K. 1968. The characterization of beryl and emerald by visible and infrared absorption spectroscopy. *American Mineralogist*, **53**: 777-799.
- Wood, S.A. 1991. Speciation of Be and the solubility of bertrandite/phenakite mineral in hydrothermal solutions. In: Pagel, M. & Leroy, J. L. (eds), *Source, Transport, and Deposition of Metals*: 147-150. A.A. Balkema, Rotterdam.
- Worst, B.G. 1956. *The Geology of the Country between Belingwe and West Nicholson*. Southern Rhodesia Geological Survey, Salisbury: 218 pp.
- Wyllie, P.J. & Tuttle, O.F. 1961. Experimental investigation of silicate systems containing two volatile components. II. The effects of NH₃ and HF, in addition to H₂O on the melting temperatures of albite and granite. *American Journal of Science*, **259**: 128-143.
- Yardley, B.W.D. 1989. *An Introduction to Metamorphic Petrology*. Longman Sci. Techn., Singapore: 264 pp.
- Zakharchenko, A.I. 1976. Transition of granitic melts to fluids: their nature and metal content (as inferred from fluid inclusions in minerals). In: *International Geological Congress*: 261-273. Nauka, Moscow.
- Zhu, C. & Sverjensky, D.A. 1991. Partitioning of F-Cl-OH between minerals and hydrothermal fluids. *Geochimica et Cosmochimica Acta*, **55**: 1837-1858.
- Zhu, C. & Sverjensky, D.A. 1992. F-Cl-OH partitioning between biotite and apatite. *Geochimica et Cosmochimica Acta*, **56**: 3435-3467.
- Zwaan, J.C. 2001. Preliminary study of emeralds from the Piteiras Emerald Mine, Minas Gerais, Brazil. In: *XXVIII International Gemmological Conference, Extended Abstracts*: 106-109. Madrid.
- Zwaan, J.C. & Burke, E.A.J. 1998. Emeralds from Sandawana, Zimbabwe: the use of Raman microspectroscopy in identification of their solid inclusions. *Journal of Gemmology*, **26**: 174-187.
- Zwaan, J.C., Cheillett, A. & Taylor, B.E. 2004. Tracing the emerald origin by oxygen isotope data: the case of Sandawana, Zimbabwe. *Comptes Rendus Geoscience*, **336**: 41-48.
- Zwaan, J.C., Kanis, J. & Petsch, E.J. 1997. Update on emeralds from the Sandawana Mines, Zimbabwe. *Gems & Gemology*, **33**: 80-100.
- Zwaan, J.C., Seifert, A., Vrána, S., Laurs, B.M., Ankar, B., Simmons, W.B., Falster, A.U., Lustenhouwer, W.J., Muhlmeister, S., Koivula, J.I. & Garcia-Guillerminet, H. 2005. Emeralds from the Kafubu area, Zambia. *Gems & Gemology*, **41**: 116-148.
- Zwaan, J.C. & Touret, J.L.R. 1998. Typology of fluid/solid inclusions in emeralds. In: *Nederlands Aardwetenschappelijk Congres IV: Geowetenschappelijke grensgevallen, Abstracts*. Veldhoven, The Netherlands: 1 p.
- Zwaan, J.C. & Touret, J.L.R. 2000. Emeralds in greenstone belts: the case of Sandawana, Zimbabwe. *Münchener Geologische Hefte, Festschrift zum 65. Geburtstag von Professor Dr-Ing. Giulio Morteani*, **A 28**: 245-258.

Appendix 1. Emerald analyses by EPMA

Emeralds Sample no.	From rock type	Locality
RGM 421369 (pdd 1369)	pegmatite 15 cm away from contact	Zeus mine, 300', 23/7
RGM 421545 (pdd 1545)	contact pegmatite/schist	Zeus mine, 200', 26/28
RGM 421550 (pdd 1550)	contact pegmatite/schist	Zeus mine, 200', 26/28
RGM 421552 (pdd 1552)	emerald in pegmatite	Zeus mine, 200', 26/28
RGM 421553 (Sample 96 JCZ 3)	pegmatite with amphibole stringer	Zeus mine, 200', 26/28 (2)
RGM 421588 (Sample 96JCZ4)	pegmatite	Zeus mine, 200', 26/28 (5)
RGM 421596 (Sample 96JCZ1)	amphibole phlogopite schist	Zeus mine, 200', 26/28 (6)
RGM 421619 (Sample 96 JCZ 9)	amphibole phlogopite schist	Zeus mine, 200', 25/28
RGM 421620 (Sample 96JCZ7)	amphibole phlogopite schist	Zeus mine, 300', 23/7
RGM 421622 (Sample 96JCZ 8)	amphibole phlogopite schist	Orpheus mine, open pit

Measurements were done on carbon-coated polished sample sections and were performed at 15 kV, with a beam current of 25 nA and a spot size of 3 μm . The count time for the major elements was 25 seconds and for the trace elements 36 seconds (except 50 seconds were counted for V, Cr, F, and Rb).

Analytical standards included both natural and synthetic materials; diopside (SiO_2 , TiO_2 , MgO , CaO), corundum (Al_2O_3), fayalite (FeO), tephroite (MnO), Sc_2O_3 (Sc_2O_3), jadeite (Na_2O), V_2O_5 (V_2O_5), Cr_2O_3 (Cr_2O_3), fluorite (F), RbBr (Rb), marialite (Cl), Cs_2ReCl_6 (Cs_2O) and orthoclase (K_2O).

Detection limits (in wt.%) for TiO_2 0.015, V_2O_5 0.026, MnO 0.025, Sc_2O_3 0.012, CaO 0.012, K_2O 0.009, Rb_2O 0.036, Cs_2O 0.028 and Cl 0.009.

Emerald analyses

	1	2	3	4	9	10	11	12	17	18	19	
	RGM 421596 (Sample 96)CZ1)				RGM 421553 (Sample 96)CZ 3)			RGM 421588 (Sample 96)CZ4)				
Oxides (wt.%)												
SiO ₂	63.11	63.22	62.84	63.14	62.72	62.89	63.00	62.54	62.96	62.77	62.81	
TiO ₂	0.02	-	-	-	-	-	-	-	-	-	-	
Al ₂ O ₃	14.14	13.73	12.96	13.21	13.50	13.50	14.05	13.92	14.73	13.99	14.05	
Sc ₂ O ₃	-	-	-	-	-	-	-	0.03	-	-	-	
V ₂ O ₅	0.04	-	0.06	0.05	0.04	0.03	0.06	0.05	0.05	0.05	-	
Cr ₂ O ₃	0.48	0.52	0.76	0.69	0.81	0.69	0.63	0.67	0.04	0.27	0.17	
BeO*	13.00	13.00	13.00	13.00	13.00	13.00	13.00	13.00	13.00	13.00	13.00	
FeO	0.36	0.74	0.57	0.59	0.48	0.48	0.45	0.47	0.55	0.75	0.83	
MnO	-	0.04	0.03	-	-	-	-	-	-	-	-	
MgO	2.47	2.65	2.66	2.77	2.65	2.61	2.55	2.57	2.28	2.42	2.45	
CaO	0.03	0.04	0.03	0.03	-	-	-	-	-	-	0.02	
Na ₂ O	1.96	2.09	2.15	2.18	2.32	2.47	2.39	2.31	2.24	2.36	2.29	
K ₂ O	0.06	0.05	0.05	0.07	0.07	0.06	0.06	0.05	0.05	0.06	0.08	
Rb ₂ O	0.03	-	0.03	0.04	0.05	-	-	0.07	-	-	0.04	
Cs ₂ O	0.06	0.06	0.11	0.08	0.10	0.09	0.09	0.10	0.07	0.12	0.08	
Cl	0.01	-	-	0.01	-	0.01	0.01	-	-	-	-	
Total	95.77	96.12	95.22	95.87	95.73	95.83	96.27	95.78	95.96	95.77	95.81	

Ions based on 18 Oxygens												
Si	6.008	6.011	6.035	6.026	5.997	6.005	5.985	5.976	5.984	5.994	5.995	
Ti	0.002	-	-	-	-	-	-	-	-	-	-	
Al	1.587	1.538	1.467	1.486	1.521	1.519	1.574	1.568	1.650	1.575	1.580	
Sc	-	-	-	-	-	-	-	0.002	-	-	-	
V	0.003	-	0.004	0.004	0.003	0.002	0.004	0.004	0.004	0.004	-	
Cr	0.036	0.039	0.057	0.052	0.062	0.052	0.048	0.051	0.003	0.020	0.013	
Be *	2.974	2.970	3.000	2.981	2.986	2.982	2.968	2.985	2.969	2.983	2.981	
Fe	0.028	0.059	0.046	0.047	0.038	0.038	0.036	0.038	0.043	0.060	0.066	
Mn	-	0.003	0.002	-	-	-	-	-	-	-	-	
Mg	0.351	0.376	0.381	0.395	0.377	0.371	0.361	0.366	0.323	0.344	0.348	
Ca	0.003	0.004	0.003	0.003	-	-	-	-	-	-	0.002	
Na	0.363	0.385	0.400	0.404	0.430	0.458	0.440	0.428	0.414	0.436	0.424	
K	0.008	0.006	0.006	0.008	0.009	0.007	0.007	0.006	0.006	0.007	0.009	
Rb	0.002	-	0.002	0.003	0.003	-	-	0.004	-	-	0.003	
Cs	0.003	0.002	0.005	0.003	0.004	0.004	0.004	0.004	0.003	0.005	0.003	
Cl	0.002	-	-	0.002	-	0.001	0.001	-	-	-	-	
Total	11.367	11.394	11.406	11.413	11.430	11.440	11.426	11.431	11.397	11.428	11.425	

* BeO was not analysed

P₂O₅ was analysed but not detected

- not detected

Emerald analyses (continued)

	RGM 421620 (Sample 96)CZ7														
Oxides (wt.%)	1	2	3	4	5	8	9	10	11	12	13	14	15		
SiO ₂	61.84	62.71	62.71	62.19	62.80	62.81	62.89	62.99	63.02	62.79	62.47	62.30	62.32		
TiO ₂	0.13	0.11	-	-	-	0.06	0.02	0.02	-	0.09	-	-	-		
Al ₂ O ₃	13.22	13.21	13.13	11.92	13.62	13.36	13.17	14.27	13.68	13.55	12.85	13.18	12.77		
Sc ₂ O ₃	na	na	na	na	na	na	na	na	na	na	na	na	na		
V ₂ O ₅	0.05	0.06	0.04	0.07	0.05	0.06	0.07	-	0.04	0.04	0.06	0.06	0.07		
Cr ₂ O ₃	1.26	1.30	1.73	2.12	1.08	1.04	0.75	0.13	0.30	1.13	1.66	1.74	1.73		
BeO*	13.00	13.00	13.00	13.00	13.00	13.00	13.00	13.00	13.00	13.00	13.00	13.00	13.00		
FeO	1.00	0.96	0.85	1.17	0.69	0.54	0.78	0.66	0.81	0.50	0.63	0.59	1.15		
MnO	-	-	-	0.03	-	-	-	-	-	-	-	-	-		
MgO	2.43	2.33	2.40	2.80	2.43	2.63	2.80	2.44	2.83	2.53	2.67	2.56	2.18		
CaO	-	0.02	-	-	-	-	0.03	-	0.02	-	-	0.02	0.03		
Na ₂ O	2.31	2.29	2.31	2.44	2.30	2.30	2.38	2.26	2.35	2.25	2.28	2.27	2.40		
K ₂ O	0.03	0.03	0.03	0.05	0.01	0.03	0.05	0.01	0.04	0.03	0.03	0.03	0.03		
Rb ₂ O	-	-	-	-	0.04	-	0.08	-	0.11	-	0.08	0.04	-		
Cs ₂ O	0.06	0.06	0.07	0.06	0.05	0.05	0.03	0.06	0.05	0.08	0.06	0.09	0.07		
Cl	0.02	-	0.01	0.02	0.01	0.01	-	-	-	0.01	-	0.01	0.02		
F	-	-	-	0.04	0.09	-	-	-	-	-	-	0.05	-		
Total	95.35	96.07	96.27	95.86	96.08	95.88	96.05	95.84	96.23	95.99	95.77	95.87	95.77		

Ions based on 18 Oxygens																											
Si	5.960	5.993	5.987	5.990	5.990	5.997	6.004	5.996	5.997	5.989	5.991	5.970	5.993	5.960	5.993	5.987	5.990	5.990	5.997	6.004	5.996	5.997	5.989	5.991	5.970	5.993	
Ti	0.010	0.008	-	-	-	0.004	0.002	0.001	-	0.006	-	-	-	0.010	0.008	-	-	-	0.004	0.002	0.001	-	0.006	-	-	-	
Al	1.502	1.488	1.477	1.354	1.531	1.503	1.482	1.602	1.534	1.523	1.452	1.488	1.447	1.502	1.488	1.477	1.354	1.531	1.503	1.482	1.602	1.534	1.523	1.452	1.488	1.447	
Sc	-	-	-	-	-	-	-	-	-	-	-	-	-	-	-	-	-	-	-	-	-	-	-	-	-	-	-
V	0.004	0.005	0.003	0.005	0.004	0.005	0.005	-	0.003	0.003	0.005	0.005	0.005	0.004	0.005	0.003	0.005	-	0.003	0.003	0.005	0.003	0.005	0.005	0.005	0.005	
Cr	0.096	0.098	0.130	0.162	0.081	0.078	0.057	0.010	0.023	0.085	0.126	0.132	0.132	0.096	0.098	0.130	0.162	0.081	0.078	0.057	0.010	0.023	0.085	0.126	0.132	0.132	
Be*	3.010	2.985	2.982	3.008	2.979	2.982	2.982	2.974	2.972	2.979	2.995	2.993	3.003	3.010	2.985	2.982	3.008	2.979	2.982	2.982	2.974	2.972	2.979	2.995	2.993	3.003	
Fe	0.081	0.077	0.068	0.094	0.055	0.043	0.062	0.052	0.064	0.040	0.050	0.047	0.093	0.081	0.077	0.068	0.094	0.055	0.043	0.062	0.052	0.064	0.040	0.050	0.047	0.093	
Mn	-	-	-	0.002	-	-	-	-	-	-	-	-	-	-	-	-	-	0.002	-	-	-	-	-	-	-	-	-
Mg	0.349	0.333	0.342	0.402	0.345	0.374	0.399	0.346	0.402	0.359	0.382	0.365	0.313	0.349	0.333	0.342	0.402	0.345	0.374	0.399	0.346	0.402	0.359	0.382	0.365	0.313	
Ca	-	0.002	-	-	-	-	0.003	-	0.002	-	-	0.002	0.003	-	0.002	-	-	-	0.003	-	-	0.002	-	-	0.002	0.003	
Na	0.431	0.424	0.428	0.456	0.426	0.427	0.440	0.418	0.434	0.416	0.423	0.421	0.447	0.431	0.424	0.428	0.456	0.426	0.427	0.440	0.418	0.434	0.416	0.423	0.421	0.447	
K	0.003	0.004	0.003	0.006	0.002	0.004	0.006	0.001	0.005	0.004	0.004	0.004	0.003	0.003	0.004	0.003	0.006	0.002	0.004	0.006	0.001	0.005	0.004	0.004	0.004	0.003	
Rb	-	-	-	-	0.002	-	0.005	-	0.007	-	0.005	0.003	-	-	-	-	-	0.002	-	0.005	-	0.007	-	0.005	0.003	-	
Cs	0.003	0.002	0.003	0.003	0.002	0.002	0.001	0.003	0.002	0.003	0.002	0.004	0.003	0.003	0.002	0.003	0.003	0.002	0.002	0.001	0.003	0.002	0.002	0.004	0.003	0.003	
Cl	0.003	-	0.002	0.003	0.001	0.001	-	-	-	0.001	-	0.001	0.004	0.003	-	0.002	0.003	0.001	0.001	-	-	-	-	0.001	0.004	0.003	
F	-	-	-	0.011	0.028	-	-	-	-	-	-	0.015	-	-	-	-	0.011	0.028	-	-	-	-	-	-	0.015	-	
Total	11.450	11.417	11.425	11.494	11.446	11.420	11.448	11.402	11.444	11.410	11.434	11.448	11.445	11.450	11.417	11.425	11.494	11.446	11.420	11.448	11.402	11.444	11.410	11.434	11.448	11.445	

* BeO was not analysed

P₂O₅ was analysed but not detected

- = not detected; na = not analysed

RGM 421620 (continued)		RGM 421622 (Sample 96JCZ 8)													
Oxides (wt.%)	16	17	18	19	20	21	22	14	15	20	21	22	20	21	22
SiO ₂	62.35	62.85	62.60	62.79	62.11	62.16	62.52	63.22	63.40	63.03	63.00	63.41	63.03	63.00	63.41
TiO ₂	0.09	-	0.13	0.10	-	0.10	0.08	-	-	0.02	-	-	0.02	-	-
Al ₂ O ₃	13.17	13.05	13.35	13.20	11.30	13.29	13.27	12.98	14.22	12.86	13.07	13.98	12.86	13.07	13.98
Sc ₂ O ₃	na	na	na	na	na	na	na	0.01	0.00	0.02	0.02	0.00	0.02	0.02	0.00
V ₂ O ₃	0.07	0.08	0.06	0.05	0.14	0.06	0.05	0.07	0.04	0.09	0.08	0.06	0.09	0.08	0.06
Cr ₂ O ₃	1.14	1.56	1.20	1.18	3.05	1.22	1.19	0.66	0.38	1.33	1.48	0.42	1.33	1.48	0.42
BeO*	13.00	13.00	13.00	13.00	13.00	13.00	13.00	13.00	13.00	13.00	13.00	13.00	13.00	13.00	13.00
FeO	1.01	0.63	0.84	0.89	1.07	0.87	0.79	0.76	0.51	0.32	0.34	0.34	0.32	0.34	0.34
MnO	-	-	0.03	-	0.03	-	-	-	-	-	-	-	-	-	-
MgO	2.43	2.59	2.44	2.36	2.71	2.43	2.40	2.48	2.52	2.76	2.71	2.53	2.76	2.71	2.53
CaO	-	-	0.02	0.03	-	-	-	0.05	-	0.02	-	0.03	0.02	-	0.03
Na ₂ O	2.42	2.31	2.33	2.36	2.46	2.35	2.29	2.16	2.01	2.16	2.03	2.01	2.16	2.03	2.01
K ₂ O	0.03	0.04	0.03	0.02	0.03	0.03	0.02	0.07	0.04	0.03	0.05	0.04	0.03	0.05	0.04
Rb ₂ O	-	0.04	0.05	-	0.06	0.09	-	-	-	-	-	-	-	-	-
Cs ₂ O	0.08	0.09	-	0.03	0.10	0.03	0.04	0.09	0.10	0.03	0.03	0.07	0.03	0.03	0.07
Cl	-	-	-	-	-	-	-	-	0.01	-	-	0.01	-	-	0.01
F	-	-	-	-	-	-	0.05	-	-	-	-	-	-	-	-
Total	95.78	96.23	96.06	96.00	96.05	95.62	95.65	95.55	96.21	95.66	95.81	95.89	95.66	95.81	95.89

Ions based on 18 Oxygens													
Si	5.981	5.996	5.982	6.000	5.990	5.971	5.992	6.039	6.011	6.026	6.013	6.025	
Ti	0.006	-	0.009	0.007	-	0.007	0.005	-	-	0.001	-	-	
Al	1.488	1.467	1.503	1.486	1.284	1.505	1.499	1.462	1.589	1.449	1.471	1.565	
Sc	0.006	0.006	0.005	0.004	0.011	0.005	0.004	0.000	0.000	0.002	0.002	0.000	
V	0.087	0.118	0.091	0.089	0.232	0.092	0.090	0.050	0.003	0.007	0.006	0.005	
Cr	2.996	2.980	2.984	2.985	3.012	3.000	2.993	2.983	0.029	0.100	0.111	0.031	
Be *	0.081	0.050	0.067	0.071	0.087	0.070	0.064	0.061	2.961	2.986	2.981	2.968	
Fe	-	-	0.002	-	0.002	-	-	-	0.040	0.026	0.027	0.027	
Mn	0.348	0.368	0.347	0.336	0.390	0.348	0.342	0.391	-	-	-	-	
Mg	-	-	0.002	0.003	-	-	-	0.005	0.356	0.394	0.386	0.359	
Ca	0.449	0.427	0.431	0.438	0.460	0.437	0.425	0.401	-	0.002	-	0.003	
Na	0.003	0.005	0.003	0.003	0.003	0.004	0.002	0.009	0.369	0.401	0.376	0.370	
K	-	0.003	0.003	-	0.004	0.006	-	-	0.005	0.003	0.006	0.005	
Rb	0.003	0.004	-	0.001	0.004	0.001	0.002	0.004	-	-	-	-	
Cs	-	-	-	-	-	-	-	-	0.004	0.001	0.001	0.003	
Cl	-	-	-	-	-	-	-	-	0.001	-	-	0.001	
F	-	-	-	-	-	-	0.016	-	-	-	-	-	
Total	11.448	11.423	11.429	11.422	11.479	11.445	11.435	11.409	11.367	11.397	11.381	11.361	

* BeO was not analysed

P₂O₅ was analysed but not detected

- = not detected; na = not analysed

Emerald analyses (continued)

Oxides (wt.%)	RGM 421619 (Sample 96 J CZ 9)			RGM 421369			RGM 421545		
	32	33	34	34	35	42	43	43	
SiO ₂	63.09	62.62	62.95	62.42	62.39	62.90	63.14		
ThO ₂	0.02	0.02	0.02	-	-	0.02	-		
Al ₂ O ₃	13.09	13.33	12.67	12.21	13.41	12.76	13.06		
Sc ₂ O ₃	0.01	-	-	na	na	na	na		
V ₂ O ₅	0.07	0.05	0.07	0.06	0.06	0.05	0.04		
Cr ₂ O ₃	0.99	0.48	0.97	0.57	0.01	1.23	0.36		
BeO*	13.00	13.00	13.00	13.00	13.00	13.00	13.00		
FeO	0.58	0.59	0.68	1.23	0.84	0.45	0.57		
MnO	-	-	-	-	-	0.03	-		
MgO	2.73	2.66	2.87	2.80	2.40	2.80	2.84		
CaO	0.02	0.02	0.03	-	-	-	-		
Na ₂ O	2.37	2.36	2.48	2.19	2.08	1.58	1.65		
K ₂ O	0.05	0.05	0.05	0.03	0.02	0.04	0.03		
Rb ₂ O	-	-	-	-	-	-	-		
Cs ₂ O	0.10	0.04	0.07	-	-	0.08	0.04		
Cl	0.01	-	-	na	na	na	na		
F	-	-	-	na	na	na	na		
Total	96.11	95.20	95.85	94.51	94.21	94.93	94.72		

Ions based on 18 Oxygens									
Si	6.016	6.012	6.023	6.048	6.033	6.045	6.064		
Ti	0.002	0.001	0.001	-	-	0.001	-		
Al	1.471	1.508	1.429	1.393	1.527	1.444	1.477		
Sc	0.001	-	-	-	-	-	-		
V	0.005	0.004	0.006	0.005	0.005	0.004	0.003		
Cr	0.074	0.036	0.074	0.043	0.001	0.093	0.027		
Be*	2.978	2.999	2.988	3.026	3.020	3.001	2.999		
Fe	0.046	0.048	0.054	0.100	0.068	0.036	0.046		
Mn	-	-	-	-	-	0.003	-		
Mg	0.388	0.380	0.409	0.404	0.346	0.401	0.407		
Ca	0.002	0.002	0.003	-	-	-	-		
Na	0.439	0.439	0.461	0.412	0.391	0.294	0.307		
K	0.006	0.006	0.006	0.003	0.002	0.005	0.003		
Rb	-	-	-	-	-	-	-		
Cs	0.004	0.001	0.003	-	-	0.003	0.002		
Cl	0.001	-	-	-	-	-	-		
F	-	-	-	-	-	-	-		
Total	11.432	11.436	11.456	11.434	11.393	11.330	11.335		

* BeO was not analysed

P₂O₅ was analysed but not detected

- = not detected; na = not analysed

Oxides (wt.%)	RGM 421550										RGM 421552	
	27	28	29	30	31	32	33	34	49	50	51	52
SiO ₂	63.79	63.52	63.75	63.58	63.94	63.33	63.28	63.86	63.35	63.32	63.60	63.86
TiO ₂	0.02	-	-	-	-	-	-	0.02	-	-	0.02	-
Al ₂ O ₃	14.84	13.79	14.95	13.78	14.38	13.47	13.78	14.80	14.19	13.53	14.48	14.28
V ₂ O ₅	0.03	0.05	-	0.05	0.04	0.06	0.04	0.05	0.05	0.05	0.05	0.04
Cr ₂ O ₃	0.54	0.81	0.60	0.96	0.10	1.16	0.74	0.07	0.79	1.20	0.57	0.64
BeO*	13.00	13.00	13.00	13.00	13.00	13.00	13.00	13.00	13.00	13.00	13.00	13.00
FeO	0.26	0.43	0.35	0.44	0.58	0.51	0.51	0.51	0.47	0.52	0.36	0.39
MnO	-	-	-	-	-	-	-	-	-	-	-	0.04
MgO	2.26	2.69	2.23	2.68	2.74	2.76	2.77	2.54	2.55	2.79	2.49	2.49
CaO	-	-	-	-	-	0.02	-	0.02	-	-	-	-
Na ₂ O	1.75	1.91	2.09	2.19	1.64	1.56	2.33	2.02	1.53	1.56	2.04	2.01
K ₂ O	0.02	0.03	0.03	0.04	0.03	0.03	0.03	0.02	0.03	0.03	0.02	0.03
Rb ₂ O	-	-	-	-	-	-	-	-	-	-	-	-
Cs ₂ O	-	0.11	0.06	0.11	0.08	0.07	0.11	0.06	-	0.05	0.07	0.06
Total	96.52	96.33	97.04	96.83	96.53	95.96	96.61	96.98	95.96	96.04	96.68	96.84

Emerald analyses (continued)

Ions based on 18 Oxygens

Si	6.009	6.019	5.991	6.007	6.029	6.022	5.996	6.002	6.009	6.017	6.000	6.016
Ti	0.002	-	-	-	-	-	-	0.001	-	-	0.001	0.000
Al	1.646	1.539	1.654	1.533	1.597	1.509	1.538	1.638	1.585	1.514	1.609	1.584
V	0.002	0.004	-	0.004	0.003	0.005	0.003	0.004	0.004	0.004	0.004	0.003
Cr	0.040	0.061	0.044	0.071	0.007	0.087	0.056	0.005	0.059	0.090	0.042	0.048
Be*	2.942	2.959	2.935	2.951	2.945	2.970	2.959	2.935	2.962	2.968	2.946	2.942
Fe	0.021	0.034	0.027	0.035	0.045	0.040	0.041	0.040	0.037	0.042	0.028	0.031
Mn	-	-	-	-	-	-	-	-	-	-	-	0.003
Mg	0.318	0.379	0.312	0.377	0.385	0.391	0.391	0.356	0.361	0.395	0.350	0.350
Ca	-	-	-	-	-	0.002	-	0.002	-	-	-	0.000
Na	0.319	0.351	0.380	0.400	0.300	0.288	0.429	0.368	0.282	0.287	0.373	0.368
K	0.003	0.003	0.004	0.005	0.004	0.003	0.004	0.003	0.004	0.003	0.003	0.004
Rb	-	-	-	-	-	-	-	-	-	-	-	-
Cs	-	0.004	0.002	0.005	0.003	0.003	0.005	0.002	-	0.002	0.003	0.002
Total	11.302	11.353	11.349	11.388	11.318	11.320	11.422	11.356	11.303	11.322	11.359	11.351

* BeO was not analysed

P₂O₅ was analysed but not detected

- = not detected; na = not analysed

Appendix 2. Emerald analyses by PIXE/PIGE

Sample No.	Description
RGM	
421596 (96JCZ1)	amphibole phlogopite schist, Zeus mine, 200', 26/28 (6)
421588 (96JCZ4)	Pale green emerald in amphibole stringer in pegmatite, Zeus mine, 200', 26/28 (5)
421620 (96JCZ7)	amphibole phlogopite schist, Zeus mine, 300', 23/7
421632	Cut emerald, 1.87 ct
421672	Cut emerald, 0.29 ct
421631	Cut emerald, 0.28 ct
421614	Cut emerald, 0.12 ct
421615	Cut emerald, 0.13 ct
421630	Cut emerald, 0.15 ct
421707	Cut emerald, 0.32 ct
421708	Cut emerald, 0.24 ct
421709	Cut emerald, 0.26 ct

The cut emeralds were all faceted in the cutting factory of Sandawana Mines Pvt. Ltd. in Harare and are now part of the Naturalis gem collection.

Emerald analyses pixe/pige

Sample	421596		421588		421620		421632		421672		421631	
Analysis	Zw003	Zw004	Zw005	Zw006	Zw007	Zw008	Zw009	Zw010	Zw011	Zw012	Zw013	
Oxide (wt.%)												
BeO	11.7	12.0	12.0	12.6	13.2	13.7	14.0	13.1	13.6	11.2	11.7	
Na ₂ O	2.7	2.9	2.7	2.8	2.6	2.6	2.8	2.8	2.8	2.9	2.4	
MgO	3.0	3.4	3.1	3.2	3.0	3.0	3.2	3.1	3.3	3.1	2.7	
Al ₂ O ₃	15.4	14.8	15.0	14.9	13.8	13.9	14.2	14.2	14.4	15.2	15.3	
SiO ₂	66.1	65.7	66.0	65.7	65.1	64.6	64.4	65.2	64.3	66.4	66.7	
K ₂ O	0.03	0.03	0.05	0.04	0.01	0.03	0.05	0.06	0.02	0.04	0.04	
CaO	0.01	0.01	0.01	0.01	0	0	0.02	0.03	0.03	0.02	0.02	
Element (ppm)												
Li	1070	790	1000	1040	590	570	280	250	520	490	520	
F	20	10	20	30	20	20	40	20	60	40	10	
Ti	21	0	0	0	0	4	0	0	0	0	0	
V	218	214	108	151	248	252	277	295	279	259	237	
Cr	3502	5052	2733	1385	10833	10494	3428	3728	3773	3724	3902	
Mn	21	67	11	15	89	101	16	9	566	76	93	
Fe	3519	3382	4529	4095	4438	4153	5437	6240	5763	3767	4320	
Ni	17	16	16	15	16	18	15	15	29	16	12	
Cu	0	0	1	1	2	1	0	1	0	0	0	
Zn	59	54	55	47	59	66	24	27	60	54	77	
Ga	19	19	14	18	43	47	41	45	28	34	26	
Rb	307	298	587	564	970	761	148	175	132	163	180	
Cs	728	717	1033	1025	690	549	805	857	80	301	231	

LOD = limit of detection

421614		421615		421630		421707		421708		421709		LOD
Zw016	Zw017	Zw019	Zw020	Zw021	Zw022	Zw023	Zw024	Zw025	Zw026	Zw027	Zw028	
12.9	13.2	15.3	14.3	14.4	14.1	12.9	13.6	13.9	13.6	14.2	13.9	0.20
2.6	3.0	2.7	2.7	4.6	2.8	2.8	2.8	2.6	2.4	2.5	2.4	0.03
6.1	4.2	3.2	3.4	3.1	3.2	3.1	3.1	2.9	2.8	2.9	3.0	0.02
11.6	12.8	13.5	13.6	12.6	13.3	13.9	13.7	13.8	13.8	14.4	14.3	0.02
63.2	63.6	63.8	64.3	62.1	64.4	65.2	64.8	64.9	65.4	64.7	64.9	0.01
0.04	0.05	0.04	0.06	0.27	0.05	0.04	0.02	0.03	0.04	0.03	0.05	0.01
0.16	0.09	0.03	0.03	0.03	0.02	0.06	0.01	0.02	0.03	0.02	0.04	0.00
620	720	930	800	690	680	1070	1210	1280	1340	1080	1010	50
70	90	50	40	50	50	20	10	10	40	30	10	60
0	0	2	0	0	0	621	679	614	645	107	137	30
205	220	243	265	209	191	107	84	128	158	211	232	10
5328	5390	4915	5367	6921	6258	5953	6238	5491	5531	4688	4919	10
1435	961	45	56	39	55	50	61	65	63	25	46	20
16783	14235	5555	5941	8295	8313	6293	6433	6517	6812	4206	4826	3
55	45	18	19	18	15	11	12	18	18	26	23	2
1	0	1	0	7	0	3	3	3	2	0	1	2
143	123	82	75	95	90	45	49	59	63	53	57	2
25	28	29	27	30	31	34	39	35	33	23	23	2
272	295	333	350	323	322	275	263	325	334	246	255	2
763	520	753	1386	1297	891	735	245	708	616	721	694	100

Appendix 3. Representative mineral analyses by EPMA

Phlogopite analyses

Sample no.	From rock type	Locality
RGM 421354 (Sample pdd 1354)	contact schist-pegmatite	Zeus mine, 250', 17/16
RGM 421355 (Sample pdd 1355)	contact schist-pegmatite	Zeus mine, 250', 17/16
RGM 421551 (Sample 96/CZ2)	Amphibole/ phlogopite schist/ emerald	Zeus mine, 200', 26/28 (2)
RGM 421545 (Sample pdd 1545) (96ZW006A)	contact schist-pegmatite	Zeus mine, 200' level, 26/28

Sample Analysis	RGM 421355										RGM 421545										RGM 421354									
	pdd1355 24	pdd1355 26	pdd1355 pht.Li1	pdd1355 pht.Li2	pdd1545 46	pdd1545 pht1c	pdd1545 47	pdd1545 pht1r	pdd1545 66	pdd1545 pht2a	pdd1545 67	pdd1545 pht2b	pdd1545 68	pdd1545 pht2c	pdd1354 09	pdd1354 pht1a	pdd1354 10	pdd1354 pht1b	pdd1354 13	pdd1354 pht2a	pdd1354 14	pdd1354 pht2b								
SiO ₂	42.05	42.81	41.07	41.06	40.46	40.80	40.80	40.42	42.01	41.76	41.78	41.78	41.78	42.01	41.76	41.76	41.76	41.02	41.02	41.78	41.78	41.78								
TiO ₂	-	0.02	0.26	0.07	0.91	1.13	1.10	1.10	1.13	1.10	1.10	1.10	1.10	0.35	0.33	0.33	0.33	0.35	0.35	0.38	0.38	0.38								
Al ₂ O ₃	11.93	11.93	12.97	13.57	12.88	12.76	12.76	12.76	12.65	12.76	12.76	12.76	12.76	13.57	13.57	13.92	13.92	13.81	13.81	13.93	13.93	13.93								
V ₂ O ₅ *	0.28	0.23	0.03	0.06	0.03	0.03	0.06	0.06	-	-	-	-	-	0.03	0.03	-	-	-	-	-	-	-								
Cr ₂ O ₃	1.25	0.18	0.14	0.18	0.55	0.62	0.62	0.62	0.96	0.96	0.96	0.96	0.96	0.42	0.42	0.25	0.25	0.72	0.72	0.65	0.65	0.65								
FeO	9.46	9.68	11.71	11.87	10.43	9.96	10.20	10.20	9.96	9.96	9.96	9.96	9.96	9.72	9.66	9.66	9.66	9.28	9.28	9.58	9.58	9.58								
MnO	0.15	0.17	0.06	0.07	0.06	0.06	0.06	0.06	0.06	0.06	0.06	0.06	0.06	0.16	0.19	0.19	0.19	0.16	0.16	0.13	0.13	0.13								
MgO	19.89	20.35	18.61	18.15	19.98	19.52	19.52	19.68	19.98	19.98	19.98	19.98	19.68	19.81	19.74	19.74	19.74	19.78	19.78	19.98	19.98	19.98								
ZnO	0.03	0.10	0.08	0.08	0.07	0.07	0.07	0.07	-	-	-	-	0.07	0.05	0.05	0.05	0.05	-	-	-	-	-								
Na ₂ O	0.26	0.27	0.24	0.21	0.25	0.31	0.31	0.26	0.31	0.31	0.31	0.31	0.26	0.85	0.87	0.87	0.87	0.95	0.95	0.94	0.94	0.94								
K ₂ O	7.38	7.28	6.66	6.93	6.72	7.11	7.11	6.94	7.11	7.11	7.11	7.11	6.94	6.58	6.48	6.48	6.48	6.41	6.41	6.56	6.56	6.56								
Rb ₂ O	0.27	0.29	0.52	0.49	0.49	0.50	0.50	0.50	0.49	0.49	0.49	0.50	0.50	0.48	0.51	0.51	0.51	0.54	0.54	0.49	0.49	0.49								
BaO**	-	-	-	-	-	-	-	-	-	-	-	-	-	-	-	-	-	0.07	0.07	-	-	-								
F	0.61	0.63	0.61	0.74	0.65	0.64	0.64	0.65	0.64	0.64	0.64	0.64	0.65	1.02	1.00	1.00	1.00	1.02	1.02	0.94	0.94	0.94								
Cl	0.02	0.02	0.03	0.04	0.02	0.02	0.02	0.02	0.02	0.02	0.02	0.02	0.02	0.01	0.01	0.01	0.01	-	-	0.01	0.01	0.01								
O=F-Cl	-0.26	-0.27	-0.26	-0.32	-0.28	-0.27	-0.27	-0.28	-0.28	-0.28	-0.27	-0.27	-0.28	-0.43	-0.42	-0.42	-0.42	-0.43	-0.43	-0.40	-0.40	-0.40								
H ₂ O ₂ calc	3.81	3.82	3.75	3.70	3.77	3.77	3.77	3.76	3.77	3.77	3.77	3.76	3.76	3.69	3.69	3.69	3.69	3.65	3.65	3.74	3.74	3.74								
Total_calc	97.13	97.49	96.47	96.88	97.01	96.81	96.81	96.73	96.81	96.81	96.81	96.81	96.73	98.32	98.05	98.05	98.05	97.35	97.35	98.75	98.75	98.75								

Ions based on 20 Oxygens and 4 (OH, F, Cl)												
Si IV	6.177	6.242	6.106	6.088	5.968	6.023	5.980	6.075	6.051	5.996	6.017	
Al IV	1.823	1.758	1.894	1.912	2.032	1.977	2.020	1.925	1.949	2.004	1.983	
T site	8.000	8.000	8.000	8.000	8.000	8.000	8.000	8.000	8.000	8.000	8.000	
Al VI	0.241	0.291	0.377	0.458	0.205	0.222	0.203	0.386	0.426	0.373	0.380	
Ti VI	-	0.002	0.030	0.007	0.101	0.125	0.122	0.038	0.036	0.038	0.041	
V	0.033	0.027	0.004	0.007	0.004	-	-	0.003	-	-	-	
Cr	0.144	0.020	0.016	0.021	0.064	0.072	0.071	0.048	0.029	0.083	0.074	
Fe ²⁺	1.162	1.181	1.456	1.472	1.286	1.230	1.262	1.175	1.171	1.135	1.153	
Mn ²⁺	0.019	0.021	0.007	0.008	0.007	0.008	0.007	0.019	0.023	0.020	0.016	
Mg	4.356	4.424	4.124	4.012	4.393	4.297	4.341	4.271	4.264	4.310	4.290	
Zn	0.000	0.010	0.010	0.010	0.010	0.000	0.010	0.010	0.010	-	-	
O site	5.955	5.976	6.024	5.995	6.070	5.954	6.016	5.950	5.959	5.960	5.954	
Na	0.074	0.076	0.068	0.059	0.072	0.088	0.073	0.238	0.245	0.270	0.264	
K	1.384	1.353	1.263	1.311	1.265	1.339	1.310	1.214	1.198	1.195	1.205	
Rb	0.025	0.027	0.050	0.046	0.046	0.047	0.047	0.045	0.047	0.051	0.045	
Ba	-	-	-	-	-	-	-	-	-	0.004	-	
A site	1.483	1.456	1.381	1.416	1.383	1.473	1.429	1.497	1.491	1.520	1.514	
OH _{calc}	3.729	3.719	3.723	3.659	3.708	3.715	3.708	3.558	3.566	3.555	3.591	
F	0.268	0.277	0.271	0.331	0.288	0.281	0.287	0.440	0.433	0.445	0.407	
Cl	0.003	0.004	0.006	0.010	0.004	0.004	0.005	0.002	0.001	-	0.002	
Anion	4.000	4.000	4.000	4.000	4.000	4.000	4.000	4.000	4.000	4.000	4.000	

* corrected value, based on overlap with Ti-K8

** corrected value, based on overlap with Ti-K(alpha)

- = below detection limit

detection limits (in wt.%) for MnO 0.022, BaO 0.043, CaO 0.018, Rb₂O 0.035, TiO₂ 0.024, K₂O 0.016, F 0.055 and Cl 0.007.
 O=F or O=F-Cl is a correction for the calculation of too much O in the presence of F and/or Cl.

Phlogopite analyses (continued)

RGM 421551				
Sample Analysis Location	96JCZ2 5 2-ph.5	96JCZ2 6 2-ph.5'	96JCZ2 7 2-phl.E	96JCZ2 8 2-phl.F
SiO ₂	40.94	41.12	40.89	40.92
TiO ₂	0.95	0.63	0.81	0.81
Al ₂ O ₃	12.70	12.86	13.11	13.13
Cr ₂ O ₃	0.64	0.72	0.77	0.68
FeO	9.79	10.24	8.61	8.38
MnO	0.09	0.06	0.04	0.04
MgO	18.70	19.18	19.89	19.89
BaO	-	-	0.04	-
CaO	0.03	0.05	-	-
Na ₂ O	0.23	0.24	0.26	0.28
K ₂ O	7.16	6.89	7.39	7.39
Rb ₂ O	0.69	0.84	0.82	0.79
F	0.71	0.73	0.95	0.79
Cl	0.01	0.02	0.02	0.01
O=F	-0.30	-0.31	-0.40	-0.33
O=Cl	0.00	0.00	0.00	0.00
H ₂ O _{calc}	3.83	3.81	3.72	3.81
Total	96.18	97.07	96.92	96.58

Ions based on 22 Oxygens				
Si IV	6.100	6.070	6.030	6.040
Al IV	1.900	1.930	1.970	1.960
T site	8.000	8.000	8.000	8.000
Al VI	0.330	0.310	0.310	0.330
Th VI	0.110	0.070	0.090	0.090
Cr	0.080	0.080	0.090	0.080
Fe ²⁺	1.220	1.270	1.060	1.040
Mn ²⁺	0.010	0.010	0.000	0.010
Mg	4.150	4.220	4.370	4.380
O site	5.890	5.960	5.920	5.910
Ba	-	-	0.000	-
Ca	0.010	0.010	-	-
Na	0.070	0.070	0.080	0.080
K	1.360	1.300	1.390	1.390
Rb	0.070	0.080	0.080	0.070
Cs	0.000	0.000	0.000	0.000
A site	1.500	1.450	1.550	1.550
OH_calc	3.660	3.650	3.550	3.630
F	0.330	0.340	0.440	0.370
Cl	0.000	0.000	0.000	0.000
Anion	3.990	3.990	3.990	4.000

Actinolite analyses

Sample no.	from rock type	Locality
RGM 421354 (Sample pdd 1354)	contact schist-pegmatite	Zeus mine, 250', 17/16
RGM 421355 (Sample pdd 1355)	contact schist-pegmatite	Zeus mine, 250', 17/16
RGM 421545 (Sample pdd 1545)	contact pegmatite/schist	Zeus mine, 200', 26/28
RGM 421550 (Sample pdd 1550)	contact pegmatite/schist	Zeus mine, 200', 26/28
RGM 421596 (Sample 96JCZ1)	amphibole phlogopite schist/ emerald	Zeus mine, 200', 26/28 (6)
RGM 421619 (Sample 96JCZ 9)	amphibole phlogopite schist/ emerald	Zeus mine, 200', 25/28

Sample Analysis Location	RGM 421355			RGM 421545			RGM 421354													
	pdd 05	am1e	am1g	pdd1545 53	am2f	pdd1545 60	pdd1545 61	trem1	pdd1545 62	trem2	pdd1545 63	trem2	pdd1545 01	am1c	pdd1354 02	am1	pdd1354 03	am1r	pdd1354 04	am1l
SiO ₂	54.08		53.28	57.33		55.15	55.95		56.46		57.04		56.19		53.06		55.07		54.35	
TiO ₂	0.15		0.08	0.04		0.04	-		0.04		0.02		0.04		0.06		0.07		0.07	
Al ₂ O ₃	2.89		2.84	0.75		2.73	2.16		1.39		0.89		0.90		3.72		2.77		2.95	
Cr ₂ O ₃	0.00		0.01	0.11		0.20	0.12		0.28		0.21		0.01		0.20		0.13		0.04	
FeO	12.54		12.33	6.10		7.45	7.27		6.83		6.20		7.16		8.68		8.12		11.21	
MnO	1.46		0.90	0.34		0.47	0.47		0.46		0.39		0.60		0.85		0.80		1.31	
MgO	17.04		16.62	20.66		19.14	19.70		20.05		20.43		19.85		18.33		19.00		18.70	
CaO	8.67		8.92	12.01		11.24	11.32		11.64		11.96		11.96		10.54		10.59		8.20	
Na ₂ O	1.68		1.48	0.43		1.09	0.92		0.71		0.52		0.54		1.40		1.26		1.11	
K ₂ O	0.04		0.03	0.02		0.04	0.04		0.02		-		-		0.08		0.05		0.04	
F	0.20		0.13	0.18		0.26	0.30		0.26		0.15		0.39		0.45		0.42		0.27	
Cl	-		-	-		-	-		-		-		-		-		-		-	
O=F-Cl	-0.08		-0.06	-0.08		-0.11	-0.13		-0.11		-0.06		-0.16		-0.19		-0.18		-0.11	
Total	98.67		96.57	97.90		97.70	98.13		98.04		97.76		97.48		97.18		98.10		98.14	
H ₂ O _{calc}	2.02		2.01	2.08		2.02	2.01		2.03		2.09		1.96		1.90		1.95		1.99	

Ions based on 22 O and 2 (OH,F,Cl)												
	7.698	7.728	7.959	7.748	7.810	7.873	7.940	7.906	7.579	7.738	7.701	
Si IV	0.302	0.272	0.041	0.252	0.190	0.127	0.060	0.094	0.421	0.262	0.299	
Al IV	8.000	8.000	8.000	8.000	8.000	8.000	8.000	8.000	8.000	8.000	8.000	
T site	0.182	0.213	0.082	0.200	0.165	0.101	0.086	0.055	0.205	0.196	0.193	
Al VI	0.016	0.009	0.004	0.004	-	0.005	0.002	0.004	0.006	0.007	0.007	
Ti	0.000	0.001	0.012	0.022	0.013	0.031	0.023	0.001	0.023	0.015	0.005	
Cr	3.616	3.593	4.276	4.008	4.100	4.167	4.240	4.164	3.903	3.980	3.950	
Mg	1.186	1.184	0.626	0.766	0.722	0.696	0.649	0.776	0.863	0.802	0.845	
Fe ²⁺	5.000	5.000	5.000	5.000	5.000	5.000	5.000	5.000	5.000	5.000	5.000	
M1,2,3	0.307	0.312	0.082	0.109	0.127	0.101	0.073	0.066	0.174	0.152	0.483	
Fe ²⁺	0.177	0.111	0.040	0.055	0.056	0.054	0.046	0.072	0.102	0.096	0.157	
Mn	1.322	1.386	1.786	1.692	1.693	1.739	1.784	1.803	1.613	1.594	1.245	
Ca	0.194	0.191	0.092	0.144	0.124	0.106	0.097	0.059	0.111	0.158	0.115	
Na	2.000	2.000	2.000	2.000	2.000	2.000	2.000	2.000	2.000	2.000	2.000	
M4 site	0.271	0.226	0.024	0.154	0.125	0.087	0.044	0.088	0.277	0.184	0.190	
Na	0.007	0.005	0.003	0.008	0.007	0.004	-	-	0.015	0.008	0.007	
K	0.278	0.231	0.027	0.162	0.132	0.091	0.044	0.088	0.292	0.192	0.197	
A site	1.920	1.940	1.925	1.892	1.875	1.890	1.938	1.837	1.807	1.825	1.885	
OH _{calc}	0.080	0.060	0.074	0.108	0.125	0.110	0.062	0.163	0.193	0.175	0.115	
F	-	-	-	-	-	-	-	-	-	-	-	
Cl	-	-	-	-	-	-	-	-	-	-	-	
Anion	2.000	2.000	2.000	2.000	2.000	2.000	2.000	2.000	2.000	2.000	2.000	

- below detection limit

detection limits (in wt.%) for TiO₂ 0.024, K₂O 0.016, F 0.055 and Cl 0.013.

O = F-Cl is a correction for the calculation of too much O in the presence of F and/or Cl.

Actinolite analyses (continued)

Sample Analysis Location	RGM 421550		RGM 421596				RGM 421619				
	pdd1550 41	pdd1550 42	96JCZ1 1	96JCZ1 2	96JCZ1 3	96JCZ1 4	96JCZ1 5	96JCZ1 6	96JCZ9 amf-a1	96JCZ9 amf-a3	96JCZ9 amf-a6
SiO ₂	56.07	55.92	54.06	53.26	54.55	55.63	54.78	54.80			
TiO ₂	0.04	0.07	0.05	0.05	0.03	0.09	0.07	0.11			
Al ₂ O ₃	1.65	1.59	2.91	3.52	2.76	1.66	2.27	3.63			
Cr ₂ O ₃	0.00	0.02	0.31	0.36	0.42	0.07	0.22	0.33			
FeO	6.77	6.95	8.40	7.97	6.68	7.12	7.18	7.03			
MnO	0.45	0.49	0.41	0.43	0.37	0.34	0.32	0.36			
MgO	19.81	20.11	18.28	17.99	19.10	19.55	19.15	17.72			
CaO	11.09	11.24	11.93	11.94	11.82	11.75	11.94	10.45			
Na ₂ O	0.76	0.77	0.96	1.08	1.01	0.79	0.89	1.23			
K ₂ O	0.04	0.03	0.06	0.07	0.05	0.02	0.02	0.03			
F	0.17	0.22	0.22	0.32	0.26	0.21	0.19	0.25			
Cl	-	-	-	-	-	-	-	-			
O=F-Cl	-0.07	-0.09	-0.09	-0.13	-0.11	-0.09	-0.08	-0.10			
Total	96.76	97.33	97.51	96.86	96.95	97.14	96.95	95.84			
H ₂ O _{calc}	2.05	2.04	2.01	1.95	1.99	2.03	2.02	1.99			

Cummingtonite analyses

Sample no.	from rock type	Locality
RGM 421355 (Sample pdd 1355)	contact schist-pegmatite	Zeus mine, 250', 17/16
RGM 421545 (Sample pdd 1545)	contact pegmatite/ schist	Zeus mine, 200', 26/28
RGM 421550 (Sample pdd 1550)	contact pegmatite/ schist	Zeus mine, 200', 26/28
RGM 421552 (Sample pdd 1552)	amphibole/emerald in pegmatite	Zeus mine, 200', 26/28
RGM 421596 (Sample 96[CZ1])	amphibole phlogopite schist (in emerald)	Zeus mine, 200', 26/28 (6)
RGM 421622 (Sample 96[CZ 8])	amphibole phlogopite schist	Orpheus mine, open pit
RGM 421619 (Sample 96 [CZ 9])	amphibole phlogopite schist	Zeus mine, 200', 25/28

Sample Analysis	RGM 421355						RGM 421545						
	pdd 1355 01	pdd 1355 02	pdd 1355 18	pdd 1355 am2core	pdd 1355 19	pdd 1355 21	pdd 1355 22	pdd 1355 48	pdd 1355 49	pdd 1355 50	pdd 1545 am2a	pdd 1545 am2b	pdd 1545 am2c
Location	am1a	am1b	am2core	am2rim	am3a	am3b	am3b	am2a	am2b	am2c			
SiO ₂	55.91	55.47	55.90	56.00	55.76	55.94	55.94	56.91	57.04	56.92			
TiO ₂	0.02	0.04	-	0.02	-	0.02	0.02	-	0.03	0.02			
Al ₂ O ₃	0.46	0.54	0.47	0.38	0.44	0.45	0.45	0.59	0.60	0.81			
Cr ₂ O ₃	-	-	0.08	0.07	0.03	-	-	0.13	0.17	0.19			
FeO	18.51	19.05	19.41	19.33	18.90	19.11	19.11	16.66	16.66	16.13			
MnO	3.24	2.98	3.32	3.24	3.29	3.25	3.25	1.60	1.57	1.51			
MgO	18.14	17.83	18.07	18.39	18.25	18.28	18.28	21.13	21.19	21.19			
CaO	0.98	1.12	0.93	1.01	1.06	0.89	0.89	0.45	0.43	0.43			
Na ₂ O	0.61	0.75	0.55	0.48	0.63	0.59	0.59	0.35	0.38	0.39			
K ₂ O	-	-	-	-	-	-	-	-	-	-			
F	0.13	0.18	0.10	0.13	0.13	0.14	0.14	0.14	0.13	0.15			
O=F	-0.06	-0.08	-0.04	-0.05	-0.05	-0.06	-0.06	-0.06	-0.05	-0.06			
Total	97.94	97.89	98.78	99.00	98.44	98.60	98.60	97.90	98.15	97.68			
H ₂ O _{calc}	2.02	1.99	2.05	2.04	2.03	2.03	2.03	2.06	2.07	2.06			

Ions based on 22O and 2 (OH,F)										
Si IV	8.058	8.027	8.024	8.017	8.020	8.030	8.048	8.046	8.045	
Al IV	0.000	0.000	0.000	0.000	0.000	0.000	0.000	0.000	0.000	
T site	8.058	8.027	8.024	8.017	8.020	8.030	8.048	8.046	8.045	
Al VI	0.078	0.092	0.079	0.064	0.075	0.076	0.098	0.100	0.135	
Ti	0.002	0.004	-	0.002	-	0.002	-	0.003	0.002	
Cr	-	-	0.009	0.008	0.004	-	0.014	0.019	0.021	
Mg	3.898	3.847	3.866	3.925	3.913	3.912	4.455	4.456	4.465	
Fe ²⁺	1.022	1.057	1.046	1.001	1.008	1.010	0.433	0.422	0.377	
Ca	0.000	0.000	0.000	0.000	0.000	0.000	0.000	0.000	0.000	
M1,2,3	5.000	5.000	5.000	5.000	5.000	5.000	5.000	5.000	5.000	
Fe ²⁺	1.209	1.249	1.284	1.313	1.265	1.284	1.537	1.543	1.530	
Mn	0.395	0.365	0.403	0.393	0.401	0.395	0.192	0.188	0.181	
Ca	0.151	0.174	0.143	0.155	0.163	0.137	0.068	0.065	0.065	
Na	0.169	0.211	0.154	0.133	0.170	0.165	0.097	0.103	0.107	
M4 site	1.924	1.999	1.984	1.994	1.999	1.981	1.894	1.899	1.883	
Na	0.000	0.000	0.000	0.000	0.006	0.000	0.000	0.000	0.000	
K	-	-	-	-	-	-	-	-	-	
A site	0.000	0.000	0.000	0.000	0.006	0.000	0.000	0.000	0.000	
OH_calc	1.940	1.920	1.960	1.950	1.950	1.940	1.941	1.946	1.938	
F	0.060	0.080	0.040	0.050	0.050	0.060	0.059	0.054	0.062	
Anion	2.000	2.000	2.000	2.000	2.000	2.000	2.000	2.000	2.000	

- below detection limit

detection limits (in wt.%) for TiO₂ 0.023, Cr₂O₃ 0.020, K₂O 0.018, F 0.072 and Cl 0.012.

O = F-Cl is a correction for the calculation of too much O in the presence of F.

Cummingtonite analyses (continued)

Sample Analysis Location	RGM 421622				RGM 421619					
	96JCZ8	96JCZ8	96JCZ8	96JCZ8	96JCZ8	96JCZ9	96JCZ8	96JCZ8	96JCZ8	96JCZ8
	1 amf-a1	2 amf-a2	3 amf-b1	4 amf-b2	1 amf-a2	2 amf-a4	3 amf-a5	1 amf-a2	2 amf-a4	3 amf-a5
SiO ₂	56.26	56.33	54.00	56.44	55.57	55.94	55.48	55.57	55.94	55.48
TiO ₂	0.03	0.00	0.03	0.01	0.01	0.00	0.02	0.01	0.00	0.02
Al ₂ O ₃	0.38	0.39	0.44	0.45	0.29	0.23	0.30	0.29	0.23	0.30
Cr ₂ O ₃	0.06	0.03	0.10	0.13	0.12	0.03	0.06	0.12	0.03	0.06
FeO	15.55	15.66	15.66	15.76	17.59	17.49	17.30	17.59	17.49	17.30
MnO	0.60	0.54	0.54	0.66	1.53	1.41	1.44	1.53	1.41	1.44
MgO	22.57	22.55	21.87	22.66	20.17	20.86	20.72	20.17	20.86	20.72
CaO	0.54	0.52	0.59	0.61	0.96	0.84	0.80	0.96	0.84	0.80
Na ₂ O	0.13	0.14	0.19	0.19	0.24	0.20	0.24	0.24	0.20	0.24
K ₂ O	0.00	0.00	0.00	0.00	0.00	0.00	0.00	0.00	0.00	0.00
F	0.03	0.09	0.10	0.00	0.05	0.18	0.10	0.05	0.18	0.10
O=F	-0.01	-0.04	-0.04	0.00	-0.02	-0.07	-0.04	-0.02	-0.07	-0.04
Total	96.14	96.21	93.48	96.91	96.51	97.11	96.42	96.51	97.11	96.42
H ₂ O _{calc}	2.09	2.05	1.99	2.11	2.05	2.00	2.02	2.05	2.00	2.02

Ions based on 22 O and 2 (OH,F)										
Si	8.161	8.094	8.062	7.987	8.108	8.124	8.113	8.153	8.142	8.112
Ti	0.012	0.006	-	0.003	-	-	-	0.002	-	0.001
Al	1.083	1.443	1.651	1.914	1.781	1.791	1.784	1.718	1.740	1.755
Cr	-	-	-	-	-	0.052	0.044	0.049	0.057	0.060
Fe	1.950	1.630	1.425	1.155	1.146	0.684	0.693	0.667	0.680	0.696
Mn	0.024	0.017	0.017	0.035	0.021	0.010	0.010	0.007	0.012	0.009
Mg	2.054	1.959	1.954	1.959	1.986	2.359	2.394	2.428	2.388	2.404
Li*	1.932	1.906	1.895	1.852	1.857	1.831	1.832	1.841	1.845	1.853
Ca	0.003	0.006	0.001	0.008	0.001	0.003	0.001	0.004	0.003	0.003
Na	0.058	0.135	0.100	0.126	0.048	0.020	0.027	0.019	0.020	0.019
Cat total	15.277	15.196	15.105	15.039	14.948	14.874	14.898	14.888	14.887	14.912
F	0.026	0.037	0.026	0.091	0.024	0.028	-	0.033	0.021	-
OH _{calc}	1.973	1.962	1.974	1.909	1.975	1.971	2.000	1.967	1.979	2.000
Anion	1.999	1.999	2.000	2.000	1.999	1.999	2.000	2.000	2.000	2.000

* Li not analysed

- below detection limit

detection limits (in wt.%) for TiO₂ 0.023, Cr₂O₃ 0.020, CaO 0.018, and F 0.055.

O = F is a correction for the calculation of too much O in the presence of F.

RGM 421552						
Sample	pdd1552	pdd1552	pdd1552	pdd1552	pdd1552	pdd1552
Analysis	62	63	64	65	64	65
Location	am3a	am3b	am3c	am3d	am3c	am3d
SiO ₂	61.31	60.41	62.16	60.81		
TiO ₂	-	0.04	0.01	0.03		
Al ₂ O ₃	11.97	8.28	12.25	10.39		
Cr ₂ O ₃	0.10	0.08	0.05	0.53		
FeO	8.59	12.73	7.81	9.98		
MnO	0.13	0.31	0.14	0.18		
MgO	11.30	11.75	11.72	11.50		
Li ₂ O*	3.50	3.50	3.50	3.50		
CaO	0.03	0.07	0.01	0.06		
Na ₂ O	0.22	0.11	0.14	0.08		
F	0.08	-	0.08	-		
O=F	-0.03	-	-0.03	-		
Total	97.20	97.28	97.83	97.05		
H ₂ O ₂ _calc	2.25	2.23	2.28	2.24		
Ions based on 22 O and 2 (OH,F)						
Si	8.043	8.113	8.061	8.062		
Ti	-	0.004	0.001	0.003		
Al	1.848	1.309	1.870	1.622		
Cr	0.011	0.008	0.005	0.055		
Fe	0.942	1.430	0.847	1.106		
Mn	0.015	0.035	0.015	0.020		
Mg	2.210	2.351	2.265	2.273		
Li*	1.846	1.890	1.825	1.866		
Ca	0.004	0.011	0.001	0.009		
Na	0.055	0.028	0.035	0.021		
Cat total	14.974	15.179	14.925	15.037		
F	0.031	-	0.031	-		
OH ₂ _calc	1.969	2.000	1.969	2.000		
Anion	2.000	2.000	2.000	2.000		

Fluorapatite analyses

Sample no.	from rock type		Locality
RGM 421354 (Sample pdd 1354)	contact schist-pegmatite		Zeus mine, 250', 17/16
RGM 421551 (Sample pdd1551)	amphibole phlogopite schist/ emerald (in emerald)		Zeus mine, 200', 26/28 (2)
RGM 421354			
Sample	pdd1354	pdd1354	
Analysis	21	22	
Location	apa1a	apa1b	
P ₂ O ₅	43.18	42.91	
SiO ₂	-	-	
FeO	0.04	0.11	
MnO	0.06	0.07	
CaO	52.45	56.13	
SrO	0.06	0.05	
F	3.23	3.42	
Cl	-	-	
O=F-Cl	-1.36	-1.44	
Total	97.66	101.24	
RGM 421551			
Sample	pdd1551	pdd1551	pdd1551
Analysis	35	36	37
Location	apa1c	apa1ra	apa1rb
P ₂ O ₅	42.81	42.82	42.73
SiO ₂	0.14	-	0.19
FeO	0.04	-	0.10
MnO	0.07	0.03	0.04
CaO	56.41	56.04	55.87
SrO	0.06	0.08	0.12
F	2.75	2.99	3.44
Cl	0.01	0.02	0.06
O=F-Cl	-1.16	-1.26	-1.46
Total	101.12	100.71	101.09
Ions based on 12 O and 1 (OH,F,Cl)			
P	3.094	3.005	2.992
Si	-	-	0.011
Fe	0.003	0.007	0.003
Mn	0.004	0.005	0.005
Ca	4.756	4.974	4.989
Sr	0.003	0.002	0.003
Cations	7.860	7.993	8.003
F	0.819	0.848	0.680
Cl	-	-	0.001
-below detection limit			
detection limits (in wt.%) for SiO ₂ 0.013, FeO 0.025, MnO 0.026, SrO 0.028, Cl 0.008.			
O = F-Cl is a correction for the calculation of too much O in the presence of F and/or Cl.			

Albite analyses

Sample no.	from rock type										Locality				
RGM 421619 (Sample 96 J CZ 9)	emerald in amphibole phlogopite schist										Zeus mine, 200', 25/28				
RGM 421355 (Sample pdd 1355)	contact schist-pegmatite: pegmatite										Zeus mine, 250', 17/16				
RGM 421355															
Sample	pdd1355	pdd1355	pdd1355	pdd1355	pdd1355	pdd1355	pdd1355	pdd1355	pdd1355	pdd1355	pdd1355	pdd1355	pdd1355	pdd1355	96J CZ9
Analysis	08	09	10	11	12	13	14	15	16	17	18	19	20	21	2
Location	55p1	55p2	55p3	55p4	55p5	55p6	55p7	55p8	55p9	55p10	55p11	55p12	55p13	55p14	alb-b3
SiO ₂	68.64	68.76	68.35	68.69	68.7	68.44	68.07	68.86	68.06	68.55	68.55	68.82	68.82	68.82	67.31
Al ₂ O ₃	19.68	19.63	19.93	19.61	19.75	19.86	19.73	19.53	19.54	19.66	19.66	20.15	20.15	20.15	20.42
FeO	-	-	-	-	-	-	-	0.039	-	-	-	-	-	-	0.18
CaO	0.14	0.2	0.17	0.09	0.15	0.15	0.14	0.05	0.23	0.07	0.07	0.84	0.84	0.84	0.91
SrO	0.068	-	0.054	-	0.048	-	-	-	-	-	-	-	-	-	-
Na ₂ O	12.16	11.97	11.93	11.94	11.81	11.74	11.97	11.91	11.97	11.78	11.78	11.32	11.32	11.32	11.27
K ₂ O	-	0.02	-	-	-	0.026	-	-	0.027	0.025	0.025	0.04	0.04	0.04	0.03
Total	100.7	100.58	100.434	100.33	100.458	100.216	99.91	100.389	99.827	100.085	100.085	99.17	99.17	100.12	100.12
RGM 421619															
Si	2.983	2.989	2.976	2.991	2.987	2.982	2.979	2.996	2.983	2.99	2.99	2.95	2.95	2.95	2.95
Al	1.007	1.005	1.022	1.006	1.011	1.019	1.017	1.001	1.008	1.01	1.01	1.05	1.05	1.05	1.05
Fe	-	-	-	-	-	-	-	0.001	-	-	-	-	-	-	-
Ca	0.007	0.009	0.008	0.004	0.007	0.007	0.007	0.002	0.011	0.003	0.003	0.04	0.04	0.04	0.04
Sr	0.002	-	0.001	-	0.001	-	-	-	-	-	-	-	-	-	-
Na	1.025	1.009	1.007	1.008	0.996	0.992	1.016	1.005	1.017	0.996	0.996	0.97	0.97	0.97	0.96
K	0	0.001	0	0.001	0.001	0.001	0	0	0.002	0.001	0.001	0	0	0	0
Cations	5.024	5.013	5.014	5.01	5.003	5.001	5.019	5.005	5.021	5	5	5.01	5.01	5.01	5
Ab	99.3	99	99.2	99.5	99.2	99.2	99.3	99.8	98.7	99.6	99.6	96.0	96.0	96.0	96.0
An	0.7	0.9	0.8	0.4	0.7	0.7	0.7	0.2	1.1	0.3	0.3	4.0	4.0	4.0	4.0
Or	0	0.1	0	0.1	0.1	0.1	0	0	0.2	0.1	0.1	0	0	0	0

- below detection limit

detection limits (in wt.%) for FeO 0.023, SrO 0.028, K₂O 0.011.